Numerical prediction of flow induced noise in free jets of high Mach numbers

A thesis accepted by the Faculty of Aerospace Engineering and Geodesy of the Universität Stuttgart in partial fulfilment of the requirements for the degree of Doctor of Engineering Sciences (Dr.-Ing.)

by

Olaf Schönrock

born in Frankfurt(Oder)

main referee: Prof. Dr. rer. nat. habil. Claus-Dieter Munz
co-referee: Prof. Dr.-Ing. habil. Bernhard Weigand

Date of defence: 20.03.2009

Institute of Aerodynamics and Gasdynamics
Universität Stuttgart
2009

Acknowledgements

This doctoral thesis was written in the context of an industrial study performed at the Robert Bosch GmbH in Gerlingen-Schillerhöhe. Here I had the opportunity to experience industrial research in a very professional environment. The working conditions in terms of computational and measurement equipment as well as on a personal level were excellent. I especially profited from the live discussions and the collaboration across department bounds. Eventually coworkers turned into good friends.

As my doctoral adviser at Bosch Dr. Martin Fischer trusted in me and arranged for everything I needed. He left me the space to do research independently of the day-to-day business an employee normally has to cope with, yet I got an invaluable insight into the strategic thinking and the benefit-driven research in industry. Thus he took a reasonable part in making this work a success on one hand and a huge personal gain for me on the other hand.

Due to the product-relation of my studies I came into contact with several engineering departments outside the corporate sector research as well. Amongst others Dr. Förster as one of the initiators of this work, Thorsten Allgeier and Andreas Binder helped me to develop a better product comprehension and get an insight into advance engineering, market and product requirements. They supported me with directions and additional measurements. I am very grateful for this experience far beyond research and hope to have contributed to the engineering project in return.

On side of the Universität Stuttgart my doctoral adviser Prof. Claus-Dieter Munz deserves a lot of appreciation for the courtesy of providing the NSDG2D code and for his continuous support and guidance over more than just the last couple of years. In fact, without his advice I would not have even known about the vacant position at Bosch.

Moreover, several (former) PhD students at the Universität Stuttgart, first of all Christoph Altmann, Dr. Gregor Gassner and Dr. Jens Utzmann helped by their qualified technical support and effort to push forward my investigations into the research code NSDG2D.

Last not least my parents supported me in any possible way and since I can think. Amongst others they cared for my financial independence during my studies abroad and at the University, and of course with words and deeds. Thank you!

Contents

List of Figures

List of Tables

List of Abbreviations

Abbrevation	Term
ABC	Absorbing Boundary Condition
BC	Boundary Condition
BEM	Boundary Element Method
CAA	Computational Aero-Acoustics
CFD	Computational Fluid Dynamics
CFL	Courant-Friedrichs-Lewy number
CNG	Compressed Natural Gas
DNS	Direct Numerical Simulation
DES	Detached Eddy Simulation
DoF	Degree(s) of Freedom
JICF	Jet In CrossFlow
LEE	Linearized Euler Equations
LES	Large-Eddy Simulation
LHS	Left Hand Side
NPR	Nozzle Pressure Ratio (ratio of the stagnation pressure to the ambient pressure)
NRBC	Non-Reflective Boundary Conditions
N.-S.	Navier Stokes
OASPL	Over All Sound Pressure Level
PDE	Partial Differential Equation
PML	Perfectly Matching Boundary Layer
RANS	Reynolds–Averaged Navier—Stokes equations
RHS	Right Hand Side
SAS	Scale-Adaptive Simulation Turbulence Model
SGS	SubGrid-Scale
SNR	Signal-to-Noise Ratio
SPL	Sound Pressure Level
SST	Shear Stress Transport Turbulence Model
WCx	Engine's Working Condition

List of Symbols

Symbol	Explanation
c	Speed of sound
Re	Reynolds number
St	Strouhal number $\frac{fd}{U}$
$\mathcal{R}$	Universal gas constant
R	Distance from the injector
$\mathcal{M}$	Molar mass
M	Mach number
M_c	Eddy convection Mach number $\frac{U_j}{c_j + c_a}$
Φ	Flux vector
U	Velocity
d	Equivalent jet exit diameter
α	Jet pitch angle relative to cross-flow, degrees
β	Jet yaw angle relative to perpendicular, degrees
ρ	Density
p	Pressure
δ_{ij}	Dirac delta

Subscript	Explanation
0	Tank state
j	Jet
a	Ambient region
cf	Cross-flow

Superscript	Explanation
$*$	Critical state
$'$	(acoustic) Fluctuation

Abstract

A direct aeroacoustic simulation methodology is developed on the basis of the numerical schemes implemented in the commercial tool ANSYS CFX. The focus lies upon the efficient and direct numerical prediction of the flow-induced noise generated by natural gas and pneumatic applications. The respective compressed gas related components are characterized by tiny supersonic gas jets, strong noise emissions, poor accessibility by measurement techniques and excessive simulation costs in particular. Highly resolved computational grids close to DNS requirements become necessary just in order to capture the time-averaged flow profile, tiny shocks and gradients correctly. Furthermore the coexistent supersonic flow velocity results in an exceptionally small timestepping in compliance with the CFL condition, e.g. for LES aeroacoustic simulations. Considering the assumably nonlinear noise propagation and the acoustic feedback within enclosed environments the well-established hybrid approaches cannot be employed here as well. The flow and acoustics of the whole domain rather have to be captured within a single tool instead. In fact, the corresponding simulation costs inhibit the numerical prediction and reduction of the emitted noise levels for those compressed gas components at the industrial scale.

In this work the test subject is a dedicated natural gas injector in an open and a confined environment and with varying boundary conditions. Specific to the injector nozzle, four underexpanded supersonic gas jets (M=1.4, Re=30000) are formed and cause a strong flow three-dimensionality. Furthermore a turbulence cluster establishes between the jets driving jet fluctuations and aeroacoustics.

To enable aeroacoustic simulations in the first place, ANSYS CFX is augmented by a transient inlet boundary condition and a non-reflective farfield boundary condition based on an implicit damping sponge layer. In order to reduce the simulation costs the scale-adaptive turbulence model (SAS-SST) recently implemented in ANSYS CFX is validated for the gas injection problem and especially for CFL numbers much larger than one. Since a degrading solution quality has to be expected then a timestep study is conducted in order to detect the limit for aeroacoustic simulations. Bottom line the different turbulence modeling allows a strongly increased global timestepping such that a net simulation costs reduction by a factor of 19 compared to LES is achieved. In spite of the generally lower solution quality the predicted noise levels, spectral distributions as well as noise sensitivities are in well agreement with own experimental data.

In an alternative simulation approach the research code NSDG2D is applied to a simplified 2D setup with very promising results. The more sophisticated solver numerics based on an explicit Discontinuous Galerkin scheme allows local dynamic adaption to the problem, amongst others by local timestepping and locally adaptive element orders. These features prove to be feasible especially for locally varying unsteady compressible flows and the supersonic gas injection in particular. Considering these advantages a further reasonable simulation costs reduction compared to ANSYS CFX can be projected for the 3D application as well.

Kurzfassung

Auf Grundlage der numerischen Verfahren innerhalb des kommerziellen Strömungslösers AN-SYS CFX wird eine Simulationsmethodik mit Fokus auf die effiziente und direkte numerische Vorhersage strömungsbedingten Schalls für Erdgas- und Pneumatik-Anwendungen entwickelt. Die entsprechenden gasführenden Komponenten sind insbesondere durch kleine Überschall-gasstrahlen, starke Lärmemissionen, schlechte messtechnische Zugänglichkeit und extreme Aeroakustik-Simulationsanforderungen gekennzeichnet. Hochaufgelöste Gitter an der Grenze zur DNS-Qualität sind notwendig, nur um das gemittelte Strahlprofil mit seinen sehr kleinen Stößen und Scherschichten richtig abzubilden. Unter Einhaltung der CFL Bedingung führen die gleichzeitig sehr hohen Strömungsgeschwindigkeiten weiterhin zu außerordentlich kleinen Zeitschrittweiten, u.a. für LES Simulationen. Aufgrund der zu erwartenden nichtlinearen Schallausbreitung und den Rückkopplungen in einer umschlossenen Umgebung sind etablierte hybride Ansätze hier nicht anwendbar. Vielmehr muß die Strömung und Akustik des gesamten Problems in einem einzigen Tool abgebildet werden. Die daraus resultierenden Simulation-skosten verhindern die industrielle Anwendung numerischer Methoden zur Vorhersage und Reduktion des strömungsinduzierten Lärms für solche Komponenten.

Das Testbeispiel in dieser Arbeit ist ein spezieller Erdgas-Injektor in offener und um-schlossener Freistrahlanordnung und mit variierenden Umgebungsrandbedingungen. Spezi-fisch für den Injektor ist seine besondere Düsengeometrie. Sie formt vier stark dreidimension-ale unterexpandierte Überschallgasstrahlen (M=1.4, Re=30000) und einen Turbulenzballen zwischen ihnen, der die Strahlen zu Schwingungen anregt und so die Lärmemissionen treibt.

Um Aeroakustiksimulationen überhaupt erst zu ermöglichen, wird ANSYS CFX mit einem transienten Inlet und einer nicht-reflektierenden Fernfeld-Randbedingung auf Basis einer im-pliziten Sponge Layer erweitert. Zur Reduktion der Simulationskosten wird das seit kurzem in ANSYS CFX implementierte skalen-adaptive Turbulenzmodell (SAS-SST) für dieses Beispiel und insbesondere für CFL Zahlen deutlich größer als eins validiert. Aufgrund der dann ab-nehmenden Lösungsqualität wird eine Zeitschrittstudie durchgeführt, um die Grenzen für die Lärmvorhersage zu bestimmen. Im Ergebnis erlaubt die geänderte Turbulenzmodellierung eine deutlich vergrößerte globale Zeitschrittweite und damit eine Reduktion des Simulationsaufwan-des um den Faktor 19 gegenüber LES. Trotz der allgemein schlechteren Lösungsqualität stim-men die simulativ ermittelten Lärmpegel, Spektren und Sensitivitäten gut mit eigenen Mes-sungen überein.

In einem alternativen Simulationsansatz wird der Forschungscode NSDG2D auf ein vereinfachtes 2D-Problem angewendet. Die fortschrittlichere Numerik auf Basis eines expliziten Discontinuous Galerkin Verfahrens erlaubt die lokale dynamische Anpassung an das Problem, unter anderem mit lokalen Zeitschrittweiten und lokal adaptiven Elementordnungen. Es wird gezeigt, dass diese Fähigkeiten sich insbesondere bei instationären und lokal stark variierenden kompressiblen Gasströmungen wie der Gasinjektion auszahlen. Damit kann eine weitere deutliche Reduktion der Simulationskosten im Vergleich zu ANSYS CFX auch in 3D angenommen werden.

Chapter 1

Introduction

1.1 Motivation

In context of environmental protection, global warming and forseeable shortage of crude oil derivatives, alternative fuels in mobility applications are not only ecologically and economically reasonable but even politically demanded. Growing prices and the global agreement on a reduction of carbon dioxide emissions call for new powertrain technologies and successive replacement of gasoline and diesel. However, entirely new concepts such as hybrid engines and fuel cells are just being developed and not very competitive yet. Renewable biofuels on the other hand only have potential to replace a small portion of the anticipated fuel requirements. This is where compressed natural gas (CNG) can be a comparably simple, cheap and quick alternative without the need for wholly new engine concepts.

In fact, CNG can be used in common OTTO engines without major modifications. Its higher energy content (octane number of 130) allows higher compression ratios and a by 5% better fuel efficiency. At the same time CO_2 emissions are reduced by more than 20% over gasoline and the purity of CNG (e.g. no sulfur ingredient) is leading to a reasonably less toxic exhaust gas. Last not least the availability and price of natural gas might develop positively in the next decades. There are still vast and widespread reserves. Costly extraction and refinement is hardly necessary. Thus CNG is a consequential successor for gasoline, at least on a temporary basis.

In recent years these considerations led to a political framework within the European Union requiring its member states to reach a natural gas share of 10% by the year 2020. This is *5 million* cars just in Germany. Simultaneously the automotive manufacturers are demanded to reduce the average fleet CO_2 emissions to 120 grams per kilometer. Consequently all major automotive companies (Toyota, Opel, Daimler, VW, Ford, Volvo,..) have their own CNG powered models already in the market while reduced tax on natural gas guarantees amortization within a few years. Besides the willingness to buy alternative fuel cars grew rapidly in recent years, in Germany to very high 94.9% (DEKRA survey, 2005). Indeed sales numbers are growing rapidly as well: 55000 CNG powered cars were registered in Germany in

January 2007 (Kraftfahrtbundesamt). For 2010 the estimated total is *360000* (Roland Berger Study 'Solving the powertrain challenge', 2007) with an annual growth rate of 60%.

However, there are also some disadvantages associated with CNG requiring further development and research. Next to range and storage issues it is first of all the noise emitted during refueling and injection that does not comply with comfort and durability expectations. In fact, unaware passengers might even be scared by unexpected noise.

The increased noise levels are supposed to trace back to supersonic gas flow. However no efforts have been undertaken yet to understand noise generation and propagation in detail. Measurements are difficult to perform due to the small problem dimensions and poor accessibility. Numerical simulations using accepted and commercially available tools and methods are intolerably computationally expensive since very dense meshes and very small timesteps are generally required for this kind of problem.

Thus a reasonably more efficient simulation methodology is essential to enable understanding and optimization for such challenging problems. Indeed there is a whole class of often neglected applications characterized by small model dimensions and supersonic flows as well: valves, blowers, cutters, pressure regulators, filters and suppressors. The approaches presented in this work might be applicable for those as well.
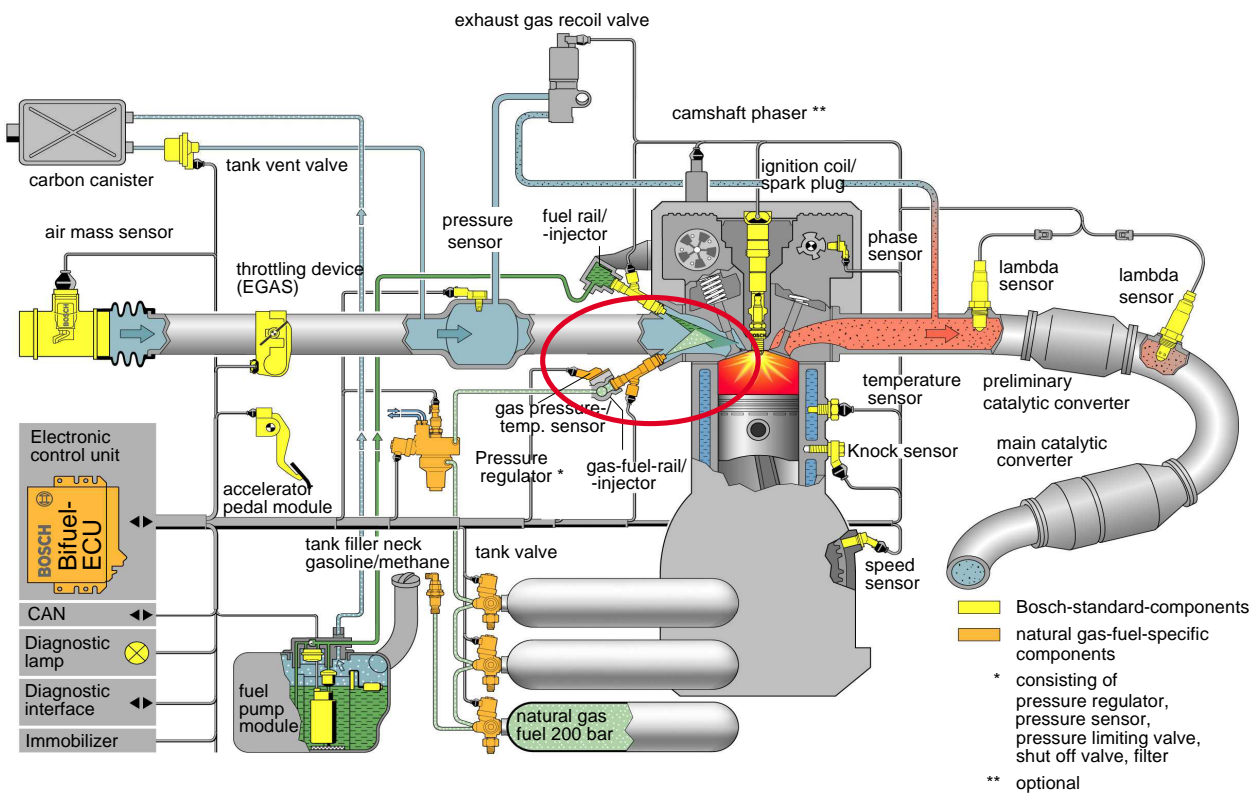
Figure 1.1: Complete system schematics of a bivalent engine

1.2 Problem Description

The problem setup governing this work is related to the framework of a bivalent engine. Since such an engine hot-swaps between gasoline and CNG operation the difference in emitted noise levels is striking most. Even more, the swapping is done automatically in dependency of engine and tank states such that the sudden change from familiar OTTO-sound to an actual Diesel-like noise is in fact surprising and therefore repeatedly causing customer complaints.

Having a look at the system schematics (Fig. 1.1) the natural gas (mainly methane) is stored in a compressed state at 200 bar. While passing the tank valve and the pressure regulator it is throttled down to a supercritical pressure of 7 bar when it reaches the injector. Thus the gas is injected into the intake manifold at generally supersonic velocities and in a pulsed operation. Eventually the natural gas mixes with the air cross-flow and gathers in the combustion chamber before it is burnt. In this sequence the actual CNG injection into the intake manifold (encircled in red) is identified as the dominant noise contributor.
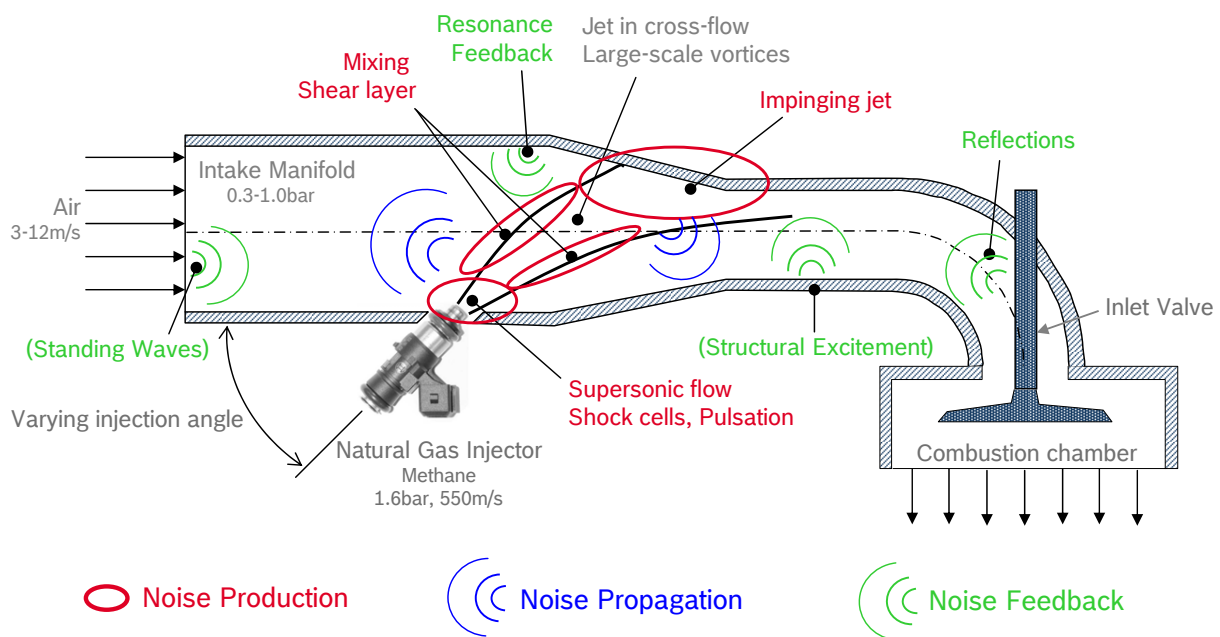
Figure 1.2: Problem sketch

This is leading to the problem sketch presented in Fig. 1.2. The setup is simplified yet quite close to reality. It shows the intake manifold with an adjustable but time-invariant pressure and cross-flow velocity representing the engine load, an injector that can be rotated for parameter studies and optimization purposes, an opened inlet valve and the upper part of the combustion chamber. In this sketch the supersonic jet might be the dominant noise contributor. However the presence of cross-flow and a confining environment might be influential as well. Additional large scale vortices, jet fluctuations, a possibly impinging jet, acoustic reflections and feedback

back to the jet and its aeroacoustics have to be considered. The complexity of this problem, the difference in space and time scales between noise production and propagation regions, the possible acoustic feedback and the lack of functionality and efficiency of commercially available software effectively prevents hybrid and direct aeroacoustic simulations for this problem.
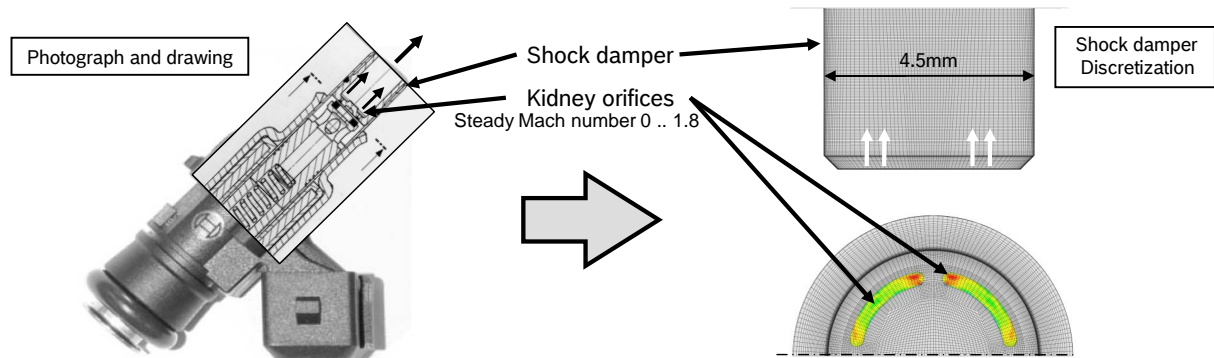
Figure 1.3: Natural gas injector

In automotive applications a dedicated natural gas injector is employed. It features a number of tiny kidney-shaped orifices placed within a so-called shock damper (Fig. 1.3). Thus a supersonic flow with reasonable three-dimensionality establishes requiring a very dense mesh and millions of elements to resolve. The pulsed mode of operation makes the injection furthermore a highly dynamic process with variable inlet conditions over time, transient jet formation and a shock-wave inducing pressure release.

1.3 Objectives

An efficient and reliable aeroacoustic simulation methodology shall be developed and applied to the natural gas injection problem. Since the latter is wholly uninvestigated until now the stationary flow profile, the turbulent characteristics as well as the governing sources of noise shall be characterized at first. Subsequently the numerical prediction and validation of aeroacoustic noise spectra and their sensitivities shall be focused on with the intention to enable parameter studies and future optimization.

After reviewing literature and preceding works various flow and acoustic measurements for the gas injection in freestream and intake manifold configurations shall be conducted. The objective is to provide a reference for validation purposes and to support the comprehension of the problem. Amongst other things this requires the commission and operation of a dedicated intake manifold test rig.

The main simulation approach shall be based on ANSYS CFX. This inherently not CAA-focused tool has to be augmented at first in order to enable realistic aeroacoustic simula-

tions. The implementation of a non-reflective farfield boundary condition and a transient inlet boundary condition have to be addressed primarily in order to cut clean the injection problem properly.

In the next step this approach shall be employed for the freestream configuration. Absent walls and cross-flow result in a less complex problem and allow better accessibility and validation. In order to identify the most efficient simulation approach the turbulence modeling shall be investigated in particular. Here the novel scale-adaptive simulation model (SAS) is a promising candidate. It has not been validated for the aeroacoustics of supersonic jets and for operation outside the CFL condition yet, though.

Eventually the gained experience shall be transfered to the intake manifold configuration setup. In addition to the computation and validation of flow and aeroacoustic spectra the respective sensitivities come into focus now. The engine's working conditions represented by air cross-flow and intake manifold pressure as well as the injection angle are the parameters to be varied.

In a second simulation approach the potential of the non-commercial research code NSDG2D shall be assessed. Its adaptive and highly accurate numerics make it ideally suited for aeroacoustics and fluctuating supersonic flows. Owed to its current limitations it shall be applied to a simplified 2D problem with comparison to ANSYS CFX. The solution quality and computational costs savings achievable with this approach are of primary interest.

Finally, the pursued approaches shall be characterized in terms of simulation effort, solution accuracy and applicability. The validity of the conducted model simplifications shall be appraised. Proposals regarding further model or methodology enhancements or forseeable research needs shall be outlined.

Chapter 2

Fundamentals

2.1 Background on Aeroacoustics

2.1.1 Formation of Sound in a Fluid

Noise generation in a fluid can be understood as a dissipation process where the system turns small parts of its energy, scaling with the fourth power of the flow Mach number M, into sound. Starting with the gas dynamic equations, several fluctuation modes can be identified in a flow [96]:

- vortical mode: small rotational disturbances, essentially incompressible and related to viscosity, turbulences convected by the flow

- acoustic mode: essentially irrotational disturbances related to compressibility, able to propagate

- entropy mode: small motions related to thermal conductivity

In these terms aeroacoustics is the relation and interaction of the vortical and acoustic modes (Tab. 2.1). Noise production is based on turbulences-turbulence interaction, namely vortex deformation, pairing and break-up. Furthermore the emitted noise can act back on the flow, induce turbulence and cause vortex deformation with sound emission as well. Additionally acoustic-acoustic interaction can act as equivalent sources and thus cause non-linear wave propagation especially for strong waves and at steep mean flow gradients. Interactions comprising the entropy mode are related to thermoacoustics and do not play a noticeable role in non-reactive flows.

Interaction	Acoustic mode	Vortical mode
acoustic – acoustic	non-linear acoustics	–
turbulence – turbulence	aeroacoustic production	vortex dynamics
acoustic – turbulence	direct acoustic feedback	indirect acoustic feedback

Table 2.1: Interaction of gas dynamic modes resulting in acoustic and vortical source terms

The type of turbulence deformation defines the noise source characteristics. Interactions between two vortices lead to quadrupole type noise sources with a radiated energy $\propto M^8$. On the other hand, deformation of a single vortex, e.g. when it is hitting a wall, causes dipole type sources with a radiated energy $\propto M^6$. The effective noise directivity can eventually be considered as the sum of the single noise source directivities, the Doppler effect of moving sources and refraction at mean flow gradients.

2.1.2 Sound and Pseudo-Sound

In the turbulent flow region the pressure field is dominated by quasi-incompressible inertial effects. The resulting pressure fluctuations, referred to as *hydrodynamic fluctuations* or *pseudo-sound*, do not radiate and are bound to the propagating flow structures. They decrease quickly with the distance ($\propto R^{-3}$), while propagating acoustic pressure fluctuations decrease with just $\propto R^{-1}$. If no precautions are taken and acoustic measurements are conducted within such a flow region, hydrodynamic fluctuations will mask and be wrongly interpreted as acoustics as well.

$$p'_{measured} = p'_{ac} + p'_{hydrodynamic} \tag{2.1}$$

The best practice to avoid pseudo-sound is to capture fluctuations outside the turbulent flow region, e.g. upstream or perpendicular to a jet stream. Within ducts this is particularly problematic. In a regime where pseudo-sound cannot be avoided the actual noise could be obtained by employment of several microphones and filtering of non-coherent fluctuations. These techniques generally work for unconfined and low Mach number flows only though [88]. Another approach is the so-called *mode-matching technique* employing theoretical knowledge about duct modes and their propagation (Sec. 3.3). This requires an uniform flow and least squares fitting in several cross-sections though [88] and is not applicable in this work either. Thus pseudo-sound cannot be reliably separated in the intake manifold in particular. In fact this is alright indeed since it might contribute to the external noise by structural excitation.

2.1.3 Characteristic Scales of Turbulence

Turbulences are the basis of aeroacoustic noise generation. Hence knowledge about the present scales and their properties is inherent to the mesh generation, turbulence modeling and simulation demands.

The largest emerging eddies reach the characteristic problem or shear layer dimension L and are generally dominated by the boundary conditions. Starting there the corresponding turbulent kinetic energy cascades down to the smaller scales. Eventually those become more and more universal, independent of the larger eddies and boundary conditions and thus easier

to model. The smallest persistent turbulence scale is specified by the *Universal Equilibrium Theory*: The rate at which energy is supplied by the turbulence cascade has to agree with the rate at which it is dissipated. This is leading to the *Kolmogorov Length Scale* as a measure for the smallest existing turbulence scale in dependency on the kinematic viscosity ν and the dissipation rate ε. Consequently this determines the necessary grid spacing if all existing turbulence shall be resolved numerically in a DNS approach.

$$\eta = \left(\frac{\nu^3}{\varepsilon} \right)^{\frac{1}{4}} \tag{2.2}$$

The ratio of the largest scales to the smallest scales, or the ratio of inertial forces to viscous forces, defines the *Reynolds number*.

$$Re = \frac{UL}{\nu} \tag{2.3}$$

Higher Reynolds numbers are a synonym for broader turbulence spectra and higher DNS resolution requirements in relation to the characteristic problem dimension. This is associated by increased simulation costs.

2.1.4 Modeling Viscosity

Viscosity has been shown to play a role in the turbulent energy cascade and to determine the Kolmogorov scale. Furthermore the averaged flow, shear layer dimensions and gradients are affected. Thus, viscosity is indirectly related to the noise production, the emitted frequency range and noise intensities. A realistic viscosity model is inherent to numerical aeroacoustic simulations.

For many gases, amongst others air, the dynamic viscosity $\mu = \nu\rho$ is primarily a function of the temperature while the impact of the pressure is minor. This relation is approximated by *Sutherland's formula* for temperatures between $0 < T < 555K$ and with an error of less than 10%.

$$\mu = \mu_0 \frac{T_0 + C}{T + C} \left(\frac{T}{T_0} \right)^{\frac{3}{2}} \tag{2.4}$$

Sutherland's constant C, the reference temperature T_0 and the reference viscosity at the reference temperature μ_0 are available for various gases. For methane and other hydrocarbons no such formula but just tabled data exists instead [54], though. However this is not employable in ANSYS CFX such that a constant viscosity has to be specified instead. In fact the viscosity will be shown to have just little influence on the simulation outcome especially in the regions of low temperature and noise production such that the error might be low indeed.

2.1.5 Ideal vs. Real Gas

The ideal gas law is a reasonable simplification for gases at low pressure, high temperature and for gases with low molar mass.

$$pV = n\mathcal{R}T \tag{2.5}$$

Real gases, on the other hand, additionally consider forces between volumetric molecules and deviate from that equation. They can be characterized by real gas laws, e.g. the *Redlich-Kwong equation* of state or the *ideal gas deviation factor z*. The latter is tabled in dependency of gas type, temperature and pressure.

$$pV = z \cdot n\mathcal{R}T \tag{2.6}$$

In terms of this work the pressure supply can be considered low. For air and hydrocarbons the z-factor is just a few percent and a very weak function of the temperature. Hence the ideal gas equation is completely sufficient.

A side-effect of real gas behavior is the *Joule-Thomson effect*. If a gas is throttled or ejected into a low pressure environment it commonly cools down in an isotropic expansion. For some gases, amongst others hydrogen, this is the way round. The reason is the enthalpy of real gases being pressure-dependent as well: $H = H(p, T)$. Thus, even if no displacement work is done at all during expansion into vacuum the temperature T changes. The tendency and slope is determined by the *Joule-Thomson coefficient* μ_{JT} describing a state change at constant enthalpy.

$$\mu_{JT} = \left(\frac{\partial T}{\partial p}\right)_H \tag{2.7}$$

For ideal gases μ_{JT} is zero, for real gases it can be positive or negative as a function of the temperature. For methane as well as air at the injection conditions it is weakly positive [54]. Thus, isentropic cooling is slightly supported by Joule-Thomson cooling, for methane somewhat stronger than for air. Since this effect can be considered to be negligible ideal gas equations are employed instead.

2.2 Basics for Numerical Simulations

This section is aimed to present simulation approaches as they are employed in this work. Characteristic information about ANSYS CFX as well as the research code NSDG2D is given and put into context regarding the CFD and CAA framework. Thus, this section is the basis of later discussions about the applicability and choice of numerical methods.

2.2.1 Governing Equations

The governing equations necessary for aeroacoustic purposes can be split into general CFD equations and CAA equations dedicated to noise propagation for given aeroacoustic sources. Thus even in a CAA framework CFD based on Navier-Stokes or Euler equations is necessary to deduce aeroacoustic source terms and the mean flow field in the beginning.

Navier-Stokes Equations

ANSYS CFX as well as NSDG2D implement the compressible Navier-Stokes equations. In ANSYS CFX these are considered in the form (2.8)-(2.10) with the variables pressure p, density ρ, velocity vector $\mathbf{U}$, temperature T, specific total enthalpy h_{tot} and the viscous stress tensor $\tau = \mu(\nabla \mathbf{U} + (\nabla \mathbf{U})^T) - \frac{3}{2}\delta \nabla \cdot \mathbf{U}$. Parameters are the thermal conductivity λ, the dynamic viscosity μ, and additional user-definable source terms S_C, S_M and S_E.

$$\frac{\partial \rho}{\partial t} + \nabla \cdot (\rho \mathbf{U}) = S_C \qquad \text{Continuity} \qquad (2.8)$$

$$\frac{\partial \rho \mathbf{U}}{\partial t} + \nabla \cdot (\rho \mathbf{U} \otimes \mathbf{U}) = -\nabla p \delta + \nabla \cdot \tau + S_M \qquad \text{Momentum} \qquad (2.9)$$

$$\frac{\partial \rho h_{tot}}{\partial t} - \frac{\partial p}{\partial t} + \nabla \cdot (\rho \mathbf{U} h_{tot}) = \nabla \cdot (\lambda \nabla T) + S_E \qquad \text{Energy} \qquad (2.10)$$

This system of equations is closed by two additional equations. The first is the constitutive relation for the specific total enthalpy employing the specific heat at constant pressure c_p.

$$h_{tot} = \frac{1}{2}\mathbf{U}^2 + c_p T \qquad (2.11)$$

The second equation is the thermal equation of state. Here ANSYS CFX offers a variety of modeling choices. In context of this work it is the *ideal gas equation*. Specific to ANSYS CFX, it is dependent on the molar mass $\mathcal{M}$ and the universal gas constant R while the pressure is considered as the relative variation to a preset reference.

$$\rho = \frac{\mathcal{M}(p + p_{ref})}{RT} \qquad (2.12)$$

In NSDG2D the employed continuity and momentum equations are analogue to (2.8)-(2.9). The energy equation (2.13) is different however. It is written in specific total energy form and additionally considers viscous work. In ANSYS CFX the latter can be enabled as well but is turned off by default. Since viscosity effects can be assumed to be weak during gas injection

the influence of the viscous work term is negligible however.

$$\frac{\partial \rho e_{tot}}{\partial t} + \nabla \cdot (\rho \mathbf{U} e_{tot} + p\mathbf{U}) = \nabla \cdot (\lambda \nabla T) + \nabla \cdot (\mathbf{U} \cdot \tau) + S_E \quad \text{Energy} \tag{2.13}$$

Accordingly, the constitutive equation Eq. (2.11) is replaced by the respective formulation for the specific total energy.

$$e_{tot} = \frac{1}{2}\mathbf{U}^2 + c_v T \tag{2.14}$$

Last not least, the ideal gas equation is employed in NSDG2D as well but in a formulation tracing back to the adiabatic exponent κ.

$$\rho = \frac{p}{(\kappa - 1)(e_{tot} - 0.5\mathbf{U}^2)} \tag{2.15}$$

Thus, when setting up simulations it has to be considered that the injected media are defined differently in either software. NSDG2D employs $\kappa = \frac{c_p}{c_v}$ and the specific gas constant $R_s = c_p - c_v$. In ANSYS CFX materials are determined by c_p and $\mathcal{M}$ instead. Consistent data satisfying $\mathcal{M} = \frac{R}{R_s}$ and $c_p = \frac{\kappa}{\kappa-1}R$ have to be ensured in order to obtain comparable results in either approach.

Euler Equations

NSDG2D allows to solve the Euler equations instead. Assuming inviscid flow and neglecting the viscous stress tensor τ simplifies the Navier-Stokes momentum (2.9) and energy equations (2.13).

Wave Equation

The wave equation is the most elementary aeroacoustic equation only accounting for the linear wave propagation of an acoustic pressure fluctuation p'. The propagation velocity is the speed of sound c.

$$\frac{1}{c^2}\frac{\partial^2 p'}{\partial t^2} - \Delta p' = 0 \tag{2.16}$$

This equation is neither implemented in ANSYS CFX nor in NSDG2D but is often employed in subsequent hybrid approaches, acoustic analogies or domain decompositions. It is only valid in cases where the influence of the mean flow on the acoustic propagation can be neglected.

2.2.2 Discretization

The conservation laws (2.8)-(2.10) serve as the basis for all discussed discretization approaches. In flux formulation these can be written in dependency on the state vector Φ and the flux

vector $\mathbf{f}$, where the latter comprises convective $\mathbf{f}(\Phi)$ and diffusive $\mathbf{f}(\Phi, \nabla\Phi)$ quantities.

$$\frac{\partial \Phi}{\partial t} + \nabla \cdot \mathbf{f}(\Phi, \nabla\Phi) = 0 \qquad (2.17)$$

In order to turn Eq. (2.17) into a hyperbolic advection equation the diffusive term can be dealt with separately. Since approximate continuity can be assumed for a diffusive solution the simplest approach is to compute $\nabla\Phi$ from Φ by central differencing such that the flux becomes merely $\mathbf{f}(\Phi)$.

Three discretization approaches are further detailed: Finite volumes approximating the integral average within a discretized cell, finite elements approximating a global continuous solution by a set of weighted form functions and Discontinuous Galerkin doing a mixture of both.
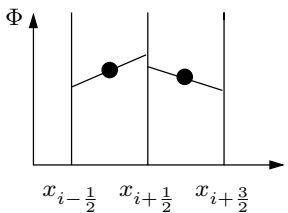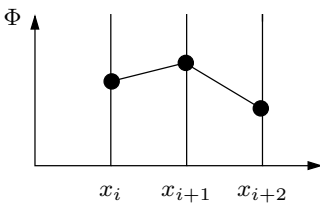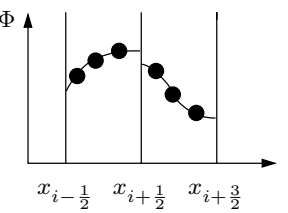
	Finite Volumes	Finite Elements	Discontinuous Galerkin
Sketch			
Basis	discontinuous solution based on integral conservation	continuous solution based on form functions	discontinuous solution based on form functions
Result	cell centered averages	nodal values	distribution in elements
Conservation	for each element	for a region	for each element
Discontinuities	captured	cause instabilities	as error indicator
Higher order accuracy	by reconstruction (increased stencil)	higher-order functions (increased stencil)	more form functions (same stencil)
	often used for CFD	often used for CAA	mixture of FV and FE

Table 2.2: Comparison of spatial discretization methods

Finite Volumes (FV)

In order to provide shock capturing and integral conservation the governing equations are integrated over discretized control volumes (cells C_k).

$$\int_{C_k} \left(\frac{\partial \Phi}{\partial t} + \nabla \cdot \mathbf{f}(\Phi) \right) dV = 0 \qquad (2.18)$$

Application of Gauß's theorem turns the flux term into an integral along the cell boundary ∂C_k. Swapping of spatial integration and time derivative for the first term, supported by the definition of integral cell averages

$$\Phi_k = \Phi_k(t) = \frac{1}{|C_k|} \int_{C_k} \Phi(\mathbf{x}, t) \, dV \, , \tag{2.19}$$

eventually turns Eq. (2.18) into an evolution equation (2.20) for the integral averages Φ_k. The integrated flux across the cell boundaries determines the temporal variation.

$$\frac{\partial \Phi_k}{\partial t} = -\frac{1}{|C_k|} \int_{\partial C_k} \mathbf{f}(\Phi) \mathbf{n} \, dS \tag{2.20}$$

This approach fully satisfies the conservation equations without the need for approximations up to this point. Assumptions have to be made computing the actual flux $\mathbf{f}$ passing between neighboring cells however. On one hand this comprises the reconstruction of a Φ-distribution within each cell in order to estimate Φ at the cell boundary. This requires to take the neighboring cells into account as well. On the other hand these reconstructions are essentially discontinuous at the cell boundaries, the flux evaluation requires a definite value though. Since the correct Riemann solution is particularly demanding – non-linear waves like shocks and expansions can occur at every cell boundary – an approximation is necessary here as well. Roe-linearization is leading to simple upwind flux computation for example.

First order (Godunov-type) methods assume a constant distribution of Φ within the cell and lead to very robust but highly dissipative schemes. In contrast, the reconstruction of linear distributions of Φ within the cells is leading to second order accurate schemes which are not total variation diminishing (TVD) though. Thus they might introduce spurious oscillations at steep gradients and shocks.

Therefore the MUSCL scheme (Monotonic Upwind Scheme for Conservation Laws) is widespread instead. It employs a slope limiter in order to provide the TVD property. It is second order accurate in smooth parts of the solution and switches to first order accuracy and clipping in proximity of discontinuities and local extrema.

Even higher order FV methods, e.g. based on ENO and WENO schemes, are less spread because they need to reconstruct higher-order polynomials from more than just directly neighboring cells. Thus the disadvantages are the increased numerical effort, lower robustness and a more demanding integration using Gauss quadrature. The enlarged stencil ($\propto$ Order^3 in 3D) furthermore reduces the parallelizability.

Finite Elements (FE)

The fundamental idea of finite element methods [113] is the continuous representation of the solution $\Phi(\mathbf{x})$ by a weighted sum of form functions ξ. The computational domain is discretized into N elements bounded by nodes. In proximity of each node i a predetermined form function ξ_i is located in the manner that it is one in node i and zero in every other supporting node. Thus the form functions contribute to the solution in a range of surrounding elements in dependency on their polynomial degree. Therewith the continuous approximation Φ_h to the global solution can be cast as the sum of all contributing form functions scaled by their weights $\hat{\Phi}_i$. This forms a sparse system of equations valid within the whole domain Ω.

$$\Phi(\mathbf{x}) \approx \Phi_h(\mathbf{x}) = \sum_{i=0}^{N} \hat{\Phi}_i \xi_i(\mathbf{x}) \qquad \mathbf{x} \in \Omega \tag{2.21}$$

Most often FE solvers employ polynomial form functions of same global order. First order solvers use piecewise linear (tent) functions such that only direct neighbors contribute. For higher-order solver, e.g. using quadratic form functions, the stencil and number of contributing form functions increases respectively.

However, Φ_h is just an approximation which does not necessarily satisfy the governing equations (2.17). It leaves a residuum $\mathbf{R}$ behind instead which is to be minimized of course. In dependency on the application there are different ways to obtain a well suited solution. In solid bodies collocation requires exact solutions (zero residuum) in the given points which is directly leading to a linear system of equations for the nodal weights $\hat{\Phi}_i$. In continuum mechanics the more general Galerkin approach is employed instead. It minimizes the weighted average of the residuum (weight functions $\mathbf{w}$) throughout the domain Ω in a so-called variational formulation.

$$\int_{\Omega} \mathbf{R} \cdot \mathbf{w} \, dV = 0 \tag{2.22}$$

The residuum can be written as the conservation equations restated in weak form. Φ is replaced by its approximation Φ_h. To furthermore ensure a globally continuous solution weight functions in consistency with the form functions ($\mathbf{w} = \xi$) are employed.

$$\int_{\Omega} \left(\frac{\partial \Phi_h}{\partial t} + \nabla \cdot \mathbf{f}(\Phi_h) \right) \xi \, dV = 0 \tag{2.23}$$

This raises parallels to a FV method indeed (cp. Eq. (2.18)): FV methods just set the weighting $\mathbf{w} = 1$, integrate over each element instead of the whole domain and consider Φ_h in the cell centers rather than the nodes.

Integration in parts now shifts the derivative of the flux term over to the form functions

and introduces natural boundary conditions along the way.

$$\int_\Omega \frac{\partial \Phi_h}{\partial t} \xi \, dV - \int_\Omega \mathbf{f}(\Phi_h) \cdot \nabla \xi \, dV + \int_{\partial\Omega} \mathbf{f}(\Phi_h)\xi\mathbf{n} \, dS = 0 \tag{2.24}$$

The weighted sum of form functions (2.21) is introduced

$$\sum_{i=0}^{N} \frac{\partial \hat{\Phi}_i}{\partial t} \underbrace{\int_\Omega \xi_i \xi_j \, dV}_{M_{ij}} - \sum_{i=0}^{N} \hat{\Phi}_i \underbrace{\int_\Omega \mathbf{f}(\xi_i)\nabla\xi_j \, dV}_{S_{ij}} + \sum_{i=0}^{N} \hat{\Phi}_i \underbrace{\int_{\partial\Omega} \mathbf{f}(\xi_i)\xi_j\mathbf{n} \, dS}_{\mathbf{b}} = 0 \tag{2.25}$$

such that a differential equation in time emerges with mass and stiffness matrices $\mathbb{M}$ and $\mathbb{S}$ and domain boundary conditions $\mathbf{b}$.

$$\mathbb{M} \frac{\partial \hat{\Phi}}{\partial t} - \mathbb{S} \, \hat{\Phi} + \mathbf{b} = 0 \tag{2.26}$$

Written for a specific node i the integrals in Eq. (2.25) actually reduce to the region of contributing form functions around the node. This is making the matrices sparse and proves the fact, that conservation is indeed given for the cluster of contributing elements around the node. For higher order solvers this region increases and local conservation becomes worse.

There are several reasons why FE is seldom used in commercial CFD, though. On one hand there are non-conservative elements and expensive non-symmetric stiffness matrices. On the other hand there is the more serious low robustness [113]. For example, the FE approach is leading to something like central finite differences for the computation of spatial gradients in the convection terms. If those terms dominate, the solution becomes oscillatory and eventually unstable. Furthermore, the approximation of discontinuities like steep gradients and shocks by a continuous function might raise oscillations persisting in a wide area of the domain and cause instability of the scheme. Possible solutions evading this problem are either the local introduction of additional artificial viscosity to damp out those oscillations (shock capturing) or Petrov-Galerkin methods with better tempered weight functions $\mathbf{w} \neq \xi$. Those lead to an upwind-like differencing of convective terms but require explicit smoothing of $\mathbf{w}$ at the element boundaries in order do ensure a continuous global solution.

Nevertheless, FE has wide-spread applications in areas where local conservation and convection are no issues and the solution is comparably smooth. Furthermore the solver order can be easily increased by switching to higher-order form functions. Then however the stencil grows, matrices are less sparse and the solver architecture needs to be readjusted.

Discontinuous Galerkin (DG)

Discontinuous Galerkin methods [18] employ a form function approach similar to FE. Now it is used to model continuous solutions within the elements only though. In particular, there are no overlapping contributions by neighboring elements and discontinuities might emerge at the element boundaries. Hence the global approximation Φ_h to the exact solution becomes just piecewise continuous analogue to FV such that the flux evaluation requires an approximate Riemann solver again.

Within each element C_k a specific set of form functions $\xi_{i,k}$ is defined. The number of form functions N_k determines the order of the element while respective weights $\hat{\Phi}_{i,k}$ modulate the solution.

$$\Phi(\mathbf{x}) \approx \Phi_h(\mathbf{x}) = \sum_{i=0}^{N_k} \hat{\Phi}_{i,k} \xi_{i,k}(\mathbf{x}), \quad \mathbf{x} \in C_k \tag{2.27}$$

Analogue to FE a variational formulation and integration in parts for the flux term is performed in order to minimize the residuum of the approximate solution Φ_h. Now this is done for each element C_k separately though.

$$\int_{C_k} \left(\frac{\partial \Phi_h}{\partial t} + \nabla \cdot \mathbf{f}(\Phi_h) \right) \xi_k \, dV = 0 \tag{2.28}$$

The result is a formulation that has similarities with both, FE and FV approaches. Indeed FV can be cast as a DG method with form functions $\xi_k = 1$.

$$\underbrace{\int_{C_k} \frac{\partial \Phi_h}{\partial t} \xi_k \, dV}_{\substack{\text{integral average (FV)} \\ \text{inertia of the element (FE)}}} - \underbrace{\int_{C_k} \mathbf{f}(\Phi_h) \cdot \nabla \xi_k \, dV}_{\text{stiffness of the element (FE)}} + \underbrace{\int_{\partial C_k} \mathbf{f}(\Phi_h) \xi_k \mathbf{n} \, dS}_{\text{flux across cell boundary (FV)}} = 0 \tag{2.29}$$

After introduction of the form function approach (2.27) the result is a local system of differential equations containing the element's mass and stiffness matrices and the flux across the element boundaries.

$$\mathbb{M}_k \frac{\partial \hat{\Phi}_k}{\partial t} - \mathbb{S}_k \hat{\Phi}_k + \mathbf{b}_k = 0 \tag{2.30}$$

Considering such a system for every single element the combined number of unknowns $\hat{\Phi}$ is indeed larger by orders compared to any other approach. The great advantage of the DG approach is its very local formulation however. Since an own set of arbitrary form functions can be defined in every single element these can be chosen favorably and without taking neighboring elements into account. Legendre polynomials can be quickly computed in preprocessing, for example, and make the combined mass matrix block-diagonal and the stiffness matrix

block-triangular. The inverse $\mathbb{M}^{-1}$ is inherently known such that the evolution equation for the unknowns can be cast easily. This makes DG extremely efficient and keeps storage requirements low indeed.

$$\frac{\partial \hat{\Phi}}{\partial t} = \mathbb{M}^{-1} \left(\mathbb{S}\, \hat{\Phi} - \mathbf{b} \right) \tag{2.31}$$

The stiffness integral in Eq. (2.29) is assumed to cover the continuous Φ_h-distribution within the elements only. Thus, integration in parts produces a surface integral in which the flux evaluation employs element-internal values at the boundary ($\mathbf{f}_{int}$) rather than a Riemann solution for the discontinuity to the neighboring element.

$$\int_{C_k} \mathbf{f}(\Phi_h) \cdot \nabla \xi_k \, dV = \int_{\partial C_k} \mathbf{f}_{int}(\Phi_h)\, \xi_k \mathbf{n} \, dS - \int_{C_k} \nabla \cdot \mathbf{f}(\Phi_h) \xi \, dV \tag{2.32}$$

Introduction into Eq. (2.29) results in the lower weak form of the variational formulation.

$$\int_{C_k} \left(\frac{\partial \Phi_h}{\partial t} + \nabla \cdot \mathbf{f}(\Phi_h) \right) \xi_k \, dV = - \int_{\partial C_k} \left(\mathbf{f}(\Phi_h) - \mathbf{f}_{int}(\Phi_h) \right) \xi_k \mathbf{n} \, dS \tag{2.33}$$

Compared to the original problem (2.28) the RHS is not zero anymore but holds an expression containing the difference of Riemann-approximated and element-internal flux evaluations at the cell boundary instead. Since Eq. (2.33) only complies with Eq. (2.28) if the discontinuity at the boundary vanishes the magnitude of the discontinuity can be figured the residuum or truncation error owed to a poor discretization. Indeed a global continuous solution is reasonable for viscous flows in particular.

The very local DG formulation simplifies the communication at the element interfaces, makes DG schemes universal and highly parallelizable. Especially the solver technology and stencil remains the same regardless of the element order. Varying local element orders, irregular meshes with hanging nodes, moving meshes and higher-order boundary conditions are inherent to the method. Local adaption of the mesh spacing (h) and/or the element order (p) using the truncation error as indicator allows to capture highly complex flows at high resolution and low costs. Furthermore there is no need for detailed previous knowledge about the flow and a manually adjusted mesh in particular. Local conservation is guaranteed as well such that DG is ideally suited for compressible flows.

Discretization Requirements and Higher-Order Schemes

In low Mach number flows the acoustic energy is by far lower than the total non-acoustic energy and other, e.g. viscous, losses. This demands for schemes with very high numerical accuracy and low diffusion to predict noise levels [30]. For larger Mach numbers the *acoustic efficiency* becomes better, such that the acoustic pressure fluctuation is of an order comparable

to the mean flow pressure. This fact indeed enables standard CFD implementing low-order FV schemes for the prediction of the noise generated by the supersonic injection presented in this work.

Low-order (non-spectral) schemes require 6-10 elements per wavelength to resolve acoustic waves. However, provided the same number of degrees of freedom the approximation error of higher-order schemes is lower [113]. Hence it is generally reasonable to employ higher-order elements rather than more and smaller low-order elements. Since higher-order elements are more expensive to evaluate adaptive approaches like DG are feasible in particular.

2.2.3 Time Marching

Evolution of the discretized solution in time furthermore requires to integrate an approach-specific function $f(\Phi)$ over a timestep.

$$\Phi^{n+1} = \Phi^n + \int_{t_n}^{t_n+\Delta t} f(\Phi)\, dt \tag{2.34}$$

Low-order methods with a time-constant (or averaged) integrand result in simple multiplication with the timestep (e.g. forward/backward Euler). For higher-order methods Gauss-quadrature and thus a way to determine the discretized solution at intermediate time levels $\Phi(t)$ with $t \in [t_n, t_{n+1}]$ is necessary. Since the solution is only available for the current time level $\Phi(t_n)$ this states a local Cauchy problem which needs to be solved approximately. Runge-Kutta, finite differences or (Discontinuous) Galerkin schemes in time are possible solution approaches.

Alternatively a space-time Taylor expansion (STE) can be employed to obtain an approximate representation $\tilde{\Phi}(\mathbf{x}, t)$ around each element barycenter $\mathbf{x}_i$ and within the time interval $[t_n, t_{n+1}]$. Here p is the order of accuracy of this approximation.

$$\tilde{\Phi}(\mathbf{x}, t) = \Phi(\mathbf{x}_i, t_n) + \sum_{j=1}^{p} \frac{1}{j!} \left((t - t_n)\frac{\partial}{\partial t} + (\mathbf{x} - \mathbf{x}_i) \cdot \nabla \right)^j \Phi(\mathbf{x}_i, t_n) \tag{2.35}$$

Time- and mixed derivatives are unknown but can be determined in a Cauchy-Kovalevskaya (CK) procedure. The conservation equation (2.17) draws a relationship between temporal and spatial derivatives: $\frac{\partial \Phi}{\partial t} = -\nabla \cdot \mathbf{f}(\Phi)$. Hence successive replacement of unknown derivatives in Eq. (2.35) with derivatives of the conservation equation enables the approximation of a continuous $\tilde{\Phi}$-distribution in space and time just based on spatial derivatives at the old time level. Eventually, STE-predictions allow evaluation of the Cauchy problem and of the time integral in Eq. (2.34).

Implicit vs. Explicit Schemes

In implicit schemes the discretized governing equations cannot be cast explicitly for the state vector at the new timestep Φ^{n+1}. Thus Φ^{n+1} has to be iterated on which is expensive for strongly varying unsteady problems in particular. Since implicit schemes are not limited by a timestep restriction they are predestined for steady state problems instead.

In contrast, explicit schemes allow quick and direct computation of the new time level Φ^{n+1} without the need for iterations. This is feasible especially for higly dynamic transient problems. However explicit schemes are just conditionally stable. The timestep has to be chosen in satisfaction of the CFL condition (2.36) in order to maintain stability.

CFL Condition

For consistency and – in terms of explicit schemes – stability reasons the timestep size has to be chosen in a way that propagation during a timestep does not overshoot the directly neighboring element. This can be expressed in form of the CFL condition as the quotient of the discrete steps in time and space, scaled by the maximum propagation velocity.

$$\text{CFL} = a\frac{\Delta t}{\Delta x} < 1 \tag{2.36}$$

Considering the Euler or Navier-Stokes equations the maximum propagation velocity is the sum of convective velocity and the speed of sound: $a = U + c$. Therewith Eq. (2.36) determines the timestep limit for explicit schemes and implicit schemes aimed at direct simulation of aeroacoustics. For implicit schemes with primary focus on the unsteady flow and turbulence consideration of just the convective flow velocity is sufficient: $a = U$. This is the definition adopted in ANSYS CFX as well as this work since it is governing the turbulence model function. However most of the computational domain indeed satisfies the stronger formulation as well.

In the context of higher-order methods (e.g. DG) it has to be considered that the CFL condition references to a smaller length than the mesh spacing depending on the solver order n.

$$\Delta x_{ref} = \frac{\Delta x}{2n - 1} \tag{2.37}$$

Furthermore the CFL condition might scale worse and drop below one in dependency on the scheme, e.g. STE-DG employed in this work.

2.2.4 Modeling Turbulent Flows

Turbulence is the driver of aeroacoustics and needs to be modeled or resolved respectively. Numerous approaches with different characteristics and fields of application are available e.g. in commercial CFD. This section details the functionality of the most prominent representatives (Tab. 2.3) and draws conclusions for their application within this work.

Approach	Accuracy	Comp. Effort	Comment
DNS	++	++	very high resolution requirements
LES	+	+	expensive for high Re-numbers
RANS	$--$	$--$	fast, single-mode turbulence only
DES	$-$	o	strong grid-dependency
SAS	o	$-$	novel, few validation, unknown potential

Table 2.3: Overview of CFD approaches modeling turbulent flows

Direct Numerical Simulation (DNS)

In a DNS approach the complete flow field including all turbulence scales down to the Kolmogorov scale (2.2) are directly resolved by the mesh. However, owed to the vast number of necessary elements the computational costs scale with $Re^3 M^{-4}$. Hence this approach is limited to low Reynolds number, high Mach number flows and simple or small geometries even on today's supercomputers [107]. DNS is a research rather than a design method. Even though the injection problem is comparably small in dimension DNS simulation costs are unaffordable here. It is employed for a simplified 2D problem though (Chap. 8).

Large Eddy Simulation (LES)

CFD developments in recent years have made LES one of the most accepted, powerful and applicable approaches for simulation of unsteady turbulence-governed problems. It provides time-accurate unsteady data for a variety of problems and at reduced costs compared to DNS. The grid resolution requirements are lower since only large boundary condition affected eddies are directly resolved and the influence of the smaller more or less universal turbulence scales is just modeled instead. In detail, the state vector Φ is split into resolved and subgrid scales (SGS) by application of a, e.g. Gaussian, filter G in space representing the characteristic element dimension $\Delta = f(\Delta x_1, \Delta x_2, \Delta x_3)$.

$$\Phi = \overline{\Phi} + \Phi^{SGS} \quad \text{with} \quad \overline{\Phi} = \int_V \Phi(\mathbf{x}) G(\mathbf{x}) \, dV \tag{2.38}$$

Introduced to the governing equations this approach raises a new unknown: the subgrid scale stress τ_{ij}^{SGS}. According to the eddy-viscosity hypothesis it is assumed to be caused - similar to molecular stresses - by a turbulent eddy viscosity μ_t in a linear function of the rate of the deformation tensor.

$$\tau_{ij}^{SGS} = \mu_t \left(\frac{\partial \overline{U}_i}{\partial x_j} + \frac{\partial \overline{U}_j}{\partial x_i} - \frac{2}{3} \frac{\partial \overline{U}_l}{\partial x_l} \delta_{ij} \right) \tag{2.39}$$

A *SGS model* is necessary to close the system. It ensures that the turbulent energy cascades on into the SGS rather than to accumulate at the smallest resolved scale. Most common, the Smagorinsky model relates the turbulent viscosity μ_t to the characteristic element dimension Δ and the local resolved strain rate tensor $\mathcal{S}$ via the Smagorinsky constant C_{SGS}.

$$\mu_t = (C_{SGS}\Delta)^2 |\mathcal{S}| \tag{2.40}$$

In this way LES enables direct aeroacoustic simulations for more complex and higher Reynolds number flows compared to DNS, e.g. [24, 107, 110]. It is most feasible for problems where the boundary condition dominated eddies are reasonably larger than the Kolmogorov scale. Then the mesh can be coarsened considerably and a wide range of weaker turbulence scales can be cheaply modeled. However four factors are known to have influence on the simulation results [3]: the SGS model, the inflow turbulence level, the accuracy of the numerical scheme and the farfield boundary condition. Furthermore LES becomes essentially undefined outside the CFL condition (2.36). Even though it is subject to a lot of ongoing research LES became one of the most accepted and best (commercially) available approaches for aeroacoustic simulations these days [107]. This makes it the first attempt and reference in terms of this work.

Reynolds-Averaged Navier-Stokes (U/RANS)

In order to further reduce grid resolution requirements and computational costs RANS approaches just capture the time-averaged flowfield directly and model all the turbulence scales instead. In contrast to LES, they decompose the flowfield into time-average and turbulent fluctuation.

$$\Phi = \overline{\Phi} + \Phi' \quad \text{with} \quad \overline{\Phi} = \frac{1}{T} \int_t^{t+\Delta t} \Phi(t) \, dt \tag{2.41}$$

Introduced to the momentum equations this raises the unknown turbulent Reynolds-stresses $-\rho\overline{u_i u_j}$. Again the eddy-viscosity hypothesis implies that the Reynolds stresses are caused by a turbulent viscosity μ_t.

$$-\rho\overline{u_i u_j} = \mu_t \left(\frac{\partial \overline{U}_i}{\partial x_j} + \frac{\partial \overline{U}_j}{\partial x_i} \right) - \frac{2}{3}\rho k \delta_{ij} \tag{2.42}$$

Now however μ_t is expressed in terms of turbulence kinetic energy k, turbulence eddy frequency ω and turbulence dissipation ε.

$$\mu_t = \rho \frac{k}{\omega} = c_\mu \frac{k^2}{\varepsilon} \tag{2.43}$$

Additional equations, the *turbulence model*, close the system by making assumptions about those statistical characteristics of the turbulent flow. The semi-empirical two-equation models k-ε, k-ω, and the shear stress transport model (SST) blending between both of the former are well-known representatives [66]. However, common to all those models, the shear strain rate is the only source term. Hence, just a single dominating turbulence scale is generated even using a two-equation model. Since the models imply homogeneous shear the generated turbulence grows to shear layer dimensions naturally.

Summarizing, URANS approaches are capturing a transient flowfield at low costs. The prediction of just a single turbulence mode is sufficient if the main vortex shedding or motion-induced turbulence is focused at. Common URANS turbulence models are inherently unable to reproduce broadband turbulence and acoustics, though, even if the mesh is further refined. Hence, its application is limited to problems dominated by the largest emerging eddies or to regions of non-essential turbulence in the framework of hybrid CFD-CAA methods. It is accepted to be unfeasible for aeroacoustics in particular.

Detached Eddy Simulations (DES)

As a compromise, DES approaches combine time-accurate but still expensive LES with fast but just single-mode URANS in an adaptive solver [95]. Depending on the mesh and local requirements it automatically switches between LES and URANS modes. Ideally, just the regions containing the relevant turbulence structures, sources of noise and acoustic-flow interactions are processed by LES while the acoustic farfield, stationary flow regions and boundary layers (where LES has excessive resolution requirements) are handled by URANS.

This approach is feasible and successfully employed for heavily separated and high-Re flows. However the blending between LES and URANS is known to be strongly grid dependent with an undefined mixture of LES and RANS components in the transition regions of a smooth mesh [94]. This explicit sensitivity results in the fact that DES is often avoided for aeroacoustic simulations.

Scale-Adaptive Simulation (SAS)

Technically, SAS [67] just describes a novel class of enhanced URANS turbulence models. These provide broadband turbulence and DES-like functionality however. The improvement comes from the introduction of the von Karman length scale L_{vK} into the turbulence model as

a measure for the characteristic dimension of the smallest emerging eddies. The shear strain rate $|S|$ remains the only source term.

$$L_{vK} = \left| \frac{\partial \overline{U}_i / \partial x_j}{\partial^2 \overline{U}_l / \partial x_m^2} \right| \tag{2.44}$$

In detail, L_{vK} adjusts to the unsteadiness in the flow and ranges between grid spacing and shear layer thickness. Thus, the turbulence model dynamically adapts to the resolved instabilities and produces turbulence of respective length-scales. The result is a wholly modeled LES-like broadband turbulence spectrum. Advantageous for thin shear layers, just the minimum element dimension needs to be of the smallest turbulence scale to be generated while LES requires an equally dense spacing in flow direction as well.

However, if no unsteadiness is produced by the flow or resolved by the mesh, e.g. due to a too coarse grid or a too large timestep (CFL > 1), the old single-mode ('URANS-like') solution remains as fallback. This motivates to employ SAS as a DES-replacement since it does something like an implicit LES-RANS blending but smoothly and with a less grid-dependent solution.

The first available augmented turbulence model – and focused in this work – is named SAS-SST (short: SAS). Owed to its novelty and implementation just in ANSYS CFX it is validated for very few tests cases up to now, e.g. [23]. Most are more or less academic and hardly any is focused on aeroacoustics or supersonic flows. Since SAS is meant to be run within the CFL condition no detailed information or publication is available concerning the exact behavior for large CFL numbers in particular.

2.2.5 Hybrid CFD-CAA Methods

These approaches describe an explicit and manual splitting of the computational domain into sound generation and propagation rather than automatic blending. In each region dedicated solvers run completely detached from each other, just being interconnected by exchanging data in some way. Advantages are that different solvers, governing equations, numerical methods and discretizations can be employed just as it is fitting best and saves most computational time. In most cases LES is used in the source domain while an acoustic analogy, LEE [16], APE [31], or the wave equation (2.16) is solved in the propagation region. The major problems are the kind and implementation of the data exchange and to ensure a conservative non-reflective coupling, though. In worst case this means time-consuming manual data exchange and sequential rather than parallel code runs.

Volumetric Coupling

One way to couple solvers and domains is to employ superposing meshes and transfer aeroacoustic source terms between them. Source terms such as acoustic quadrupoles, Lighthill stresses or the Lamb vector [39] can be deduced from the turbulent flow solver and re-employed as basis for the acoustic propagation. Common to all source terms is however that they build upon theories about the noise generation. Thus it is possible that they do not cover all necessary sound generation mechanisms of the problem. Furthermore source term coupling assumes that the sound waves propagate linearly, without interaction or feedback and in superposition to a constant base flow from the source location to the far-field. These assumptions are fine for many problems, will become an invalid for fluctuating supersonic flows as in this work though.

Surface Coupling

Surface coupling on the other hand allows to compute aeroacoustics for arbitrary flows and in arbitrary environments. The CFD solver directly captures all noise generation and propagation within the source region while it steadily exports state vector fluctuations in an enclosing surface. These fluctuations can be re-employed in an attached CAA domain to compute the acoustic far-field. If no simple CAA treatment is possible (e.g. BEM) this is leading to a heterogeneous domain decomposition which requires sophisticated interpolation of time and space discretizations between the codes in order to ensure conservation and avoid reflections. Another disadvantage is the typically high dissipation of common CFD tools requiring the source region to be as small as possible.

One-way vs. Two-way Coupling

Often data transfer is only considered to be one-way: from the sources into the far-field. If the far-field is confined however, scattered waves can propagate back into the source region, cause feedback and generate noise. Fully coupled parallel or sequential CFD and CAA runs become necessary. This can not be handled manually anymore and calls for dedicated code coupling and harmonization tools, like e.g. MpCCI. Considering the injection into the intake manifold two-way coupling might be imminent, source and propagation regions might be hard to separate though. Furthermore commercial software capable of two-way coupling is hardly available.

2.3 Theory of Non-Reflective Boundaries

Computational boundaries truncating the far-field by inlets, outlets and openings are supposed to allow the aerodynamic field to pass freely with minimal reflections and influence on the solution within the computational domain. However it is known that especially acoustic waves might be reflected at any, although theoretically passable, boundary. This point is crucial in computational aeroacoustics since spurious acoustic waves generated by poor boundary conditions may mask the physical sound field radiated by turbulence [99].

Spurious reflections can occur within the mesh as well. At hanging nodes or when the grid spacing is coarsening too quickly the phase speed can become negative and the wave is spuriously reflected. This is not in focus here. In contradiction, poor boundary conditions strictly specify fluid state variables without room for fluctuations, e.g. the static pressure at an outlet. Thus incident waves can not develop naturally and are reflected instead.

The application of an averaged boundary condition provides a workaround for weak acoustic waves. The integral average taken over the whole boundary surface is constrained to a specified value such that the flow variables can float and fluctuate within limits. However, the magnitudes of acoustic waves are often too large to be treated by an averaged boundary condition only [15].

In these cases an optimized boundary placement can be supportive since the reflection properties are more favorable if the outgoing wave angles are small [86]. Often the boundary placement is predetermined by the problem or the sources of noise are spread throughout the domain, though.

2.3.1 Non-Reflective Boundary Conditions

In order to minimize spurious reflections for the variety of aeroacoustic problems dedicated boundary treatment such as non-reflective boundary conditions (NRBC) become necessary [15]. Two modeling approaches were found to be effective in particular.

Characteristic BC The first to mention was proposed by Thompson [105] and Poinsot and Lele [81]. It is based on a one-dimensional characteristics analysis and is meanwhile implemented in many CFD tools. The fundamental idea is to compute the invariants of the governing hyperbolic system, and to recast the outgoing invariants perpendicularly to the boundary. Since this method is intrinsically 1-D it is only efficient for perpendicularly incident perturbations. It is badly suited for oblique waves since it can cause numerical instabilities due to trapped tangential components. These instabilities are intolerable and further amplified in the presence of strong mean shear. Furthermore there is a discontinuity in the boundary definition in the corners of the computational domain. Recently, a lot of improvements have

Approach	Pro's	Con's
Averaged pressure BC	simply applicable, available in commercial CFD	effective only for weak fluctuations, unnatural forcing possible
Optimized BC placement	simply applicable	just supporting other means
Grid stretching	simply applicable	effective only for weak fluctuations
Slowly powering jet up	weakens amplitudes during injector opening, more realistic transient results	requires transient inlet BC and transient inlet data
Characteristic NRBC	weakens reflections, partially available in commercial CFD	usually just 1-D, ineffective for oblique incident waves
Radiation NRBC	very effective	simply applicable only for linearized Euler equations or wave equation, not available in commercial CFD
Artificial viscosity ABL	simply applicable	effective only for weak fluctuations, raises problems for strong fluctuations and flow discharge
Implicit damping ABL	effective, widely applicable, available in commercial CFD	can cause instabilities, effectiveness dependent on discretization
Artificial convection ABL	more effective than implicit damping	requires to alter governing equations, not available in commercial CFD
Explicit damping ABL	very effective, fail-safe	requires write access to solution vector, not available in commercial CFD
Perfectly Matching ABL	strongly effective	requires to alter governing equations, not available in commercial CFD

Table 2.4: Overview of less-reflective and non-reflective boundaries

been proposed accounting for the mentioned effects, e.g. [111]. However there are no known implementations in commercial CFD solvers yet.

Radiation BC   The second approach modeling NRBC was firstly suggested by Bayliss and Turkel in 1982 [5]. Its basic idea is to reduce the governing system of equations to a simplified form reflecting the far-field, e.g. a convective wave equation, and construct an asymptotic solution to it. Thus differential equations can be derived which allow to obtain realistic values for the flow variables at the boundary. If these are specified at the numerical domain boundary, reflections vanish. However, these asymptotic far-field formulations are problem-dependent. They require a known mean flow, a known radiation pattern (e.g. in terms of approximate locations of acoustic monopoles) and an asymptotic formulation reflecting the presence of obstacles and walls in the farfield. Ducts, for example, result in a different noise propagation and thus asymptotic solution than exterior problems. All this complicates the condensation of an radiation BC for complex flows. Hence radiation BCs are only implemented in research codes dedicated to specific problems so far.

In either approach, NRBC are quite difficult to implement and just partially non-reflective indeed. Furthermore the efficiency depends on a number of parameters like the wavelength, the out-going wave angle and the mean flow velocity. Hence support by e.g. wave-splitting [25] or spatial filtering [107, 112] methods might become necessary additionally. These techniques require further code adjustments and new equations to be solved, though. If any, simple 1D characteristic NRBC are implemented in commercial CFD tools like ANSYS CFX instead.

2.3.2 Absorbing Boundary Condition

In a more general approach, absorbing boundary conditions (ABC) damp the magnitudes of (acoustic) fluctuations before they can reach the domain boundary [86]. This requires to alter flow or fluid properties in the region close to the boundary intentionally. Hence the numerical result is not physically valid there anymore. Consequently, ABCs demand for an extension of computational domain by dedicated *sponge layers*. Often these comprise about 20% additional elements accompanied by respectively increased simulation effort.

The performance of the ABC depends on a number of parameters as well. In detail, the solver convergence is inversely proportional to the sponge strength σ [12]. Furthermore an increased sponge layer width significantly reduces wave reflections and improves performance at all outgoing wave angles [86, 12]. However, defining minimum lengths for adequate performance is difficult as the sponge zone performance is problem specific. Greater wavelengths and wave angles close to being parallel to the boundary require larger sponge layers, though.
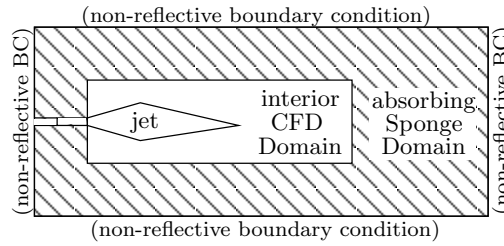
Figure 2.1: Application of an absorbing boundary layer to a jet problem

The ABC and its interface to the interior domain pose an additional boundary condition which can alter the simulation result unintentionally. Discontinuities at the interface will reflect waves and poor ABC definitions will force unnatural flow within the sponge layer as well as in the actual flow domain. Therefore a smooth transition into the sponge layer is imminent and generally achieved by a blending function for σ.

Artificial Viscosity   A simple way to damp acoustic waves is to dissipate any fluctuations by artificially increased viscosity. This introduces a stronger resistance to shear stresses in the momentum equation and acts on local velocity gradients. Amongst others those are caused by the particle velocity induced by passing sound waves.

However, for strong fluctuations and a highly increased viscosity this approach might cause undesired side-effects. The hydrodynamic solution might be affected as well even outside the ABC. Furthermore the fluctuation energy is transformed into thermal energy such that this approach gives rise to the local temperature for stronger waves.

Implicit Damping   A more sophisticated approach is based on the definition of additional source terms in the governing equations (2.8)-(2.10). Thus perturbations are damped by forcing the flow towards a specified mean flow (Dirichlet condition). The corresponding mass, momentum and energy is not transformed but taken out of the system indeed.

$$S_C = -\sigma_1(p - p_{spec}) \tag{2.45}$$

$$S_M = -\sigma_2(U - U_{spec}) \tag{2.46}$$

$$S_E = -\sigma_3(T - T_{spec}) \tag{2.47}$$

The effect of the source terms is timestep- and fluctuation magnitude-dependent, though. Hence the identification of an appropriate setting for σ_i is particularly difficult with the chance to cause instabilities. Furthermore, if the steady mean flow is unknown in advance the Dirichlet condition is not applicable anymore. Exploiting gradients or derivatives could be alternatives instead.

Artificial Convection This method proposed by Freund [33] adds a convection term $\nabla \cdot (\rho \mathbf{U_c} \otimes \mathbf{U})$ to the governing system of equations alongside with implicit damping source terms. The motive is to accelerate all waves towards the outer boundary layer edge by a superposed convection velocity $\mathbf{U_c}$. Then any reflected waves are slowed by this opposing convection and are subject to increased damping. Hence the overall performance is better than experienced without the additional convection term.

A particular case of this approach is the acceleration to supersonic velocities. Then, of course, no reflected acoustic waves can propagate back into the interior domain. This indeed eliminates the need for any damping terms and a non-reflecting boundary condition [97]. Since this approach requires to alter the governing system of equations it is not applicable in commercial software though.

Explicit Damping This approach has parallels with implicit damping. However, perturbations are not damped by source terms during a timestep computation but by explicit relaxation towards the specified mean flow state vector Φ_{spec} after each timestep.

$$\overline{\Phi_{n+1}} = \Phi_{n+1} - \sigma(\Phi_{n+1} - \Phi_{spec}) \tag{2.48}$$

This is simple to implement yet much more efficient and robust than the implicit approach. In fact, it only requires sponge widths of the order of the incident wavelengths because explicit damping causes the waves to fold up within the sponge layer [86].

Explicit damping requires write access to the state vector on a regular basis however. In research codes this is not an issue. Commercial software commonly prohibits to alter the solution by the user tough.

Perfectly Matched Layer The ABC approaches so far require a blending function slowly increasing the sponge strength σ within the sponge domain in order to avoid reflections at the interface to the interior domain. This is leading to the facts that a reasonable portion of the sponge is of little use for damping and quite wide sponge layers become necessary.

Initially developed for electro-magnetics by Berenger [6], Hu [43] showed that it is possible to design a governing system of equations also for fluid dynamics such that waves passing the inter-domain interface at any angle and frequency are not reflected anymore at all. The basic principle is the spacial splitting of the governing equations and the introduction of a new auxiliary state variable. This allows σ to be constantly high throughout the sponge domain such that waves are dampened exponentially. Consequently, the additional costs for an ABC can be reasonably reduced [101] while the performance is similar to or better than implicit damping [55].

However PML can give rise to waves of distinct phase speeds. In fact, the stability of PML equations is highly mean flow dependent [43]. Thus, especially in a confined environment PML may not be suitable as an absorbing boundary condition unless there is no mean flow [100]. As this approach requires to alter the governing system of equations it is not applicable in commercial software.

Grid Stretching   Due to smooth but increasing grid stretching disturbances become worse resolved as they propagate. Then turbulent structures and waves which are no longer supported by the numerical scheme are dissipated. However if the grid is stretched too far spurious reflections can occur. In practice it is reasonable to combine this approach with some sort of active damping in a sponge layer or a solver scheme with higher numerical damping (e.g. an Upwind scheme) in order to improve efficiency [19].

2.4 Solver Technology of Applied Codes

Two specific approaches are pursued in this work by the employment of quite different tools (Tab. 2.5). On one hand this is the commercial ANSYS CFX which can be considered one of the standard CFD solvers at the industrial scale. It is very robust and applicable to a wide range of problems today but neither intended for aeroacoustics nor highly unsteady compressible problems. On the other hand, the research code NSDG2D is dedicated to very high efficiency and accuracy for compressible flows in particular. Owed to its research status and currently still missing implementations (Tab. 2.5) the field of application is still quite limited, though. Nevertheless it is a promising approach and therefore assessed in terms of solution quality and potential (Chap. 8).

2.4.1 ANSYS CFX

As a commercial tool aimed at versatility and robustness rather than accuracy ANSYS CFX employs FV and implicit backward Euler schemes of up to second order (MUSCL). Near steep gradients it blends down to 1st order accuracy indeed to improve stability. However, it does not obey a timestep limit and features numerous turbulence models, amongst others the novel SAS-SST. Since there is no direct access to the code and state vector, own implementations, e.g. with respect to better NRBC, are limited though.

In its solver strategy the discretized hydrodynamic equations (continuity and momentum) are considered as a single fully coupled system. It is linearized and solved by an incomplete LU-factorization. Subsequent pressure-correction is not necessary. Based on the hydrodynamic result, all remaining equations (total energy, turbulence model, mass fraction, ..) are solved

Property	ANSYS CFX	NSDG2D
Discretization	FV (MUSCL), 3D	DG (CK-predictor), 2D
Governing Equations	N.-S.	N.-S. and Euler
Accuracy	2nd order (1st order at steep gradients)	2nd-8th order preferred (preset or local adaptive)
Time Marching	implicit, backward Euler	explicit, STE+CK proc.
Timestep	global, preset or adaptive	locally adaptive
Turbulence Model	DNS, LES, k-ϵ, k-ω, SST, SAS-SST and others	DNS
NRBC/ABL	characteristic (beta)	explicit damping
State Vector	pressure driven, primitive variables	density driven, conservative variables
Specifics	algebraic multigrid solver	hp-adaption, local timestepping, curved elements
Status	robust and versatile standard tool with focus on steady and weakly compressible flows	highly efficient research code for compressible flows, under development, few validation

Table 2.5: Solver technologies of ANSYS CFX and NSDG2D

successively. Since the governing system of equations is inherently non-linear the obtained solution might be inconsistent and iteration of the linearization point becomes necessary. All equations are solved over again in so-called coefficient loops till convergence or the preset maximum number of loops is reached.

Specific to ANSYS CFX, the linear solver employs an algebraic multigrid method. While stepping through the coefficient loops, the mesh is virtually coarsened by summing up sub-equations of the linearized system. However, the determination of which elements are combined is done only once for the flow initialization. If the emerging flow changes reasonably over time this can cause bad convergence and instability.

The solver technology implemented in ANSYS CFX is aimed to provide robust results for a variety of problems but with focus on stationary or weakly transient flows and just low compressibility. It is not very efficient and accurate for strongly transient and supersonic flows. Aeroacoustic noise is inherently produced as a result of captured or modeled turbulence. Due to the high numerical dissipation noise propagation over long distances should be avoided, though.

2.4.2 NSDG2D

Developed at the Institute of Aerodynamics and Gasdynamics of the Universität Stuttgart this research code [27, 58, 38] combines a DG approach for spatial discretization with a STE approach augmented by a CK procedure for time marching (Sec. 2.2.3). It allows to handle

highly unsteady compressible flows with higher-order accuracy, dynamic hp-adaptivity, explicit local timestepping and low diffusion. Besides it tolerates mixed-type unstructured meshes with hanging nodes and curved elements.

Indeed NSDG2D implements a DG scheme in predictor-corrector formulation. This is by 30% faster than the normal formulation (2.30) since no volume integral (stiffness matrix) is computed anymore. In detail, the STE+CK prediction $\tilde{\Phi}(\mathbf{x}, t)$ is introduced to Eq. (2.33) to enable the time-integration.

$$\int_{t_n}^{t_{n+1}} \int_{C_k} \left(\frac{\partial \Phi}{\partial t} + \nabla \cdot \mathbf{f}(\tilde{\Phi}) \right) \xi_k \, dV dt = - \int_{t_n}^{t_{n+1}} \int_{\partial C_k} \left(\mathbf{f}(\tilde{\Phi}) - \mathbf{f}_{int}(\tilde{\Phi}) \right) \xi_k \mathbf{n} \, dS dt \qquad (2.49)$$

Since $\tilde{\Phi}$ complies with the conservation law as well, $\frac{\partial \tilde{\Phi}}{\partial t} = -\nabla \cdot \mathbf{f}(\tilde{\Phi})$, the gradient of the flux can be replaced by the time-derivative of the prediction.

$$\int_{t_n}^{t_{n+1}} \int_{C_k} \left(\frac{\partial \Phi}{\partial t} - \frac{\partial \tilde{\Phi}}{\partial t} \right) \xi_k \, dV dt = - \int_{t_n}^{t_{n+1}} \int_{\partial C_k} \left(\mathbf{f}(\tilde{\Phi}) - \mathbf{f}_{int}(\tilde{\Phi}) \right) \xi_k \mathbf{n} \, dS dt \qquad (2.50)$$

On the left hand side spatial and temporal integrals are swapped. Exact integration in time and using the identity of prediction and solution at the current time level $\Phi^n = \tilde{\Phi}^n$ this results in a predictor-corrector formulation eventually.

$$\underbrace{\int_{C_k} \Phi^{n+1} \xi_k \, dV}_{\text{DG-solution}} = \underbrace{\int_{C_k} \tilde{\Phi}^{n+1} \xi_k \, dV}_{\text{CK-predictor}} - \underbrace{\int_{t_n}^{t_{n+1}} \int_{\partial C_k} \left(\mathbf{f}(\tilde{\Phi}) - \mathbf{f}_{int}(\tilde{\Phi}) \right) \xi_k \mathbf{n} \, dS dt}_{\text{Corrector with influence from neighboring elements}} \qquad (2.51)$$

Application of the form function approach (2.27) turns the remaining volume integrals into mere (mass) matrix-vector multiplications. Employment of Legendre polynomials makes M diagonal such that the explicit time-evolution of $\hat{\Phi}$ just requires a comparably cheap CK-prediction for the new time level and the evaluation of a surface integral.

$$\hat{\Phi}_k^{n+1} = \hat{\tilde{\Phi}}_k^{n+1} - M_k^{-1} \int_{t_n}^{t_{n+1}} \int_{\partial C_k} \left(\mathbf{f}(\tilde{\Phi}) - \mathbf{f}_{int}(\tilde{\Phi}) \right) \xi_k \mathbf{n} \, dS dt \qquad (2.52)$$

Hence the new time level is predicted just based on the spatial distribution within the elements at current time level. The surface integral then introduces a correction in compliance with the DG approach compensating a discontinuous prediction between neighboring elements. Since this correction can be considered the truncation error of the discretization as well it is the basis for a dynamically hp-adaptive scheme.

This is enhanced by local timestepping. The timestep size is chosen for each element separately in fulfillment of the stability condition, and the CK-prediction for the new time level

is obtained right away. Then the prediction is successively corrected in terms of contributions of neighboring elements to the surface integral within the timestep.

Since the code is still under development validation is performed for just few test cases up to now and some implementations are still missing. Amongst others the extension to 3D, parallelization with dynamic load balancing and implementation of LES turbulence modeling are just planned or currently being processed. On the other hand it offers great flexibility in adding new techniques like more efficient sponge layers for the attenuation of spurious reflections.

Chapter 3

Preliminary Work

Primary focus of this chapter is to summarize preliminary studies conducted in the fields of jets in cross-flow, jet aeroacoustics, noise propagation in ducted environments and noise control. This comprises the classification and formation of flow and acoustic phenomena as well as respective simulation approaches. Furthermore, preceding simulations on the very problem geometries of injector and intake manifold are outlined in sections 3.5 and 3.6. Eventually everything is appraised in terms of relevance for this work.

3.1 Jet in Cross-Flow (JICF)

A (supersonic) gas jet transverse to a subsonic cross-flow is accompanied by a number of large scale vortical structures affecting the jet shape and altering noise generation and propagation. The four known vortical structures are: the horseshoe vortices, the jet shear layer, the wake structures and the counter-rotating vortex pair (CVP) [92].
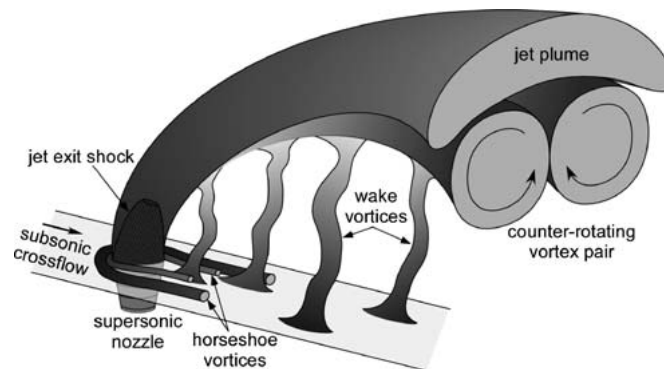
Figure 3.1: Major vortex structures of JICF [7]

From the crossflow's point of view a transverse jet is similar to a solid body. The pressure at the jet's leading edge is increased while it is reduced at the trailing edge. This causes the characteristic JICF trajectory. At the same time, the bypassing crossflow is responsible for deformation of the jet's shear layer and cross section. In detail it shears the jet fluid around its

perimeters such that the resulting vorticity redistribution ultimately develops into a counter-rotating vortex pair (CVP). It has been shown to persist up to hundreds of jet diameters downstream and is known to reduce noise by absorbing nearby turbulences [68]. The hanging vortices on the other hand arise from the Kelvin-Helmholtz instability between the jet and the crossflow [21].

Pitch and Yaw Angles

Milanovic and Zaman [68] performed a parameter study with respect to pitch and yaw angles the jet is injected with into the crossflow. Their experiments reveal that the peak streamwise vorticity is practically independent of the pitch. The upward penetration of the jet and the curvature of the jet cross section are more pronounced at higher pitch angles.

When it comes to the yaw angle their investigations reveal that yawed jets spread more, distort the kidney shape in a way that peak velocities are closer to the wall and have considerably lower values compared to the zero yaw (symmetric injection) case. Yawed jets are found to remain closer to the wall, enhance turbulence in the vicinity of the boundary layer and to have higher peak streamwise vorticity.

Simulations

Experiments generally point to reasonable flow asymmetry [21]. Thus, simulations in only half the geometry using a symmetry plane would result in unrealistic results even for symmetric (zero yaw) injection. RANS computations with $k-\varepsilon$ turbulence model and LES computations have been performed successfully for the JICF [21].

3.2 Sources of Noise During Gas Injection

Noise generation in a supersonic gas jet is a very complex problem, especially under presence of nearby walls and cross-flow. In fact no comprehensive analysis is found in literature for such a case. Therefore the noise generation mechanisms known for free and impinging jets are outlined here instead. Eventually this will be the basis for noise source localizations and classifications and for interpretation of simulations and experimental results in context of this work. Noise caused by unsteady (pulsed) injection is not explicitly listed here but might be a reasonable contributor as well.

	Turbulent Mixing	Shock Noise	Screech	Impingement
Type of noise	broadband	broadband	tonal	broadband & tonal
Requirements	–	supersonic flow	supersonic flow	impingement wall
Cause	turbulences-turbulence interaction in shear layer	turbulence-shock interaction	shock-to-nozzle feedback loop	wall-pressure fluctuations, wall-to-nozzle feedback loop
Effect	–	–	flapping and helical jet modes	flapping and helical jet modes, shocks in impingement region
Physical Parameters	jet velocity (noise $\propto U_j^3$ to U_j^6), jet temperature, turbulence intensity	shock cell strength, turbulence intensity	shock cell strength, shock cell spacing, feedback path, turbulence intensity	impingement plane distance, shock cell spacing, feedback path
Design Parameters	nozzle shape, NPR, inlet turbulence level	nozzle shape, NPR, inlet turbulence level	fully expanded jet Mach number, nozzle shape (esp. lip), NPR, inflow turbulence level	fully expanded jet Mach number, nozzle shape (esp. lip), NPR, impingement plane distance
Control devices	distributed exhausts, corrugated jets, microjets, trailing edge modifications, frequency excitation	distributed exhausts, corrugated jets, microjets, cross-wire device, frequency excitation	distributed exhausts, microjets, trailing edge modifications, cross-wire device, frequency excitation	distributed exhausts, microjets, trailing edge modifications, cross-wire device, frequency excitation
Recent Simulations	enhanced RANS [103, 104, 101], SAS [67], LES [107, 24]	DNS [62, 63, 64]	enhanced RANS [90, 56], linearized N.-S. [70, 34], LES [107, 11] and others	–
References	[47, 42, 57, 75, 45, 71, 34, 89]	[80, 46]	[84, 90, 44, 102, 98, 50, 1]	[52, 108, 106, 82]

Table 3.1: Possible noise sources during CNG injection

37
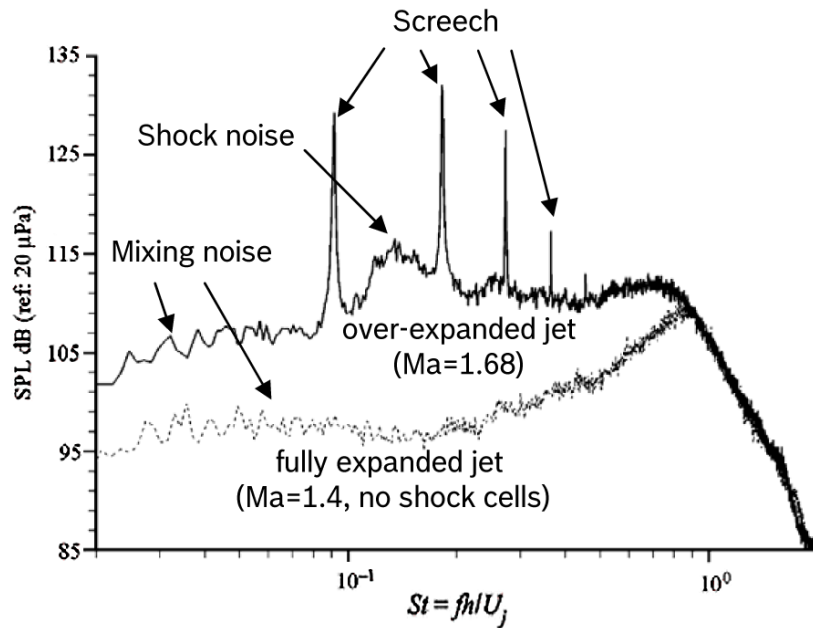
Figure 3.2: Typical near field microphone spectrum at $R = 25D_j$ of over-expanded and fully expanded supersonic jets [1]

3.2.1 Background Noise and Inflow Turbulence

Broadband noise coming from the inlets, structural oscillations, turbulent boundary layers and nearby installations can mask measurements and result in deviances to simulations. Furthermore, the inlet turbulence level is known to be imminent for aeroacoustic simulations. Both has to be considered when performing and comparing measurements and simulations.

3.2.2 Turbulent Mixing (Jet Noise)

Turbulent mixing appears for any jet with a steep velocity gradient to the ambient domain. The result is a strong *mixing shear layer* generating noise outside the potential core (Fig. 3.3). This so-called *jet noise* is broadband, extending over a frequency range of almost three decades, and typically has a peak at $St \approx 0.3$ [101]. The major influence factor is the jet velocity, which contributes with large exponents.

It is assumed that there are at least two distinct sources of jet mixing noise in supersonic jets [42]. The first of which is associated to the large highly energetic instability waves in the shear layer interacting with the mean flow. These sound sources are of quadrupole type, mainly located around the end and downstream of the potential core and radiate low frequency noise [75] at angles close to the jet axis (confined within the Mach cone) [103]. This process is usually referred to as *Mach wave radiation* of supersonicly moving eddies or *shear-noise* [45].

The second source of jet mixing noise is connected to the quite isotropic much weaker
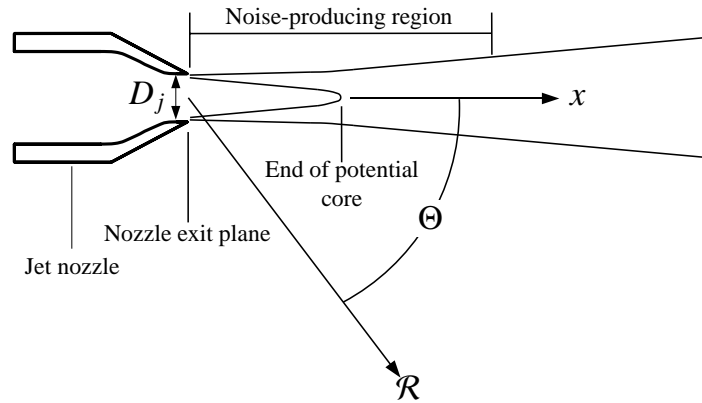
Figure 3.3: General schematics of a turbulent jet

fine scale turbulence [103]. They behave like monopoles [101] and radiate non-directional broadband noise [75]. This is referred to as *self-noise* and is the dominant source of noise outside the Mach cone [103], especially upstream and in lateral directions.

Simulations

Recent studies using LES, e.g. [107, 24], are in excellent agreement with experimental observations. However, the standard SGS turbulence models were shown to be insufficient, especially for high frequencies and highly compressible flows at high Reynolds numbers. Therefore, a number of more or less statistical models are under development momentarily [14, 13].

Computationally less demanding RANS approaches with subsequent noise source models have been implemented and tested as well with good results [103, 9, 10, 101]. To obtain better results from time-averaged flow data, and to overcome compressibility and nonlinear effects in supersonic jets, these approaches still need to be enhanced, e.g. by dedicated turbulence models, though [77, 91, 104, 71].

3.2.3 Shock Noise

Shock noise is broadband as well but ranges at a higher frequency spectrum than jet noise making it hard to separate. It generally appears in imperfectly expanded supersonic jets where shocks and shock cells are prominent fluid structures. It is radiated by the shock cells, mostly in the upstream direction of $40°.. 50°$ to the jet axis [17]. It is primarily influenced by the turbulence levels and the shock cell strengths.

The shock-associated noise generation traces back to the interaction of the instability waves in the shear layer with the shock cell structure within the potential core [46]. Shock motions are the key elements in the process. Once the shear layer disturbances are grown large enough

while convecting within the shear layer, they force the shocks to undergo large streamwise fluctuations in position, orientation and strength. This is leading to repeated compression and expansion of the air within the shock cells, and thus intense noise generation [80].

Simulations

Just few simulation results exist for the shock noise problem. These were performed using DNS for highly simplified problems in order to understand the noise generation in the first place [62, 63, 64]. Most research work concerning shock associated noise is headed for the screech phenomenon described in the next section instead.

3.2.4 Jet Screech

Jet screech describes a set of discrete tones having extreme intensities. It requires shock cell structures and a feedback loop back to the nozzle lip. However, jet screech is not just an entirely acoustic phenomenon. Due to the amplification of particular large-scale structures in the shear layer it also has impact on the jet flow itself. In fact, the resulting periodic shear layer deformations can cause jet shape oscillations, referred to as axisymmetric or flapping/helical *screech modes* [90]. Dominating influence factors are the shock cell strength and nozzle lip shape (intensity), and the shock cell spacing (frequency).
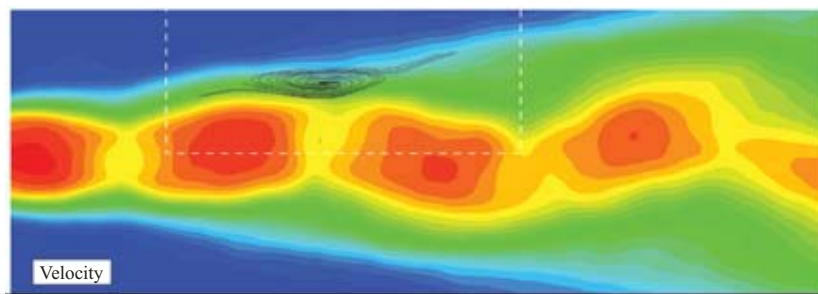
Figure 3.4: Large-scale turbulence structure causing flapping mode of the jet [1]

The basic noise generation mechanism of jet screech is the broadband shock noise. Then however, a portion of the generated noise propagates upstream in the ambient medium and amplifies instability waves of particular frequencies (depending on the feedback path length) in the shear layer near the nozzle lip. This is leading to stronger shock noise generation at these frequencies in return, and thus, to a self-sustained acoustic feedback loop [46]. The whole phenomenon is highly nonlinear and the screech modes with their respective feedback loops are not completely understood yet [90]. Thus frequencies and intensities can be predicted analytically for a few modes and simple jets only [102]. For very small jets the screech tones might be well above audible range, though.

Simulations

Simulations regarding the screech phenomenon have been undertaken using numerous approaches. For example an enhanced RANS approach [90] predicted the screech tones quite well in terms of frequencies and intensities. Furthermore approaches solving the quasi-gasdynamic (QGD) system of equations [65], the linearized Navier–Stokes equations [70, 34] and a number of more common LES [107, 11] and DNS attempts [11, 34] were carried out with good results.

3.2.5 Impinging Jet

Noise generation upon impingement is related to two separate phenomena [52]. Firstly, the large scale turbulences within the jet are causing wall-pressure fluctuations and *broadband noise* sources in the impingement area. Secondly, there is a wall-to-nozzle feedback phenomenon similar to jet screech. The latter is, even under absence of shock cells, responsible for excitation of shear layer turbulences of particular frequencies and, thus, the domination of discrete, high amplitude tones referred to as *impinging tones* or *impingement screech*. In cases where the impingement plane is close to the potential core an additional *stand-off shock* and pulsating *stagnation bubble* can emerge and act as noise sources as well [41]. The physics of these phenomena are not well understood yet though.

Simulations

Most of this understanding comes from experiments. Recent simulations, e.g. [48], focus the flow instability problem only. In fact, no attempts have been made so far to incorporate noise generation and propagation.

3.3 Propagation of Noise within a Duct

Within ducted environments the continuous reflection of noise at the confining walls results in the formation of coherent wave patterns called *duct modes*. These superpose and shape a complex sound field which is dependent on the duct geometry, axial flow and the induced frequencies. Besides duct acoustics is generally subject to mode coupling, mode cut-off conditions, different phase and group velocities, dispersion and partial reflections at cross-section variations [28, 29]. This will be detailed in the following.

3.3.1 Duct Modes

Duct modes can be derived mathematically [29] on basis of the three-dimensional wave equation (2.16). Assuming an axisymmetric round duct in which only harmonic solutions $p' = \phi e^{i\omega t}$

are allowed and taking the boundary conditions into account

$$\text{hard wall boundary condition} \qquad \frac{\partial p'}{\partial r}(R) = 0 \qquad (3.1)$$

$$\text{circumferential periodicity} \qquad p'(\theta) = p'(\theta + 2\pi) \qquad (3.2)$$

$$\text{continuous solution in the duct axis} \qquad p'(z, r = 0, \theta, t) = p'(z, t) \qquad (3.3)$$

the acoustic pressure related to the mode $(m, n) \in (\mathbb{N}, \mathbb{N})$ can be cast as a function of the location within the duct, a Bessel function J_m and the acoustic frequency.

$$p'_{mn}(z, r, \theta, t) = \underbrace{\left(A_1 e^{-ik_{mn}z} + B_1 e^{ik_{mn}z} \right)}_{(I)} \cdot \underbrace{A_2 J_m(k^*_{mn} r)}_{(II)} \cdot \underbrace{\left(A_3 e^{-im\theta} + B_3 e^{im\theta} \right)}_{(III)} \cdot \underbrace{e^{i\omega t}}_{(IV)} . \qquad (3.4)$$

Term (I) in Eq. (3.4) defines the pressure distribution in axial direction, term (II) the radial pressure distribution, term (III) the circumferential pressure distribution and the term (IV) finally the harmonic pulsation of the whole field. Graphically n represents the number of wave knots in radial and m the number of periods in circumferential direction.
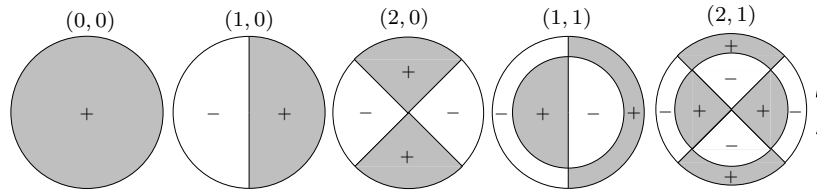
Figure 3.5: Pressure distribution in a cross-section for duct mode (m, n)

The *axial* sound pressure field is governed by waves with wave number $k_{mn} \in \mathbb{R}$ and the phase velocity $\frac{\omega}{k_{mn}}$. The parameters A_1 and B_1 define the propagation of the pressure field in $-z$- and $+z$-direction. In case $A_1 = B_1$ the solution states a standing wave in axial direction.

The *radial* pressure distribution is dominated by the *Bessel function* of m-th order

$$J_m(s) = \sum_{l=0}^{\infty} \frac{(-1)^l (0.5s)^{m+2l}}{l!(m+l)!} \qquad m \in \mathbb{N} . \qquad (3.5)$$

For boundary condition reasons this function needs to be scaled such that it has a minimum or maximum at the wall. As the Bessel function has unlimited local extrema there are unlimited solutions as well. A particular solution can be referenced by k^*_{mn} with

$$\left. \frac{dJ_m(s)}{ds} \right|_{k^*_{mn} R} = 0 . \qquad (3.6)$$

This k^*_{mn} is often referred to as the radial wave number. It can be shown to be connected to

the wave number in axial direction [29] by the relationship

$$k_{mn}^{*}{}^{2} + k_{mn}^{2} = \left(\frac{\omega}{c}\right)^{2} . \tag{3.7}$$

This interconnection is responsible for mode coupling in radial and axial directions and, subsequently, the cut-off condition (Sec.3.3.2).

The *circumferential* pressure field is generally affected by the mode index m defining the number of periods along the circumference. If this is considered in conjunction with the time fluctuation

$$p_{\theta}'(z_0, r_0, \theta, t) \propto A_3 e^{i(\omega t - m\theta)} + B_3 e^{i(\omega t + m\theta)} \tag{3.8}$$

and assuming for example $A_3 = 1$ and $B_3 = 0$ a particular circumferential pressure wave is propagating with $\omega t - m\theta = const$. Thus, in a given cross-section, the pressure distribution is in fact rotating with an angular velocity determined by the quotient of wave frequency and the mode index m. The rotation direction as well as additional modulation is defined by the parameters A_3 and B_3.

Superposed to the axial wave propagation this rotation is leading to so-called *spinning modes* as the general solution for axisymmetric ducts. Special cases without spinning occur only for standing waves in θ-direction ($A_3 = B_3$) and for the plane wave mode $(0,0)$.

Another outcome is that the pressure fluctuation in a particular point on the wall ($r = R$) can be derived as the sum of simple harmonic wave equations

$$p_{\text{wall}}'(z_0, R, \theta_0, t) = \sum_{m,n,\omega} K_{mn}(z_0, R, \theta_0) \cdot e^{i\omega t} \tag{3.9}$$

with mode-dependent constant factors

$$K_{mn}(z_0, R, \theta_0) = \left(A_1 e^{-ik_{mn}z_0} + B_1 e^{ik_{mn}z_0}\right) \cdot A_2 J_m(k_{mn}^{*} R) \cdot \left(A_3 e^{-im\theta_0} + B_3 e^{im\theta_0}\right) . \tag{3.10}$$

Summarizing, waves of given frequency $\omega = 2\pi f$ can propagate in form of different whole-numbered modes (m, n). The complete pressure field is not just a superposition of all existing frequencies but in fact of all modes waves of those frequencies can propagate in. Even though Eq. (3.10) is not explicitly dependent on the radial mode index n, the mode coupling (3.7) results in an implicit dependency: The cut-off condition is limiting the number of propagating modes for a frequency, and thus, determines the noise level of this frequency e.g. on the wall.

3.3.2 Cut-off Condition

Assuming a spinning mode with k_{mn}^* exists, and considering that the corresponding axial wave number k_{mn} has to be real-valued as well, Eq. (3.7) states a constraint. The following inequality condition has to be satisfied.

$$\omega > k_{mn}^* c = \frac{s_{mn}}{R} c \tag{3.11}$$

This can be interpreted such that the spinning modes need a minimum angular velocity ωR to keep up with the axial phase velocity to be able to propagate at all. The lowest solution $s_{mn} = k_{mn}^* R$ to Eq. (3.6) is obtained for mode $(1, 0)$. Here the cut-off frequency yields

$$f_{10} = \frac{1.84}{2\pi R} c \,. \tag{3.12}$$

Below this frequency no spinning mode can propagate at all such that the pressure fluctuations are uniform within the duct cross-sections. Only plane waves $(0, 0)$ with

$$p'(z, t) = \left(A_1 e^{-ikz} + B_1 e^{ikz} \right) \cdot e^{i\omega t} \tag{3.13}$$

can propagate and noise levels are reasonably decreased. Generally speaking, this is always the case when the tube diameter d is much smaller than the wavelength λ. With increasing frequency more and more modes are enabled increasing the noise levels successively.

3.3.3 Dispersion and Phase Velocity

For external problems acoustic signals are known to propagate with a constant velocity. The phase (and group) velocity is equal to the speed of sound.

$$c^{ph} = \frac{\omega}{k} = c \tag{3.14}$$

For internal problems this is only true for the plane wave mode $(0, 0)$ though [28]. Higher order duct modes, on the other hand, with their additional angular component generally obey a relationship between the wavenumber, frequency and the mode. This is given by Eq. (3.7) actually yielding a *dispersion relation*.

$$\omega = \omega(k_{mn}) = c \sqrt{k_{mn}^2 + k_{mn}^{*\,2}} \tag{3.15}$$

Subsequently the phase velocity in axial direction, or the velocity pressure fluctuations related to a mode (m, n) are propagating with, becomes frequency- and mode-dependent.

$$c_{mn}^{ph}(\omega) = \frac{\omega(k_{mn})}{k_{mn}} = c\frac{\sqrt{k_{mn}^2 + k_{mn}^{*~2}}}{k_{mn}} \tag{3.16}$$

For ducted modes the phase velocity in axial direction always is greater than the speed of sound. Geometrically this can be interpreted as the vector addition of two waves with velocity c which enclose an angle given by their mode. Accordingly, the observed wavelength is larger by the same ratio $\Lambda = \lambda\frac{\sqrt{k_{mn}^2 + k_{mn}^{*~2}}}{k_{mn}}$ in relation to the free-field wavelength λ.

Group Velocity

Dispersion has a lot of influence on the mode and frequency spectrum in a duct. On one hand a signal of frequency f can propagate in different modes, on the other hand a mode (m, n) can comprise different frequencies. The overall pressure field is a summation of all contributing combinations representable with Eq. (3.4).

Consequences are that a mode containing a number of frequencies, and thus waves of different velocities, actually propagates with the group velocity of the envelope formed by the summation of all the waves, similar to beat. For this velocity a respective relationship can be deduced again.

$$c_{mn}^{gr} = \frac{d\omega(k_{mn})}{dk_{mn}} = c\frac{k_{mn}}{\sqrt{k_{mn}^2 + k_{mn}^{*~2}}} \tag{3.17}$$

The interpretation is that higher order duct modes containing a band of frequencies propagate slower than with speed of sound. The same accounts for the more practical case of waves of constant frequency propagating in a number of modes.

3.3.4 Influence of Axial Flow

All the previously deduced relations apply in a frame of reference moving with the axial flow. In terms of this work this is the cross-flow with Mach number M_{cf}. Returning to a reference frame at rest the Doppler effect causes a frequency shift of the observed waves.

$$\omega = \omega_{moving}(1 \pm M_{cf}) \tag{3.18}$$

$$= \omega_{moving} + k_{mn}U_{cf} \tag{3.19}$$

Of course the observed ω depends on whether the cross-flow is in-bound or out-bound to the observation point, and M_{cf} has to be added or subtracted (3.18). This can resolved implicitly, and in consistency with all previous formulae, by allowing negative observed wavenumbers

k_{mn} for propagation against the cross-flow (3.19), though.

As the radial wave number k_{mn}^* remains unaltered, the two axial wavenumbers can be computed form Eqs. (3.15) and (3.19), leading to

$$k_{mn} = \pm\sqrt{\frac{(\omega - k_{mn}U_{cf})^2}{c^2} - k_{mn}^{*2}}\,. \tag{3.20}$$

After solving this equation for k_{mn} (see [28]), and considering the requirement for a real-valued k_{mn}, the new cut-off condition becomes

$$\omega > k_{mn}^* c\sqrt{1 - M_{cf}^2}\,. \tag{3.21}$$

Hence, the cut-off frequency is lowered by subsonic axial flow and generally larger overall noise levels have to be expected. Below the cut-off frequency modes still cannot transport acoustic energy.

As there is acoustic drift by the cross-flow however, the corresponding energy transport has to be compensated by respective upstream propagating waves. These are represented by modes k_{mn} that are not entirely imaginary below the cut-off condition as for cases without axial flow, but have a real part as well. The result is upstream wave propagation superposed to the usual damping.

3.3.5 Varying Cross-Section

When an acoustic wave comes across a (rapid) cross-section change $S_1 \rightarrow S_2$ only part of it will transmit on while the rest is reflected. Generally a *reflection factor* and a *transmission factor* can be defined. For plane waves these factors are independent on the frequency.

$$R = \frac{S_1 - S_2}{S_1 + S_2} \quad \text{and} \quad T = \frac{2S_2}{S_1 + S_2} \tag{3.22}$$

Now assume an incident wave $p' = A_1 e^{i(\omega t - kz)}$ propagating in positive z-direction. Due to energy and mass conservation the whole sound field can be written as a function of the incident plane wave of amplitude A_1. On the incident wave side it becomes

$$p'(z, t) = A_1 e^{i(\omega t - kz)} + RA_1 e^{i(\omega t + kz)} \tag{3.23}$$

and on the transmission side

$$p'(z, t) = TA_1 e^{i(\omega t - kz)}\,. \tag{3.24}$$

Thus, the reflected wave is shifted by 180° while on the transmitted wave is just reduced in amplitude. The cross-section transition actually behaves like the surface to another medium or introduced impedance. In passage between the cross-sections however, reflections might excite a very complex sound field of higher order modes, which then decay quickly tough.

For higher order modes and existing base flow the constants in the modal equations generally become non-constant. For example in sub-sonic base flow there are different velocities and corresponding wave numbers on either side of the cross-section transition, and R and T become additional dependent on M_{cf}, densities and the speed of sound. This limits the application of an analytical modal expansion to very few problems. Here, the *multimode propagation method* [8] and the *multiple-scales technique* [73, 87] provide semi-numerical generalizations of the modal approach allowing amplitudes and wavenumbers to be slowly varying functions, rather than constants.

3.3.6 Wall Boundary Condition

Up to now, and for all the simulations in this work, the walls are considered acoustically hard. The acoustic velocity normal to the wall is assumed to be zero ($U' = 0$) such that the acoustic impedance is infinite. The theoretical opposite are soft walls, saying that the acoustic pressure is zero ($p' = 0$) and the wall has zero acoustic impedance. Realistically, the wall impedance might be generally finite and different for every material. This especially counts for the intake manifold test equipment in this work.

In terms of internal acoustics any boundary condition results in similar mode solutions though [28]. Especially k_{mn} and k_{mn}^* remain the same, just the pressure field is phase-shifted. The only major difference is that plane wave modes cannot propagate in a soft walled duct and settle exponentially. Again, the above mentioned generalizations allow detailed computation.

Concerning the noise transmission through walls, a transfer function can be defined mapping internal wall pressure fluctuations to external ones [22]. This is strongly dependent on the wall material and the eigenmodes of the duct though.

3.3.7 Conclusions for Intake Manifold Simulations

Due to the presence and superposition of channel modes, no recognizable acoustic waves but seemingly erratic pressure fluctuations will be visible in any instantaneous image. Furthermore different propagation velocities of the modes might make the fluctuations (or their envelopes) move at different velocities and actually overtake each other. Furthermore the general superposition of hydrodynamics and acoustics in an confined environment alongside with the varying propagation velocities of the acoustic waves will make it hard to separate both by

correlation techniques. Last not least the varying cross-section and base flow will cause a very complex sound field and prohibit any simple modal solution.

However, cut-off frequencies can be predicted for the intake manifold. Above each of them an additional mode is enabled to propagate and increased noise levels have to be expected. Below the lowest cut-off condition only plane waves and hydrodynamic fluctuations propagate. The cross-flow will reduce noise levels upstream of the injector.

3.4 Noise Control Approaches

A great deal of experimental studies have been conducted to reduce the supersonic jet noise, mostly with future aircraft noise requirements in mind. The investigated noise reduction techniques can be divided into variation of inflow conditions, augmentations altering the shear layer shape and turbulence generation near the nozzle, and disrupting feedback loops and shock cells-turbulence interactions. Some of the most effective and promising approaches are described in the following.

Generally the focus should be on ways to reduce noise production rather than damping noise in the aftermath. However especially a ducted environment like the intake manifold allows later noise attenuation by design means. Key words are for example cut-off, resonators and structure-borne sound.

3.4.1 Inflow Conditions

Next to the obvious approaches of reducing the jet *Mach number*, operating the jet at fully expanded condition, lowering the *inlet turbulence level* or *heating* the jet [76, 109], *frequency excitation* is another feasible way of noise reduction. It is known that exciting a jet at its characteristic frequencies has influence on the jet shape, its spreading rate and noise emission. Subsequently, if various forcing frequencies are applied at the inflow boundary, it can even cause shock cell destruction [17]. Furthermore it can force particular jet oscillation modes and suppression of sound radiation [69].

3.4.2 Flow Shaping

The effectivity of *streamwise vorticity* modifying turbulence structures and enhancing entrainment is fairly well accepted. It reduces the peak noise level while increasing noise at higher frequencies. The mechanisms of vortex generation, vortex interaction and noise reduction are still largely unexplored though.

In case of supersonic jets, *avoiding/destroying shock cells* and *altering/disrupting feedback*

loops will lead to significant drop in shock and screech noise levels. This can be reached, for example, by blocking feedback paths using baffles or paddles [85], shaping the nozzle trailing edge in a way instead that it is not flat but 'fuzzy' (in order to broaden the screech tone peaks), or completely disrupting the shear layer.

Corrugated jets and modifications to the trailing edge such as tabs, chevrons and grooves are already employed in industry-scale applications like jet engines these days [49]. The aim is to introduce streamwise vortices, shorten the potential core and weaken the shear layer [93] in order to reduce noise production.

Cross-wire devices are very thin perpendicular wires placed into the jet close above the nozzle. They effectively destroy the shock cell structures generating broadband shock and screech noises. Consequently this is leading to considerable noise suppression [53], can however also produce additional instability waves.

Distributed Exhaust(DE) Nozzles describe the use of a number of smaller exhausts instead of a single round one. A special version, the "Sound Suppressor Exhaust Structure", was patented by Northrop Grumman already in 1998. It ensures that there is no continuous shear layer starting from the nozzle since it will not form until the jets unite further downstream. DE nozzles work by cutting the screech feedback loops off and weakening shock structures. Furthermore, compared to the round nozzle, much lower mean Mach numbers and turbulence intensities are seen downstream of the nozzle exit. Eventually the total result is a decrease of OASPL and shift of the peak to higher frequency in comparison to a round nozzle of equivalent area [36]. The injector in focus of this work is a DE nozzle having four exhausts.

Microjets describe a single main jet into which much smaller jets are injected from the sides. This was identified to be a very effective way of flow and noise control for a variety of applications such as free and impinging jets [2, 4, 61, 60, 59]. Microjets cause substantial streamwise vorticity while also introducing more three-dimensionality into the flow and limiting the number of the unstable modes. They also have been shown to effectively disrupt the screech feedback loop [4] and to reduce the potential core and shock cell length [51].

Suppressors are a widespread (and well-patented) mean to reduce exit velocities and discharge blasts of pneumatic systems. The working principle is varying depending on the application. If a strong jet is not required it can simply be a porous material covering the exhaust. In the other case shells of absorbent materials and noise confining volumes can be employed instead.

3.4.3 Duct Design

Reduction of ducted noise is generally leading to either raising the cut-off frequency or to methods increasing the acoustic impedance within the duct. In either case the noise decays faster and noise levels, especially at the duct exits, are measurably reduced. Here however also the acoustics within the geometry are of interest since it excites wall oscillations and transpose to external acoustics. In the following, some examples of general design means and techniques are described.

Tube with Concentric Walls   can be a solution in cases where the duct radius cannot be decreased, e.g. for mass-flow or usability reasons, but the cut-off frequency shall to be shifted higher. The introduction of internal concentric walls reduces the effective acoustic cross-section and turns additional modes into non-propagating ones while leaving the outer radius constant [72].

Mufflers   are making use of the impedance increase at cross-section steps. The phase-reversed reflected waves effectively cancel noise in incident wave direction, the transmitted wave is greatly reduced in amplitude as well. Mufflers can however act as resonators themselves. This is leading to noise transfer functions which need to be tuned to the problem.

Resonators in Lined Ducts   can be used to passively alter the impedance of the walls in order to increase the transmission loss along the duct. The wall is perforated and augmented with Helmholtz-Resonators such that it becomes acoustically soft for specific resonance frequencies. Then, plane wave modes in a narrow bandwidth around these specific frequencies cannot propagate and noise is damped. However, this approach does not work for higher order modes and numerous liners tuned to various frequencies would be necessary for broadband attenuation.

Active Noise Control   is the cancellation of noise by injecting acoustic energy with suitable power and frequency and reversed phase. This requires to measure the current local noise by microphones or pressure transducers, and to feed the computed reversed waves via a controller to loudspeakers or a piezoelectric panel. This is also known as anti-noise and varies in effectiveness. The controller has to be very fast and the wall properties have to be considered for its formation. It can be used for relatively broadband attenuation though.

3.5 Preceding Internal Injector Flow Simulations

Starting from a constant storage-side pressure and a supercritical pressure relation between inlet and outlet internal flow simulations (URANS, SST turbulence model, methane injection) were performed for the very same injector as governing this work. The objective was to assess the flow during the opening process based on the measured injector needle motion. The latter was modeled in terms of a moving mesh of constant topology and stretching elements. Consequently, the concession was that the simulations started with an already slightly open injector instead of a closed one.

Therefore, the simulations produce tiny jets above the orifices from the beginning. During the actual injector opening these jets are undergoing heavy fluctuations while the Mach number increases rapidly within fractions of a millisecond. After the flow becomes supersonic in the orifices, shock cells evolve in the shock damper and jets finally stabilize above each orifice.

Conclusions for This Work

The heavy jet fluctuations indicate that the injector opening process might be a strong noise contributor next to steady injection aeroacoustics. Since this is visible in URANS simulations already the opening process could be addressed separately using such an approach.

Transient flow variables, exported from the preceding internal injector flow simulations, can be re-employed for cutting free the actual injection by modeling a realistic inlet boundary condition in the injetor outlet (Sec. 5.1). Placed in the orifices, the new inlets would yield a realistic profile and even support the opening process, without the need to model the whole injector and its needle motion all over again. A steady-state inlet profile can be deduced as well as transient fluctuations at steady injection. The latter could prove beneficial for acousic simulations as these are known to depend on the inlet turbulence level (Tab. 3.1). The average flow characteristics during constant injection can be deduced with $1.8\,\mathrm{bar}$, $550\,\mathrm{m/s}$ and $219\,\mathrm{K}$.

3.6 Preceding Intake Manifold Mixing Simulations

For the same intake manifold geometry as in this work, but different inlet and working conditions, a number transient RANS simulations were performed with the aim to characterize the general mixing mechanisms and steady flow [37]. In fact, the problem setup (Fig. 3.6) is similar to the one in Chapter 7. However the mesh was quite coarse (1.3 million elements) and the inlet, placed in the orifices as well, was constant instead of profiled.

The most prominent outcome was that steady RANS approaches were generally not converging even when artificially increased viscosity was employed. The probable cause was traced
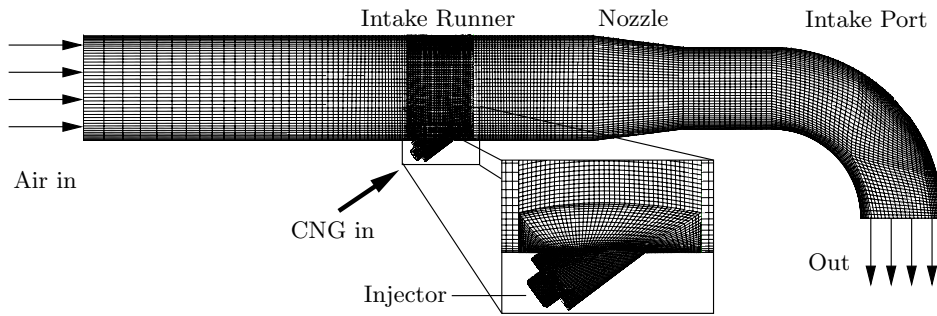
Figure 3.6: Preceding intake manifold simulation setup

back to large weakly damped transverse pressure waves and a flapping jet. In transient simulations the flow finally showed a supersonic jet containing shock cells, typical JICF trajectory, large vortex systems and, in dependency on the ambient conditions, an impinging jet.

(a) Velocity   (b) Averaged Pressure
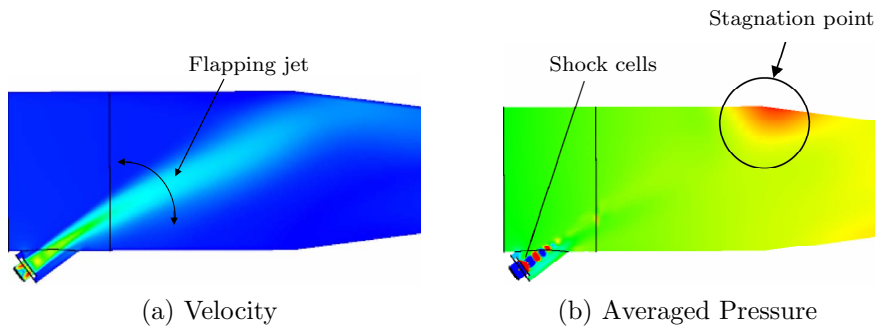
Figure 3.7: Preceding intake manifold simulation results [37]

Conclusions for This Work

The actual cause of the strong pressure waves is unclear and needs to be investigated by further simulations (Sec. 5.2). Theoretically the waves could be a result of acoustics (feedback loops, screech), flow (strong unsteady vortex separation forcing a flapping jet) or poor boundary conditions or initialization (reflecting sound waves, injector opening acoustics).

The already existing structured mesh is a good starting point for this work. However it needs to be refined in proximity of the jet in order to capture acoustics. Furthermore the domain has to be enlarged, now including the inlet valve and passage to the combustion chamber since these will take part in acoustics. Although the working conditions are different in this work, supersonic and impinging jets as well as a strong dependency of the global vortex systems, velocities and jet trajectories on the working conditions have to be expected.

Chapter 4

Measurements

4.1 Freestream Configuration

All the measurements documented here are performed for the freestream configuration and the actual injector governing this work. The gas (compressed air or nitrogen) is injected right into the atmosphere at 1 bar ambient pressure. Thus, these measurements can be employed to validate and support the freestream simulations in Chapter 6 and to draw conclusions about the gas flow and the noise introduced into the intake manifold. All the measurements were conducted by the author and in the facilities of the Robert Bosch GmbH.

4.1.1 Schlieren Optics

The objective of the Schlieren measurements is the visualization of steady and unsteady flow structures during pulsed as well as steady injection. The focus is especially on the jet evolution and the presence and shape of shock cell structures. Furthermore Schlieren images can give an impression of the unsteadiness in the jet and the source of acoustic waves. Two complementary measurements are performed: one employing a high-speed camera for capturing the unsteady processes, and another one using a high-resolution camera to highly resolve the time-averaged stationary flow structures (Tab. 4.1).

	High Speed	High Resolution
Configuration	freestream, nitrogen ejection	
Cycle	frequency 1 Hz, duty time 10 ms	
Measurement Equipment	LaVision HighSpeedStar Mono @ 512×512 pixels (capturing an area of 61 × 61 mm), 10000 fps and $5.07\mu s$ exposure	LaVision ImagerIntense @ 1376×1040 pixels (capturing an area of 41.7 × 31.5 mm), 9.9 fps and $200\mu s$ exposure
Post-Processing	image enhancement	averaged over 50 images, image enhancement

Table 4.1: Schlieren optics measurement setup

Measuring Principle and Setup

The Schlieren method allows to visualize spacial gradients in the refraction index n of a translucent medium. For this purpose the bright light emitted by an arc lamp is focused and an as monochromatic and uniform portion of the focal point as possible is selected by an aperture (Fig. 4.1). Then this light is parallelized by Lens 1 before it reaches injector and gas jet. There flow disturbances or another ejected medium cause density gradients and the light is refracted. Finally, all light is focused again by Lens 2 and directly projected on the CCD chip of a camera.
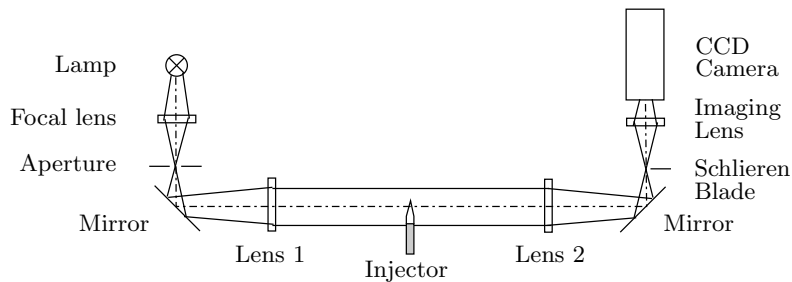
Figure 4.1: Schematics of Schlieren optics measurement setup

Up to here the measurement setup is actually the same as for shadowgraphs. The light refractions manifest in darker and brighter spots in the photograph, which correlate to the second derivative of the density, though. For Schlieren on the other hand an additional blade is applied in the second focal point to remove light that is bent towards the blade. Now the arising dark and bright spots are connected to the refraction angle or the first spacial derivative of the density perpendicular to the blade. However, the Schlieren method inherently is an integral method with too little information for a reconstruction or magnitude estimation. Thus, interpretation of Schlieren images is qualitative only.

The major issue, next to the very sensitive adjustment of the optical components, is chromatic aberration. The wavelength-dependent refraction index of the lenses results in different focal distances for every color. This smearing of the focal point is undesirable as it is making especially the blade placement and generation of an all-sharp Schlieren photograph very difficult. There are three ways to tackle this problem. Firstly one can use achromatic lenses, secondly one could use monochromatic light, and thirdly one could use an aperture to extract a specific focal point to at least weaken this effect. The last way is chosen here and found to be sufficient.

As the resulting photographs only make use of a small portion of the gray spectrum, subsequent image processing is applied in order to adjust the gamma value and extend the gradient information to the whole spectrum, and thus, enhance contrast. Furthermore the constant

background image is divided from the Schlieren photographs in order to compute away everything that is not a result of the injection.

Knowing the general space and timescales of the injection process, the cameras are triggered relative to the injector cycle and their timings are adjusted according to the task. To visualize dynamic processes a highspeed camera is employed with exposure times that allow to capture sound waves, and frame rates that allow to take about a dozen photographs during the opening process. For high-resolution images of the time-averaged stationary jet shape, on the other hand, a highly sensitive camera is used. It covers just a third of the area, but with more than 5 times the number of pixels. In order to filter out non-stationary fluctuations averaging over 50 images is employed additionally to a large exposure time.

Results

(a) $T_0 + 100\mu$s   (b) $T_0 + 200\mu$s   (c) $T_0 + 300\mu$s   (d) $T_0 + 400\mu$s

(e) $T_0 + 500\mu$s   (f) $T_0 + 600\mu$s   (g) $T_0 + 700\mu$s   (h) $T_0 + 800\mu$s
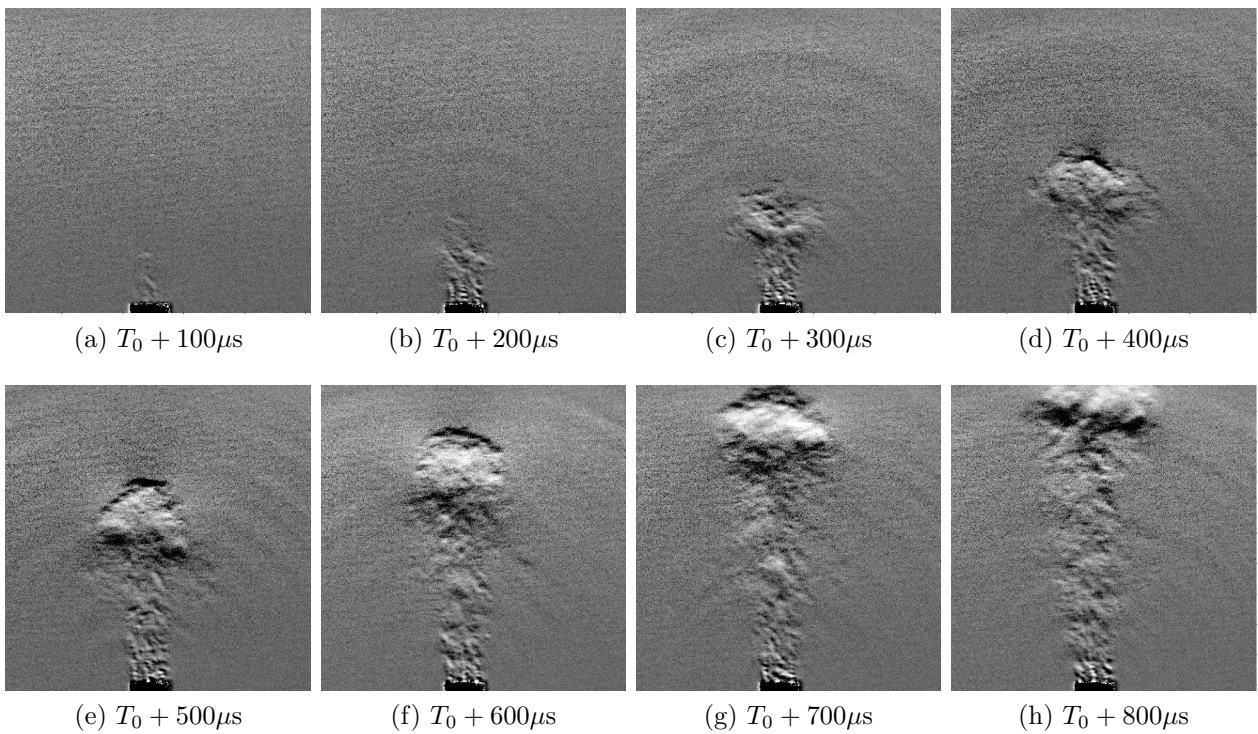
Figure 4.2: High-speed Schlieren photographs of injector opening (relative to random time T_0), vertical gradients

Injector opening Four major flow structures can be observed during injector opening. These are a mushroom cloud, separated entrainment vortices, fluctuations in the shear layer and arrays of density bubbles in the jet above the orifices. Furthermore spherical sound waves are visible emanating from the injector edge. Since sound waves generally propagate much

(a) $T_1 + 100\mu s$ (b) $T_1 + 200\mu s$ (c) $T_1 + 300\mu s$
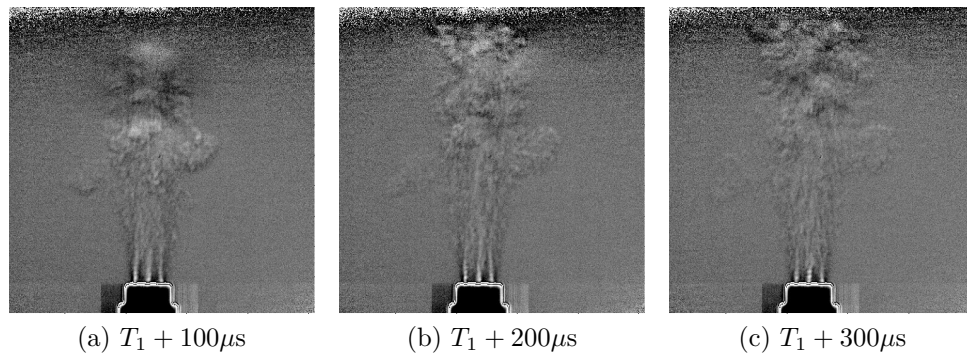
Figure 4.3: High-speed Schlieren photographs of separated entrainment vortices (relative to random time T_1), horizontal gradients

faster than flow structures they are passing and are eventually shielded and refracted by jet and large vortices (Fig. 4.2). Only the initial sound wave can propagate freely. The waves in Fig. 4.2 have a funnel-like look because vertical gradients are shown only. Indeed sound waves do really become weaker with increasing angle to the jet axis but they do not vanish.

The whole jet evolution is taking roughly $1\,\mathrm{ms}$. During this time, the jets starting above each orifice unite and displace the ambient air. This is a highly unsteady process causing the generation of entrainment vortices and strong sound emission (Fig. 4.2(a)–(c)). Shear layer fluctuations are still weak and equally spaced density bubbles, seemingly little shock cells, are visible above the orifices.

As the entrainment vortices are excited and pushed forward by the incident jet they become stronger and eventually form a single moving mushroom cloud of constantly changing shape (Fig. 4.2(d)–(f)). The migration velocity of this cloud is up to $100\,\mathrm{m/s}$ but quickly slowing down with increasing distance to the injector. Shear layer fluctuations become stronger as well, increasingly masking the image of the inner jet, blurring and distorting it. Sound production seems to become generally lower but to decrease and increase periodically. This could be an indication of superposing sound waves and beat, or a pulsating sound source due to jet instabilities. All the visualized sound waves are emanating from the injector edge though. Noise generated by downstream portions of the gas jet seems to be of subordinate magnitude.

In fact, the whole injector opening process is highly asymmetric. It is even possible that vortices separate from the mushroom cloud and migrate slowly away from the jet (Fig. 4.3). Of course these vortices will be less excited and affected by the passing jet and have a lower migration velocity and a higher dissipate rate therefore. Nevertheless they can persist over long times in vicinity of the jet and influence the flow, noise generation and mixing.

Stationary Injection   The stronger the jet gets the stronger and larger the shear layer fluctuations become (Fig. 4.2(f)–(h)). Often an alternating fluctuation mode, probably vortex

shedding, emerges. Downstream, where the jet collapses, large scale turbulence structures are generated.

Due to the integrative nature of the Schlieren measurements shear layer turbulences act like moving lenses and might mask the image of the inner jet. Thus, in order to get a clear and highly resolved picture of the inner jet the Schlieren blade can be readjusted such that weaker density gradients and acoustic waves vanish (Fig. 4.4). The longer exposure times also improve comparability with RANS simulation results. This will be referred to in Sec. 6.3 again.

(a) Schlieren measurements   (b) Simulation
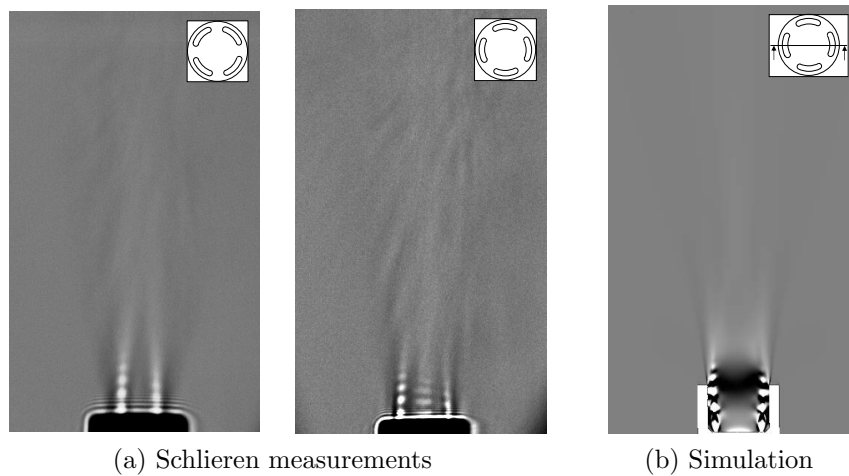
Figure 4.4: Averaged Schlieren photographs of stationary injection with comparison to RANS simulation (Sec. 6.3), horizontal gradients

The averaged gas flow features a number of tiny bar-like shock cells lined up above each orifice (Fig. 4.4). The jets unite not until outside the shock damper. Furthermore the jet is heavily fluctuating and asymmetric in the photographs. Seemingly a turbulent flow within the shock damper is exciting the jets.

Preceding simulations for the intake manifold injection showed a flapping jet (Sec. 3.6). Here, measurements show that the jet is indeed moving in itself. Sometimes its width is narrowing and widening, sometimes it is slightly moving to either side, and sometimes the shock cell spacing is changing, partially by more than a millimeter. However there is no sign of any flapping motion. It can be supposed that the observed jet instabilities are driven by large-scale turbulences and maybe screech within the shock damper.

Injector Closing   After cutting off the power supply to the injector the jet and its density gradients become weaker within a fraction of a millisecond. For a short moment sound waves become stronger before they eventually fade out. Remaining fumes and large scale turbulences slowly dissipate while moving out of the picture.

4.1.2 Laser Vibrometry

	Scanning laser head	Scanning traverse
Configuration	freestream, dry air ejection	
Cycle	Frequency 10 Hz, duty time 10 ms/180 ms (FFT mode)	
Measurement Equipment	Polytec scanning vibrometer PSV200 (Laser head OFV 055, Digital card OFV 3001 S) @ metering range 25 mm/s/V	Polytec vibrometer CLV-1000 (Laser head CLV-700), ISEL 3-axes traverse, dedicated LabVIEW program and raster generator @ metering range 25 mm/s/V
Time mode	16 ms @ Δt=1.953 μs	16 ms @ Δt=1.953 μs
FFT mode	0..200 kHz @ Δf=125 Hz	0..20 kHz @ Δf=6.25 Hz
Post-Processing	averaged over 50 cycles, 30 Hz high-pass filtered	averaged over 20 cycles, 30 Hz high-pass filtered

Table 4.2: Laser interferometry measurement setup

Complementary to Schlieren photography laser vibrometry allows the visualization of hydrodynamic and acoustic pressure fluctuations in great detail, and in time and frequency domains. Stationary structures such as shock cells and the jet shape cannot be captured though. Accordingly, the objective of these measurements is the investigation of the dynamic injector opening and closing processes, and the analysis of the (shear layer) fluctuations during steady injection as a possible source of noise. Again, two different setups are utilized. Scanning from a distant point allows to capture wide images, while a scanning traverse is employed for high-resolution near-field images (Tab. 4.2).

Measuring Principle and Setup
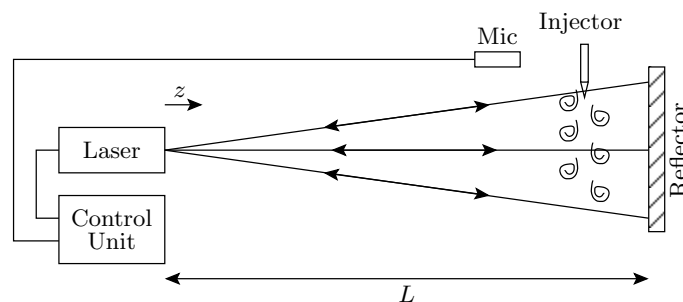
Figure 4.5: Laser interferometry schematics (scanning head)

Similar to Schlieren measurements before, laser interferometry is based on the refraction index alteration of a gas caused by density perturbations. But instead of visualizing deflection angles, the optical path length variation is measured now. Employing a laser this is done by exploiting the frequency shift Δf between emanated and reflected beam due to the Doppler
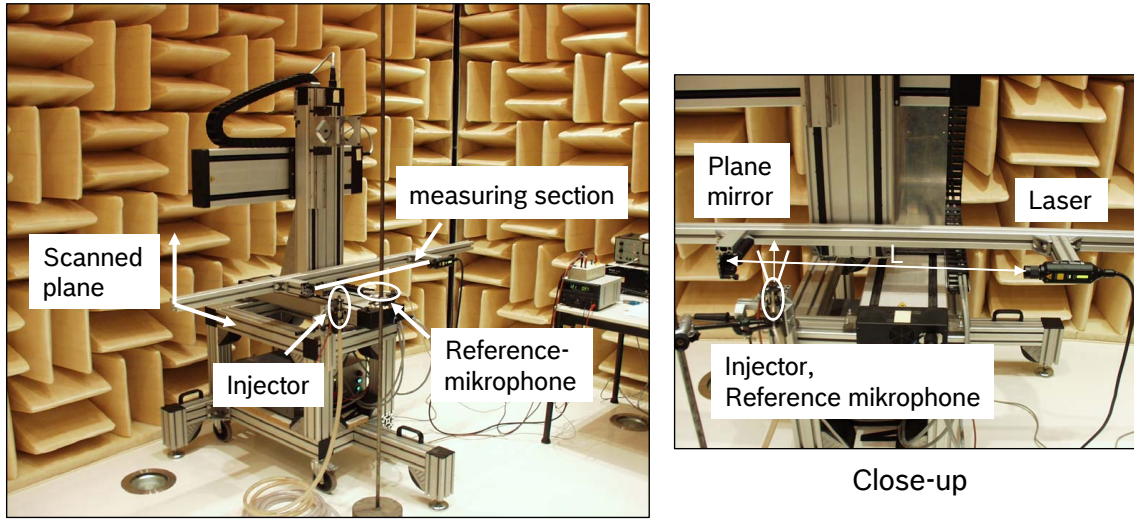
Figure 4.6: Laser interferometry setup (scanning traverse)

effect (4.1). Eventually, this shift can be transformed into an effective fluctuation velocity v_{eff}[1] which is directly related to integral fluctuations in the refraction index field $n(z,t)$ along the beam.

$$v_{eff}(t) = \frac{\lambda \Delta f(t)}{2} = 2\frac{d}{dt}\int_L n(\rho(z,t))\, dz = 2\frac{dn}{d\rho}\int_L \frac{d\rho(z,t)}{dt}\, dz \qquad (4.1)$$

The subsequent integration of this velocity over time gives a length $L_{eff}(T)$ which is a qualitative measure for the density (or pressure) level, integrated along the laser beam and relative to the ambient pressure.

$$L_{eff}(T) = \int_T v_{eff}(t)\, dt = f(\rho(T)) \qquad (4.2)$$

As laser interferometry only evaluates a single laser beam at a time the measurement area has to be rasterized and physically scanned in order to assemble an image. Therefore, only fluctuations that are reproducible in relation to a global trigger (e.g. the injector opening) become visible in a combined image. Random sound waves on the other hand just appear as local static noise, allow a subsequent frequency analysis though.

Utilization of a standard scanning vibrometer is the fastest way to perform the measurements and combine them to an image, but also exhibits some shortcomings. Most importantly, the tilted laser beam and the scattering reflector cause the reflected beam to be well wider than the incident one. Consequently, the region actually covered by the measurement becomes quite large and prevents high-resolution images. These are necessary here, though, since the whole jet to be resolved is just a few millimeters wide.

This is leading to a traverse setup. Here laser and plane mirror are always in direct opposition to each other featuring a well-defined laser beam in either direction.The drawback is

---

[1]In common vibrometry this is the vibration velocity of the reflector. Here it has no physical relevance.

(a) Scanner (PSV)   (b) Traverse (CLV)
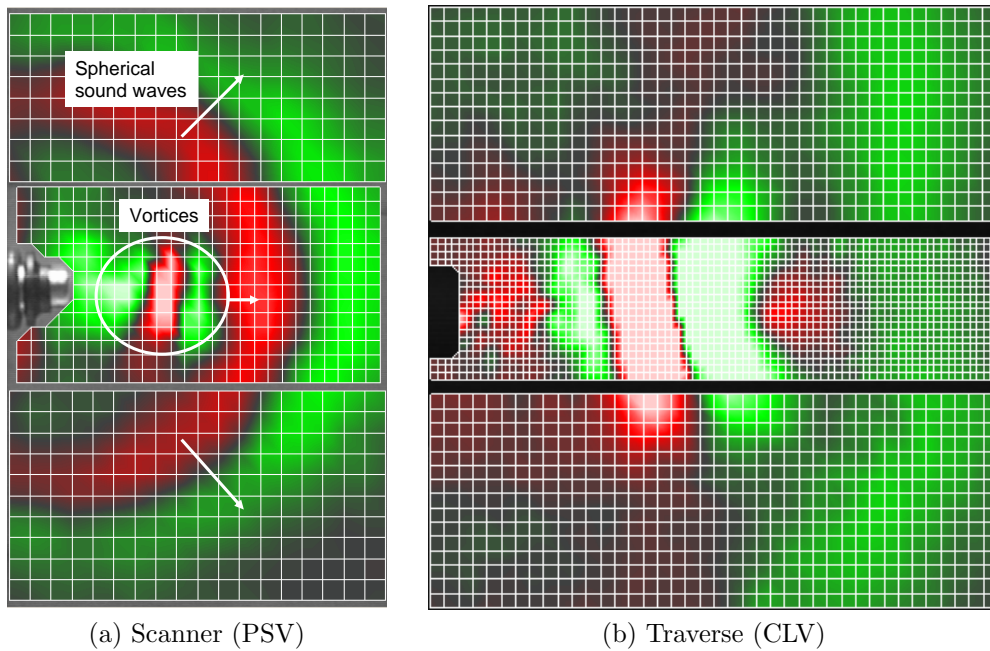
Figure 4.7: Injector opening, instantaneous PSV and CLV images; $L_{eff} \pm 10$nm

however that the setup is not as massive and decoupled as a distant scanning vibrometer. Traverse and especially the mirror can catch vibrations and thus contaminate the measurements. Thus, some dead time has to be planned between traverse movement and measurement to settle oscillations. Furthermore automatization is quite complex using a combination of various hardwares and softwares for raster generation, traverse control, injection timing, data logging and post-processing. Eventually this required some Visual Basic scripting, a dedicated LabVIEW environment[2] coordinating everything and a day-long measurement time.

Time Domain Results

During injector opening two major structures emerge: spherical sound waves emanating from within the shock damper and hydrodynamic vortical structures moving along the injection direction at about one third of the speed of sound (Fig. 4.7a). Hydrodynamic fluctuations seem to be up to eight times larger than the strongest opening sound waves. The dominating frequency of the opening acoustics is about 18 kHz. However also weaker sound waves are visible that seem to be related to the injector dynamics, first of all the needle impact.

During steady injection shear layer fluctuations and stochastic background noise are visible (Fig. 4.8a). The latter is mainly caused by random acoustic waves and can be leveled by averaging to some extent. The better reproducible vortical fluctuations remain.

During injector closing the supposably low pressure in the shock damper, in conjunction

---

[2]with programming support by a coworker

(a) stationary injection

(b) closing + 0.53ms

(c) closing + 0.63ms

(d) closing + 0.71ms
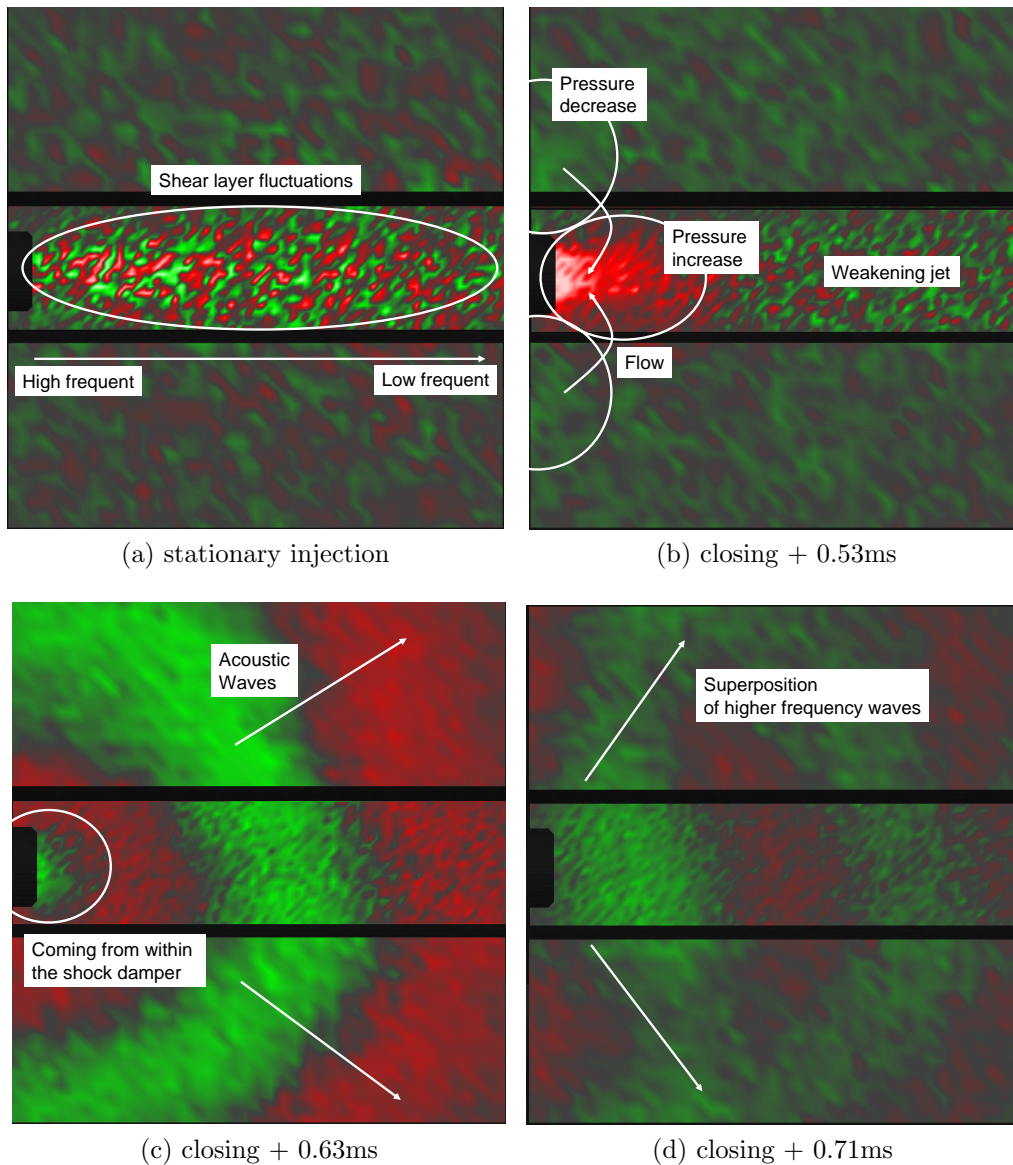
Figure 4.8: Steady injection and injector closing, instantaneous CLV images; $L_{eff} \pm 10nm$

with the inertia of the already ejected fluid, causes ambient air to be drawn into the former jet region (Fig. 4.8b). There the pressure rises while it falls in the proximity. This kind of implosion causes an explosion in return, visible in form of spherical sound waves emanating from within the shock damper (Fig. 4.8c). These are of similar magnitude as the opening blast, yield a lower frequency of about 13 kHz and appear to be longer lasting. Thus, for pulsed injection this might be a reasonable noise contributor as well. Later, other waves modulate the pressure field causing an interference pattern (Fig. 4.8d). Possibly this is caused by injector vibrations rather than aeroacoustics.

(a) Spectrum in point marked (b)

(b) RMS of 0-20kHz band

(c) RMS of 15-20kHz band

(d) RMS of 0-5kHz band
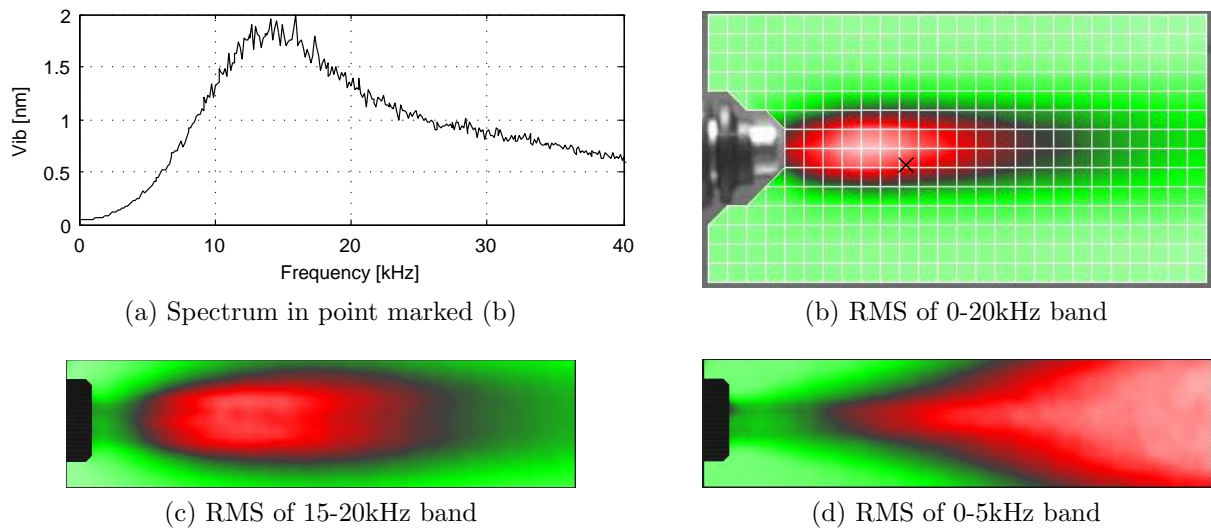
Figure 4.9: Steady injection in frequency domain, PSV and CLV images; $L_{eff} = 0..2.5$nm

Frequency Domain Results

The averaged spectrum of turbulent fluctuations in the jet is quite smooth with a maximum usually being between 10 and 20 kHz (Fig. 4.9a). Highest overall RMS values, and thus globally strongest fluctuations, are reached about 1 cm downstream of the injector (Fig. 4.9b), where the jet is probably breaking down.

Fluctuation levels close to the injector are governed by high-frequency content (Fig. 4.9d), while there is a shift to, and general amplification of, lower frequencies farther downstream (Fig. 4.9c). Turbulence levels in close proximity are always very low. This correlates with the theory of generally growing turbulences in a mixing shear layer (Sec. 3.2.3). Turbulences from within the shock damper do not seem to play a role.

Correlation between fluctuations within the jet and the emitted noise captured by a reference microphone yields that most of the hydrodynamic fluctuations indeed emit sound. Maximum noise levels during steady injection are reached between 15 and 20 kHz, depending on the microphone position.

4.1.3 Acoustics

Microphone measurements are aimed to determine the actual levels, spectra and directivity of the emitted noise during injector operation. The influence of transient effects like vortex formation and injector clicker noise is investigated in time domain, while steady injection noise and noise generation mechanisms (Sec. 3.2) are analyzed in frequency domain (Tab. 4.3). Most measurements are conducted in the acoustic far-field, some are taken in the near-field for better comparison with simulations, though.

	Time Domain	Frequency Domain
Configuration	freestream, dry air ejection	
Cycle	1 Hz, duty time 50 ms	constant injection
Measurement Equipment	$9 \times 1/4$" pre-amplified ICP microphones at R=60 cm, 20-channel LDS-Dactron dynamic signal analyzer, $1 \times 1/4$" condenser microphone with Brüel&Kjær amplifier	
Post-Processing		spectrum averaged over 30 samples, Hanning window

Table 4.3: Acoustics measurement setup

Measuring Principle and Setup

In an anechoic chamber nine 1/4" ICP microphones are placed at same distance in the same plane but at different angles to the injector (Fig. 4.10). An additional partially foam-coated condenser microphone is employed to measure broader spectra and suppress hydrodynamic fluctuations for measurements close to the jet axis and in jet direction. The injector is rotated in every direction to comprehend the picture of the noise directivity.

In order to assess the contribution of the structural injector clicker noise additional measurements are conducted for an unpressurized injector and in combination with laser vibrometry measurements focused at injector body vibrations.
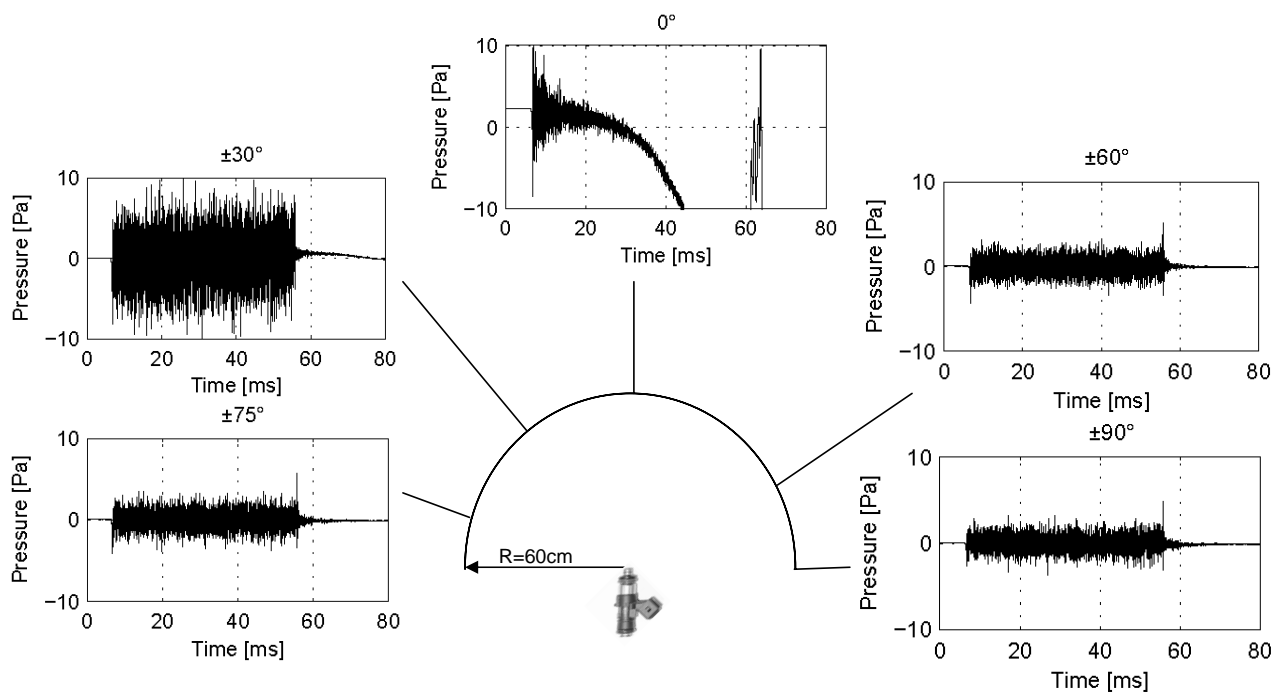
Figure 4.10: Injector acoustics, time domain

Time Domain Results

In lateral directions (90°) the opening and closing bursts dominate the steady injection noise by up to 8 dB (Fig. 4.10). Here, the closing blasts are often stronger and longer lasting than the opening ones. Starting from there the steady injection noise rises with decreasing angle to the jet axis till maximum radiation direction is reached at about 30°. Opening and closing bursts are not separable from the steady the noise anymore. Since the injector orientation around the vertical axis has no greater influence on the measurement a widely rotational-symmetric emission pattern can be assumed.

In injection direction (0°) the influence of large-scale vortical structures is dominating. After the opening blast, vortical structures formed by the ejected fluid increasingly shield the acoustic radiation. Once they reach the microphone they cause low-frequent hydrodynamic fluctuations of up to 300 Pa amplitude (in 60 cm distance) displacing the reference pressure for acoustics.
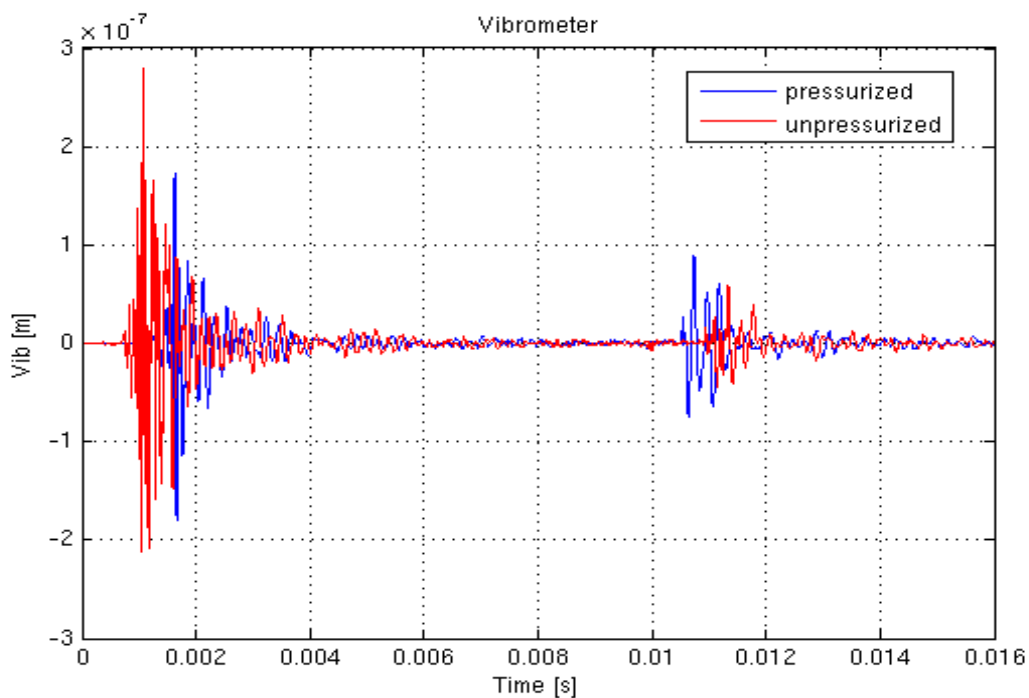
Figure 4.11: Laser vibrometry for shock damper, 10ms duty time

Concerning contributions by structural injector clicker noise laser vibrometry measurements are conducted with the focus on structural vibrations during pressurized and unpressurized pulsed injector operation (Fig. 4.11). For the unpressurized injector the fluctuation amplitudes are somewhat larger during opening and somewhat lower during closing. Furthermore there is a time shift due to an altered injector dynamics for this pressure-unbalanced injector. Nevertheless the structural fluctuations and thus the emitted noise levels are of similar
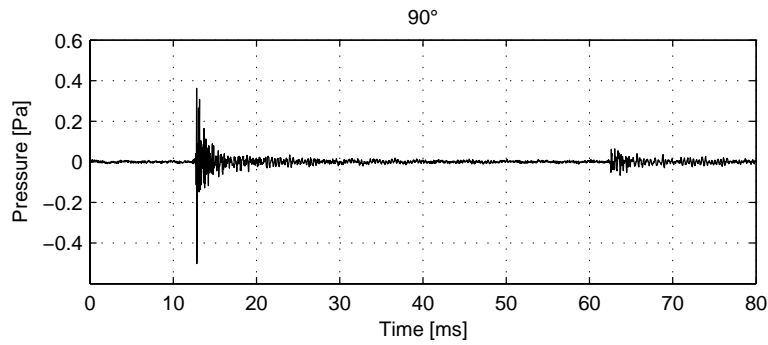
Figure 4.12: Injector clicker noise in time domain

level. Consequently, taking actual microphone measurements for the unpressurized injector into account (Fig. 4.12) the clicker noise is more than two orders of magnitude lower than the jet formation acoustics (Fig. 4.10) and can be neglected indeed. It does radiate directly into the audible far-field however while the jet will be confined within the intake manifold in the practical application.

Frequency Domain Results
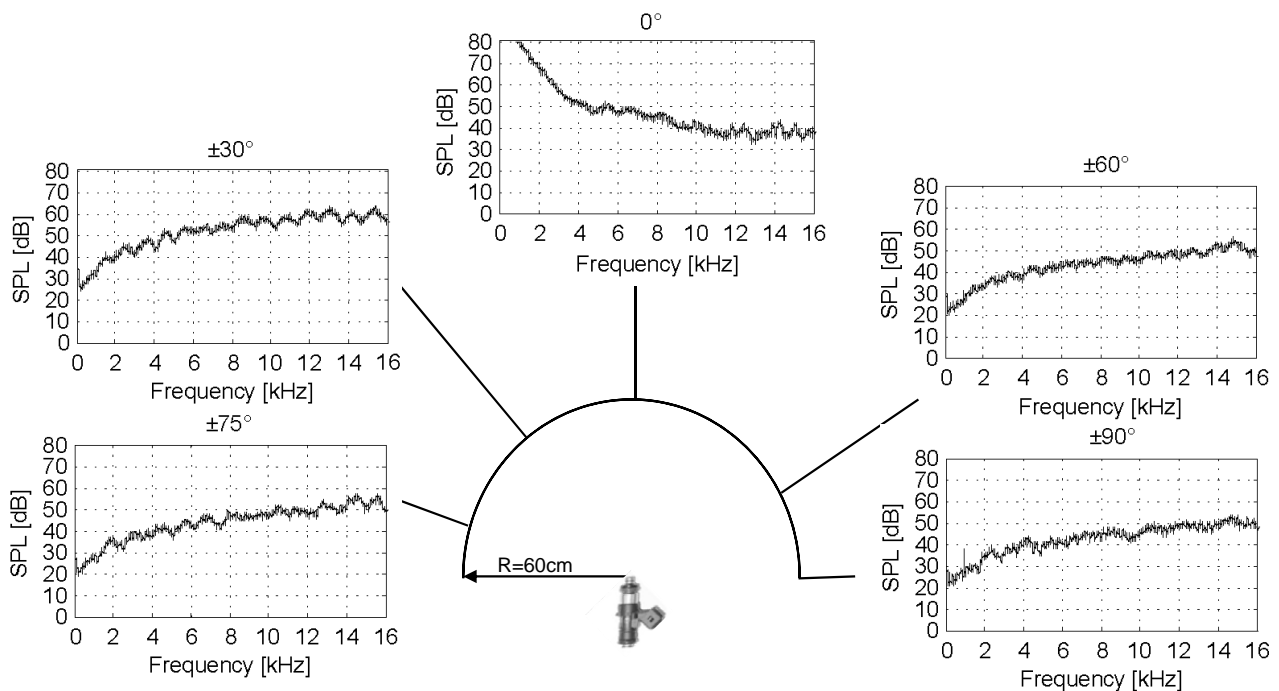
Figure 4.13: Injector acoustics, spectra

The noise spectra during steady injection are generally broadband (Fig. 4.13). In particular, no screech tones are present within as well as above audible range. In jet direction

hydrodynamic fluctuations cause highly increased pressure levels below 5 kHz. This is just pseudo-sound, but could turn into actual noise or excite structural oscillations when impinging on walls such as the intake manifold. Higher frequencies are lowered in magnitude due to shielding effects on the other hand.
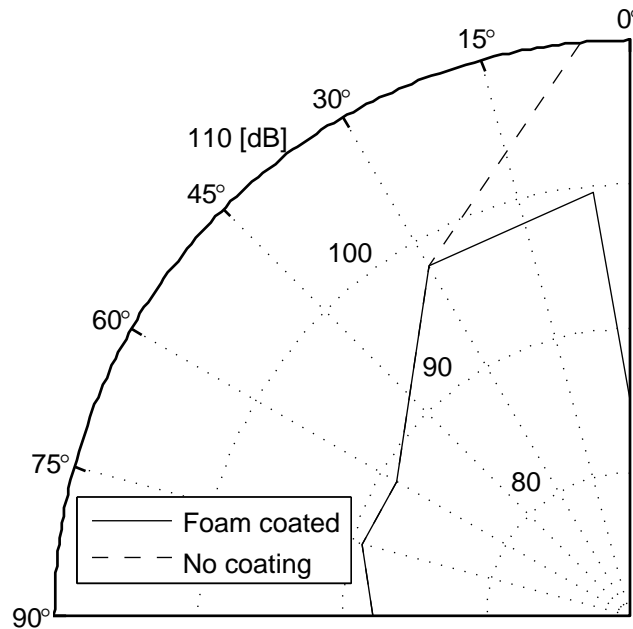
Figure 4.14: Injector acoustics, OASPL directivity

Integration of the acoustic spectra yields the characteristic directivity of the jet (Fig. 4.14). A foam coated microphone is employed to attenuate hydrodynamic contributions close to the jet. The resulting directivity is approximately axisymmetric with a clear influence of hydrodynamic fluctuations. The acoustic directivity is downstream-pronounced with an OASPL varying between about 87 and 100 dB in R=60 cm. For angles larger than 90° there is no distinct directivity anymore and the radiation becomes similar to a monopole. Turning to pulsed injection increases noise levels below 3 kHz and the overall sound pressure levels in consequence.

The combination of the quite smooth broadband spectra and a main radiation direction of around 30° to the jet axis implies turbulent mixing as the dominant source of noise rather than shock noise or screech.

4.2 Intake Manifold Configuration

This section finally presents measurements performed for the actual intake manifold config-
uration. The gas is injected into a simplified yet quite realistic intake manifold at various
working conditions (Tab. 4.4) and injection angles (37° and 90° to the manifold axis). Thus,
these measurements are aimed to support simulation results obtained in Chapter 7 and to
gain additional information about the emerging vortical structures, noise levels and spectra
as well as sensitivities. With exception of thermal imaging the measurements were conducted
by the author within Robert Bosch GmbH facilities.

WC	Cross-flow velocity	Pressure	Description
1	$3\,\mathrm{m/s}$	$38{,}0\,\mathrm{kPa}$	2000rpm, idle
2	$4\,\mathrm{m/s}$	$98{,}0\,\mathrm{kPa}$	2000rpm, full throttle
3	$10\,\mathrm{m/s}$	$26{,}5\,\mathrm{kPa}$	6000rpm, idle
4	$12\,\mathrm{m/s}$	$84{,}0\,\mathrm{kPa}$	6000rpm, full throttle

Table 4.4: Intake manifold working conditions used for parameter variation, corners of the
working envelope characteristic for a four cylinder 1700cc bivalent engine

4.2.1 Test Rig

To enable various measurements and validation for the upcoming aeroacoustic simulations a
modular and optically accessible test rig is assembled[3] and commissioned. It comprises the
intake manifold with rail and gas injector as well as an inlet valve and a stylized combustion
chamber (Fig. 4.15). The flow conditions within the intake manifold (cross-flow and pressure)
are controlled by the means of a BOSCH 0 280 750 076 throttle at the air intake in conjunction
with the power setting of the two water-cooled Becker VARIAIR SVw 380/4-900 side channel
blowers (2x7.5 kW) at the outlet. The flow conditions are measured by a BOSCH HFM3
massflow and temperature sensor and a BOSCH 0 261 230 030 absolute pressure transducer.
Due to the noise generated by the blowers and the throttle and in order to delay contamination
by reflections at the tube endings the blower cart is connected via long flexible tubes and placed
outside the anechoic chamber while the measurements take place inside.

For sensitivity measurements the injector can be continuously rotated in two planes such that
arbitrary injection angles can be adjusted (Fig. 4.17). Besides the internal flow is optically
accessible owed to the utilization of diverse plexiglass parts. Furthermore probes can fed
through drill holes in numerous locations in order to capture (wall) pressure fluctuations
and internal acoustics. A dedicated LabVIEW environment is developed with programming

---

[3]The test rig was designed and some parts were already manufactured and delivered when starting this work.

(a) Measurement cart

(b) Blower cart
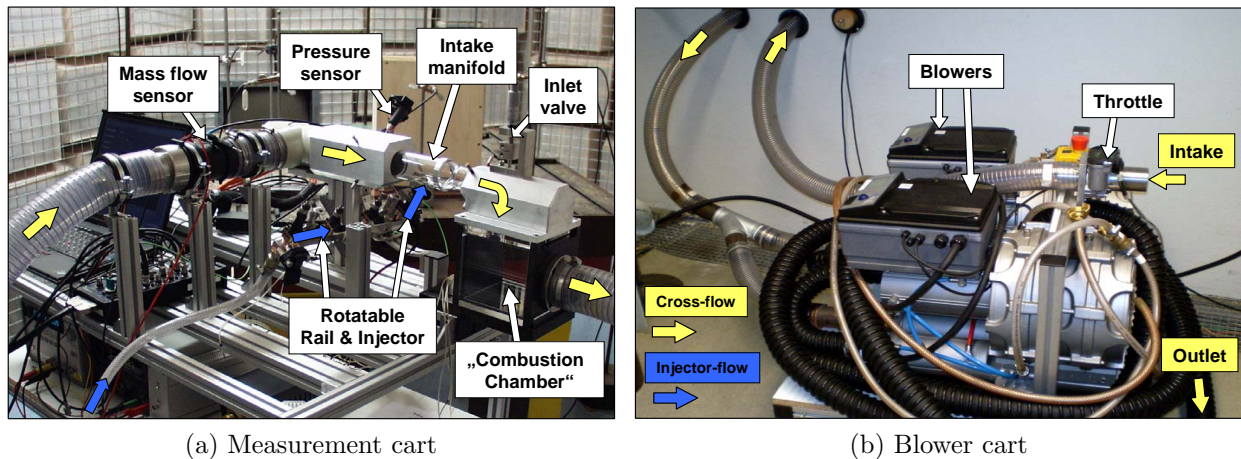
Figure 4.15: Intake manifold test rig

support by a coworker controlling the test rig function as well as performing measurements and partially also post-processing.

4.2.2 Thermal Absorption Imaging

Configuration	intake manifold, carbon dioxide injection, various injection angles and working conditions
Cycle	1 Hz, duty time 20 ms
Measurement Equipment	heated plane radiator (160℃), Thermo Sensorik IR camera CMT 384 M @ 130Hz frame rate
Post-Processing	background subtraction, image enhancement

Table 4.5: Thermal absorption imaging setup

Thermal absorption by injected carbon dioxide can be employed as a qualitative measure and visualization for the large scale vortices and fuel mixture homogenization in the intake manifold. The fundamental idea is to place a heat radiator on one side of the glass intake manifold and a thermal imaging camera on the other side. Then the injected carbon dioxide will absorb a portion of the heat radiation and become visible in infrared images. The extent of the absorption, or the brightness of a pixel in the image, is dependent on the integral carbon dioxide concentration along the axis between radiator and camera.

Unfortunately quantitative comparability between measurements is not definite as well since the confining plexiglass also absorbs some of the heat radiation in dependency on its own temperature. Even though the plexiglass temperature is tried to held constant the amount of heat radiation reaching the carbon dioxide plumes as well as the stationary background in
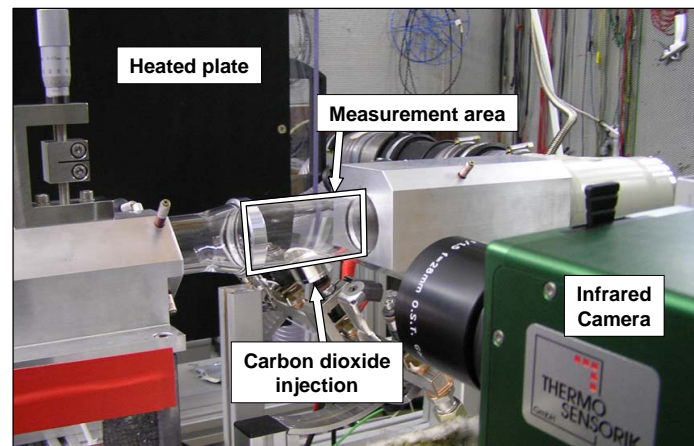
Figure 4.16: Thermal absorption imaging setup

the IR images might vary. Thus, after background subtraction and image enhancement the pixel brightness does not necessarily relate to the actual carbon dioxide concentration anymore. Furthermore, the camera does not allow triggered measurements such that different time offsets in relation to the injector operation have to be considered. Nevertheless the measurements give a good impression about the transient mixing mechanisms within the intake manifold and thus enable the validation of respective simulation results.

Results

In dependency on the adjusted pressure and cross-flow velocity as well as the injection direction very different types of mixing vortical structures establish indeed. The mixture homogenization is characteristically varying over time and space during an injection cycle allowing separation and to draw conclusions about the present flow and large scale vortices. This is further detailed in Chapter 7.

4.2.3 Wall Pressure Fluctuations

Wall pressure fluctuations are measured in order to qualitatively and quantitatively validate the aeroacoustic simulation results in Chapter 7. Furthermore the sensitivities of noise levels and spectra as well as opening and closing acoustics and the pressure drop across the jet are assessed by measurements for several working conditions and injection angles. The measurements take place in time domain. Spectra are derived and analyzed for constant as well as pulsed injection employing postprocessing in Matlab.

Configuration	intake manifold, dry air injection, various injection angles and working conditions
Cycle	2 Hz, duty time 10 ms to continuous injection
Measurement Equipment	2 x Kulite XCQ-062 miniature differential pressure transducers, 1 x Bosch 0 261 230 030 absolute pressure transducer, National Instruments BNC-2110 shielded connector block, National Instruments PCI-6281 DAQ @ 100kHz sample rate, dedicated LabVIEW environment for measurements and control
Post-Processing	20 kHz low pass filtering, partially averaging over 10 samples, Hanning window, FFT (Matlab)

Table 4.6: Wall pressure fluctuations measurement setup

Measurement Principle and Setup

Two miniature pressure transducers are placed upstream and downstream of the injector with respect to the cross-flow, in the very same locations the transient simulation data is logged in as well. The probes are fed through drill holes and aligned flatly to the internal intake manifold wall. Employment of differential rather than absolute pressure transducers allows a much better resolution of weak pressure fluctuations but might require to supply an additional reference pressure to the probes.
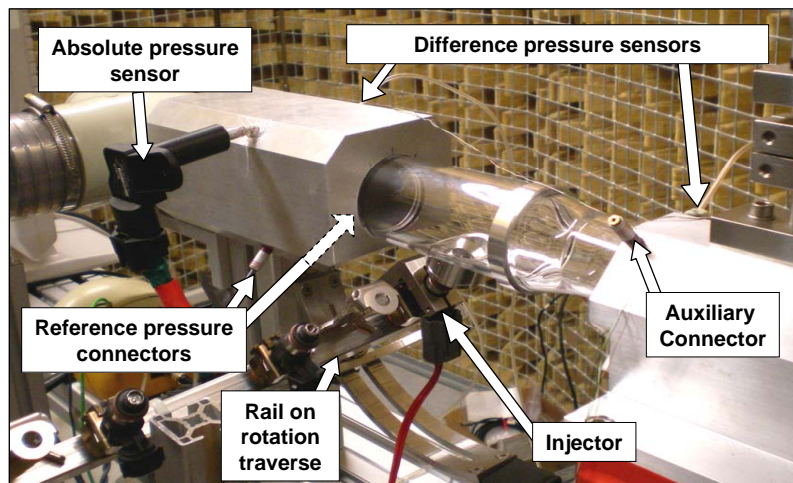
Figure 4.17: Wall pressure fluctuations measurement setup

For the working conditions 2 and 4 (Tab. 4.4) the metering range of the relative pressure transducers of ± 13.8 kPa is sufficient to cover all fluctuations just with the atmospheric pressure as the reference. The emerging offset can be corrected with the absolute pressure adjusted and measured within the intake manifold. For the other two working conditions the metering range is surely exceeded, though. Thus, the probe's reference side is connected to an upstream

location of the intake manifold (Fig. 4.17). Owed to the length of the employed tubes these act as a low-pass filter such that just the average pressure within the intake manifold is provided as the reference. In fact this reference is very similar to what the absolute pressure transducer measures within a dead volume attached to same intake manifold cross-section. Thus the measurements could be corrected with the absolute pressure measurement as well. However, especially for the low-pressure working conditions the reference pressure fluctuations are not just comparably low-frequent but also more than an order of magnitude weaker than the acoustic fluctuations such that corrections would have just a minor effect.

Considering the noise introduced by the test rig itself, a high cross-flow velocity (e.g. WC3) increases the background noise. In air intake direction the signal-to-noise ratio (SNR) with respect to the pressure levels can indeed drop below 3 dB in the ranges around 3 kHz and 9 kHz. Mostly however, and especially in intake valve direction, the SNR is more than 10 dB though. Notable noise contribution by the blowers is not observed.

Eventually, the measurements are averaged in time respectively frequency space for 10 samples in post-processing. The same Matlab script as in Chapter 7 is employed for deduction of acoustic spectra by the Welch's method.

Agreement with Numerical Simulations

While the measurement region of the test rig is widely equivalent to the computational domain in Chapter 7, especially the intake manifold endings might be different due to technical and measurement requirements. Additional or altered reflections and feedback paths and thus different internal acoustics are thinkable. The commutator, the optically accessible bend and the throttle in air intake direction might be of particular influence. The inlet valve position could have some impact as well.

Therefore, half an injection cycle is investigated for modified test rig setups: opened and closed inlet valve, removed commutator and removed commutator as well as bend. Since the response to the well reproducible plane wave caused by the injector opening is most telling the measurements are time-averaged to get rid of other random acoustics. The comparison takes place in the measurement points on either side of the injector and for 37° injection angle within the first 4 ms. Respective non-averaged simulation data is pulled up as an additional reference.

Indeed the response alters noticeably for varying problem setups (Fig. 4.18). Different duct endings reflect more or less phase-shifted waves of varying amplitudes. An open duct end results in cancellation of the incident pressure increase while it rather further increases the pressure for a closed end. Among the simulations the URANS air inlet acts as a closed end while SAS suppresses any reflection by a sponge layer (Sec. 5.2.2).
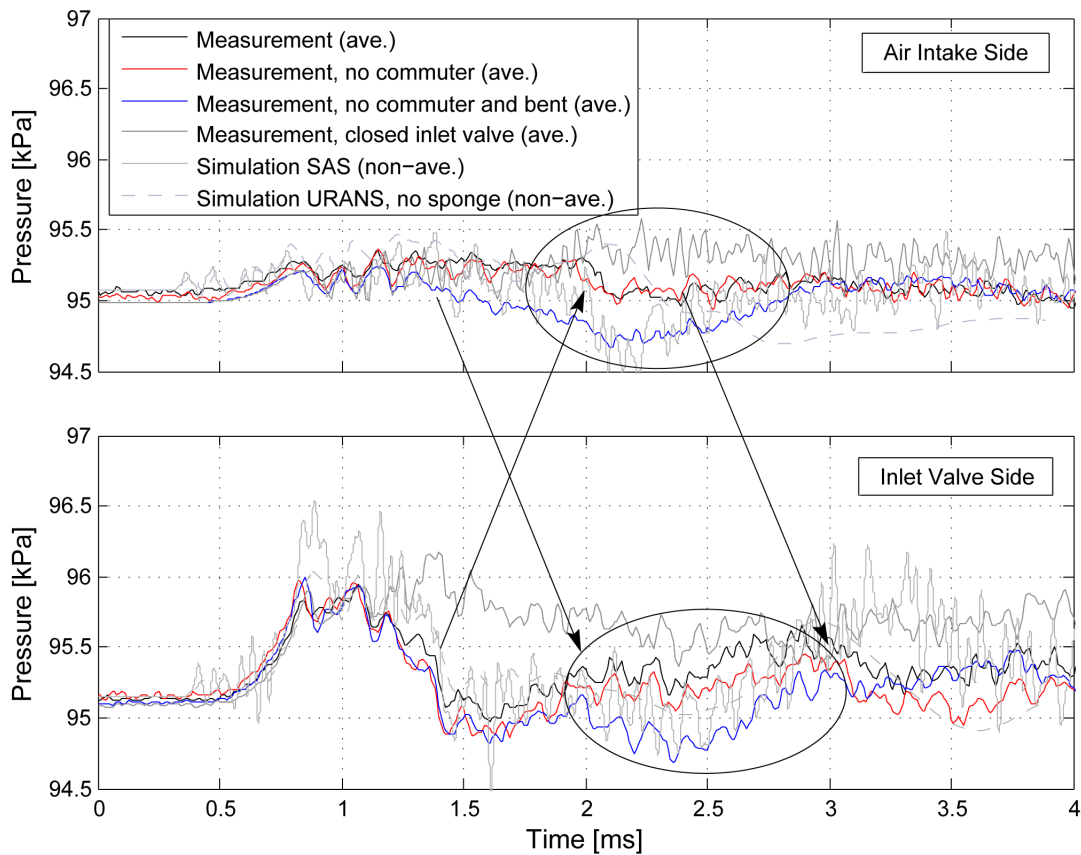
Figure 4.18: Influence of different intake manifold endings on time response

As long as reflections do not occur, namely during the first 1.3 ms, numerical simulations and measurements match very well. Then deviations start however depending on the duct endings. At air intake side the fully open setup departs noticeably from the others and the SAS simulation. At the inlet valve side the fully opened valve behaves very similar the setup in the simulations.

The reflected plane waves propagate along the intake manifold (symbolized by arrows) and eventually affect the measurement on the other side of the injector at around 2 ms (ellipses). Here, the pressure drop at air intake side seems to be somewhat weaker in the measurements compared to the simulation while measurements enclose the simulation on the combustion chamber side. Even though the absolute time response deviations become quite large here indeed quantitative similarities remain.

Eventually, the plane waves will be reflected at the duct endings again and propagate in reverse direction repeatedly. Doing so they interact with the jet flow. They might be emphasized or damped and also excite the jet. Even though the waves become less pronounced and broader over time they are seemingly energized and thus persisting for by far longer than an injection cycle.
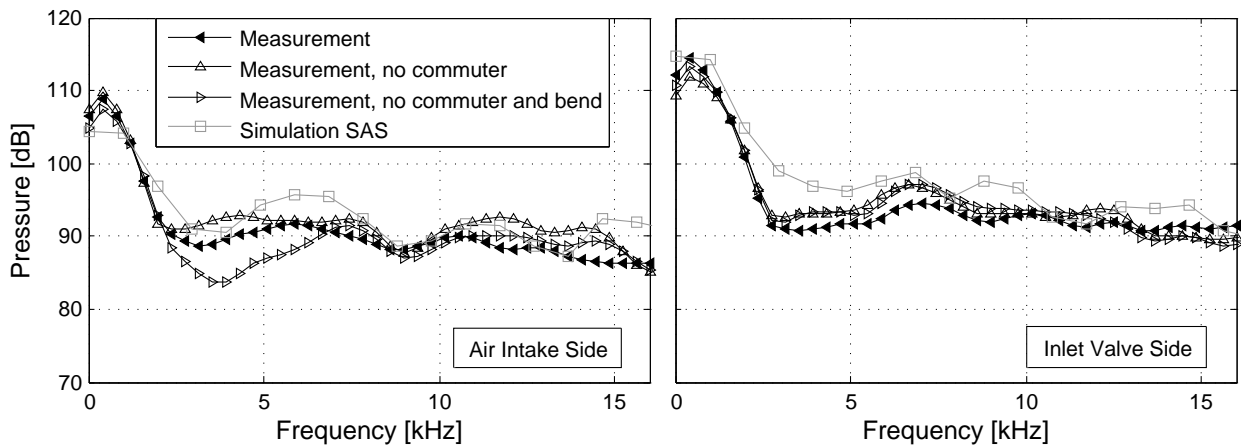
Figure 4.19: Influence of different intake manifold endings on frequency response

The altered reflection properties of the duct endings condense in altered spectra for the respective non-averaged measurements of course (Fig. 4.19). Apart from partially lower levels in air intake direction for the measurement without commuter and bend, deviations in terms of levels and distribution are often low over wide ranges especially in inlet valve direction. In particular, the measurement for the standard test rig reproduces the simulated characteristics quite well as well.

Summarizing, the measurements do not exactly match the simulation, first of all due to the bend at the air intake side. Still they provide good results for validation purposes. Strong reflections at the throttle limit the measurement period to 38 ms after the injection.

Time Domain Results

Analog to the injector in freestream configuration (Sec. 4.1.3), the closing blast is often larger and longer lasting than the opening one, especially for perpendicular injection. New sensitivities emerge however in form of weaker closing blasts for increased cross-flow velocity (WC3/4) and lower ambient pressure (WC1/3), and stronger opening blasts in injection direction and lower pressure respectively (Fig. 4.20, Tab. 4.7).

Considering the sensitivity towards the injection direction in particular this concerns not just acoustics but also the stationary flow. Perpendicular injection blocks the cross-flow and increases the average pressure at air intake side by several 100 Pa. The resulting pressure drop across the jet becomes even more pronounced for low pressure WCs. Then an additional equally strong pressure decrease arises at inlet valve side due to the drawing effect of the jet. Oblique injection on the other hand generally attenuates this effect. The strong jet in WC1 can even reverse the relation towards a pressure increase across the jet and reduced pressure at the air intake side, thusly drawing additional air from the intake.
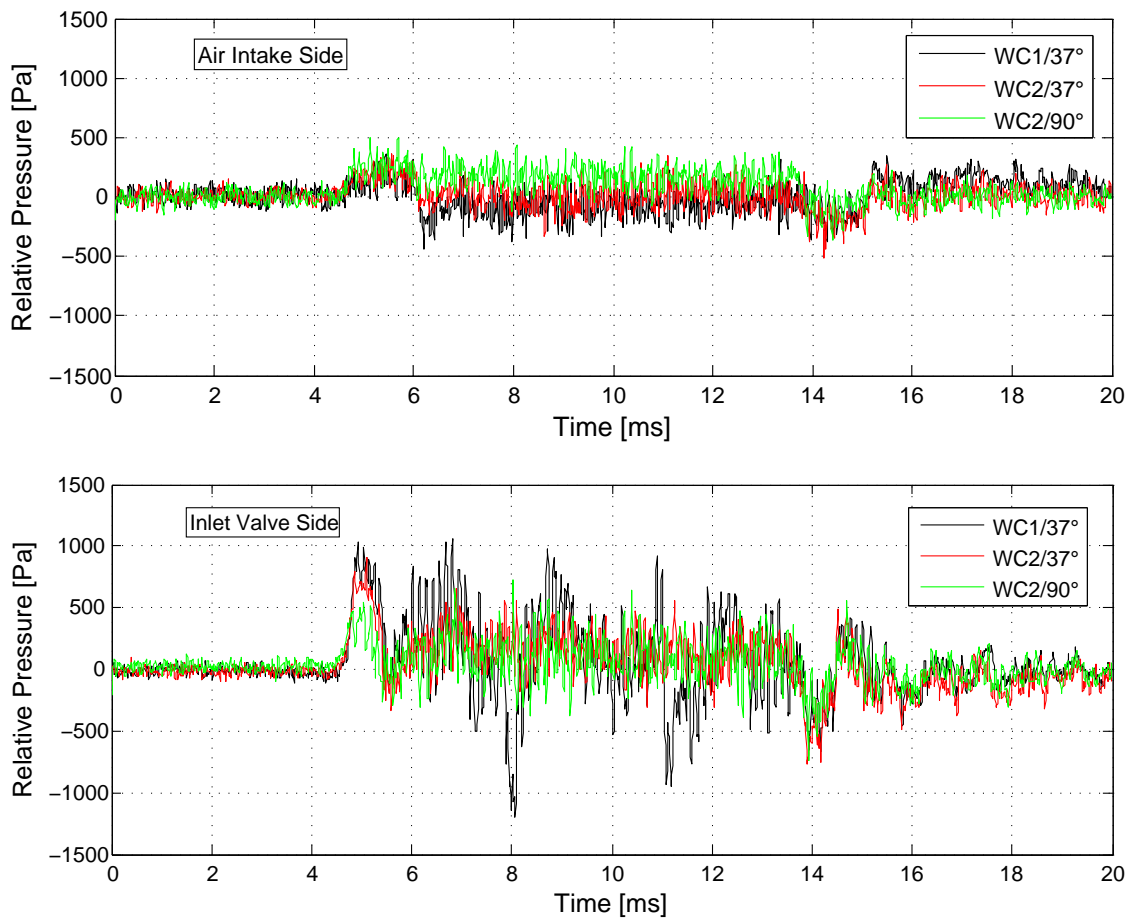
Figure 4.20: Exemplary time domain results of intake manifold injection cycles

Frequency Domain Results

The steady injection noise is investigated in frequency domain. Although the derived spectrum proves to be widely independent from the chosen measurement interval length and location some influence is still notable. On one hand low-frequent contributions are weakly damped over time due to the weakening leftovers of the opening blast. On the other hand a new peak develops at 7.7 kHz at inlet valve side. This is identified to be caused by the measuring equipment rather than being actual aeroacoustics, though. In detail, the pressure transducer was not tightly fixed by mistake but could in fact oscillate within its mount due to pressure differences between reference and intake manifold sides. Thus, low pressure WCs are mostly affected by exaggerated pressure levels at the respective resonance frequency which therefore is excluded from the following considerations. Unfortunately the measurements could not be repeated.

The measurements are processed for the time range 3-15 ms of respectively longer cycles as a trade-off between spectral detail and clarity of plots containing multiple curves. In Fig. 4.21

	Opening blast	Closing blast	Pressure Drop	Jet noise
Lower ambient pressure	↗	↘	↑↓[a]	↗[a]
Stronger cross-flow	→	↓	↗↘[b]	→
Larger injection angle	↓[c]	→	↑	↘[d]

[a]increase of low frequency content, decrease at the air intake around 7 kHz and 12 kHz (weak cross-flow)
[b]stronger for large injection angles, weaker for small injection angles
[c]in inlet valve direction, otherwise slight increase
[d]in inlet valve direction

Table 4.7: Sensitivities to parameters variations

the resulting averaged spectra are compared for all considered working conditions and injection angles. Furthermore the lowest cut-off frequency (Sec. 3.3.2) is marked by a dashed line.

Globally, there is strong broadband noise of partially very similar shapes and levels. It is by about 5 dB louder in inlet valve than in air intake direction and drops by approx. 5 dB for frequencies below cut-off. Deviations among the WCs are mostly confined within a 5 dB range as well. Larger deviations are mostly driven by stronger opening blasts and hydrodynamics of low pressure WCs.

When it comes to the sensitivity towards the problem parameters, it is first of all the low injection angle and low pressure WCs which increase low frequent contributions in injection direction. Perpendicular injection into low pressure environments furthermore reduces noise above 12 kHz at the inlet valve. At air intake side the noise levels for low pressure WCs are up to 5 dB lower in the range 5-8 kHz. The cross-flow has no greater influence but some minor frequency shift. The sensitivities can be considered to be quite weak globally.
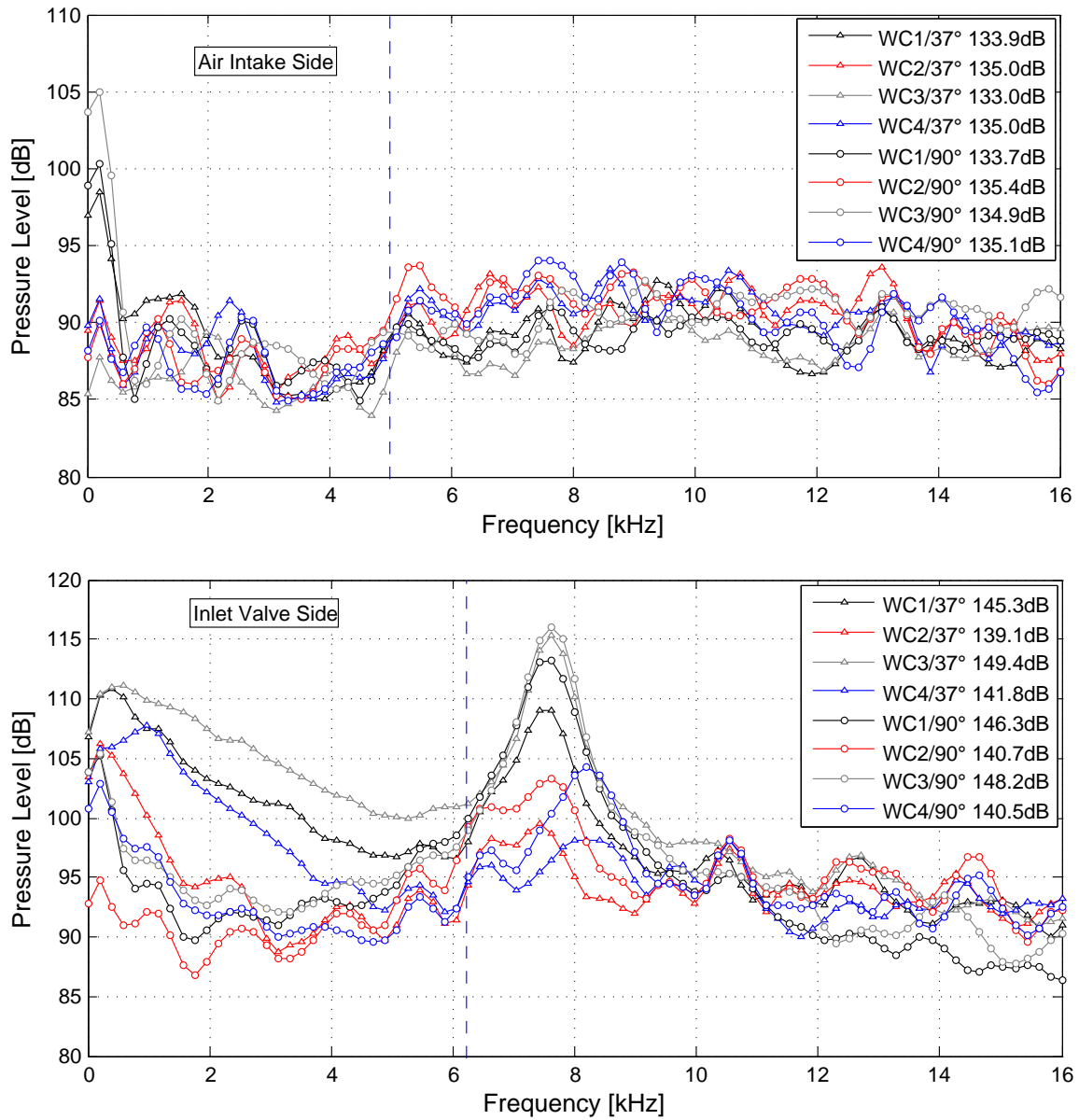
Figure 4.21: Working condition and injection angle study of steady injection noise

Chapter 5

Enabling Simulations with ANSYS CFX

The primary aeroacoustic simulation approach shall be based on a commercial software, namely ANSYS CFX. On this basis a methodology shall be developed able to simulate the aeroacoustics of a supersonic gas jet. This chapter will point out deficiencies and offer solution approaches enabling this inherently not aeroacoustics-focused software for this purpose. Bottom line, this is leading to Matlab and Fortran routines programmed by the author, accordingly adjusted expert parameters, and eventually, first working simulations. The test application is the very same gas injector in freestream configuration and simplified in terms of grid resolution, domain dimensions, inlet and farfield boundary conditions.

Since data from preceding internal injector flow simulations is available (Sec. 3.5), a more realistic inlet boundary condition located in the kidney-shaped orifices is modeled in the first step. This trims the necessary numerical domain and avoids the need for moving meshes during injector opening for all subsequent simulations without losing functionality. Then, the cause of the RANS simulation instabilities experienced in preceding simulations (Sec. 3.6), namely numeric reflections at open domain boundaries, is investigated and respective solution approaches are detailed and tested. Finally, stability issues characteristic to the ANSYS CFX solver are disclosed and partially resolved.

5.1 Development of a Transient Inlet

Next to the already mentioned domain decrease modeling a new inlet boundary condition has several more advantages the standard ANSYS CFX inlet does not offer. On one hand this is the ability to plant a realistic velocity and pressure profile in the inlet instead of constant values or an analytic function. On the other hand the inlet can be re-defined timestep-wise in order to model detailed transient behavior like the injector opening process or transient fluctuations.

The export from a preceding simulation generally provides data with a non-matching spatial and temporal discretization. To enable its further use interpolation onto the new setup is necessary. Time interpolation is easily done in Matlab using splines. This produces profile files

for every timestep which then need to be read into ANSYS CFX accordingly. This is achieved by a user-programmed Fortran *Junction Box Routine* being executed in the beginning of each timestep[1].

The spatial interpolation is more complex. ANSYS CFX demands the inlet variables at the collocation points of the new grid. Thus, even though providing identical meshes for both simulations interpolations become necessary. However there is virtually no way to obtain the exact locations of barycenters of the grid elements and their projection onto the inlet surface beforehand using ANSYS CFX-Pre or -Post. Consequently interpolation is done during runtime. This requires a *CEL Function* for each inlet variable pointing to a *USER Fortran Routine* which is then doing the actual interpolation each time inlet data is requested by the solver. Eventually this is leading to the definitions necessary when setting up a new simulation as presented in Sec. A.1.
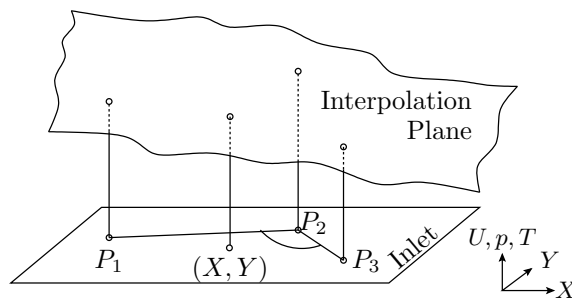
Figure 5.1: Delauney interpolation sketch

The chosen spatial interpolation algorithm is largely based on the Delauney triangulation. It is not conservative and just piecewise linear (or planar) but very fast and well-suited for an unstructured cloud of points. Indeed the interpolation problem is not easy since node densities vary a lot locally due to very bad element aspect ratios and a curved structured grid. Furthermore the variables are subject to steep gradients which might easily result in bad or even illegal out-of-bound interpolations. Bilinear interpolation would fail here for example.

The actual interpolation algorithm is shown in Fig. 5.1. The Fortran routine is called by the solver each time the inlet variables are accessed. As arguments this provides a list of coordinates (X, Y) representing the collocation points data is demanded for in the current share of the inlet surface considering a parallel environment. Then the routine searches the available data for the three closest points to each (X, Y) with the constraint to form a respectable triangle. This allows to define a plane in 3D through these points with the requested inlet variable as Z-coordinate. Eventually the interpolation result for (X, Y) is obtained by solving the plane equation. In case no three suitable points are found (e.g. at the boundary of the inlet face) or in cases (X, Y) is indeed very close to a point in the interpolation table

---

[1]In steady state simulations it can be executed in the beginning of each coefficient loop iteration instead.

the nearest neighbor approach is used instead. Finally the result is checked for a value within reasonable bounds. Otherwise the process is repeated with a new set of points.

(a) Original   (b) Interpolated
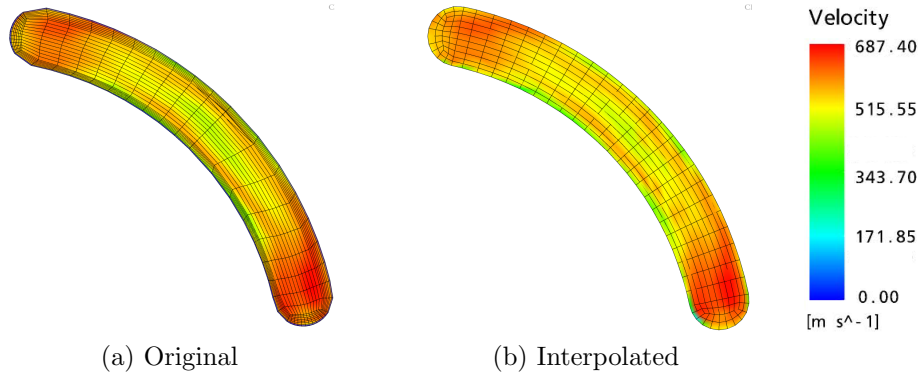
Figure 5.2: Comparison of original and interpolated inlet velocity profile

Even though this type of interpolation is not conservative it results in correct levels and well-matching profiles even for such a inhomogeneous cloud of nodes (Fig. 5.2). Nevertheless it is recommended to cross-check the inlet massflow. For more regular grids, better matching meshes and weaker gradients even better results can be expected. Some minor speed up could be achieved by doing the search for triangulation points just the first time it is encountered. Then however a result within bounds is still not guaranteed yet. Indeed the interpolation of the comparably few nodes does not contribute reasonably to the simulation costs.

5.1.1 Turbulent Inlet

Noise generation is a turbulence-driven phenomenon. Hence the simulation results depend on the captured and modeled turbulence in the flow. If the dominating turbulence structures are not generated within the computational domain (as in most jet simulations) the modeling of inlet fluctuations has reasonable influence. A constant inlet would cause unrealistic results in particular.
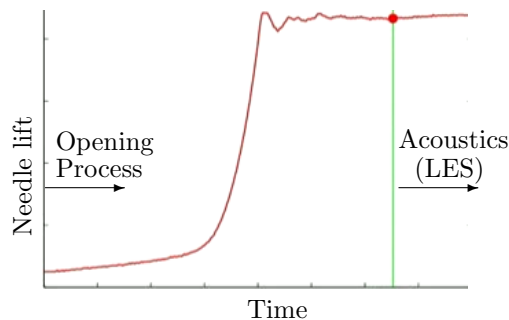
Figure 5.3: Proposed re-application of preceding simulation results for a transient inlet

Inlet disturbances can be introduced by artificial forcing [20] or by a streamwise periodic function [32] for example. The better and more realistic alternative is however to re-apply data from a preceding simulation comprising the domain upstream of the currently modeled inlet. In this work the available data (Fig. 5.3) in conjunction with the transient inlet boundary condition provides turbulence information even for the phase of stationary injection. Hence an actually turbulent inlet boundary condition is available as well e.g. for subsequent LES simulations.

5.2 Development of Non-Reflective Boundaries

Preceding RANS simulation attempts for the gas injection problem proved to be non-converging even if applying artificially increased viscosity in the whole domain (Sec. 3.6). Subsequent transient simulations showed strong pressure waves propagating along the duct axis and a flapping jet instead.
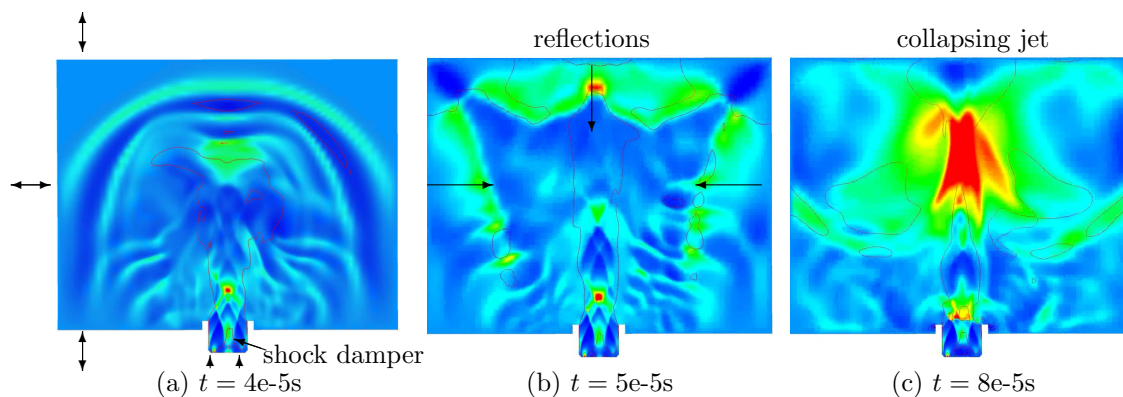
Figure 5.4: Numerical reflections on open domain boundaries, RANS, pressure

In new preparatory simulations the axial waves are identified to be there first subsequently forcing the jet into oscillations. Furthermore the formation of the waves is traced back to a poor domain initialization, namely constant velocity in x-direction rather than a profile along the duct axis, and open domain boundaries numerically reflecting the waves instead of having them leave the domain. While the former can be easily avoided, e.g. by a preceding cross-flow initialization run, the latter requires a dedicated boundary treatment during the simulation. Indeed a non-reflective boundary is imminent for all aeroacoustic simulations since unphysical acoustic feedback would contaminate the result or even blow the simulation in case of a strong opening blast (Fig. 5.4). Hence, a number of boundary condition enhancements (Sec. 2.3, Tab. 5.1) are tested here in order to identify applicable methods preventing those reflections.

Approach	Applicable in ANSYS CFX	Efficiency and Robustness
Averaged pressure BC	yes	low
Optimized BC placement	yes	low
Grid stretching	yes	very low
Slowly powering jet up	yes	low
Characteristic NRBC	yes (1D)	medium, limited, instable
Radiation NRBC	no	–
Artificial viscosity ABC	yes	medium, problematic
Implicit damping ABC	yes	high
Artificial convection ABC	no	–
Explicit damping ABC	no	–
Perfectly Matching ABC	no	–

Table 5.1: Overview of approaches for non-reflective boundaries

5.2.1 Non-Reflective Boundary Condition

Next to the passive means of grid stretching and an averaged pressure boundary condition ANSYS CFX provides non-reflective characteristic boundary conditions (Sec. 2.3.1) as a beta feature[2]. Its current functionality is tested for an injector in freestream configuration (Fig. 5.5a, half-model, URANS/k-ε) however with little success.

Firstly, the non-reflective boundary condition proves to be increasingly instable if it is applied to outlets also being subject flow unsteadiness and hydrodynamic fluctuations. Furthermore the averaged pressure outlet results in strong arbitrary fluctuations throughout the boundary. Thus the top plane of the computational domain is tied to just a common 'reflective' outflow and has to be moved further downstream in order to at least slightly weaken the reflections supported by grid stretching.

Secondly, at the sides of the computational domain the performance of the characteristic NRBC is weak (Fig. 5.5). The boundaries are just a little less reflecting and the shortcomings of a 1D characteristics analysis come to the fore: Tangential wave components are trapped and propagate within the boundary elements. Eventually they act as additional sources of noise indeed.

For better performance the boundary would have to be a sphere with the noise source in the center such that incident acoustic waves are always perpendicular. This would require a much larger domain though and is hardly achievable for distributed sources of noise. Bottom line, the current implementation in ANSYS CFX is insufficient and quite unstable indeed. Its application can not be recommended for the injection problem.

---

[2]*acoustic reflectivity* flag available in release 10, undocumented, no further development planned
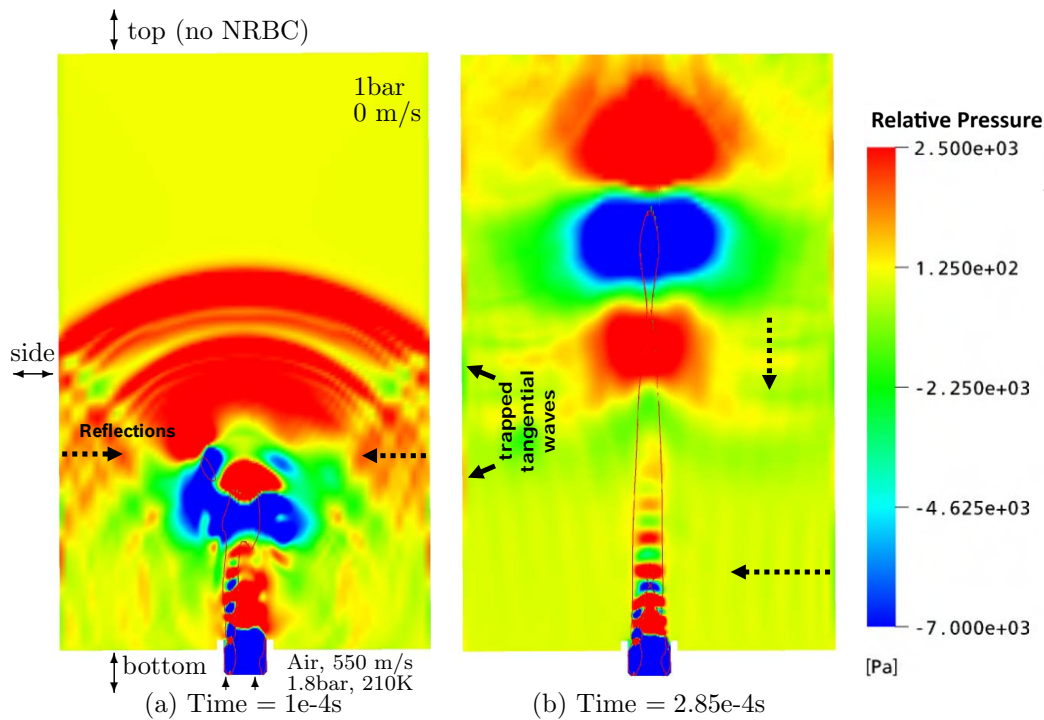
Figure 5.5: Test of characteristic NRBC in ANSYS CFX

5.2.2 Absorbing Boundary Condition

Alternatively spurious reflections can be avoided by actively damping acoustic waves (and other fluctuations) before they reach the boundary. This is leading to absorbing boundary conditions (ABC) or sponge layers as described in Sec. 2.3.2. Additional elements in which the solution becomes physically wrong coat the actual boundary condition. The result is numerical overhead and increased computational effort. Furthermore ABCs generally act as a boundary conditions themselves and, when unwisely tuned, can force the flow in the 'inner domain'. Therefore the aim is to model an effective absorbing sponge layer that leaves the inner domain flow wholly unaffected. Amongst other things fluid must still be able to enter and leave the domain smoothly.

Owed to the very limited access ANSYS CFX permits to the code and the current state vector solution the list of known sponge layer concepts condenses to just two applicable versions (Tab. 5.1). For the sake of quick testing the computational setup is cut down to a quarter-model. Additional 25% coarse elements in any far-field direction form the respectively tested type of ABC (Fig. 5.6a).

Artificially Increased Viscosity

Dynamic viscosity physically dissipates a portion of any fluctuation or gradient into thermal energy (Sec. 2.3.2). The implementation of locally increased viscosity in ANSYS CFX is

(a) computational setup with
boundary markers

(b) sponge strength 0..10
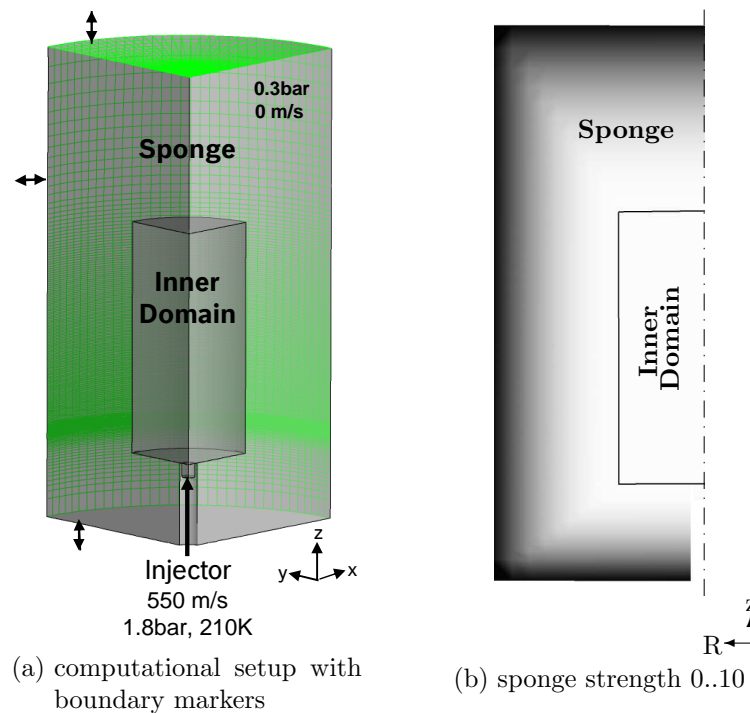
Figure 5.6: Absorbing boundary layer setup

straight forward. Using expressions the viscosity can be defined as simple functions of the actual location (x, y, z) or the subdomain flag[3] for example (Sec. A.3).

In view of the strong opening blast to dissipate the viscosity has to be extremely increased to show any effect at all. Then however there is strong resistance to the flow development as well. The result is unphysical flow forcing into persistent recirculation and a significant temperature increase while strong waves still may reach the outer domain boundaries (Fig. 5.7).

Thus this approach is only applicable to problems exhibiting just weak fluctuations or with already initialized farfield mean flow. Increased viscosity might be advantageous dissipating large-scale vortices slowly propagating towards the outlet, though.

Implicit Damping

More sophisticated absorbing boundary conditions can be designed using source terms in the governing equations (Sec. 2.3.2). Indeed ANSYS CFX provides a variety of predefined source term types (e.g. a porous and directional loss model) and also generalized source terms for each one of the governing equations separately.

Loss models mean momentum sources acting on the velocity vector in particular. The flow is slowed down by imposing a resistance to it which is not applicable here. The alternative

---

[3]A variable valued one within predefined subdomains such as the sponge and zero everywhere else.

(a) velocity and streamlines

(b) relative pressure
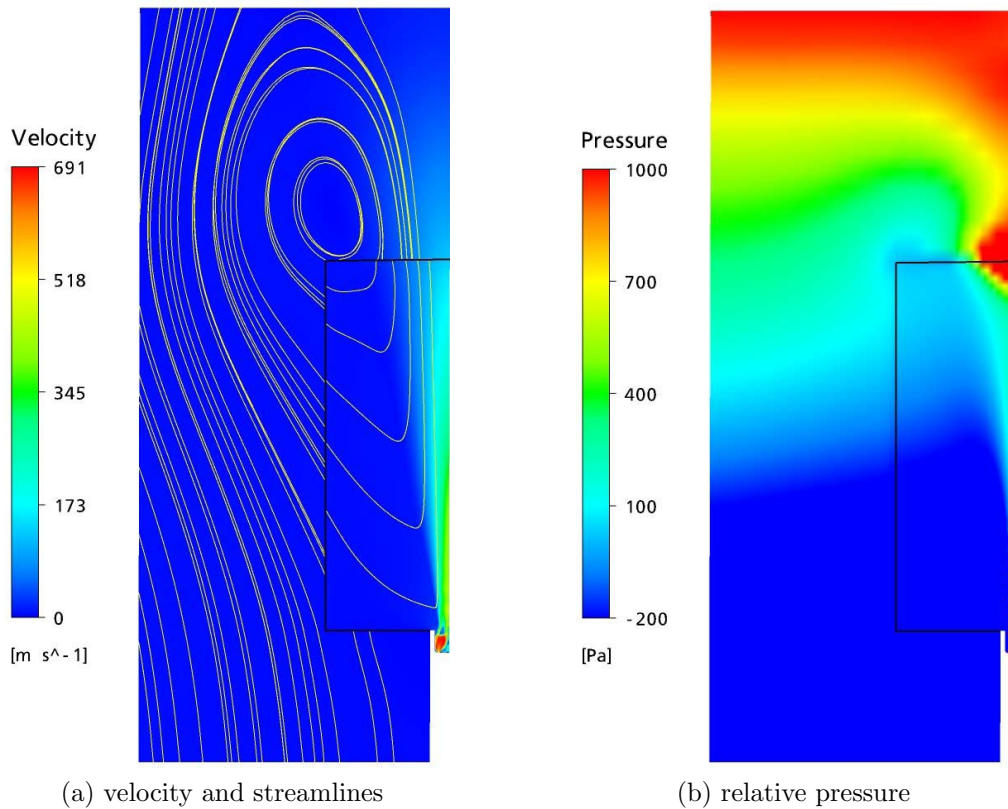
Figure 5.7: Test of artificial viscosity ABC in ANSYS CFX

employment of a generalized ABC in accordance to Eqs. (2.45)-(2.46) enables the specification a non-zero farfield mean flow instead. Still, the far-field flow has to be known in advance in order to avoid unrealistic flow forcing. In this work it is not exactly predictable yet known to be non-uniform and varying over time, though.

In order to avoid the need for an explicitly specified far-field flow other source term constructions are theoretically thinkable as well, e.g. containing filtered gradients or time derivatives (Tab. 5.2). However these approaches require more sophisticated programming and often raise other issues like a very sensitive and problem-dependent tuning of additional parameters or reduced robustness.

Eventually another variation is identified to be simple to implement yet very effective. Since it is pressure waves being reflected at the open domain boundary these need to be damped or forced towards a known far-field reference pressure p_∞ in the first place. The other governing equations remain without an explicit source term.

$$S_C = \sigma \cdot (p - p_\infty) \tag{5.1}$$

Thus pressure fluctuations are suppressed by locally adding or subtracting fluid mass. Normally this would also affect the other state variables as well. Here ANSYS CFX offers to add

#	Type	Advantage	Disadvantage
1	$\sigma_1 \cdot (F - F_{spec})$	Resistance to far-field deviations, simple to implement	Far-field solution must be known, probable flow forcing
2	$\sigma_2 \cdot \frac{\partial F}{\partial t}$	Resistance to quick fluctuations, flow can develop slowly	Time derivatives must be computed manually
3	$\sigma_3 \cdot \nabla F$	Resistance to shear, filtering and directive pattern possible	Potentially instable or forcing, problem-specific limiters

Table 5.2: Implicit source term types with respect to state variables F

and subtract fluid of a specified state similar to an inlet or outlet however. Employing the local fluid state (Sec. A.4) the oder state variables remain widely unchanged while acoustic waves are suppressed effectively. In particular, the flow can develop freely.

This approach is supported by a blending function for the sponge strength σ to avoid discontinuities and spurious reflections at the inter-domain interface (Fig. 5.6b). A USER Fortran routine provides σ in dependency of the location as outlined in Fig. 5.8a and thus a smooth transition into the sponge. In fact very sophisticated formulations are thinkable such as a time-dependent $\hat{\sigma}$ or a wall distance[4]-dependent formulation.

(a) Schematics

$$\sigma(x) = \hat{\sigma} \left| \frac{(x-x_0)}{(L-x_0)} \right|^\gamma, \quad x \geq x_0$$

(b) Exemplary blending functions
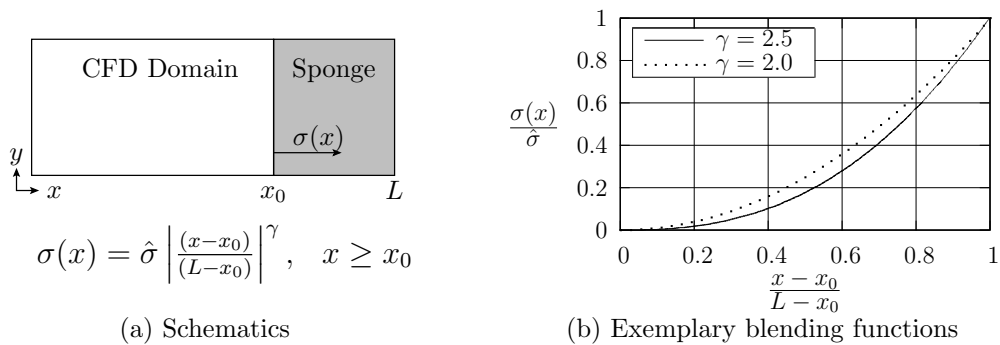
Figure 5.8: ABC sponge strength blending simplified to 2D

The best choice for the exponent γ has been shown to be a function of the mean velocity within the sponge [86]. For subsonic flows it ranges between 2 and 2.5 with latter for resting fluid (Fig. 5.8b). This is chosen here.

However since this approach takes just implicit effect during a timestep its performance is highly dependent on the discretization. Especially if the timestep size is altered $\hat{\sigma}$ must be readjusted as well to maintain the same results. Otherwise the damping could become too

---

[4]This is computed by the SST turbulence models or when it is explicitly demanded by CCL code.
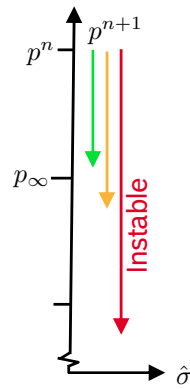
Figure 5.9: Implicit damping with continuity sources, pressure change during a time step in dependency on sponge strength

weak or the local pressure could overshoot the specified reference (Fig. 5.9, yellow) or even overshoot the preceding absolute deviation (red) causing instability.

(a) Disabled sponge layer   (b) Enabled sponge layer
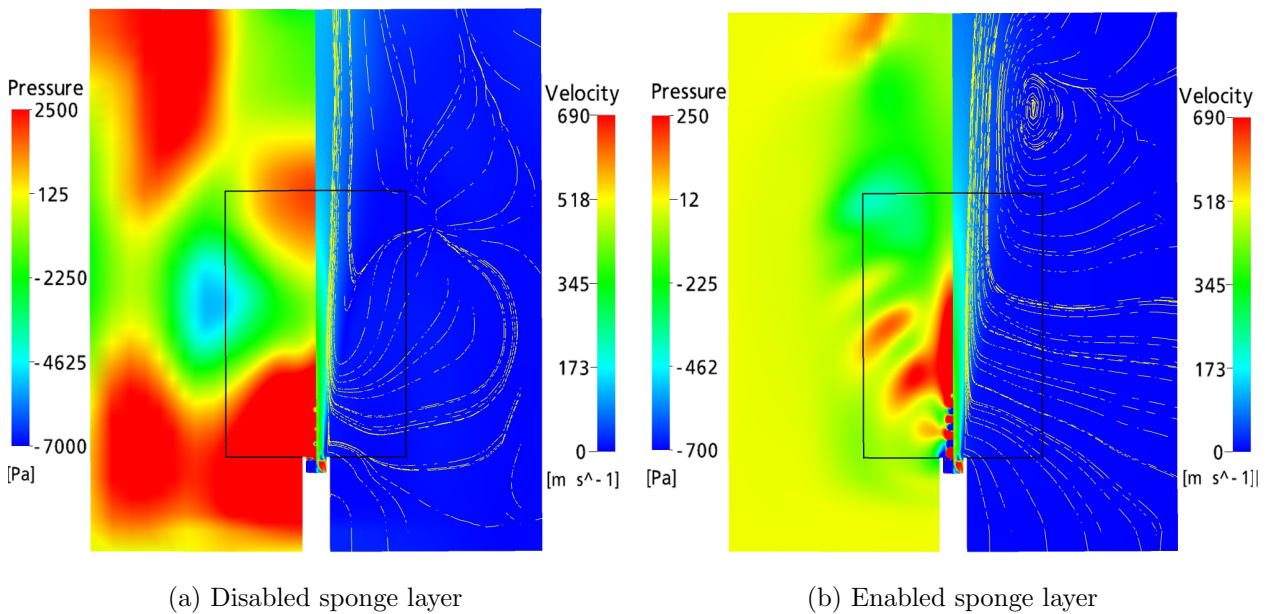
Figure 5.10: Test of implicit damping ABC, RANS at the same iteration, with streamlines

Nevertheless provided a good $\hat{\sigma}$-setting this implicit damping approach works very well indeed for steady-state as well as transient simulations. In the direct comparison the untreated RANS simulation (Fig. 5.10a) develops massive pressure fluctuations and erratic streamlines throughout the computational domain. The result is very bad convergence. Enabling the implicit sponge layer instead suppresses waves effectively before they reach the outer boundary (Fig. 5.10b, mind the different scale). Flow and streamlines can develop freely.

5.3 Overcoming Stability Issues

The solver and the standard settings implemented in ANSYS CFX might be feasible for the majority of problems encountered at the industrial scale. For the injection problem governing this work and featuring strong compressibility, shocks and Mach discs this is not necessarily true though. The major issues met during this work and potential solution approaches are outlined in the following.

Carbuncle Effect   The Carbuncle effect [79] describes numerical instabilities that can arise when bow shocks are aligned to a structured grid. The solution starts to oscillate transversely to the shock owed to flux vector or pressure-velocity coupling effects. Simulations using meshes that are finer in transverse direction than in flow direction are affected most [26].

With respect to this work instabilities occur especially in transient aerocoustic LES and SAS simulations when the jet's shear layers within the shock damper are well resolved in a structured grid. Strong bow shocks emerge for low pressure working conditions in particular. Consequently, the supposed shock locations have to be refined in flow direction to a similar level as across the shear layer.

There are also some numerical approaches to avoid the Carbuncle phenomenon. They mostly artificially increase the dissipation and smear the shocks though. In ANSYS CFX this can be enabled by the solver option named 'high speed numerics'. Indeed it makes the Mach discs unphysically vanish and results in wholly different flows shapes.

Shock Capturing   ANSYS CFX is inherently unable to fit the shocks in their exact location. They are averaged and smeared within the control volumes instead. This is not an issue as long as exact shock locations and oscillations are not important for the solution. Problems could arise however when grid refinement becomes necessary or for simulations aimed at shock and screech noises in particular. Any grid variation causes the shocks to relocate. Subsequently these start to oscillate emitting huge amounts of noise. The effort necessary to settle the resulting fluctuations again makes any grid variation around shock locations particularly expensive. This should be considered during mesh generation and disqualifies automatic mesh refinement.

Multigrid solver   By default ANSYS CFX employs an algebraic multigrid algorithm in order to speed up the linear equation solver. It is summing up weakly influential equations in the linear system of equations and thus virtually merging control volumes during intermediate coefficient loop iterations. Hence it is not just a geometry-based but also a solution-dependent operation. The actual process of coarsening is performed only once for the initialized flow

by default. The same coarsened linear systems are re-employed in the whole simulation. If a reasonably different flow develops over time this approach might fail.

In the injector application this is leading to instabilities especially during the initial time steps when the jets establish within the shock damper. Turning off the multigrid solver by the respective expert setting makes the stability issues disappear.

Domain Initialization   The discontinuity at the inlet at $t = 0$ (Fig. 5.3) results in a shock wave and excessive flow velocities in the boundary elements during the first few time steps. Since this can blow the simulation it might be reasonable to choose a non-zero domain initialization in support of the robustness. In terms of this work a weak flow with $1\,\mathrm{m/s}$ in jet direction is employed for the freestream configuration in particular.

Chapter 6

Freestream Configuration Simulations

For development and validation of the numerical setup and method, and to understand jet structure and noise generation mechanisms governing this application, a freestream configuration is investigated first. The absence of cross-flow and surrounding walls allows direct measurement of the jet shape and emitted sound field, and thus, enables direct validation for a simplified problem. Simulation tool of choice is ANSYS CFX.

During pulsed operation two independent types of noise can be identified in the measurements (Sec. 4.1): Short strong burst are emitted during injector opening and closing, broadband noise of just half the magnitude is emitted during steady outflow. The respective noise generation mechanisms can be assumed to be uncoupled as well: While the bursts are caused by pressure release and fluid displacement, the stationary jet noise is based on shear layer fluctuations, shock motion and turbulence. Both noise entities have different modeling and mesh requirements (grid resolution, turbulence model, time stepping) such that injector opening and steady injection noise is addressed separately. Since transient inlet data is only available for the injector opening (Sec. 5.1) the closing process is not investigated separately. Measurements indicate generally similar behavior though.

LES is one of the most common, versatile and commercially available approaches for unsteady turbulence-governed problems, amongst others aeroacoustics (Sec. 3.2). For the prediction of the steady injection noise it is found to be intolerably computationally expensive, though, even on today's parallel computers. The reason is that the combination of a very fine mesh resolution and supersonic velocities force very small (global) timesteps according to the CFL condition (2.36). For larger timesteps LES becomes essentially undefined and might result in earlier overflow in ANSYS CFX. Therefore, the novel SAS-SST turbulence model (Sec. 2.2.4) is employed and validated for the injection problem instead. It is shown to remain stable and produce reliable results in a wide range of timesteps outside the CFL condition, and thus, at noticeably reduced costs. This advancement is essential for subsequent aeroacoustic simulations in Chapter 7 and other e.g. pneumatic flow problems.

6.1 Solution Approach

In a first step the *injector opening* process is investigated (Sec. 6.2). It is governed by shock waves and noise tracing back to simple pressure release and fluid displacement. Here fast unsteady RANS simulations on a comparably coarse mesh and k-ϵ turbulence modeling is completely sufficient.

After formation of the jet the flow gradients allow mesh refinement at shear layers and shocks. Here ANSYS CFX allows automatic mesh adaptation by a series of mesh refinements and steady RANS simulations. However, shocks are refined first of all. Their relocation in the subsequent RANS simulation causes oscillations with massive noise emission and bad convergence in return. Furthermore, the opening simulation indicates considerable jet fluctuations such that refinement of a single shock location is not reasonable. Therefore, the mesh is refined manually with focus on shear layers and wall boundary layers. The flow is converged on the new mesh thusly providing an initialization and steady-state reference for upcoming LES and SAS simulations (Sec. 6.3).
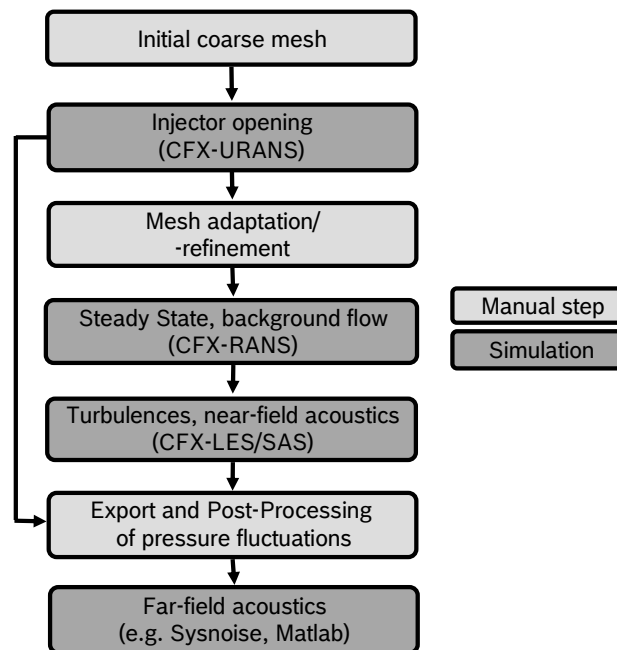
Figure 6.1: Freestream configuration strategy

Direct *aerocoustic noise* simulation for the nearfield of the gas jet is performed on a LES-enabling mesh using LES and SAS approaches (Sec. 6.4). LES and measurements provide a reference while SAS is assessed at various timesteps to determine the influence of the timestep on the solution quality and computational costs, and eventually identify a favorable setting for the injection problem.

Evaluation of the *acoustic farfield* is separated from the noise source simulation since standard CFD is too expensive and too dissipative for noise propagation over long distances. Acoustic analogies and hybrid methods with coupling of transient fluctuations or acoustic source terms to a dedicated CAA solver are possible solutions (Sec. 2.2.5). Owed to the predominant formation of concentric spherical waves an analytical approach and a more sophisticated 3D-BEM approach based on LMS SYSNOISE are pursued. Even though volumetric source term coupling is not allowed here due to non-linear propagation and a heavily fluctuating base flow the Lamb vector [39] is analyzed in order to locate the dominating sources of noise (Sec. 6.4.2).

All presented simulations employ the numerical setup developed in Chap. 5. Basis is a structured hexahedral mesh extended to half-model and with a resolution of down to $\Delta x \approx$ 1.8e-5 m. This small spacing is necessary to capture the emerging shear layers and shock cells, just in a URANS-like manner. LES simulations on such a mesh are close to DNS indeed since the grid spacing is just by two orders of magnitude larger than the Kolmogorov scale. An absorbing boundary layer based on continuity source terms and artificial viscosity is employed to model the farfield in the CFD simulations (Sec. 5.2.2). The transient inlet (Sec. 5.1) and ANSYS CFX settings to overcome stability issues (Sec. 5.3) are applied as well.

6.1.1 Methane vs. Air Injection

Transient inlet data is available for CH_4 only while the freestream simulations and measurements are performed with compressed air. Due to different isotropic exponents, molar masses and viscosities (Tab. 6.1) flows of different shapes and characteristics might form. Hence the available inlet data is transformed considering isentropic gas flows determined by the same tank state and critical cross-section.

	CH_4	Air
κ	1.32	1.4
$\mathcal{M}$	$16\,^{g}/_{mol}$	$29\,^{g}/_{mol}$
μ	$1.11 \times 10^{-5}\,^{kg}/_{m \cdot s}$	$1.83 \times 10^{-5}\,^{kg}/_{m \cdot s}$

Table 6.1: Properties of methane and air

The difference in κ results in a slightly different supersonic expansion and acceleration. However since the kidney orifices are just little larger than the critical cross-section the Mach number difference in the orifices is less than one percent. Pressure and temperature do not change too much as well assuming ideal isentropic expansion (Tab. 6.2). The flow velocity (6.1)

is reasonably scaled however since the molar mass $\mathcal{M}$ affects the speed of sound.

$$U = M\sqrt{\kappa \frac{R}{\mathcal{M}}T} \tag{6.1}$$

Analogue to the preceding simulations (Secs. 3.5 and 3.6) the simulations in this work are performed with constant viscosity (Sec. 2.1.4). Supporting runs with varying viscosity, and comparison of Euler and Navier-Stokes solvers in a research code (Sec. 8.2.3), confirm very similar results for the jet shape and its properties even for inviscid flows. Viscous forces are virtually negligible over inertia forces as long as the local velocity is high.

	M	U	p	T	ρ	Re
Air/CH$_4$	1.008	0.775	1.018	0.943	1.063	0.501

Table 6.2: Air inflow conditions

A different viscosity changes the problem's Reynolds number (Sec. 2.1.3) and thus determines the smallest scales of turbulent motion. This has effect on turbulent mixing, the steepness of gradients and DNS resolution requirements. The influence on audible noise can be assumed not to be dominating here though such that results obtained for air injection should be widely representative for Methane as well.

6.2 Injector Opening Process

The simulation setup is given in Fig. 6.2 and Tab. 6.3. In comparison to the setup in Chap. 5 the internal domain has been enlarged to ensure that the developing entrainment vortex ring does not reach into the sponge. Otherwise it would be energized and growing continuously.

Type	unsteady RANS (half-model)
Turbulence model	$k - \epsilon$
Mesh	1.76 million hexahedra, 22% in sponge
Time/-step	3.5 ms at $\Delta t = 2.5 \times 10^{-6}$s
Conditions	freestream, air into air at 1 bar, transient inlet

Table 6.3: Injector opening simulation setup

It has to be considered that the transient inlet does not start from zero mass flow but rather exhibits a weak but existent flow at $t = 0$ s (Fig. 5.3). Thus there is an initial discontinuity between inlet and computational domain causing a noticeable acoustic emission even though the injector is still assumed to be closed (Figs. 6.3(a) and (b)). When the injector actually opens, some more seemingly less pronounced spherical waves are emitted (Fig. 6.3c). They
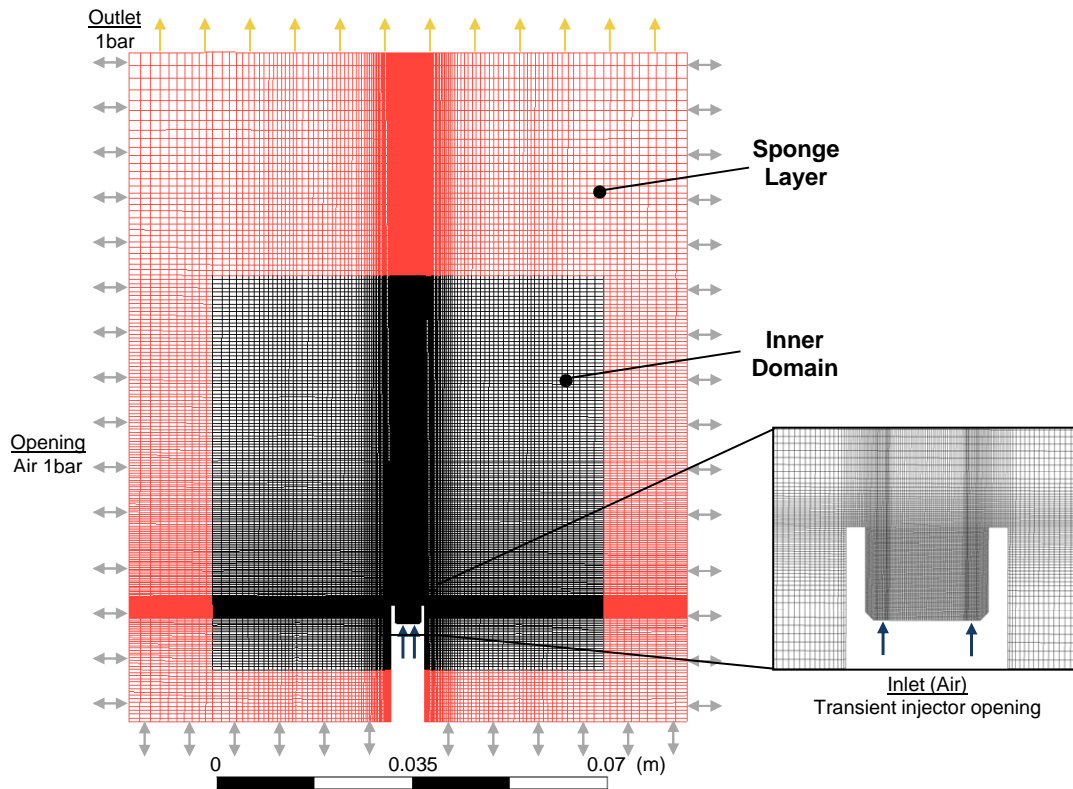
Figure 6.2: Fresstream opening simulation setup

are just masked by hydrodynamic gradients formed by displaced air in the nearfield, though. Thereon an entrainment vortex ring follows with propagation velocities of more than 100ms^{-1} (Fig. 6.3d). While convecting downstream it is successively slowing down. And when it finally left the inner domain the jet stabilizes and acoustic waves are not noticeable anymore (Figs. 6.3(e) and (f)). All of the observed fluid structures, the velocity/time scales of the opening process and the convection velocity of the vortex ring match quite well with vibrometer as well as Schlieren measurements (Sec. 4.1).

To enable detailed validation of the opening acoustics, nodal pressure data is exported in two distinct points (Fig. 6.3f). This data, compared to microphone and vibrometer measurements, shows next to similarities also reasonable differences (Fig. 6.4). Some of the latter can be traced back to incompatible properties of measurement and simulation:

1. URANS inherently does not capture broadband turbulence-based noise. Just a smooth time-averaged response is produced exhibiting dominant fluctuations only.

2. The simulation just covers aeroacoustic noise. Vibroacoustics and injector clicker noise are not considered but captured by the measurements.

3. Nearfield flow data generally consists of hydrodynamic as well as acoustic fluctuations.
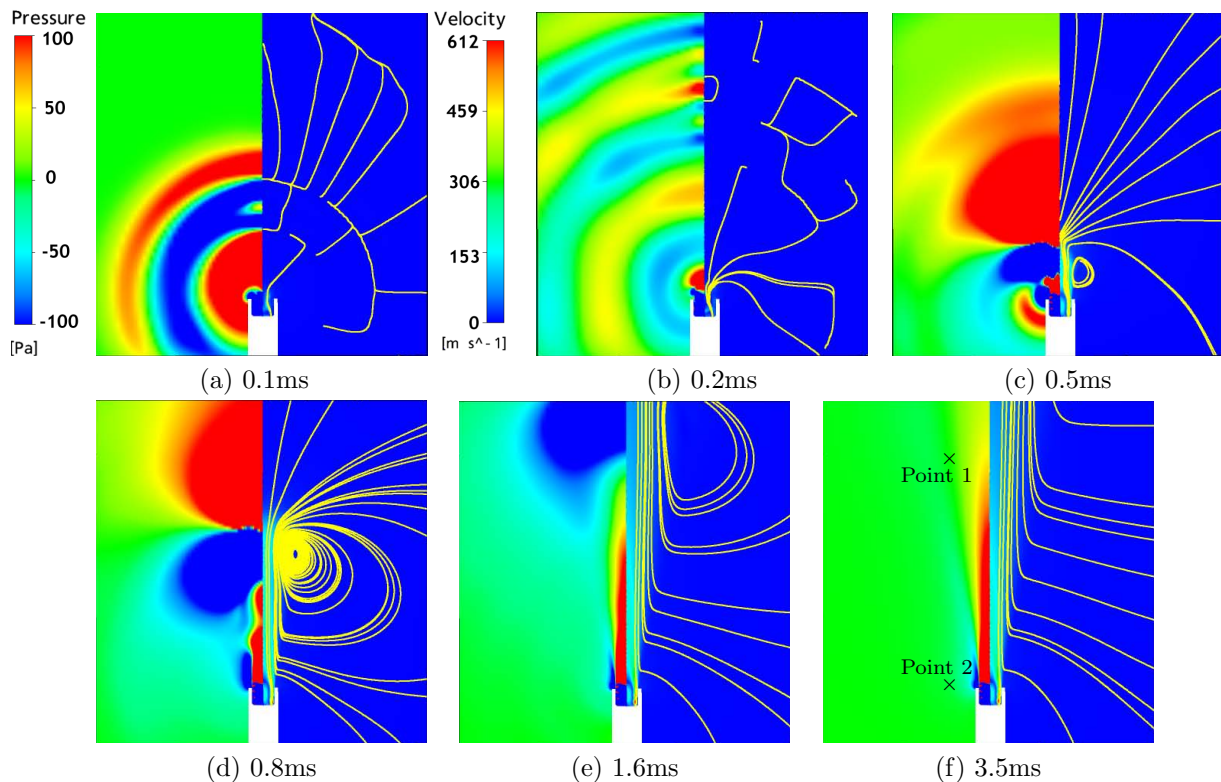
Figure 6.3: Freestream injector opening, inner domain simulation results

The microphones in the farfield only measure acoustics though[1].

4. Laser vibrometry data is qualitative only. Owed to integral measurements additional deviances might occur by superposition of fluctuations along the laser beam.

The already mentioned presence of acoustic waves caused by the inlet initialization is the first eye-catching difference in Fig. 6.4. Naturally, the initialization waves are not visible in the measurements. They allow however to reference later fluctuations as acoustic and hydrodynamic by their propagation velocities (arrows). Besides they vanish before the actual opening blast is emitted and are therefore no harm.

Second notable difference is that the vortex ring seemingly grows somewhat larger in the simulation compared to the measurement (cp. Figs. 6.3 and 4.7). Besides, the vortex ring propagation is generally slowed down or even blocked by the numerics at the outlet boundary condition. Consequently, it is dominating the simulation output in point 1 over a longer period with its low-frequency content, while the (weakly high-pass filtered) vibrometer data is influenced for just a short moment (gray ellipses in Fig. 6.4). In either case the acoustic waves become a mere modulation of the hydrodynamic pressure field.

In spite of all deviances, the major acoustic waves are reproduced correctly by the simulation.

---

[1]Simulation exports are scaled by $p' \propto \frac{1}{R}$ for spherical sound waves emanating from the injector.
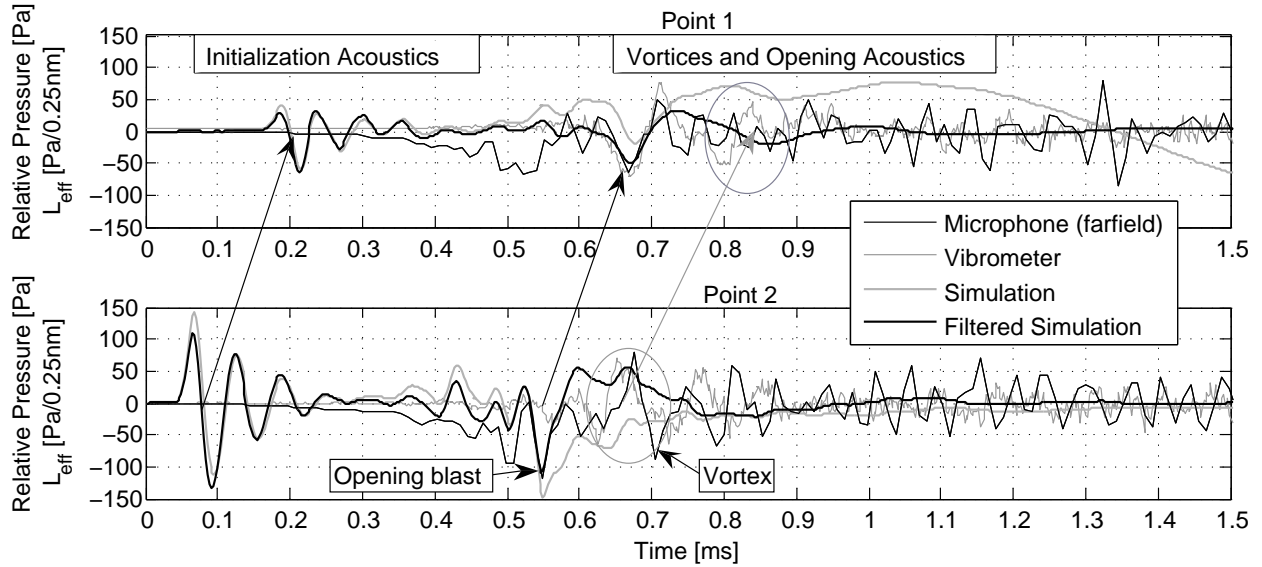
Figure 6.4: Opening pressure response. Comparison of simulation and measurement results in the points marked in Fig. 6.3f.

After a 3 kHz high-pass filter is employed to get rid of low-frequent hydrodynamic content peak amplitudes compare well to the farfield microphone measurements.

Summarizing, the transient inlet boundary condition in the framework of a simple URANS simulation yields results well comparable to observations and measurements. The slightly larger vortex ring might result from unavoidable interactions with the sponge layer and numerical outflow boundary condition rather than a bad numerical setup.

6.3 Averaged Stationary Flow

Since now the approximate jet geometry is known the mesh is further refined to capture the jet profile better and enable subsequent LES and SAS simulations (Fig. 6.5). Owed to heavily fluctuating jets refinement concerns whole regions rather than single locations. The wall boundary layer is resolved to LES level in particular. A dense streamwise mesh within the shock damper proved to be especially important in order to avoid the carbuncle effect (Sec. 5.3). As there are no large opening vortices anymore the sponge layer is enlarged and weakened again. This ensures that there is neither acoustic reflection nor flow forcing by the farfield boundary condition. The inlet is fixed to steady injection (Tab. 6.4). Since the averaged flow serves as initialization for upcoming aeroacoustic simulations it is converged in terms of residues, and additionally, pressure fluctuations captured in two points (Fig. 6.3f).

Coming from within the injector the flow is underexpanded and supersonic, such that escape into the shock damper results in further expansion and acceleration (Fig. 6.6). Local Mach

Type	steady RANS (half-model)
Turbulence model	$k - \epsilon$
Mesh	3.38 million hexahedra, 24% in sponge
Timestep	$\Delta t = 10^{-6}$s
Conditions	freestream, air into air at 1 bar, fixed inlet

Table 6.4: Steady state injection simulation setup
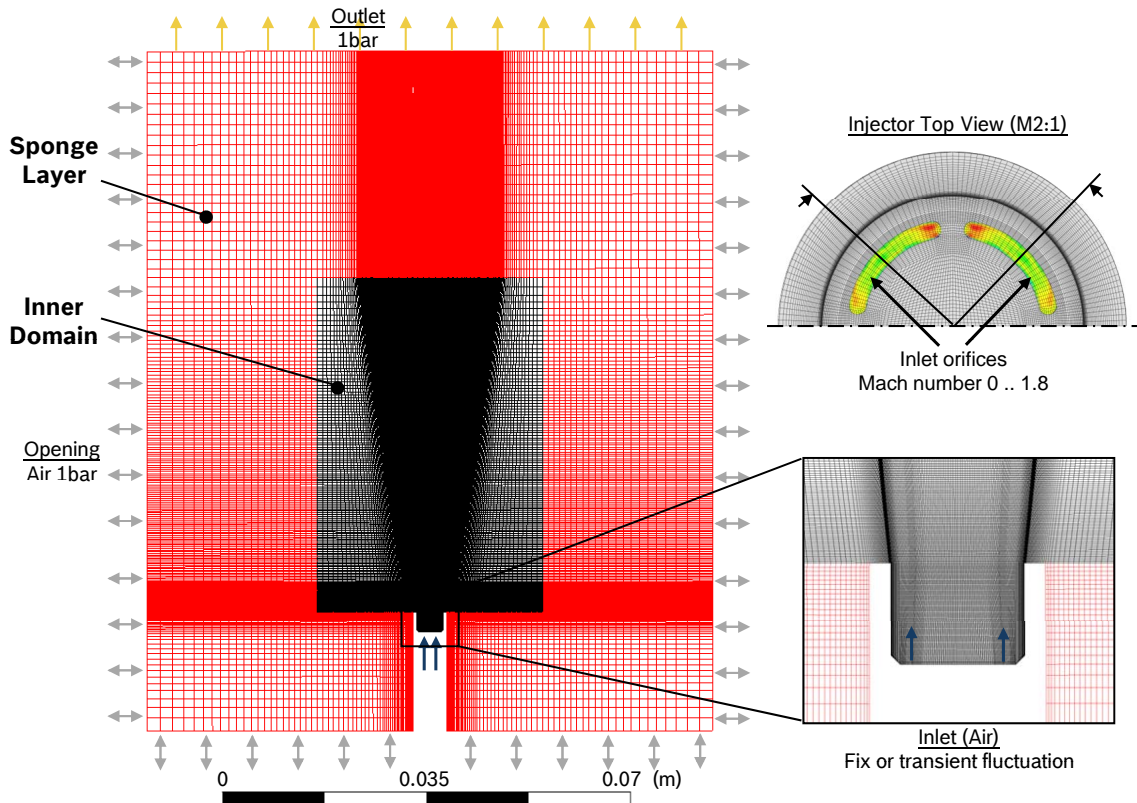
Figure 6.5: Freestream acoustics simulation setup

numbers up to three and multiple shock cells above each injector orifice are the consequence. The latter are accompanied by density gradients in well consistency with Schlieren images (Fig. 4.4). The maximum local Reynolds number within the shock damper is 30000, based on the orifice width.

Between the jets a cluster of vortical fluid establishes. In conjunction with the steep shear layer gradients it is responsible for strong turbulence production within the shock damper. Hence turbulence is generated by the flow rather than coming from inlet – ideal conditions for SAS-SST turbulence modeling (Sec. 2.2.4).

The curved orifice shape and interactions with the turbulence cluster cause a strong three-dimensionality of the flow. The jets are further flattened and pushed towards the wall (Fig. 6.7). Downstream the shock damper and the turbulence cluster's sphere of influence
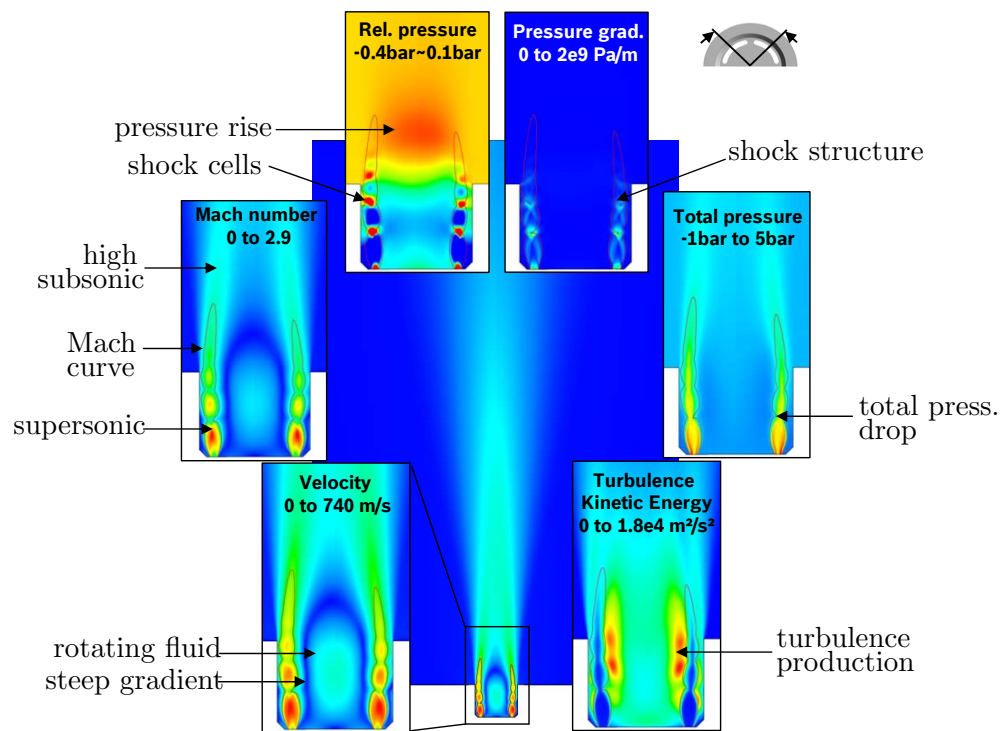
Figure 6.6: Steady freestream flow, simulation results

the jets reshape again and become circular eventually. Further downstream they seemingly unite to a single round jet enclosed by a continuous shear layer. Reshaping and unification of the jets absorbs turbulent energy and reduces noise (Fig. 6.6, Sec. 3.4). Inner shear layers and turbulence propagation are effectively interrupted. Along the way the flow drops to subsonic with local Reynolds numbers of 150000 for the united jet and based on the shock damper diameter.

Considering possible types of noise production (Sec. 3.2), turbulent mixing noise might play a dominant role due to the high jet velocities. The total pressure and jet velocity reduction by the shocks reduce downstream noise production however. Within the shock damper additional shock noise might occur. Screech tones probably do not manifest since the feedback paths are limited and might be fluctuating. Noise propagation from within the shock damper will be non-linear and partially shielded due to the presence of steep gradients and supersonic flow regions. Direct noise simulation is essential to capture the injector acoustics in the nearfield.

6.3.1 Sensitivity towards Inlet and Ambiance Variations

Against the background of varying inlet and ambiance conditions for future modifications and different duty points in intake manifold configuration the inlet velocity is increased by 30% in order to assess the sensitivity of the averaged flow. Greater deviances can have influence on

(a) forming round jets   (b) forming single jet
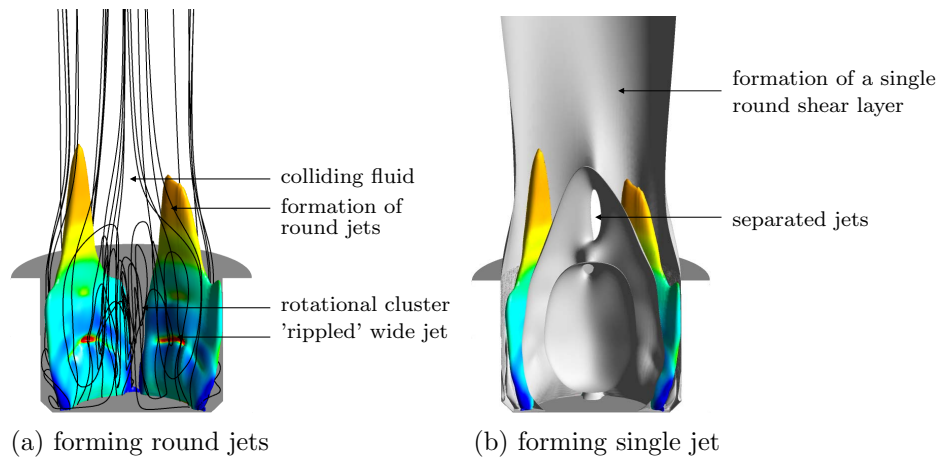
Figure 6.7: Three-dimensionality of steady freestream flow, simulation results; Mach isosurface(M=1) with pressure mapping(-0.4..1bar); left: with 3D streamlines; right: with Mach isosurface (M=0.3)

the mesh and simulation requirements for example.

Indeed the effect of the increased inlet Mach number on the forming flow structures as well as velocity and pressure scales is enormous (Fig. 6.8). The combination of increased jet velocities and the confined environment of the shock damper results in a potent attraction between the jets and further enforced over-expansion. Noticeably lower pressures within the shock damper and Mach numbers up to five are the consequence. When the ambient pressure takes effect downstream the shock damper the jets are compressed again substantially. Strong bow shocks and Mach discs with limited attached subsonic flow regions arise. From thereon the jets are united right away, supersonic and exhibit more shock cells. The supersonic flow region reaches for approximately another 40 mm, or two-third of the intake manifold diameter.

Consequently, potential boundary condition variations can result in wholly different problems – in terms of the emerging flow structures as well as solver requirements and aeroacoustics. Dedicated meshes and different timestep and solver settings could become necessary e.g. for intake manifold simulations. Amongst others the Mach discs showed to be very prone to the Carbuncle effect in particular.

6.4 Aeroacoustics with LES/SAS

The preceding URANS simulations are comparably fast but are known to produce single-mode turbulence only. Therefore, ANSYS CFX offers three alternative approaches providing the broadband turbulence scales required for prediction of flow-induced noise: LES, DES and SAS-SST (Sec. 2.2.4).

LES is the most accepted, powerful and applicable approach but limited to setups in com-
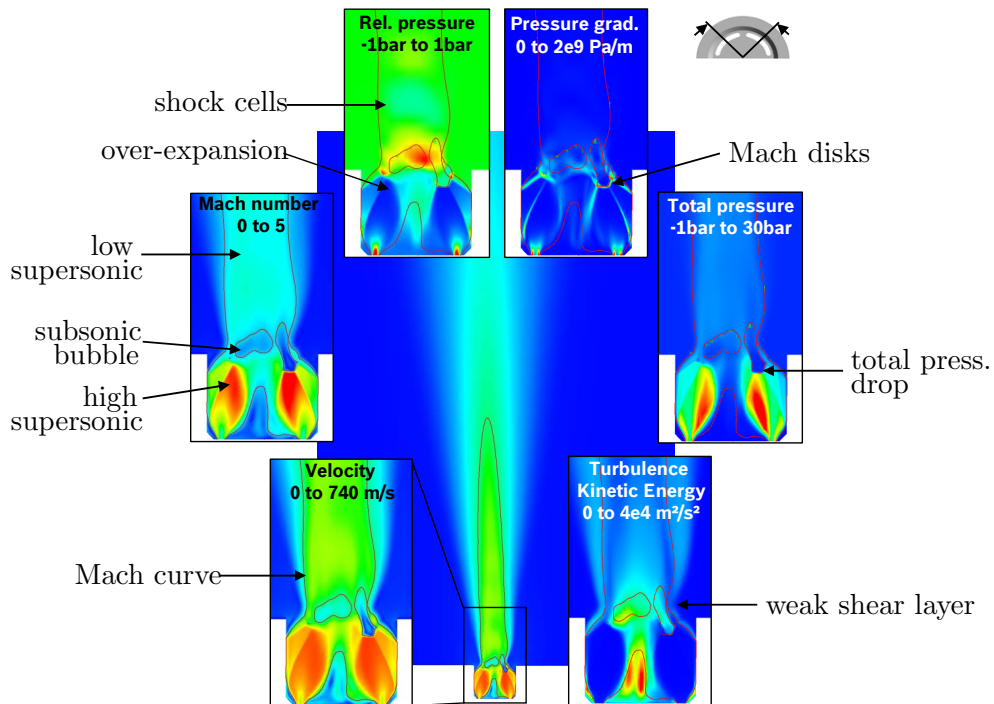
Figure 6.8: Steady freestream flow for increased mass-flow, simulation results

pliance with the CFL condition (2.36). In context of this work it provides a reference in conjunction with microphone measurements. Application of DES could save some computational costs but since the solution is known to be very grid-sensitive this approach is often avoided for aeroacoustics, likewise in this work. Last not least, SAS-SST is a novel approach aimed at wholly modeled broadband turbulence and a DES-like functionality. Owed to its novelty it is validated for just very few and mostly academic tests cases up to now, though. Especially no prior application to the aeroacoustics of supersonic jets or outside the CFL condition (2.36) is documented.

Applied to the injection problem the LES approach is very inefficient and expensive. The computational domain is small in dimension but the presence of much smaller shear layers and shock cell structures require a very dense mesh just in order to resolve the averaged flow. Since the corresponding grid spacing is just two orders of magnitude larger than the Kolmogorov scale, a LES simulation is quite close to DNS indeed – in terms of grid resolution and simulation costs.

But it is not just the large grid making aeroacoustic simulations expensive. It is also the combination of a small grid spacing ($\Delta x \approx 1.8\text{e-}5\text{m}$) and supersonic velocities ($U \approx 720\text{m/s}$) in the same places. Following the CFL condition (2.36) in order to avoid stability issues and operate the LES model within parameters this is leading to exceptionally small timesteps of $\Delta t = 2.5\text{e-}8\text{s}$. The consequential simulation costs inhibit prediction of emitted noise spectra

at the industrial scale. Using ANSYS CFX the computational costs are unaffordable 1400 CPUdays per millisecond simulation time. And actually more than a millisecond simulation time is necessary to deduce quality high-resolution spectra.

Furthermore the captured spectrum reaches up to $f_{max} = \frac{1}{2\Delta t} = 20$MHz. This is not just far above the audible spectrum aimed at but also far above the actual noise production range reaching up to approximately 45kHz. Hence, the small simulation timestep and the massive amounts of additional data are of no practical use for the aeroacoustics of such a component. Simulations within the CFL condition are not reasonable.

Solvers dedicated to this kind of applications should allow larger global timesteps in the first place and thus circumvent the CFL condition. Implicit solvers, as implemented in ANSYS CFX, actually allow this already. However, even though the solver numerics remain stable in the beginning, LES becomes essentially undefined and might result in earlier overflow in ANSYS CFX when the solver can not handle the non-linearities anymore. As the following sections will show, it exhibits increased noise levels before it eventually crashes. Time-averaging URANS on the other hand indeed allows a much larger timestep without experiencing stability issues or going into undefined state. Up to now no decent turbulence model was available providing broadband turbulence, though. Hence application to aeroacoustics was widely unthinkable, except for few enhancements such as SNGR for subsonic flows [9]. Now however the scale-adaptive turbulence models reveal a path for direct aeroacoustic noise simulations based on a URANS approach.

In fact, SAS-SST is meant to be run within the CFL condition as well. In contradiction to LES it just smoothly blends over to single-mode SST for larger timesteps, though, such that there is a trade-off between large timesteps and fast computation times on one hand, and sufficient captured turbulence scales on the other hand. No detailed information or publication on the actual influence of the timestep on captured turbulence and noise generation is available however. Thus, the solution quality of SAS-SST is assessed at various timesteps to identify a favorable setting for the injector application (Tab. 6.5).

Type	LES / SAS-SST (half-model)
Mesh	3.38 million hexahedra, 24% in sponge
Time[a]/-step	1 ms (0.5 ms) at $\Delta t = 2.5 \times 10^{-8} s \sim 5 \times 10^{-6}$s
Conditions	freestream, air into air at 1 bar, fixed inlet

[a]after convergence of transient statistics

Table 6.5: Freestream aeroacoustics simulation setup

6.4.1 Turbulence Structures

The smaller turbulence scales, inherent to non-audible very high-frequent noise, are mostly confined within the lower part of the jets (Fig. 6.9a). Naturally this is also the region where the SAS turbulence model breaks down for increased timesteps (large CFL in Fig. 6.10). Thus there is a substantial reduction of captured turbulence in the lower jet region for SAS-SST operation outside the CFL condition (Figs. 6.9(c) and (d)).

(a) LES, Δt=2.5e-8s   (b) LES, Δt =5e-7s   (c) SAS, Δt=5e-7s   (d) SAS, Δt=5e-6s
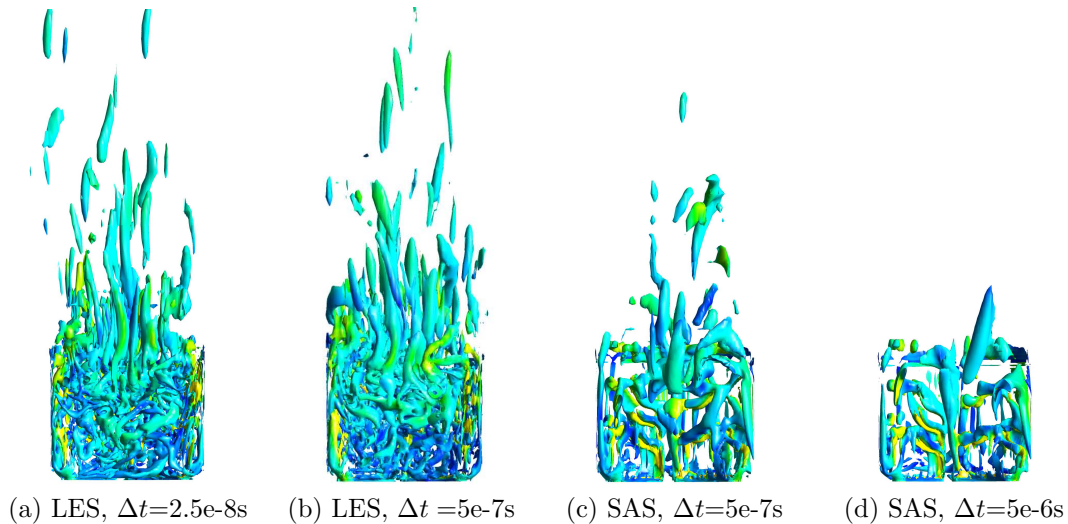
Figure 6.9: Influence of the timestep on vortical structures in the lower jet. shear strain rate invariant $3e11s^{-2}$, colormap: velocity $0..650$ms^{-1}
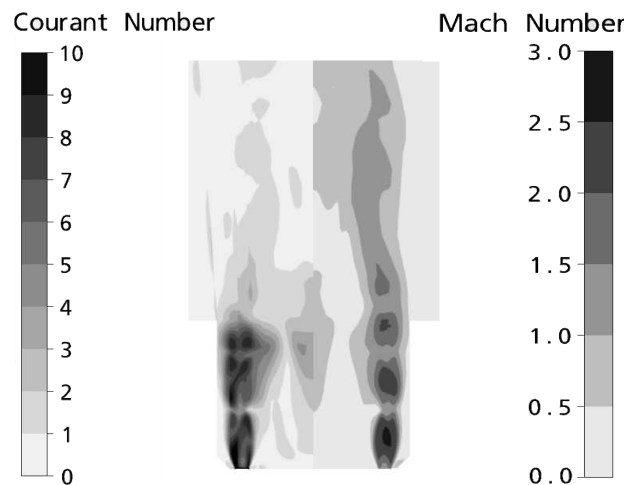
Figure 6.10: Local CFL and Mach numbers for SAS $\Delta t = 5$e-7s

Now, one could assume that these missing turbulences are negligible for aeroacoustics, as they are non-audible and seemingly not far propagating anyway. However they indeed influence the vortical structures throughout the computational domain (Fig. 6.11), even in regions

where the CFL condition is still completely satisfied (Fig. 6.10). For example, SAS with a very large timestep (Fig. 6.11d) shows just little more than the largest vortical structures downstream the injector: the vortex shedding from the injector rim and a few streamwise vortices. This is URANS behavior in a CFL < 1 region and essentially insufficient for aeroacoustics. Nevertheless those largest turbulence scales agree well with the structures visible in Schlieren photographs (Fig. 4.2).

Two separate causes for this impact on downstream turbulence can be identified. Firstly, eddies that are not captured upstream naturally cannot convect downstream and eventually become audible while growing in the shear layer. Secondly, the turbulence cluster between the jets is the driver of jet fluctuations (Fig. 6.12). Differences there affect and downstream unsteadiness, turbulence and noise generation, amongst others due to shock cell motion.

The effect of an increased SAS timestep on global turbulence levels is hard to predict. In particular, the maximum or average global CFL number, local CFL numbers in noise emitting regions or simply the impression global turbulence structures make cannot be employed as a direct measure for an adequate global timestep. New timestep studies might be necessary for varying applications.

(a) LES, Δt=2.5e-8s   (b) LES, Δt =5e-7s   (c) SAS, Δt =5e-7s   (d) SAS, Δt =5e-6s
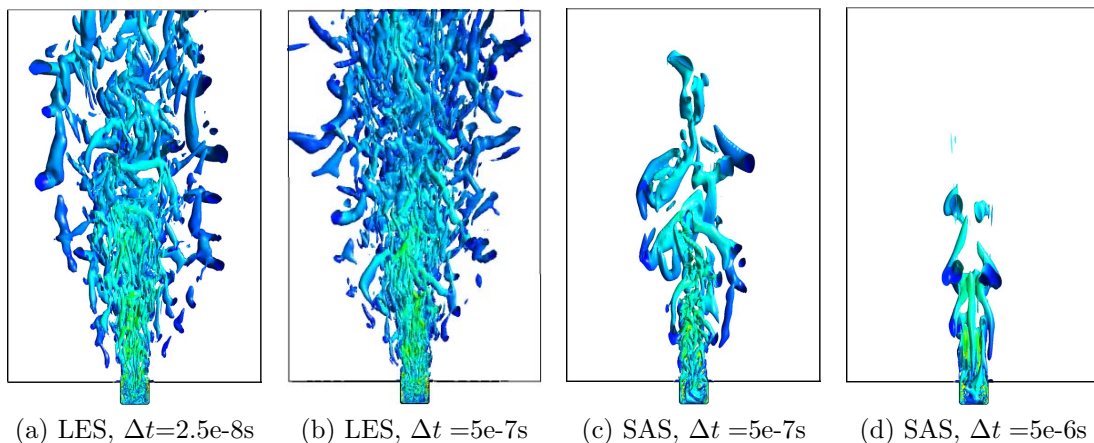
Figure 6.11: Vortical structures in the free jet. shear strain rate invariant $5e8s^{-2}$, colormap: velocity $0..650$ms^{-1}

In comparison, the LES simulation remains stable within a range of larger timesteps as well but produces noticeably more turbulence than the reference (Fig. 6.9b, Fig. 6.11b).

6.4.2 Sources of Noise

The Lamb vector fluctuation $L' = (\omega \times U)'$ is known to be the primarily contributing source term for turbulence related noise in subsonic and supersonic flows [39]. Hence it allows to locate the dominating sources of noise in a flow and enables source term coupling in the framework of hybrid methods.

(a) T_0 (b) T_0+1e-5s   (c) T_0+2e-5s   (d) T_0+3e-5s
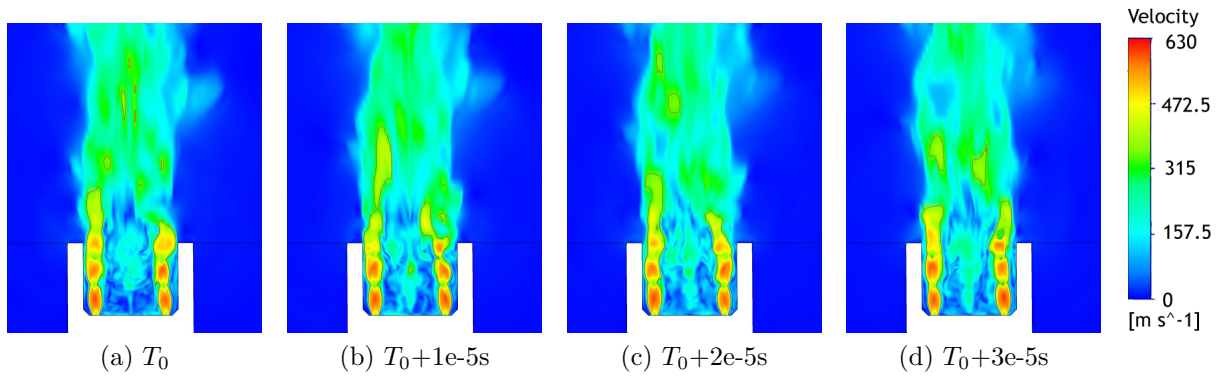
Figure 6.12: Instantaneous jet flow, LES at Δt =2.5e-8s

(a) T_0 (b) T_0+1e-5s   (c) T_0+2e-5s   (d) T_0+3e-5s
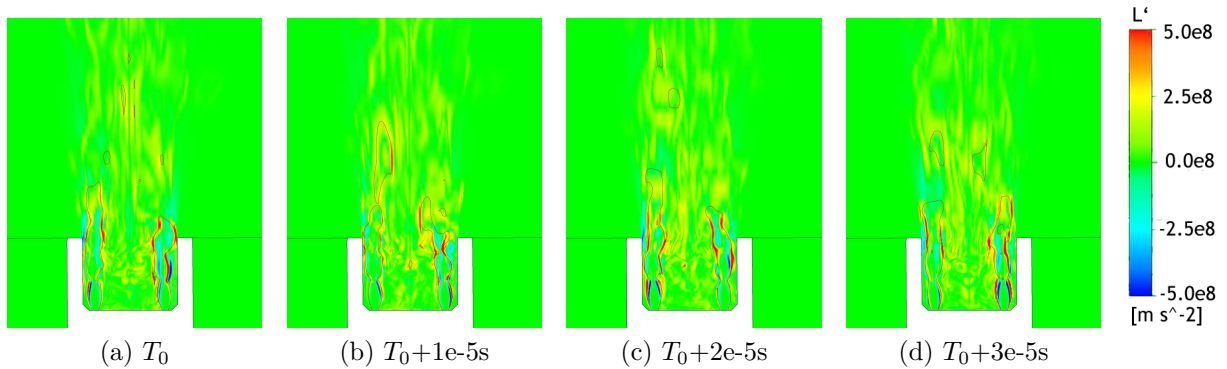
Figure 6.13: Instantaneous Lamb vector fluctuations, LES at Δt=2.5e-8s

During steady injection the strongest noise contributors are the shear layers between subsonic and supersonic flow regions (Fig. 6.13). Owed to strong jet fluctuations (Fig. 6.12) these sources fluctuate as well in terms of location and strength. The turbulence cluster between the jets and streamwise vortices leaving the shock damper (Fig. 6.9a) are weaker but noticeable sources of noise. Last not least, the turbulent mixing of the united subsonic jet is the by two orders of magnitude weakest noise producer.

Hence the dominating sources of noise are mostly located within or in close proximity to the shock damper and to supersonic flow regions. Furthermore supersonic 'bubbles' successively separate from the jets and convect downstream (Fig. 6.12). Nonlinear noise propagation and noise blocking by supersonic flow regions has to be expected. The base flow is heavily fluctuating as well. These are arguments against the application of hybrid methods based on volumetric source term coupling (Sec. 2.2.5). Direct simulation of the nearfield acoustics is essential instead, possibly with surface coupling to a CAA code in a hybrid framework.

103

6.4.3 Acoustic Field

After transient statistics converged and turbulence spread throughout the computational domain pressure fluctuations are captured for another millisecond simulation time (Tab. 6.5). This is about three times as long as an acoustic wave needs to propagate across the domain. In case of LES with Δt=2.5e-8s the simulation costs proved to be too high, though, such that the respective simulation time had to be limited to 0.5 ms instead. Consequently, validity as a reference is given for higher frequencies first of all.
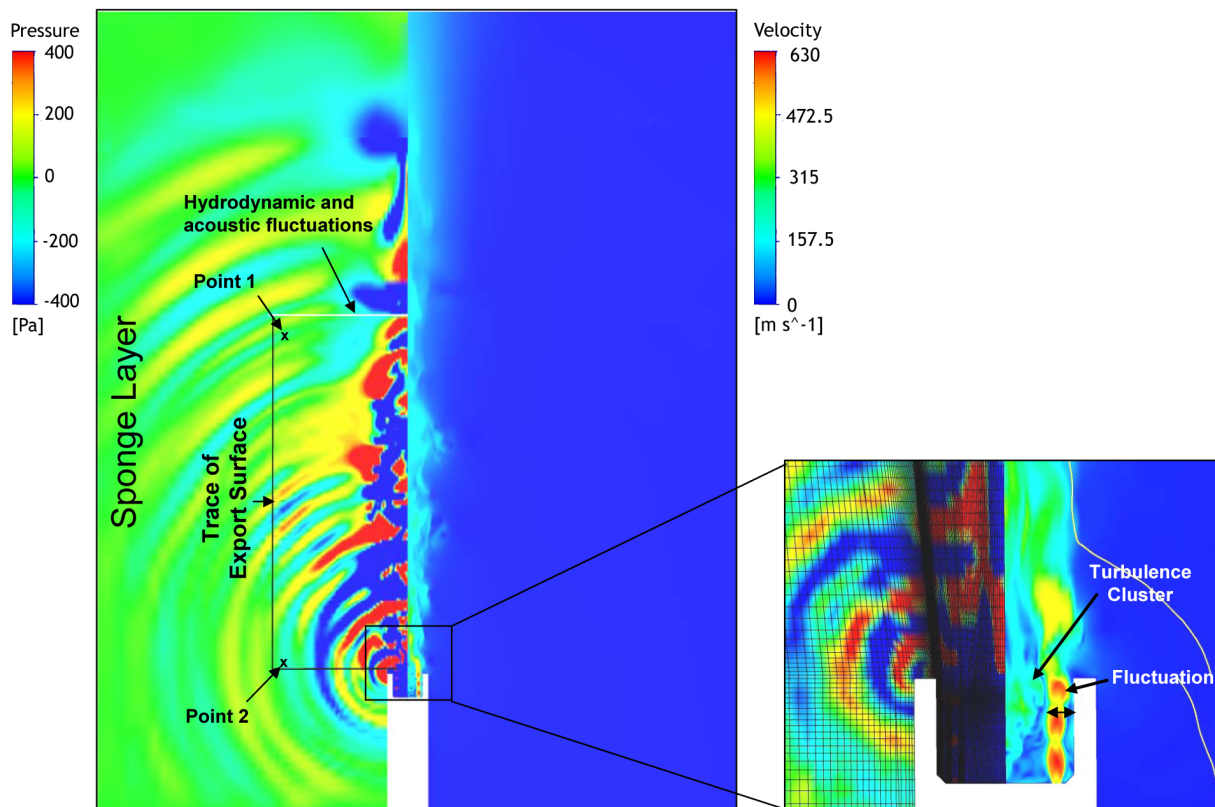
Figure 6.14: Instantaneous flow with export locations, LES Δt =2.5e-8s

The instantaneous flow image (Fig. 6.14) shows acoustic waves of reasonable amplitudes emanating from the injector where the strongest sources of noise are located. Application of the sponge layer effectively prevents reflections at the farfield boundaries without forcing of the inner flow. Direct simulation of noise with ANSYS CFX is enabled.

For further analysis transient data is exported in two points and in a cylindric surface around the jet (Fig. 6.14). The locations are chosen such that they are widely unaffected from hydrodynamic fluctuations (Fig. 6.11) but still close to the noise sources in order to keep numerical dissipation low. In the top plane of the cylinder (Fig. 6.14, coloured in gray) hydrodynamic fluctuations due to the passing jet and vortices cannot be avoided though.

Time Domain

The influence of the SAS timestep size on transient pressure fluctuations is assessed in point 2, lateral to the injection (Fig. 6.15). The focus is not on how well the curves match but rather on the general similarity, fluctuation amplitudes and sampling of the CFD exports as basis for a subsequent frequency analysis. In fact, erratic but representative portions of simulation and measurement data are compared to each other. Amongst others they contain beat in conformity with Schlieren images (Sec. 4.1.1). The microphone measurement performed in 60 cm distance is transformed using the $p' \propto \frac{1}{R}$ law for spherical waves emanating from the injector.
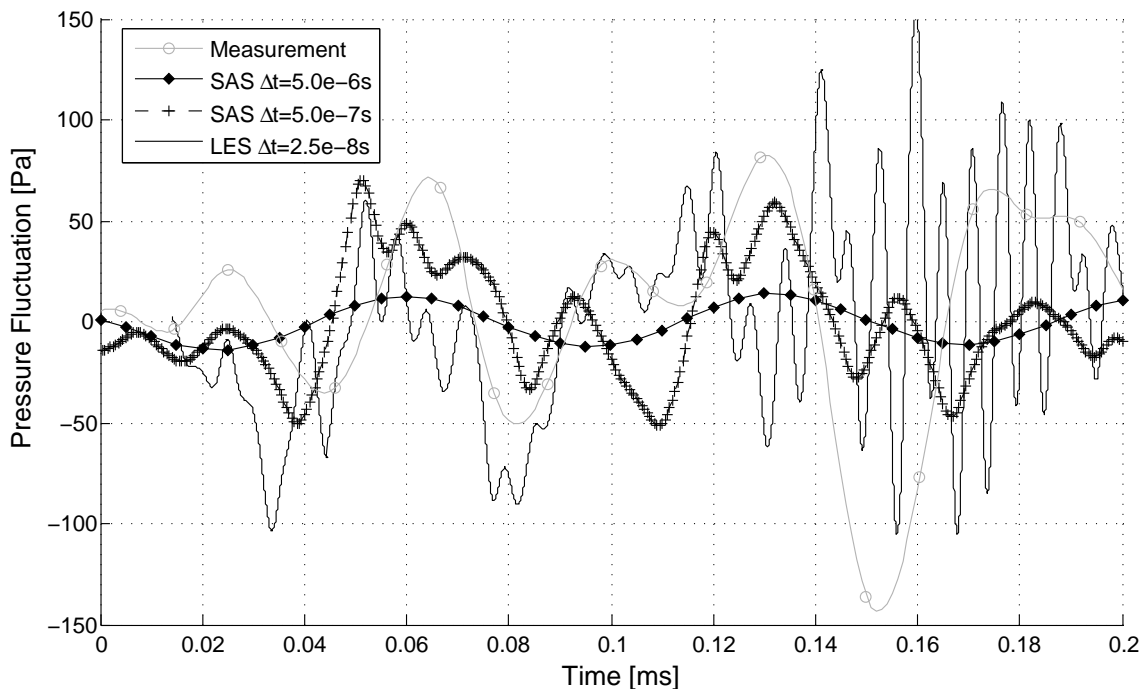
Figure 6.15: Pressure fluctuations in lateral direction, time response

Noticeable distinctions among the time responses can be observed. Starting with the measurement, it employs a low sampling rate and represents frequencies within the audible spectrum only. This can be considered the ideal from the acoustic point of view. There is no unnecessary data overhead. Non-audible frequencies are damped by the measurement equipment.

In contrast, numerical simulations exhibit the whole range of emitted frequencies, in case of the injector a range up to approximately 45 kHz. Hence a higher sampling rate of at least 100 kHz has to be chosen to avoid aliasing effects. Furthermore not just acoustics but also the source mechanisms and turbulences need to be resolved by the simulation. Respecting the CFL condition this requires a simulation timestep 2.6 orders of magnitude smaller than

necessary for just sampling the acoustics (LES curve). The simulation result is representative since it reflects the whole problem. The numerical overhead and simulation effort considering the objective to deduce the audible spectrum is immense however.

Since the grid spacing is fixed by the problem the timestep has to be increased in order to reduce the overhead and make simulations more efficient (SAS curves). The danger is however that even though the simulation produces converged results the governing noise source mechanisms are not captured correctly anymore and acoustic results become unrealistic. In SAS $\Delta t = $ 5e-6s, for example, the sampling rate is sufficient to resolve any acoustic fluctuation but the captured signal is very uniform and of low amplitude. An intermediate SAS timestep of $\Delta t = $ 5e-7s on the other hand has similarities with the measurement and seems to be a good trade-off between simulation effort and solution quality. Hence simulation overhead cannot be avoided completely but at least reduced within limits.

However, comparison of instantaneous images and short-term time responses cannot be employed to choose an appropriate timestep. Any choice will produce another captured frequency range and a different looking time response. Without changing over to frequency domain for representative simulation times it is impossible to say for which timestep the SAS simulation starts to be realistic for the objected audible noise.

Local Spectrum

Similar to the measurements the simulation exports in points 1 and 2 are converted into frequency space using Welch's method and a Hanning window in Matlab. The non-averaging periodogram function is employed instead for SAS $\Delta t = $ 5e-6s because of the unavailability of sufficient data. Actually, 1 ms simulation time is indeed too short to compute quality high-resolution spectra able to resolve tonal excitations. Here however measurements provide that there is just broadband noise and an approximate comparison is indeed possible for short simulation times as well.

Audible spectra in lateral direction are plotted in Fig. 6.16. Considering the fluctuation bandwidth of the measurement, both LES simulations match quite well with the measurement at high frequencies while SAS does a very good job throughout the spectrum for timesteps $\Delta t \leq $ 1e-6s. In fact, the SAS simulation with $\Delta t = $ 5e-7s yields almost perfect results regarding the spectrum as well as the OASPL.

The most decisive difference among the SAS simulations is the deviating shape of the $\Delta t = $ 5e-6s curve. This is only a prominent example of a general trend and more accentuated due to missing averaging though: The larger the timestep is chosen the more the spectrum is underpredicted in the range between 4 and 10 kHz and overpredicted at the main vortex shedding frequency around 14 kHz. Furthermore a distinct interference pattern devel-
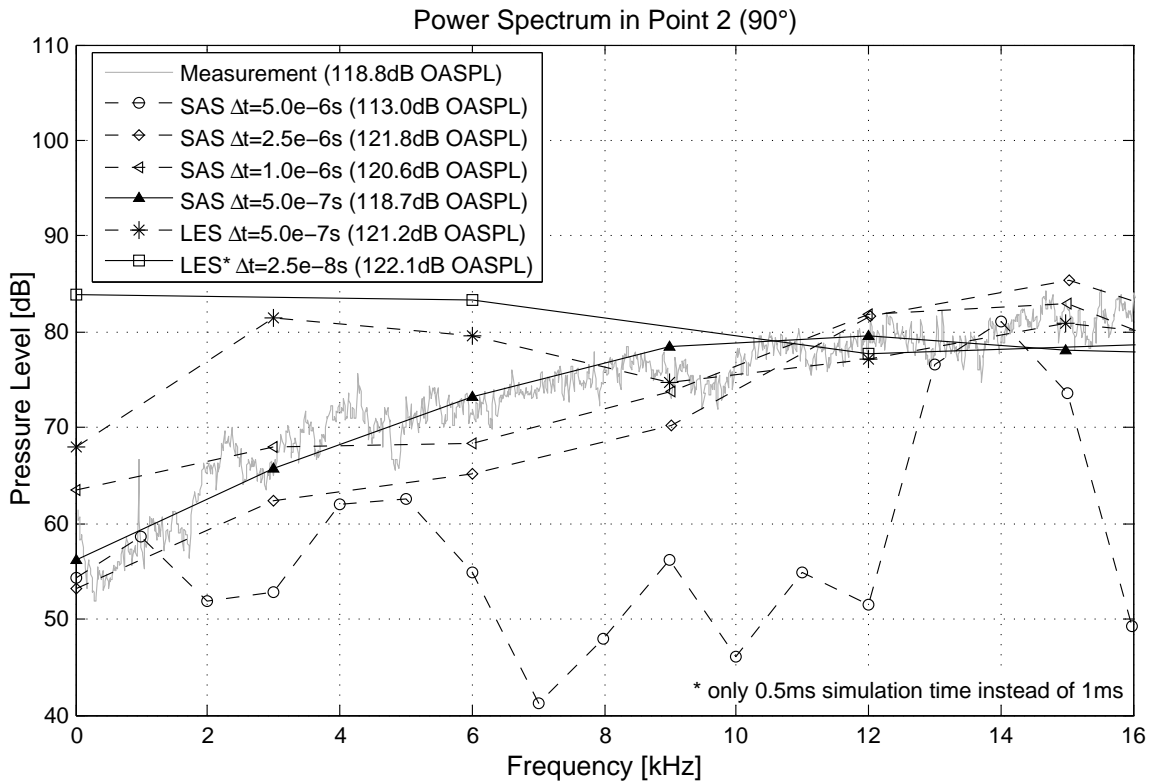
Figure 6.16: Freestream power spectra in lateral direction

ops since the jets increasingly fluctuate in a single dominating frequency only. Indeed point 2 is located in a direction where noise is canceled such that the peak of the SAS $\Delta t = 5e$-6s curve coincidentally agrees with the measurement (Fig. 6.16).

In point 1, just 18° to the jet axis, low-frequent content is more pronounced (Fig. 6.17). In spite of the short simulation time the SAS simulations agree quite well with the measurement for timesteps $\Delta t \leq 2.5e$-6s. Clipping and underprediction of the camber in the lower half of the spectrum break down to lower simulated OASPL though. In consistency with most of the domain the peak of the SAS $\Delta t = 5e$-6s curve is reasonably above the measurement. The LES simulation with a larger timestep exhibits increased noise levels at high frequencies and has problems to reproduce the spectral distribution.

Directivity

The noise directiviy is assessed at 60 cm distance to the injector. The simulated pressure fluctuations are exported in a cylindrical surface around the jet (Fig. 6.14), transformed into frequency space just like before, averaged over all nodes with similar angles to the jet and converted to measurement distance using the $p \propto \frac{1}{R}$ law for spherical waves.

In the alternative framework of a surface coupling hybrid method the exported data can be
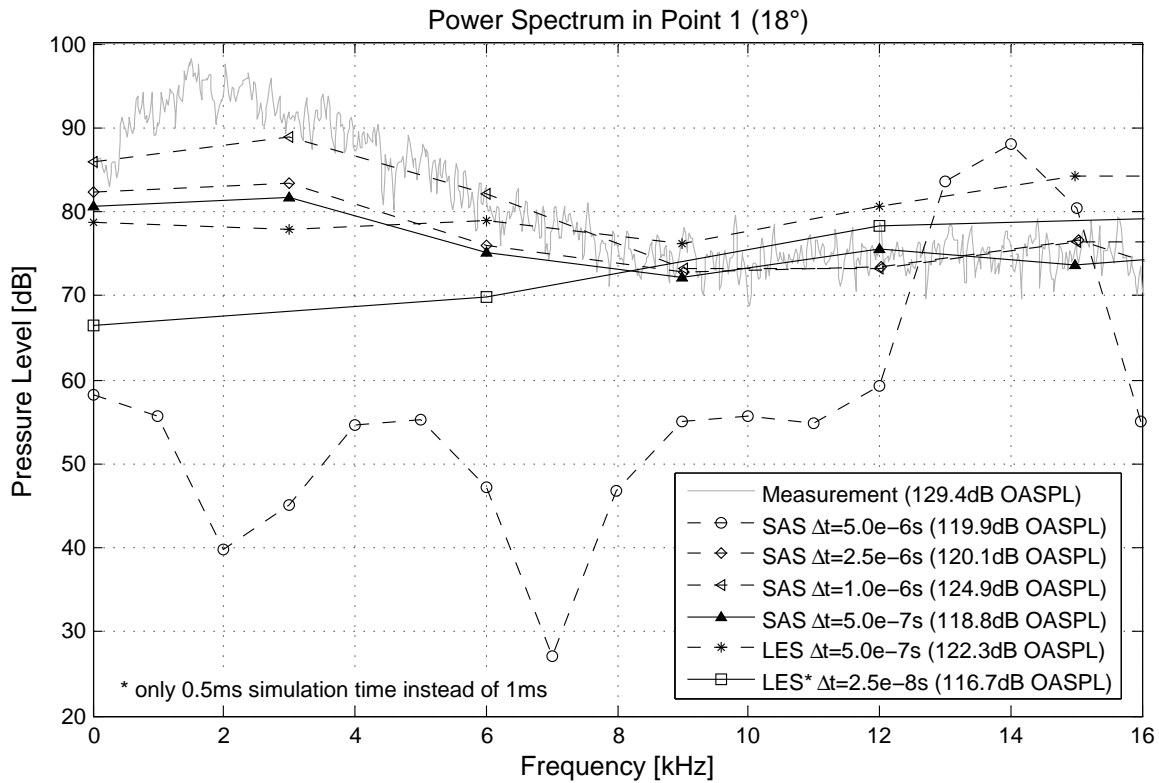
Figure 6.17: Freestream power spectra in 18deg to the jet axis

directly fed into a (commercial) tool dedicated to acoustic propagation, e.g. based on 3D-BEM. Here, LMS Sysnoise exhibits unreasonably large memory requirements and computation times to determine the acoustic farfield and noise directivity, though. Furthermore, data conversion and the noise source definition is difficult in particular. Sysnoise requires either acoustic dipoles in the BEM surface (representing a vibrating body surface, not applicable here), an acoustic quadrupole distribution within the enclosed domain (using an acoustic analogy to compute potentials of the BEM elements, not applicable here according to Sec. 6.4.2) or hardly documented libraries which then contain the complete fluctuating flowfield. The latter approach is the only feasible way but requires to handle huge amounts of data and build the libraries manually in preprocessing. Since this is not efficient and just simple wave patters emerge the analytical solution is preferred instead.

The *spectral directivity* (Fig. 6.18a) matches well with the measurements (Fig. 4.13), especially in lateral directions. The tendencies of reducing high-frequent noise and increasing low-frequent noise for lowered angles down to 60° is reproduced correctly as well. However, the smaller the angle to the jet axis becomes, the more deviations between transformed nearfield data and measured farfield data arise. Low frequencies are over-predicted while high frequencies are under-predicted, probably due to superposed hydrodynamic fluctuations (pseudo-sound). The simulation exports are locally correct as the local comparison in the two points

(a) spectral directivity for SAS Δt=1e-6s (b) OASPL directivity
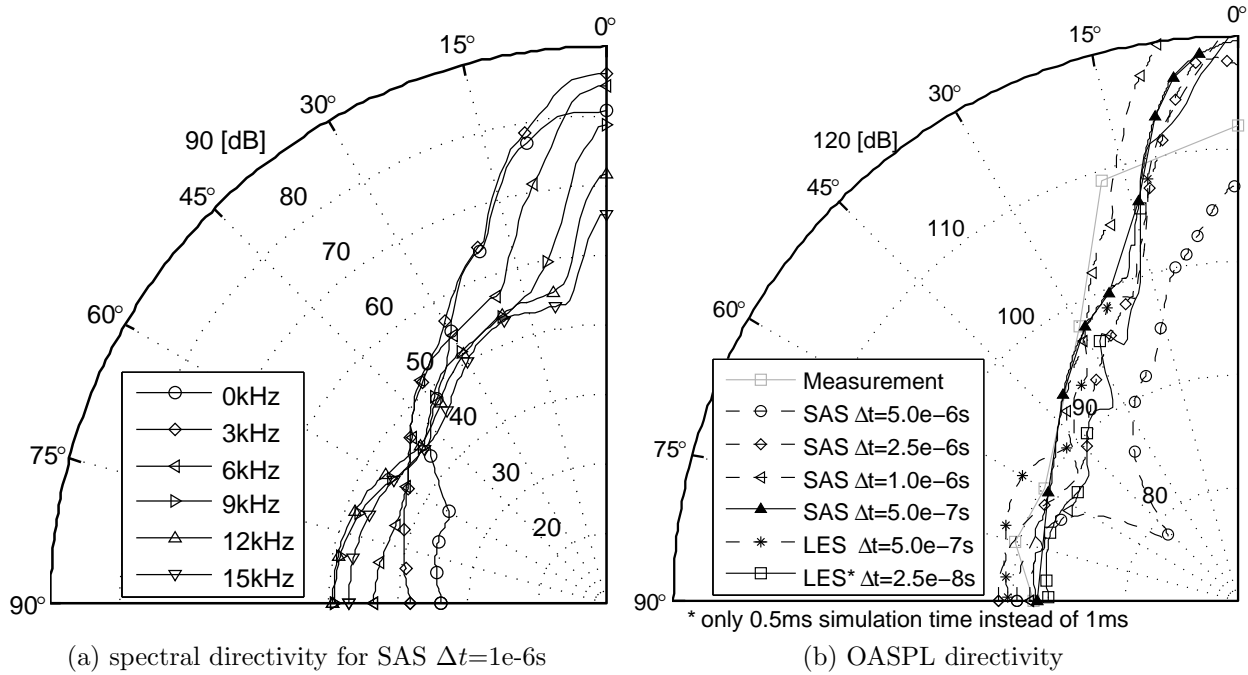
Figure 6.18: Freestream directivity in R=60cm

showed. Hydrodynamic contributions have a stronger decay law for propagation into the farfield than applied though (Sec. 2.1.2). A better prediction would require to filter the data, employ correlation techniques or place the export surface farther from the jet.

The *OASPL directivity* (Fig. 6.18b) is globally under-predicted rather than over-predicted, for one exception: In jet direction hydrodynamic fluctuations due to passing jet and vortices cause pseudo-sound and increase noise levels again. For this reason the near field measurement in point 1 is converted into farfield and added to the figure as reference. The under-prediction comes from the low spectral resolution and clipping mentioned before in the first place. Still SAS simulations with $\Delta t \leq$ 1e-6s yield good results. For larger timesteps the failing turbulence model results in a further notable noise level reduction and an interference pattern emerges, amongst others with noise cancellation in 45° to the jet axis.

6.4.4 Computational Costs

In a direct comparison for the same mesh and timestep SAS is approximately 42% more expensive than LES (Fig. 6.19). This is due to the more sophisticated SAS-SST turbulence model which is more costly to evaluate. Two more PDEs have to be solved (turbulence model), L_{vK} needs to be computed (variable update) and the modeled turbulent viscosity is eventually to be determined for the time-averaged conservation equations (momentum and mass). This additional effort for SAS has to be compensated at first before a further increased timestep

(or coarsened mesh) can result in an actual computational cost advantage. The LES subgrid model on the other hand is little more than a filter and therefore not explicitly listed in the expense analysis.
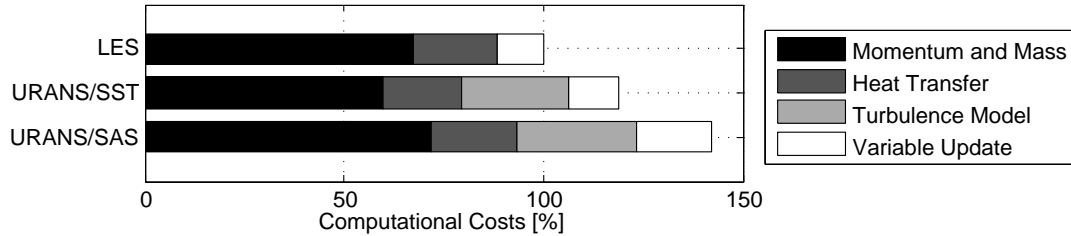
Figure 6.19: Computational costs analysis for LES and SAS

However there is another numerical effect diminishing the benefit gained by large global timesteps. In the framework of the implicit ANSYS CFX solver each timestep is iterated in so-called coefficient loops such that all governing equations are successively linearized and evaluated over and over again. Here small timesteps are privileged: They converge in just a few iterations while large timesteps often exhaust the preset maximum number of iterations. Still, considering a timestep increase by a factor of 40 a net speed-up over LES by a factor of 19 remains (Fig. 6.20).
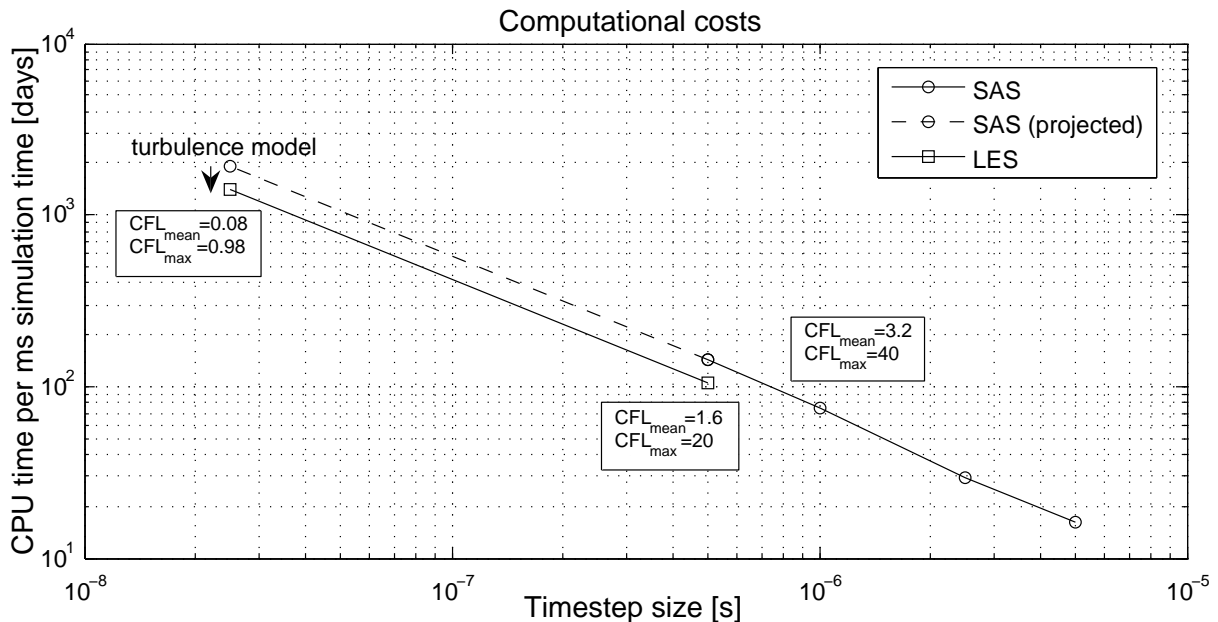
Figure 6.20: Computational costs in dependency of time stepping, measured on 4 nodes (16 processors, 32GB RAM) of a AMD Opteron 2218 (2.6 GHz) cluster

6.5 Summary

Apart from its primary application as a LES and DES replacement with reduced grid resolution requirements and sensitivity the SAS turbulence model is validated to be run outside the CFL condition. In fact, it proves to be a fast and robust way for the direct simulation of the aeroacoustics of the gas injection problem. Even more, the results in terms of acoustic spectra agree quite well with the measurements.

There is a trade-off between a large simulation timestep and representative aeroacoustics however. A significantly degrading solution quality has to be considered for strongly increased timesteps. Guidelines for the prediction of the optimum timestep, e.g. with respect to the global CFL number or short-term fluctuations, can not be generalized. Hence new timestep studies might be necessary for varying applications.

For the gas injection problem a timestep increase by a factor of 40 to $\Delta t = 1e\text{-}6$s proved to be feasible with passable loss of information. After consideration of all effects a noticeable net speed-up by a factor of 19 remains. The resulting simulation costs of 78 CPUdays per millisecond simulation time become eventually affordable on current parallel computers but are still too high for optimization purposes.

Grid optimization for a URANS approach could create some more benefits. Further significant improvements seem to be limited without changing over to solvers employing a localized approach, though. Strongly varying local CFL numbers (Fig. 6.20) imply the possibility of a reasonable advancement by local timestepping for example. This however would require wholly new solver architectures which are unlikely to be implemented within ANSYS CFX in foreseeable future. Nevertheless, this is pursued in Chap. 8 by the means of a research code.

Several noise reduction principles are applied to the gas injector, first of all corrugated jets and distributed exhausts (Sec. 3.4). Besides the shock damper seems to have a positive effect, at least for freestream configuration and stationary injection. Considering pulsed injection however the formation, presence and fluctuation of shocks might be a reasonable noise contributor as well.

Chapter 7

Intake Manifold Configuration Simulations

Based on the results gathered in the preceding chapter simulations are performed for the intake manifold configuration and for varying injection parameters (injection angle, engine load, rpm). Since strongly coupled near- and farfields as well as nonlinear noise propagation have to be considered integral methods and most hybrid approaches are not applicable. The whole intake manifold is simulated at once and in a single tool instead. Here ANSYS CFX with SAS-SST turbulence modeling allows a noticeable simulation costs reduction and thus enables the parameter studies in this chapter in the first place.

Next to a better understanding of the emerging flow and acoustic phenomena during pulsed injection within the intake manifold, the objective is to test the aeroacoustic simulation methodology for a realistic problem featuring a confined environment and varying boundary conditions. Thermal absorption imaging and wall pressure measurements (Sec. 4.2) enable the validation of the numerically predicted flow and acoustic sensitivities. Two simulation approaches are pursued: A segregated approach analog to the freestream configuration allows to investigate the injector opening, steady-states and understand the preceding simulation results (Sec. 3.6) separately at first. Then the combined approach for half an injection cycle will lay the focus upon the influence and contribution of the opening pressure wave on the steady injection noise levels.

7.1 Solution Approaches

While the problem geometry and injector placement coincide with the preceding simulations (Sec. 3.6) some reasonable changes have been made to enable aeroacoustic simulations and obtain results with more practical relevance (Fig. 7.1). Thus, direct comparison to former results is not given anymore. The changes are:

1. The upper part of the combustion chamber and inlet valve are attached to allow acoustic reflections at the inlet valve.

2. Sponge layers are attached at the air inlet and outlet to avoid acoustic reflections at the
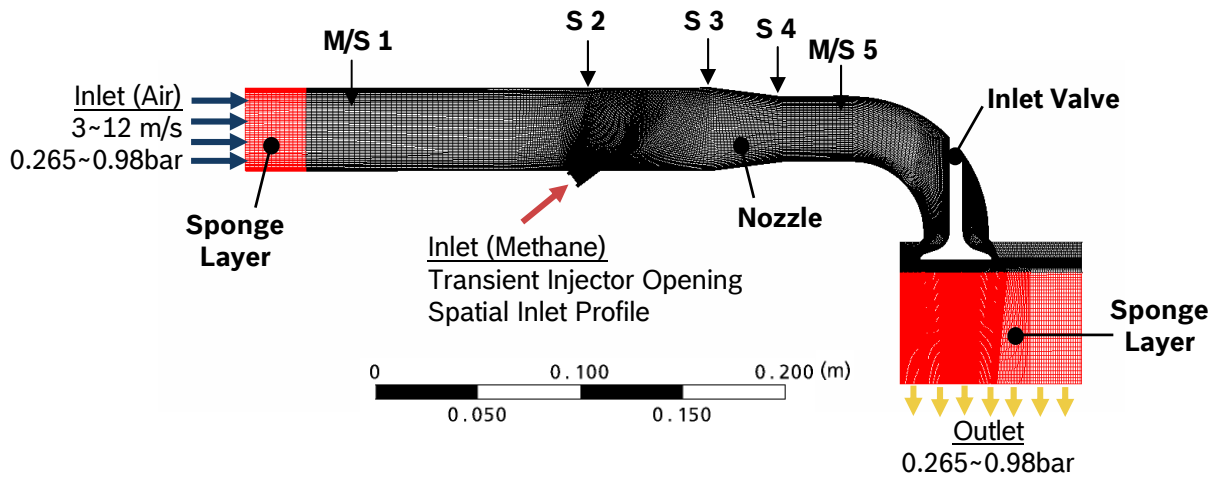
Figure 7.1: Intake manifold simulation setup

open numerical domain boundaries.

3. The mesh is globally refined, in proximity of the jet to a level similar to freestream configuration. It now comprises 1.8 million hexahedra. Due to an optimized blocking the refinement does not carry on throughout the domain but is limited to the proximity of the jet. As a drawback a worse local aspect ratio, skewness and growth rate add to the potential for numerical instabilities.

4. Transient injector opening and a spatial inlet profile rather than a time-constant and uniform distribution are employed at the gas inlet.

5. The working conditions are changed in conformance with an actual natural gas engine (Tab. 4.4).

For the sake of simplicity the same mesh is employed for every working condition. It is just adapted to varying injection angles respectively. Transient wall pressure fluctuations are logged in the five marked points (Fig. 7.1). Two of those, the one upstream and the farthest downstream of the injector with respect to the cross-flow, coincide with locations measurements are taken in (Sec. 4.2.3). The other export points are located in between, partially in proximity of stagnation points. Post-processing is performed with dedicated Matlab routines programmed by the author again.

Two distinct approaches are pursued for simulation of the intake manifold acoustics (Fig. 7.2). Firstly, this is a segregated approach adopted from the freestream simulations. Here however the separation of opening and steady injection acoustics proves to be very expensive. The strong sound waves emerging during injector opening are just weakly damped, constantly reflected within the intake manifold and seemingly exciting the jet. The result is a very bad convergence towards the steady state and thus high computational costs for just an

Computational costs*
per working condition

| Mesh |

Cross-flow initialization
(CFX-RANS) — Order of CPUhours

Injector opening
(CFX-URANS) — 185CPUdays/5ms

Steady state
(CFX-RANS) — Order of CPUmonths / Bad Convergence

Turbulence, acoustics
(CFX-SAS) — 224 CPUdays/5ms

Data export and
post-processing

Manual Step
Simulation

(a) segregated approach

Computational costs*
per working condition

| Mesh |

Cross-flow initialization
(CFX-RANS) — Order of CPUhours

Combined Simulation
of half injection cycle
(CFX-SAS) — 224 CPUdays/5ms

Data export and
post-processing

Manual Step
Simulation

(b) combined approach

Figure 7.2: Approaches for intake manifold simulations; *measured on 4 nodes (16 processors, 32GB RAM) of a AMD Opteron 2218 (2.6 GHz) cluster

intermediate step in the course of action. Furthermore it is unknown in how far the opening pressure waves are part of the aeroacoustic system and affect the steady injection acoustics in the practical application. Therefore the second approach captures the combined opening and steady injection acoustics in a single SAS simulation. This reduces the computational costs and the effort setting up the simulations reasonably.

In either way, the cross-flow and pressure within the intake manifold are converged in separate simulations at first representing the working condition before the actual aeroacoustic simulation is conducted. On the one hand this agrees better with the test rig mode of operation (Sec. 4.2.1). On the other hand poor initialization with uniform horizontal velocity throughout the domain in conjunction with fully reflective boundaries is identified as the cause of immediate acoustic reflections with amplitudes exceeding 15 kPa in the preceding simulations (Sec. 3.6).

7.2 Injector Opening

In order to assess the sponge layer function, the influence of broadband turbulence on the opening acoustics and the processes during transient jet formation, the first milliseconds of an injection cycle are simulated in two ways: On one hand the sponge layer is disabled in a URANS/SST simulation (Fig. 7.2a), on the other hand the sponge is enabled in a SAS-SST

simulation (Fig. 7.2b). The former can also be seen as the attempt to improve the results of the preceding simulations (Sec. 3.6) just by better flow initialization.

Type	transient URANS
Turbulence model	SST, SAS-SST
Mesh	3.14 million hexahedras, 8% in sponge
Time/-step	5 ms at $\Delta t = 10^{-6}$s
Conditions	intake manifold, methane into air injection for WC2 (Tab. 4.4), transient inlet, enabled/disabled sponge layers

Table 7.1: Injector opening simulation setup for intake manifold simulations

Analog to the freestream configuration the injector opening in intake manifold configuration is governed by the formation of specific flow and turbulence structures owed to fluid displacement and acoustic emission due to the pressure release.

Flow and Turbulence

In the early stages when the jet is still weak the injected fluid undergoes highly turbulent fluctuations. The cause can be traced back to flow separation and recirculation within the cavity the injector is attached to owed to the cross-flow. Furthermore nearby walls and cross-flow result in unsymmetric propagation of sound waves (Fig. 7.3a) and entrainment vortices (Fig. 7.3b).

While the injected mass-flow grows the flow within the shock damper stabilizes and the jet draws more and more air (Fig. 7.3c). The cross-flow has to bypass the jet such that it aligns to the downstream side of the jet in this configuration. The result is further reasonable unsymmetry of jet and turbulence.

The entrainment vortices propagate on and are increasingly deformed by the cross-flow (Fig. 7.3(d) -(e)). However they do not dissipate completely nor do they leave the domain. They remain stuck at the nozzle and dominate the steady state instead.

The shape and complexity of the emerging flow and vortical structures is highly dependent on the working condition. The acoustic waves do not have visible influence on the flow on the other hand. In particular, no flapping jet is observed (Sec. 3.6). The influence of the WC on the averaged steady state is further detailed in Sec. 7.3.

Acoustics

Due to reflections and feedback within the confined environment of the intake manifold configuration the noise propagation deviates reasonably from the freestream configuration. A spherical pulse is emitted again but cannot leave the computational domain (Fig. 7.4). It

(a) pressure, t=5e-5s   (b) velocity, t=4e-4s   (c) velocity, t=8e-4s

(d) velocity, t=3e-3s   (e) velocity, t=3.5e-3s
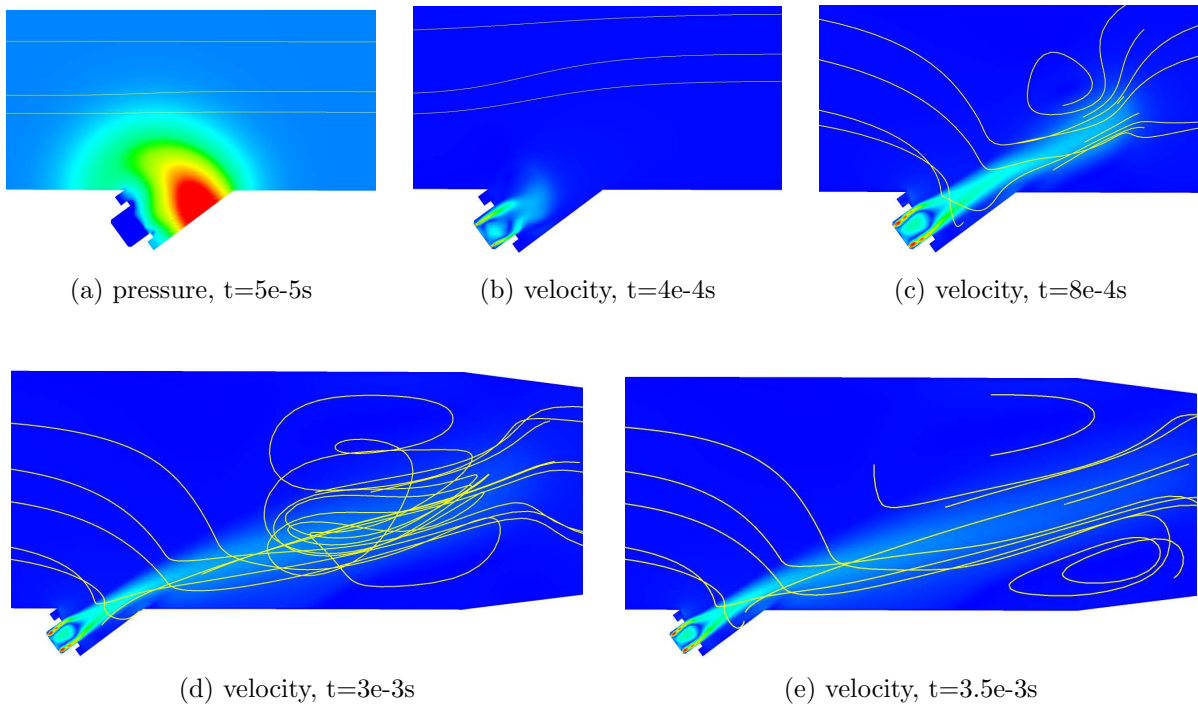
Figure 7.3: Transient injector opening in intake manifold configuration

is reflected at the walls forming a plane wave followed by higher-order duct modes instead (Sec. 3.3.2). Furthermore any incident acoustic wave is partially reflected at the opened inlet valve. The result is a phase shift and a reverse propagation direction.
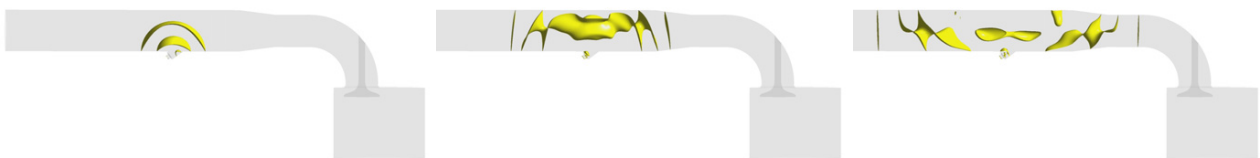
Figure 7.4: Formation of duct modes during injector opening (pressure isosurfaces); images taken at 1e-4s+i*1.5e-4s (left to right)

In agreement with measurements (Sec. 4.2.3) the propagation of the primary pulse is widely symmetric to the injector location at first. The displacement effect due to the base flow is weak. The pulse is just somewhat stronger in injection direction (Fig. 7.5).

At around 1.1 ms the primary pulse is reflected and inverted at the inlet valve. Then it reaches W/S 2 at approximately 1.4 ms leveling the preceding pressure increase. It passes the jet exciting it by a pressure drop and thus causing a secondary pulse. Finally it reaches W/S 1 at around 2 ms. Here the different air inlet boundary condition starts to take visible effect: In the SAS simulation the passing pulse lowers the pressure before it propagates on and is damped within the sponge. In the SST simulation on the other hand the air inlet behaves
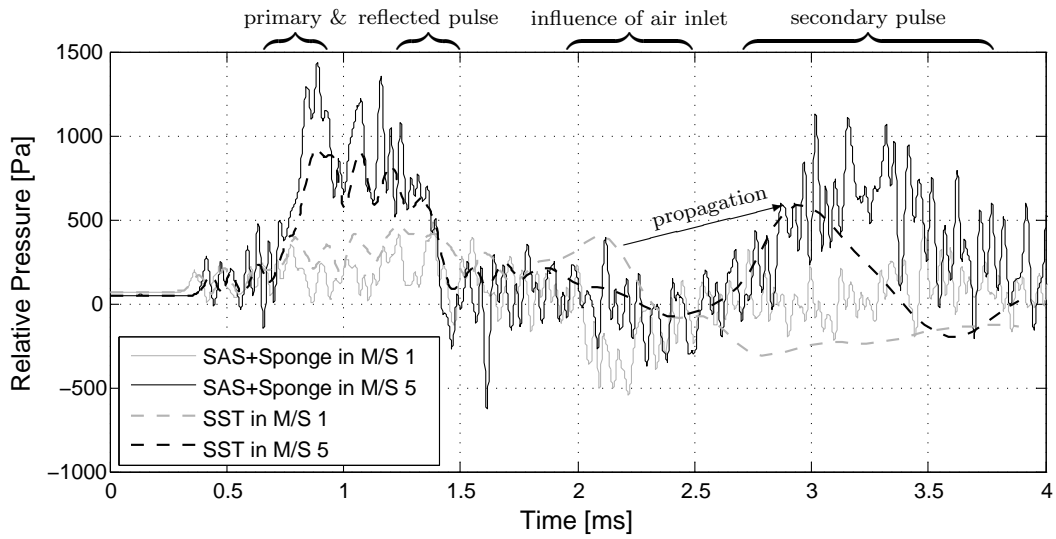
Figure 7.5: Injector opening aeroacoustics: sponge layer function, broadband noise vs. single mode noise

like a wall. The pressure increases and the pulse is reflected, propagating along the duct and interacting with the jet once more. The sponge layer seems to effectively prevent reflections at the air inlet and to produce better and more realistic results compared to measurements. The interaction of the opening acoustics with the jet seems so be a reasonable noise contributor as well.

Since the pulse is driven by pressure release rather than turbulent flow the SAS simulation results in a broadband modulation of the SST baseline (Fig. 7.5). The processes during injector opening can be assumed to be similar for all working conditions and just varying in pressure amplitudes. Since the emerging wave lengths are small in comparison to the duct diameter the duct nozzle has minor influence on the duct acoustics.

Mode (m,n)	f_{mn}
(1,0)	4.9 kHz
(2,0)	8.3 kHz
(3,0)	11.4 kHz
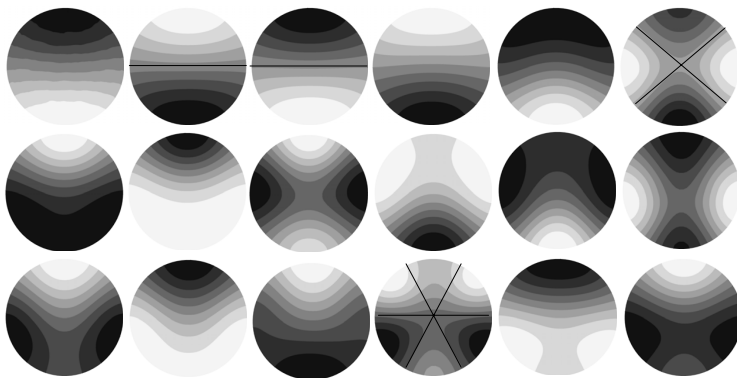
Figure 7.6: Duct modes during injector opening; images taken at 4e-4s+i·5e-5s (left to right)

Table 7.2: Cut-off frequencies for emerging duct modes

The relative pressure distributions in the domain interface to the inlet sponge (Fig. 7.6)

visualize the emerging duct modes. Within the first millisecond there are neither radial (n is always 0) nor spinning modes (pressure distribution is always symmetric to vertical axis). The images just show superpositions of modes of up to third circumferential order. Even higher order and radial modes emerge and modulate the pressure field over time. Spinning modes are still not identified.

Duct modes are subject to a cut-off condition Eq. (3.11) below which they cannot propagate. For the dominating modes present in this problem this requires minimum frequencies as listed in Tab. 7.2. Below those frequencies the noise level can be expected to be reduced noticeably.

7.3 Parameter Variation

The cause-effect relationships are determined for varying working conditions (Tab. 4.4) and injection angles (37° and 90°) and in terms of the arising averaged stationary flow as well as actual aeroacoustics. WC2 compares best to the freestream configuration due to a comparable ambient pressure and just low cross-flow. Nevertheless the confined environment causes new vortical structures to emerge (Sec. 7.2). In comparison, WC1 represents the influence of lower ambient pressure and WC4 the influence of a stronger cross-flow. Last not least the fourth corner of the engine's working envelope (WC3) features both, lower ambient pressure and stronger cross-flow (Tab.4.4).

7.3.1 Averaged Stationary Flow

Weakly damped plane waves arise during injector opening and prevent fast convergence of the fluid-dynamic steady-state. They cause further flow eruptions each time passing the jet. The sponge layers are ineffective since they do not prevent reflection at the inlet valve. In the worst case the fluctuations are even intensified causing instability. Indeed the respective RANS simulation costs can exceed the costs for the actual aeroacoustic simulation making this approach questionable for low pressure WCs in particular.

Instead of an initialization with the preceding opening simulation results (Fig. 7.2a) it rather proved feasible to start over from the initialized cross-flow. Then the jet is smoothly and slowly powered up within 300 timesteps by the definition of a new transient inlet in dependency of the accumulated timestep.

$$\text{current profile} = \text{steady-state profile} \cdot \left(1 - \exp \left(-\frac{\text{acc. timestep}}{500 \cdot \exp(-\frac{\text{acc. timestep}}{100})} \right) \right) \qquad (7.1)$$

In combination with a very large timestep of at least $\Delta t = 1e\text{-}5$s in the beginning this helps to smear and weaken the plane waves sufficiently and allow convergence for all WCs and in spite

of disabled sponge layers. Still, this approach is expensive since the damping of fluctuations remains weak and the timestep cannot be chosen too large for stability reasons once the jet Mach numbers become larger.

(a) WC1/37°   (b) WC2/90°   (c) WC2/37°
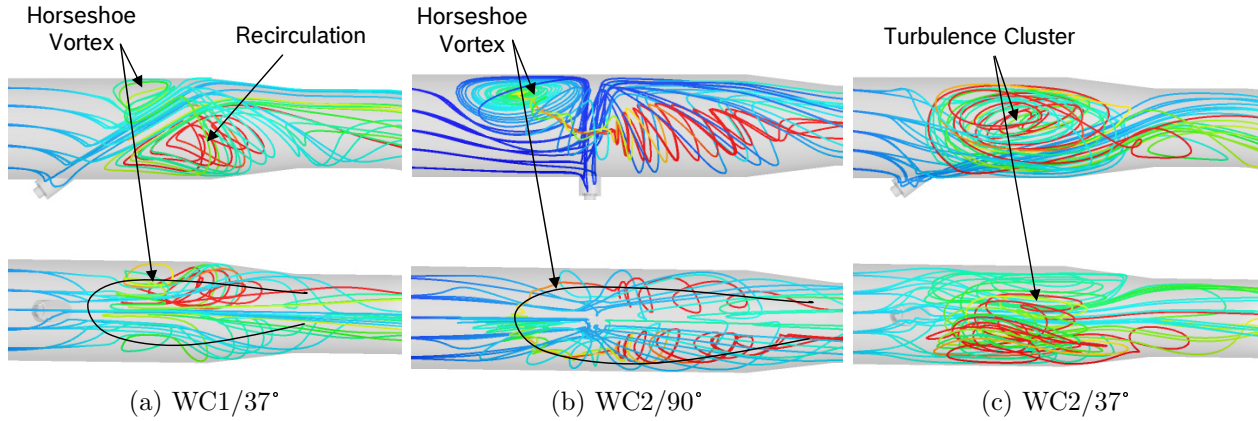
Figure 7.7: Global flow structures, 3D streamlines, colormap: time on streamlines

Compared to the freestream configuration new characteristic flow structures emerge in dependency of the working conditions (Fig. 7.7). This comprises the known structures for a jet in cross-flow (Fig. 3.1) combined with structures related to the confined environment and impingement. For example, an additional horseshoe vortex around the impingement location forms (Fig. 7.7a). For strong jets and perpendicular injection it can even grow so large that it dominates the whole intake manifold flow between jet and nozzle by a strong counter-rotating vortex pair (Fig. 7.7b). Furthermore the entrainment vortex generated during powering the injector up does not leave the domain but may be stuck in front of the nozzle instead as long as the cross-flow is not too large. For non-impinging jets (WC2/37°) this vortex can grow over time and eventually dominate the flow in proximity of the jet with noticeably amounts of injected fluid flowing upstream the intake manifold (Fig. 7.7c). The bend always straightens out the flow.

The averaged flowfield is hard to capture by measurements due to the highly unsteady and three-dimensional flow and the small and confined environment. Hence a secondary effect of the flow and large-scale turbulence, namely the mixture homogenization, is employed for validation instead. The simulation of a two component gas (methane injection) allows direct extraction of the local mass fraction of the injected gas. Thermal absorption imaging produces an integral picture of the mass fraction for carbon dioxide injection (Sec. 4.2.2). The different injected media should not alter flow structures and Mach numbers reasonably. Just the difference in molar masses will scale the velocity.

Indeed, a distinct mixing adjusts for each working condition and in simulation as well as measurement respectively (Fig. 7.8). Especially the mixing enhancement accompanied to the
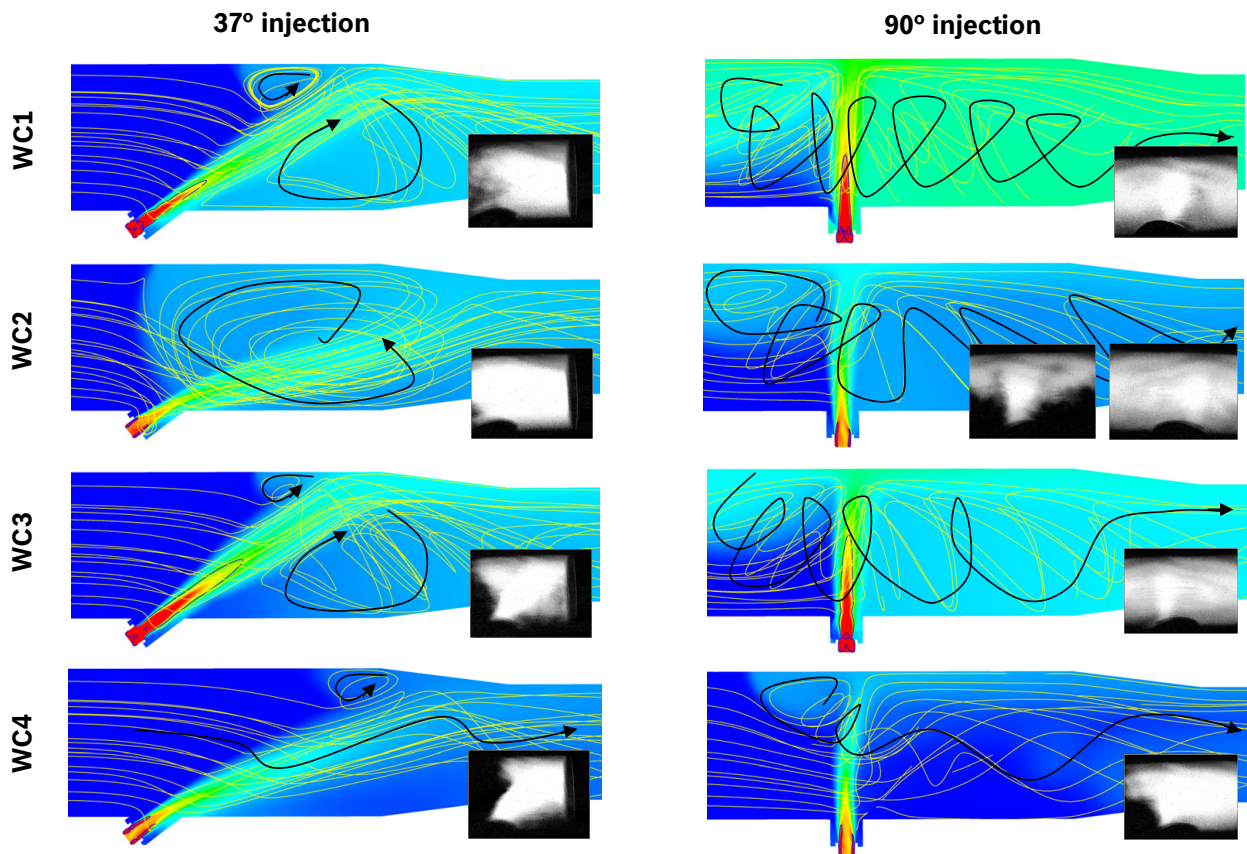
Figure 7.8: Steady state flow and mixing, CH_4 mass fraction with Mach curve and 3D stream-lines in midplane compared to integral thermal absorption images (Sec. 4.2.2)

recirculation regions allow to draw conclusions about the flow.

Low ambient pressures (Tab. 7.3) cause stronger and longer jets with larger supersonic regions, numerous shock cells also downstream the shock damper and Mach numbers up to five (Tab. 7.4). Indeed gas jets emerge very similar to Fig. 6.8. These jets pose a stronger resistance to the cross-flow, are harder to bend, cause pressure drops across the jet and might rather and at higher velocities impinge onto the manifold wall. Furthermore the jet pump effect is stronger. More ambient fluid is drawn towards the jet such that the pressure is lower in proximity (Fig. 7.9) and a large recirculation region between jet and nozzle might establish and contribute to the mixing.

Stronger cross-flow (Tab. 7.3) weakens large-scale vorticity and moves recirculation and mixing regions further towards the inlet valve. In the worst case larger recirculation regions do not manifest at all (WC6/37°). The jets are bent more by the cross-flow sometimes even avoiding impingement (WC2/37°). The jet pump effect and pressure drop across the jet is compensated to some extent. Just for large injection angles the drag and pressure drop across the jet increases.

Larger injection angles (Tab. 7.3) straighten up the jet and move the impingement location
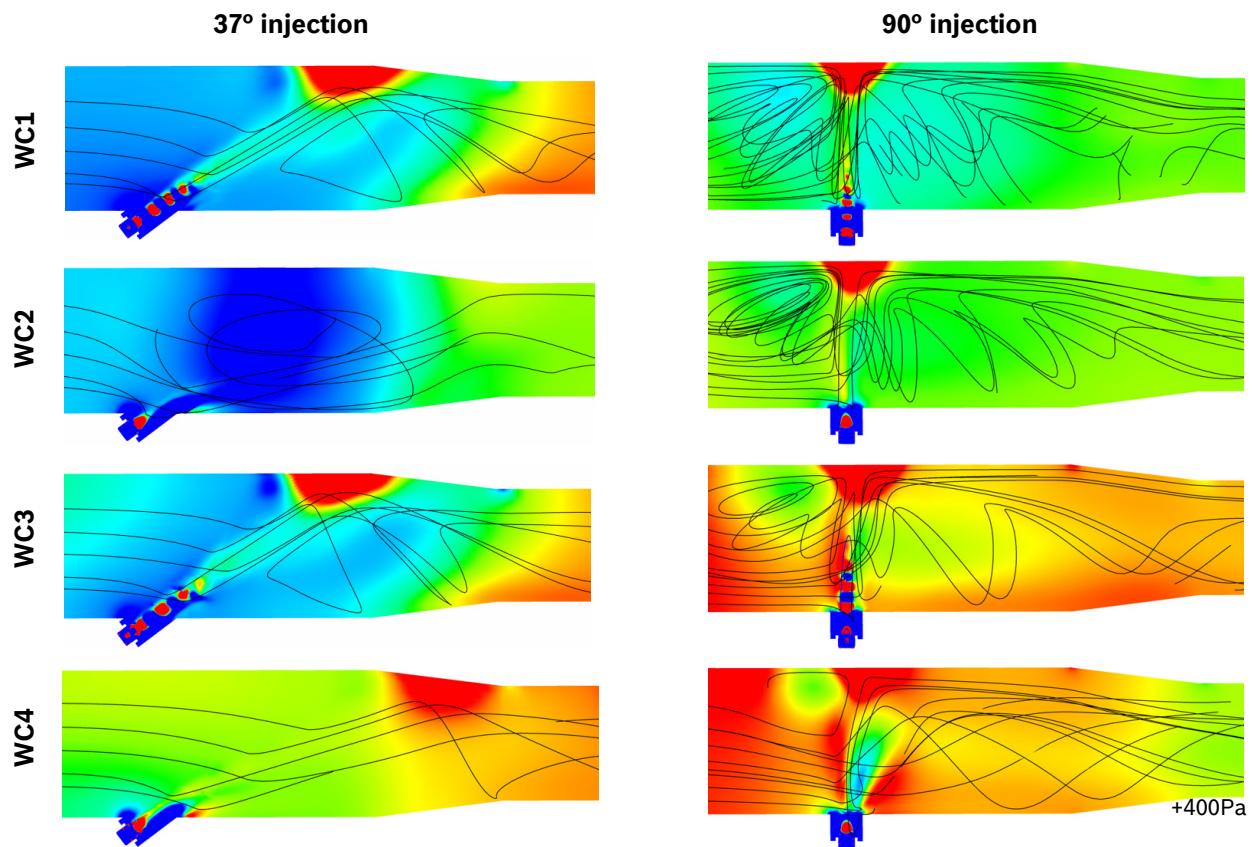
Figure 7.9: Steady state relative pressure -400..400Pa with 3D streamlines in midplane

further upstream. The impingement velocity is larger but always subsonic. The horseshoe vortex around the impingement region is more pronounced and results in enhanced mixing also upstream the injection location. The drag in the cross-flow increases naturally.

The average pressure distribution in the intake manifold is far from being uniform (Fig. 7.9). In the jet shock cells are visible with varying spacing for each WC. Furthermore lowered pressure in the injector mount and increased pressure and stagnation in the impingement region establishes. Last not least the pressure drop across the jet and by up to 500 Pa lower pressures in the vorticity cores can be deduced. This is the pressure distribution considered as zero-reference for stationary injection aeroacoustics.

Furthermore, a deviation to the specified reference pressure can manifest at the air intake side in particular. Substantial drag or drawing effects of the injected fluid cause a pressure increase or decrease of up to several hundred Pascals between jet and air intake. This is in agreement to measurements (Fig. 4.20) and has to be considered when setting up the sponge layer pressure reference for subsequent simulations.

Cause	Effect
Lower ambient pressure	Higher jet Mach numbers, stronger impingement and jet pump effect, less jet curvature, large recirculation regions between jet an nozzle
Stronger cross-flow	increased drift and rupture of large-scale vorticity, increased jet curvature and pressure drop across the jet, less likely impingement, weaker recirculation
Larger injection angle	stronger impingement and horseshoe vortex, increased drag and pressure drop across the jet

Table 7.3: Cause-effect relationship for the averaged stationary flow

WC	Inj. angle	M_{max}	CFL_{max}	CFL_{ave}	Impingement
1	37°	4.9	97	10	in S3 at 88 m/s
2	37°	2.5	96	5	none
3	37°	4.7	99	11	in S3 at 125 m/s
4	37°	3.2	101	5	in S3/4 at 40 m/s
1	90°	4.7	127	10	in S2 at 140 m/s
2	90°	2.8	107	5	in S2 at 55 m/s
3	90°	4.8	131	12	in S2 at 180 m/s
4	90°	3.1	111	5	in S2 at 45 m/s

Table 7.4: Steady-state flow characteristics for varying working conditions ($\Delta t = 1e$-6s)

7.3.2 Aeroacoustics during Stationary Injection

The flows forming for the various WCs and injection angles represent a different aeroacoustic scenario each indeed. Varying jet Mach numbers, the presence and extent of supersonic flow regions and shock cells and the type and intensity of large-scale vorticity and impingement (Tab. 7.4, Fig. 7.8, Fig. 7.9) might affect noise production and propagation. Naturally the grid resolution and timestep requirements change as well. Nevertheless, for the sake of simplicity the same generalized numerical setup is employed for all simulations (Tab. 7.5). According to the segregated approach the simulations start from converged steady injection (Sec. 7.3.1). The inlet is fixed and the sponge layers are enabled and adjusted to the steady state. Since the computational effort is still high just the four setups representing the sensitivities with respect to WC2/37° (Tab. 7.7) are further detailed in this work.

Turbulent Flow

The majority of the highly energetic vorticity is generated in the jet's shear layers and is located between jet and nozzle (Fig. 7.10). Noticeably less fine-scale turbulence is produced

Type	transient URANS
Turbulence model	SAS-SST
Mesh	3.14 million hexahedras, 8% in sponge
Time/-step	data logging for $4\,\mathrm{ms}$, $\Delta t = 10^{-6}\mathrm{s}$
Conditions	intake manifold, methane into air injection, varying WCs (Tab. 4.4), segregated approach (Fig. 7.2a), fixed inlet, sponge layers referencing to the steady-state pressure

Table 7.5: Stationary injection noise simulation setup

for WC1 since the average Courant number is twice as large using the same timestep (Tab. 7.4). Cutting the timestep down to half is not an option, though, in order to keep the simulation costs within limits.
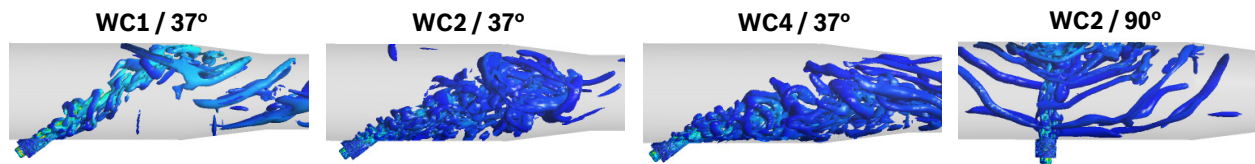
Figure 7.10: Vortical structures for varying setups, shear strain rate invariant $5e8s^{-2}$, colormap: velocity $0..890\mathrm{ms}^{-1}$

For each setup specific turbulence structures have to be considered within the intake manifold. The cross-flow velocity and ambient pressure have some influence on the produced turbulence scales and their distribution within the intake manifold. This might affect noise propagation and spectral distribution. The injection angle is most influential however since turbulence is reflected during impingement. Large injection angles might cause turbulences to approach the jet again which would alter the jet shape and fluctuation and thus noise generation additionally.

Sources of Noise

The shear layers to supersonic flow regions remain the governing noise contributors (Fig. 7.11). Subsonic shear layers, streamwise vorticity and turbulent mixing are by an order of magnitude weaker than that. Direct noise due to impinging turbulence is of subordinate importance. Structural excitation during impingement is not captured but might be a reasonable contributor for external noise in particular.

Most of the noise is generated in proximity of the injector. The source terms fluctuate even stronger in strength and location than observed for the freestream configuration because cross-flow separation and induced vorticity at the injector mount excite the jet additionally.
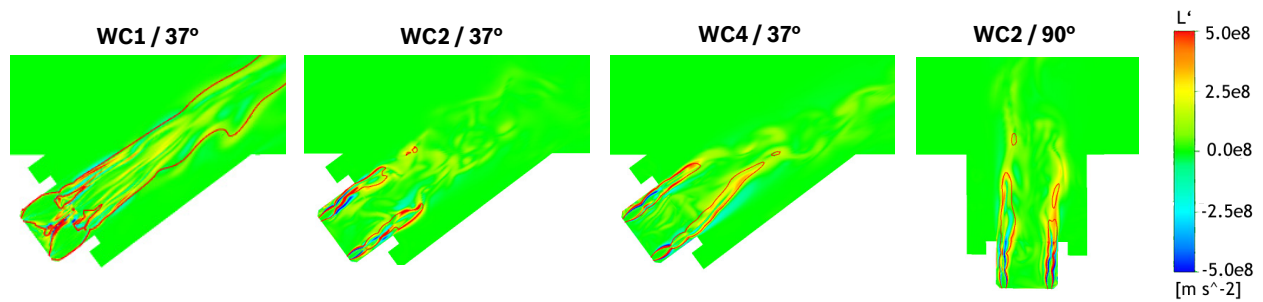
Figure 7.11: Sources of noise for varying setups, Lamb vector fluctuations L' $\pm$5e8ms^{-2}, with Mach curve

Low pressure WCs separate clearly from the others. The jet is much stronger and the supersonic flow region is reasonably increased. The lower jet is much more stable and some of the strongest sources of noise are surrounded by supersonic flow. Noise propagation along the duct axis might be blocked to some extent as well since the supersonic flow regions reach far into the intake manifold.

Noise Spectra

After the transient statistics converged the relative pressure is logged in five points on the intake manifold wall (Fig. 7.1) for another 4 ms simulation time. This data is postprocessed in Matlab using the Welch's method and compared to 12 ms of characteristic measured steady injection noise (Fig. 7.12). An error in the measurement causes the peak at 7.7 kHz in M/S 5 which can be neglected therefore (Sec. 4.2.3). The lowest cut-off frequency (Tab. 7.2) is marked by a dashed line. Below it just plane waves and hydrodynamics can exist leading to a noticeable pressure level drop and generally lowest noise levels in the range 3-5 kHz. Remarkably, WC1/37° does not perform worse than the others. Hence the chosen timestepping is sufficient for low pressure WCs as well.

The OASPL is mostly underpredicted. In M/S 5 this is intensified by lower prediction of hydrodynamics and plane waves up to 6 dB. The simulated spectral distributions compare quite well to the measurements. The global shape, the influence of the cut-off frequency and some sensitivities are captured correctly. Amongst others increased hydrodynamics and low-frequent noise for WC1/37° and increased noise levels at 7-8 kHz in M/S 5 for WC4/90° are qualitatively correct. However some sensitivities obtained by measurements (Fig. 4.21) are exaggerated, reversed, absent in the simulations, or new ones emerge additionally. For example, such a strong variation above cut-off in M/S 1 and the missing separation below cut-off in M/S 5 are not supported by measurements.

Taking the other locations into account, impingement increases broadband noise levels in proximity while the effect in other locations is minor. Fluctuations of more than 5 kPa are

reached in the impingement location of WC2/90°. Lower pressure increases low-frequent content and lowers frequencies above 12 kHz in air intake direction. Higher cross-flow has just minor influence in all locations. Feedbacks between jet, walls and nozzle as well as propagating turbulence pronounce different frequencies in different locations. The ranges around 8 and 13 kHz are mostly affected.

For purely steady injection the obtained results might be reasonable and correct. They allow to deduce the sensitivities for a constant amount of jet noise. Considering a typically pulsed injection however the segregated simulation approach is only valid within limits. The noise emitted during injector opening seems to have influence on the subsequent steady injection noise in the practical application. Feedback and excitation of the jet due to plane waves have to be considered in particular.

7.3.3 Aeroacoustics during Pulsed Injection

The same four setups are investigated, this time however following the more realistic and indeed faster combined approach (Fig. 7.2b). Half an injection cycle is simulated employing a transient inlet starting from just initialized cross-flow (Tab. 7.6). Thus the noise and jet excitation resulting from pressure release and unsteady jet formation is incorporated in the simulation as well.

Type	transient URANS
Turbulence model	SAS-SST
Mesh	3.14 million hexahedras, 8% in sponge
Time/-step	data logging for 4 ms, $\Delta t = 10^{-6}$ s
Conditions	intake manifold, methane into air injection, varying WCs (Tab. 4.4), combined approach (Fig. 7.2b), transient inlet, sponge layers referencing to the cross-flow init.

Table 7.6: Pulsed injection noise simulation setup

During pulsed injection varying drag and draw effects of the jet as well as the strong opening acoustics alter the average pressure at the air inlet over time. Nevertheless a constant reference pressure for the sponge layer with respect to the cross-flow initialization is chosen. The smooth blending of the sponge strength (Fig. 5.8b) and a not too strong choice for the strength $\hat{\sigma}$ still allows a realistic farfield to develop while fluctuations are damped such that virtually none reach the inlet boundary condition. Indeed average flow conditions establish for the investigated setups which are quite similar to the steady-state simulations before. Alternatively, the transient average of the local pressure (accessible via a user-defined function)

could be employed as farfield pressure reference of the sponge layer. Then it would unintentionally be acting on the often much stronger and longer persisting plane acoustic waves as well, though.

Noise Spectra

Again transient data is captured for 4 ms, transfered into frequency space and compared to a characteristic measurement (Fig. 7.13). Now overall and spectral noise levels are generally higher and in better agreement with the measurements. For the most part the prediction is within the fluctuation bandwidth of the measurement and the OASPL deviates by just few dB. In fact the simulation for WC1/37° performs especially well in spite of the stronger opening shock wave and higher jet velocity.

Flashy deviations from the measurement can be observed in parts of in M/S 1 and below cut-off in M/S 2 only. Often this is owed to different time windows of measurement and simulation. Frequencies below 3 kHz are quite weakly damped but indeed decrease over time in the measurements while in the simulations the opening acoustics is still dominant. The result in the ranges 5-8 kHz and around 15 kHz would be better matching for a longer simulation time as well. Here noise emitted by the initial discontinuity at $t = 0$ s (Fig. 5.3) and the resulting turbulent interaction of injector outflow and cross-flow pollutes the predicted acoustics within the first millisecond till the injector is completely opened. Working conditions with perpendicular injection emitting most noise in air intake direction are most affected. In inlet valve direction the effect is less influential since it is quickly superposed by the stronger shock wave and injection noise.

In the locations S2 to S4 the large deviations seen among the different setups for the stationary injection noise (cp. Fig. 7.12) are much less pronounced. In the impingement locations the noise above cut-off is reduced. Generally noise levels are increased due to excitation by the trapped opening shock wave. Bottom line the high-frequent noise becomes quite similar for all setups regardless of impingement. Just the excited frequencies do vary, especially in S3 and S4.

Cause	Effect
Lower ambient pressure	increased noise below cut-off, reduced noise in the ranges around 6 and 12 kHz in M/S 1
Stronger cross-flow	no significant influence
Larger injection angle	reduced noise in M/S 5, increased noise in M/S 1[a]

[a]will vanish for longer simulation times

Table 7.7: Cause-effect relationship for the aeroacoustics of the turbulent flow

The predicted noise sensitivities are not wholly reliable but agree quite well with the measurement indeed (cp. Fig. 7.13 with Fig. 4.21 and Tab. 7.7 with Tab. 4.7). In wide ranges the variation quantities are about right as well.

7.4 Summary

The simulation methodology of a combined approach has been validated for the injection problem with well agreement to measurements. The transient phenomena during injector opening and the resulting weakly damped plane waves have been shown to be imminent to consider for the prediction of the noise emissions of the practical application. Lower pressure WCs can be investigated with the same setup and without the need to decrease the timestep size or generate a dedicated mesh. However some issues remain. Primarily the discontinuity at $t = 0\,\mathrm{s}$ contaminates the result. On the other hand, numerical dissipation does not seem to be very influential for the short propagation distances.

The local spectra can be separated into the regions below and above the lowest cut-off frequency. Below cut-off pseudo-sound and plane waves form the spectrum. Here the noise emission during transient injector opening has strong influence. Above cut-off higher order duct modes dominate. Nevertheless weakly damped plane waves left over from the opening shock wave excite the jet and increases the noise emission throughout the spectrum. The lower jet and shock damper remains the major noise contributor. Turbulence within the intake manifold is of subordinate importance. However especially during impingement turbulence might excite structural oscillations in the practical application.

The influence of the parameter variation on the aeroacoustic result proved to be comparably low in the simulations as well as supporting measurements. In particular there is less variation over the engine's working envelope than initially expected. Hence it is sufficient to employ just a single working condition to compare different designs in future investigations.

In order to reduce the noise levels the most effective mean is to ensure less noise generation by slowing the gas jet and the process of opening the injector down in particular. If this is technically unfavourable the noise propagation can be damped instead. Here pushing the lowest cut-off frequencies higher, e.g. above $10\,\mathrm{kHz}$, might be effective. This can be achieved by short ranges of concentric walls of just half the diameter (Sec. 3.4) in regions where the streamlines are mostly parallel anyway and no mixing is done. Furthermore a choice of material and structural design in avoidance of resonances in the most prominent aeroacoustic frequencies as well avoidance of impingement is advisable.
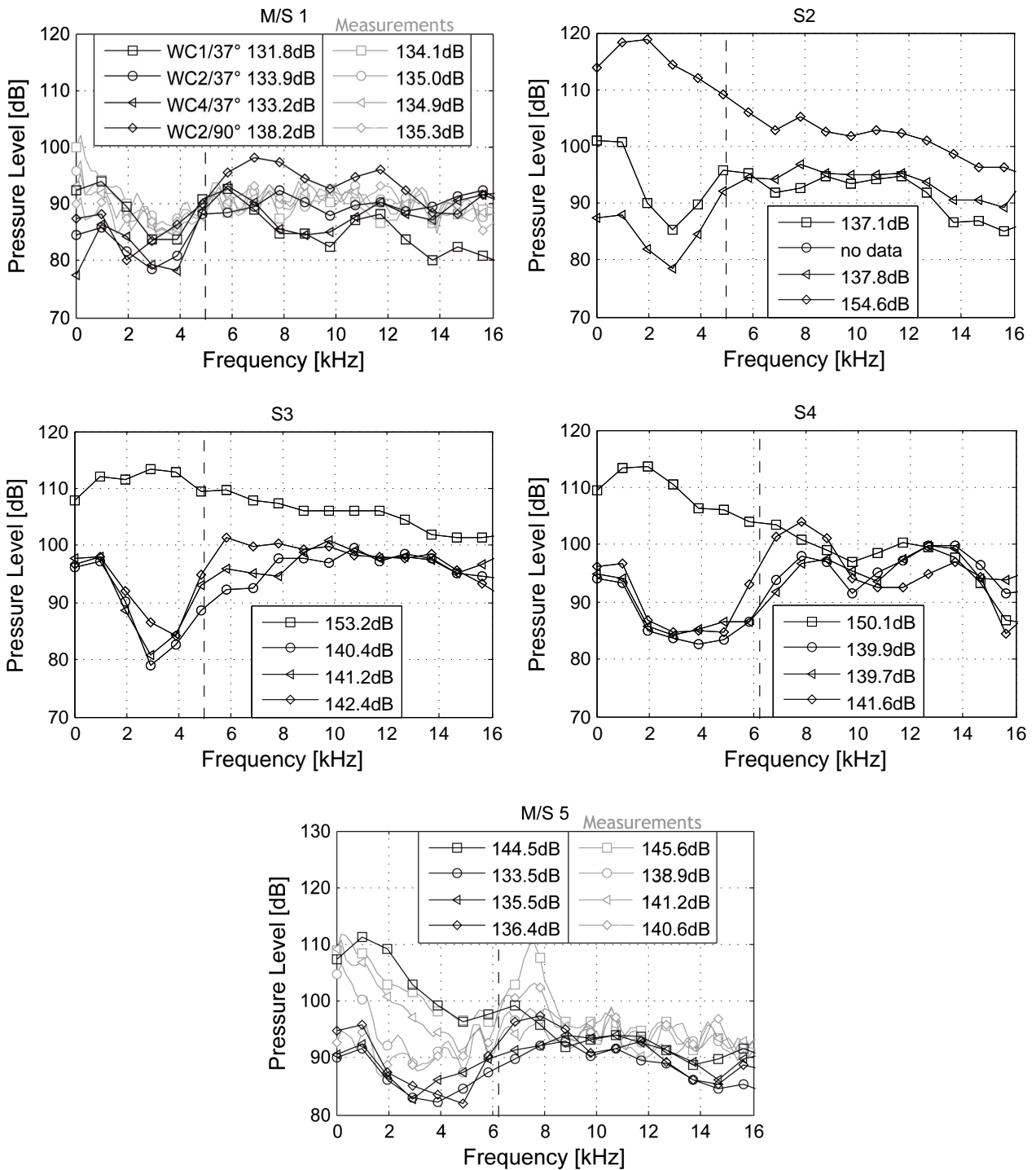
Figure 7.12: Noise spectra during steady injection
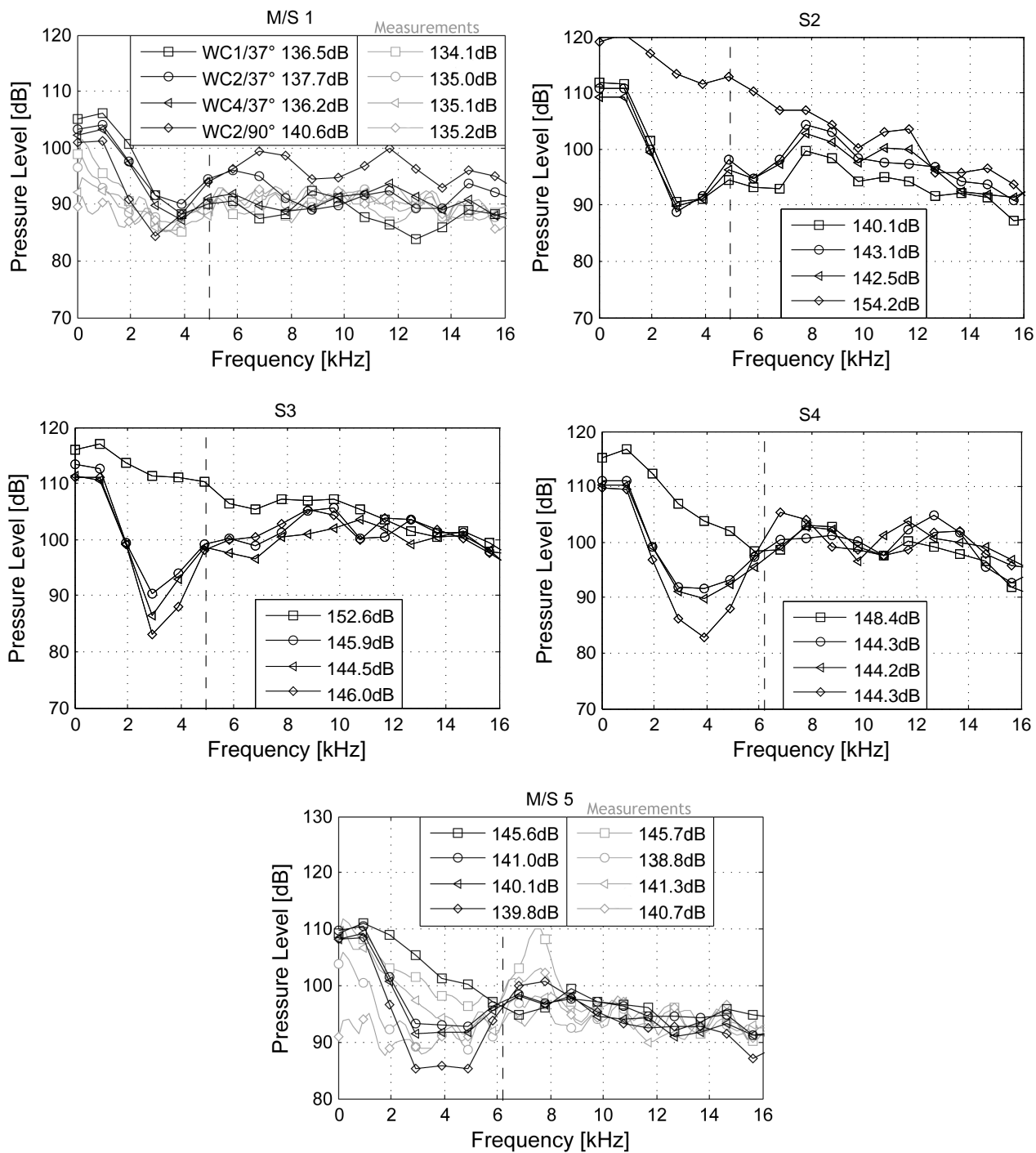
Figure 7.13: Noise spectra during pulsed injection

Chapter 8

Application of Research Code NSDG2D

Direct aeroacoustic simulations performed with a CFD tool like ANSYS CFX, which is not all optimized for aeroacoustics, is generally very costly and yields several disadvantages. High dissipation and lack of effective non-reflective boundary conditions are some of them (Tab. 8.1). Not just for sensitivity and optimization more sophisticated, more exact and first of all faster approaches become necessary. This requires wholly new approaches which are currently only available in form of research codes, though.

In this chapter the code NSDG2D (Sec. 2.4.2) developed at the Institut für Aerodynamik and Gasdynamik (IAG) at the Universität Stuttgart is compared to ANSYS CFX and assessed in terms of solution quality, computational costs and potential for future applications. Its better efficiency arises from the facts that is allows explicit local timestepping as well as solving the Euler and N.-S. equations at higher solver order or with local hp-adaptivity (Tab. 8.1). Furthermore it features low numerical dissipation and very effective non-reflective boundary conditions. Hence, a reasonable speed-up as well as higher solution accuracy can be expected for the supersonic gas jet application. In fact, its large range of scales might make optimal use of the local adaptivity features.

Code	Advantages	Disadvantages
ANSYS CFX	LES/SAS turbulence modelling, tested commercial software	general low-order CFD code, hard to couple and enhance, dissipative, reflective boundaries
NSDG2D	optimized for aeroacoustics, local adaptivity (Δt, order, grid), N.-S. and Euler equations, arbitrary non-regular meshes, possibility of own enhancements	no turbulence model yet, restricted to 2D till now, still buggy and under development

Table 8.1: Code comparison of ANSYS CFX and NSDG2D

Due to the current limitations of NSDG2D the simulations are conducted in 2D and without turbulence modeling. Here the gas injection problem with its small model dimensions indeed allows DNS simulations within affordable time. In fact, even the 3D injector setup (Fig. 6.5) is just by a mere factor of 100 coarser than the Kolmogorov scale and would allow DNS simulations if a more efficient approach was available.

8.1 Comparability of 2D and 3D Simulations

Flow-induced injection noise is an inherently 3D phenomenon of course. On one hand there is the true three-dimensional injector flow which is hard to reduce to 2D. On the other hand there is just two-dimensional turbulence and noise propagation which result in altered noise generation and decay laws. In fact, the assumption of two-dimensionality is a shortcoming even for axisymmetric jets [89]. Simulations in 2D were shown to lead to unrealistic sound signals regarding shock and screech noises and to overpredict downstream noise [35]. Nevertheless, the aim is to identify a test case allowing at least to draw conclusions about the noise generation in the jet and to estimate the efficiency of NSDG2D for a future application to 3D injection.

Main reason for the often weak similarity between 2D and 3D is the unique *inverse energy cascade* phenomenon in 2D. While in 3D turbulences always cascade towards smaller scales only with the rate of the turbulence eddy dissipation ε, they can also cascade towards larger scales in 2D. This physically validated [78] phenomenon is caused by missing vorticity in two more dimensions and leading to a significant difference in turbulence lifetimes and spectra [83]. In fact, turbulent production can even exceed dissipation. Especially for bounded low-viscosity high-Reynolds number flows, small erratic turbulences will grow and self-organize to ever-larger vortical structures which then are persistent, incorporate most of the turbulent kinetic energy and eventually dominate the flow [74]. This can even result in the instability of the 2D flow [40].

While there is no way to overcome the turbulence cascade phenomenon, the different noise decay law for propagation in 2D could be theoretically handled by a subsequent frequency-dependent pressure level correction as proposed by Ewert [31] for example.

Intake Manifold Configuration

Unfortunately, gas injection into the intake manifold belongs to those bounded, low-viscosity and high-Reynolds number flows affected most by the inverse energy cascade. Vortical structures of model dimension dominate the flow and impede steady-state convergence (Fig. 8.1). In fact, two different flow shapes emerge in dependency of the timestep size, both without even remote comparability to 3D. Additionally to the dominating vortices the cross-flow can-
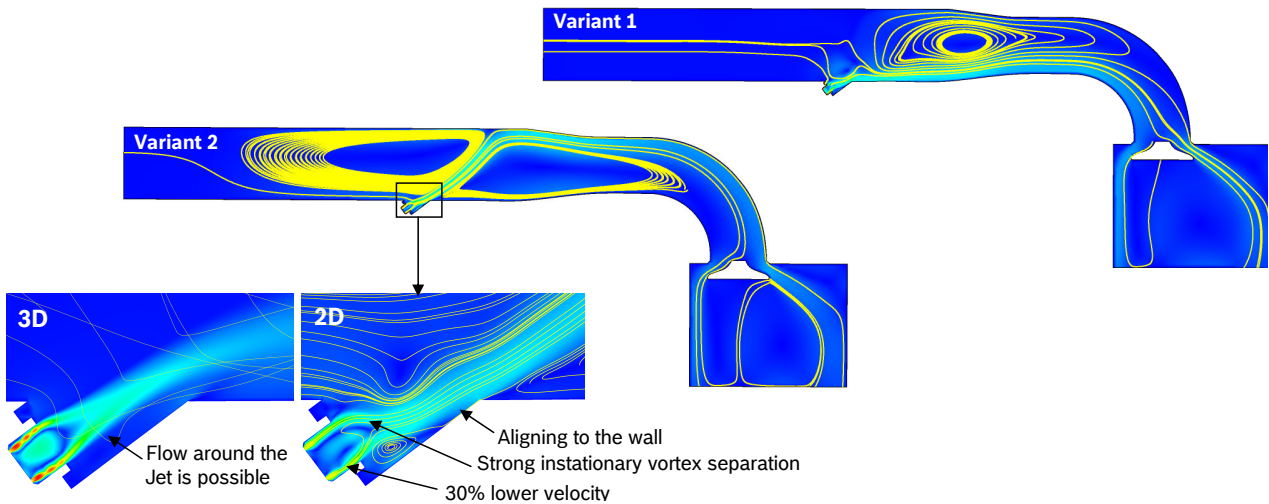
Figure 8.1: 2D intake manifold flow, duty point 2, velocity 0..600ms^{-1} with streamlines

not bypass the jet and intake valve such that the flow is unrealistically forced. And naturally, 3D acoustic duct modes cannot be reproduced as well. Summarizing, there is no chance to simplify the intake manifold to 2D without losing significance completely.

Freestream Configuration

In the freestream configuration the boundedness by the intake manifold is gone. Just the nozzle and the confinement between the jets remains. Now time-averaged simulations show similar velocity scales and at least remotely comparable flow and shock cell shapes (Fig. 8.2). However, in transient LES or DNS simulations the inverse turbulence cascade manifest again: While in 3D a cluster of small vortices governs the flow within the nozzle, a single large vortex is dominating the flow in 2D. Consequently comparability of the nozzle flow completely in transient simulations is not given anymore. Furthermore massive eruptions of the flow field occur in 2D when the vortex between the jets grows and eventually bursts out randomly. The latter is accompanied by strong noise emission which is indeed dominating by magnitudes in 2D. Summarizing, 2D simulation results are not significant for the freestream configuration as well.

8.1.1 2D Setup

This calls for further simplifications. Now the shock damper and one of the jets are removed as well such that a single 3 mm wide jet in freestream configuration remains. The inlet boundary condition is adjusted in a way that the velocity scales and Reynolds number, the shock cell strength and spacing are comparable to the 3D injector.

The numerical setup and the mesh for the initial simulations with ANSYS CFX is shown in
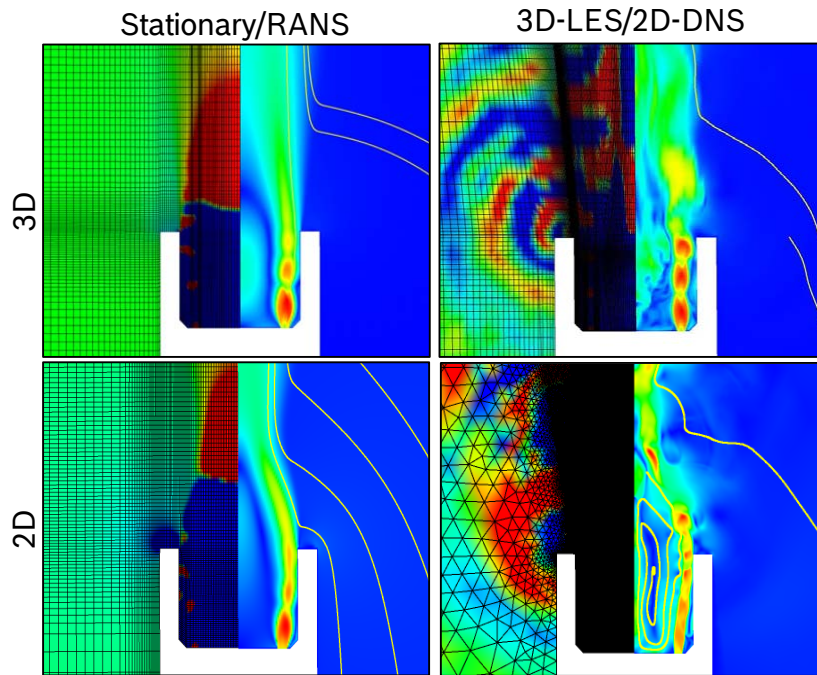
Figure 8.2: Comparability of 2D and 3D flow, freestream configuration; LHS figure: relative pressure -1kPa...1kPa with mesh; RHS figure:velocity 0..600ms^{-1} with streamlines

Type	2D-DNS, air into air at 1 bar
Inlet conditions	U=500 m/s, T=222 K, p=2.8 bar (M=1.4, Re=30000)
Mesh	110000 elements (quad-dominant, 1.6% in Sponge) for 2nd order
	35000 elements for 6th order
Timestep	Δt_{min} = 4e-9s
Conditions	sponge layer (Sec. 2.3.2), approach section

Table 8.2: 2D simulation setup

Fig. 8.3. The Kolmogorov scale in the jet is resolved up to factor 10 such that DNS simulations are indeed enabled. Using an unstructured quad-dominant mesh, element clustering in the jet region is possible while the overall number of elements and the overhead for the sponge layer is comparably low. Within the latter artificial viscosity is applied in order to dissipate vortices not leaving the domain. Furthermore implicit damping based on continuity source terms is employed in ANSYS CFX (Sec. 5.2.2) while better performing explicit damping (Sec. 2.3.2) enhanced by a characteristic non-reflective boundary condition (Sec. 2.3.1) is employed in NSDG2D. In order to avoid reflections at the transition into the sponge, the sponge strength is blended according to Fig. 5.8 again. The attached approach section is aimed to generate reproducible turbulence levels in the jet while starting from a non-fluctuating inlet.
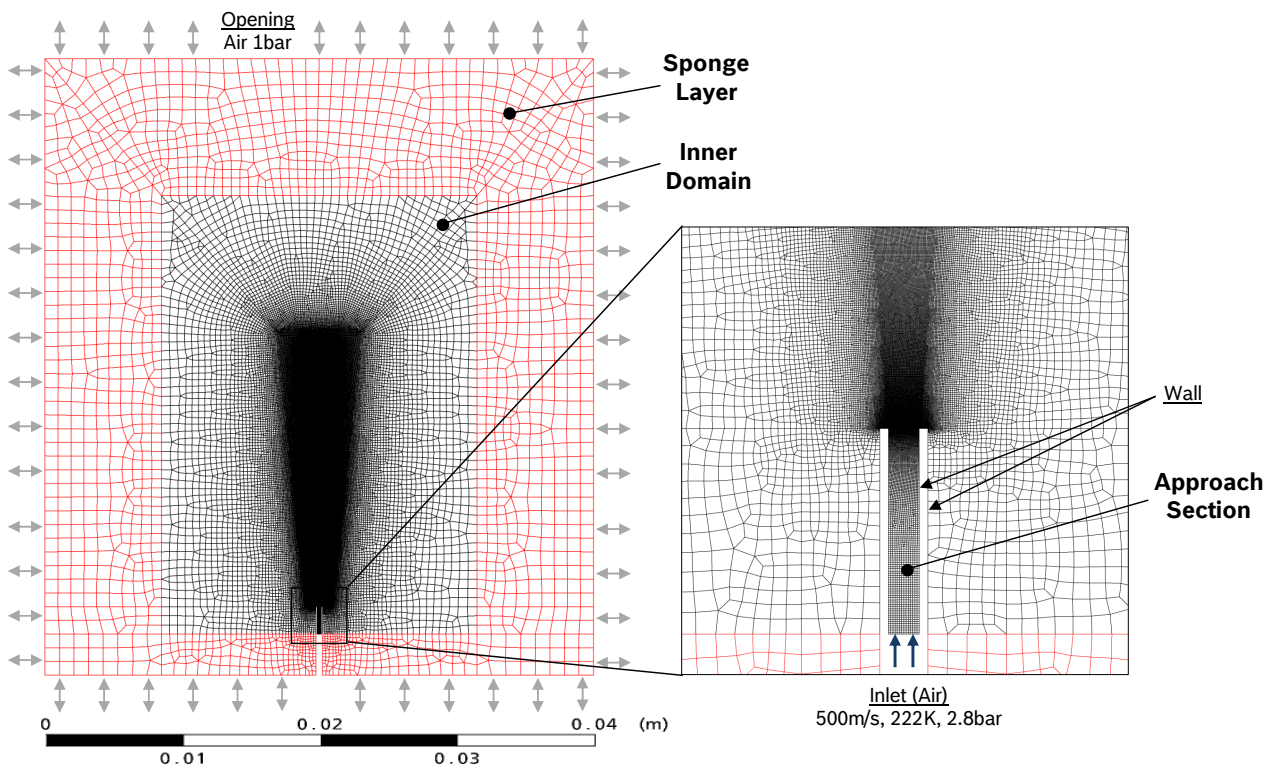
Figure 8.3: Computational setup and mesh for 2nd order simulations

8.2 Results

In contradiction to the 3D jets the single 2D jet is now generally less fluctuating and turbulence and noise generation is driven by instabilities coming from the approach section rather than the turbulence cluster. Vortices are forming in the shear layer of the lower jet, grow while propagating downstream and eventually force the third shock cell into heavy deformations, constant collapse and reformation. Eventually, just the lower two shock cells stand steady.

Considering the noise generation some weaker high-frequency content comes from the shear layer in the lower jet. Most noise comes from the jet disruptions, vortex pairing and shock oscillations downstream the second shock cell however. Furthermore acoustic-turbulence interactions are captured seemingly causing refraction of sound waves.

This result is very sensitive towards the farfield boundary conditions, though. First of all the extent and direction the jet is drawing fresh air from the sides is of importance. If a strong co-flow aligned to the jet establishes, e.g. due to recirculation caused by a poor sponge layer definition, the jet is stabilized and more shock cells emerge. On the other hand, turbulence and feedback from partially reflective boundaries can further excite jet fluctuations.

252 CPUdays/ms[1]   18 CPUdays/ms[2]
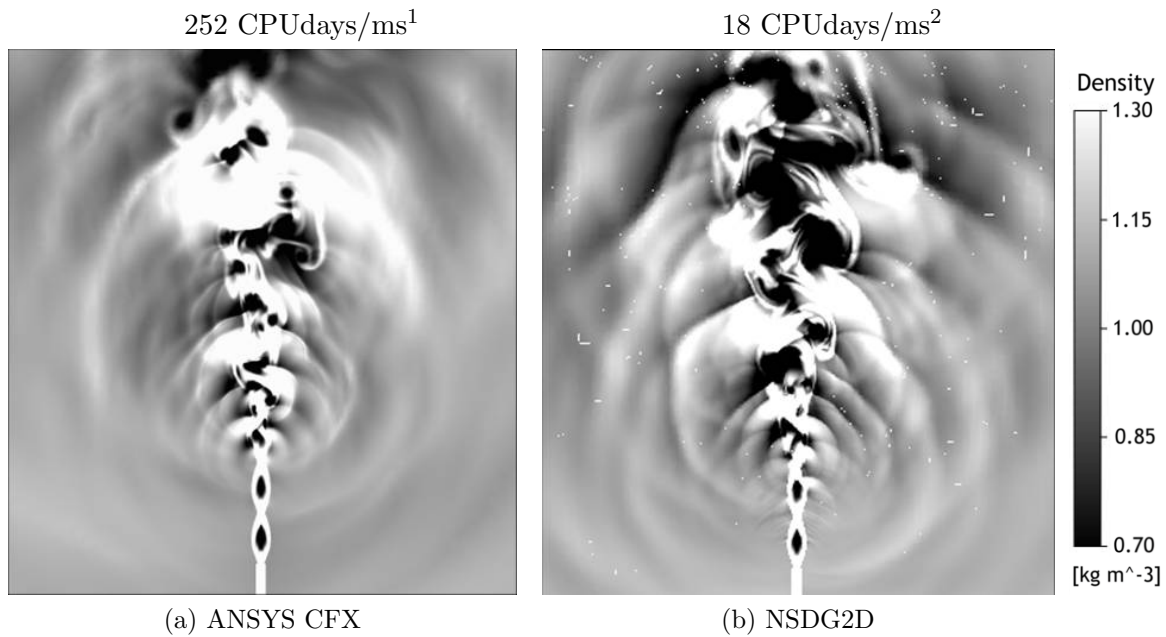
(a) ANSYS CFX   (b) NSDG2D

Figure 8.4: Comparison of ANSYS CFX and NSDG2D, 2nd order

8.2.1 ANSYS CFX vs. NSDG2D

In a direct comparison, saying same mesh, equivalent boundary conditions (Fig. 8.3) and (minimum) timestep (Tab. 8.2), NSDG2D performs reasonably better in terms of solution quality as well as computational times. In ANSYS CFX the blending down to 1st order upwinding at steeper gradients and the associated increased dissipation results in the loss of detail such that the solution seems blurry. In fact, shear layer instabilities in the lower jet virtually are not captured at all by ANSYS CFX. NSDG2D on the other hand remains 2nd order accurate and low-dissipative throughout the domain.

Nevertheless, similarity is given in spite of the shortcomings of ANSYS CFX. The major noise generation mechanisms, global noise levels, formation and interaction of vortices is captured the same by both tools. However, in ANSYS CFX downstream vortices seem to be generally somewhat smaller. One reason surely is that the vortices start to grow later in the shear layer due to the 1st order blending. Another reason might be a worse farfield boundary condition which does not suppress all feedback completely.

Considering the simulation costs (in terms of CPU time per millisecond simulation time) NSDG2D needs more than an order of magnitude less effort to obtain an even better solution. This advantage is reached by local timestepping in the first place which allows to adjust the element's timestep to the actual stability requirements and thus makes best use of the available computational power. Furthermore the explicit time marching does not require the

---

[1]AMD Dual-Core Opteron 2218 2.6GHz, pseudo-2D, implicit time marching, global timestepping
[2]Intel Dual-Core Xeon 2.6GHz, true 2D, explicit time marching, local timestepping

convergence of each timestep in a set of coefficient loops. This is generally advantageous in transient simulations. For the tiny timesteps employed here this can be assumed not to be very influential tough since convergence is mostly reached in a single coefficient loop iteration already.

However these numbers have to be taken with care because the simulations were performed on different (yet comparable) clusters and because ANSYS CFX runs in a pseudo-2D rather than a true 2D mode. The additional momentum equation contributes to the computational costs even though its solution might be quite fast as there is just a single layer of elements in that direction. On the other hand, parallelization and dynamic load balancing are quite new features of NSDG2D which still yield potential for optimization and further reduction of the computational costs.

8.2.2 Dedicated Mesh and Increased Global Solver Order

Now the initial mesh is coarsened, adapted and optimized for a sixth order accurate simulation with NSDG2D (Fig. 8.5). The new mesh comprises 35000 elements which relates to more than twice the overall number of degrees of freedom (DoF) and thus roughly twice the effective resolution.

$$\text{DoF}|_{2D} = \frac{\text{Order}(\text{Order} + 1)}{2} * \text{Elements} = \begin{cases} 330000 \text{ for 2nd order mesh} \\ 735000 \text{ for 6th order mesh} \end{cases} \qquad (8.1)$$

Furthermore the mesh topology is adapted to the reduced needs of NSDG2D. The sponge layer is dispensable at the bottom, left and right sides of the domain as the characteristic boundary conditions alone are completely sufficient. Just in downstream direction it is still employed and even somewhat enlarged to guarantee dissipation of any vortices without influencing the inner domain. Additionally, the new mesh makes use of NSDG2D's ability of handling irregular grids. Instead of being smooth with just moderate element expansion factors the new mesh consists of discontinuous blocks with strong expansion and even hanging nodes. The thusly saved elements are then spent where they might be of more use: in proximity of the jet to better resolve turbulences and acoustics.

Indeed the sixth order simulation results draw a sharper picture of flow and acoustics (Fig. 8.6b). While the general flow shape is identical to the preceding second order simulations (Fig. 8.4b), vortices and acoustic waves are more detailed due to the better resolution.

This improved result with more than twice the number of DoF and better resolution especially in the acoustic propagation region is paid for by just 33% more computational cost. However its is not just the higher solver order but also the local timestepping due to the

(a) 2nd order mesh (ANSYS CFX)   (b) 6th order mesh (NSDG2D)
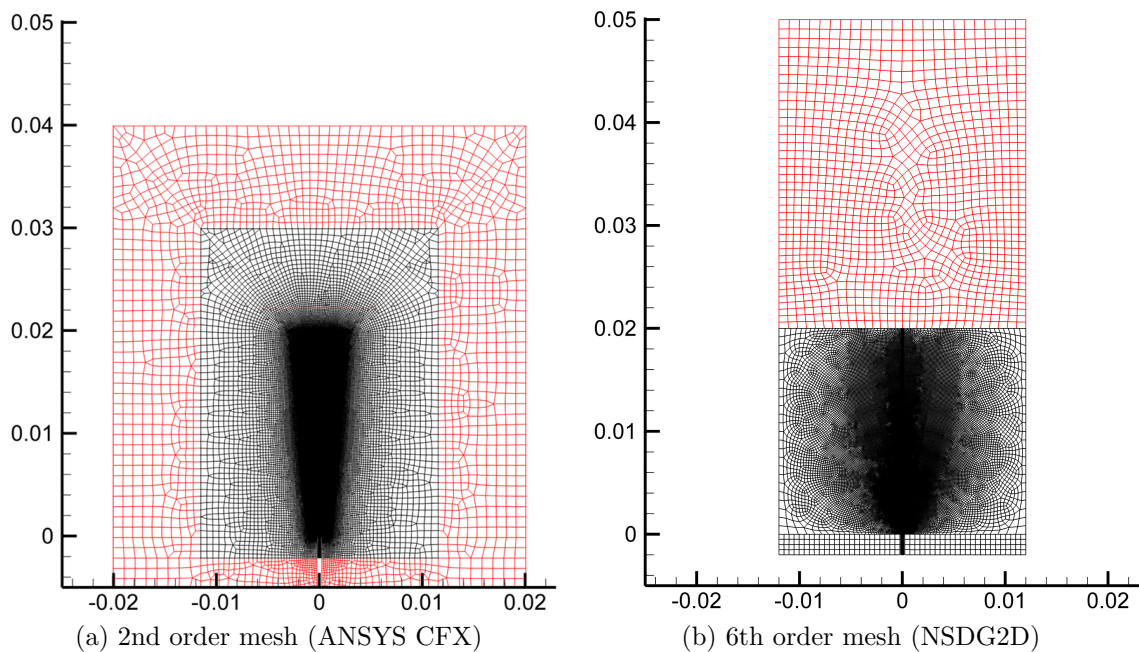
Figure 8.5: Initial ANSYS CFX and higher order NSDG2D mesh, sponge layer in red

different mesh topology that plays a role here. Indeed the evaluation of a higher order DoF is known to be slightly more expensive than a lower order DoF. The advantage of higher order schemes rather comes from the fact that the same solution quality requires less global DoF instead owed to a lower descretization error.

8.2.3 Euler vs. Navier-Stokes Equations

In order to assess the importance of viscous forces in the jet flow, simulations are undertaken solving just the Euler equations under otherwise same conditions (Fig. 8.6).

There is no dominating or even noticeable difference in the lower jet regarding jet shape, vorticity and acoustic production. If any, few larger vortices seem to be organizing further downstream instead of several smaller vortices superposing each other. This allows to draw the conclusion, that inertia effects generally dominate over viscous effects at least in the lower jet where local Reynolds numbers are comparable high (Sec. 2.1.3).

Solving the Euler equations saves 20% computational time. Employed to the lower jet at least, e.g. in a heterogeneous domain decomposition, would already be a reasonable advantage as this is the most expensive area with highest velocities and smallest timesteps. It has to be verified, though, whether vicous terms remains negligible within the 3D shock damper as well. Vortices might be held longer in place between the jets such that viscous effects could dominate again.

(a) Euler   (b) Navier-Stokes
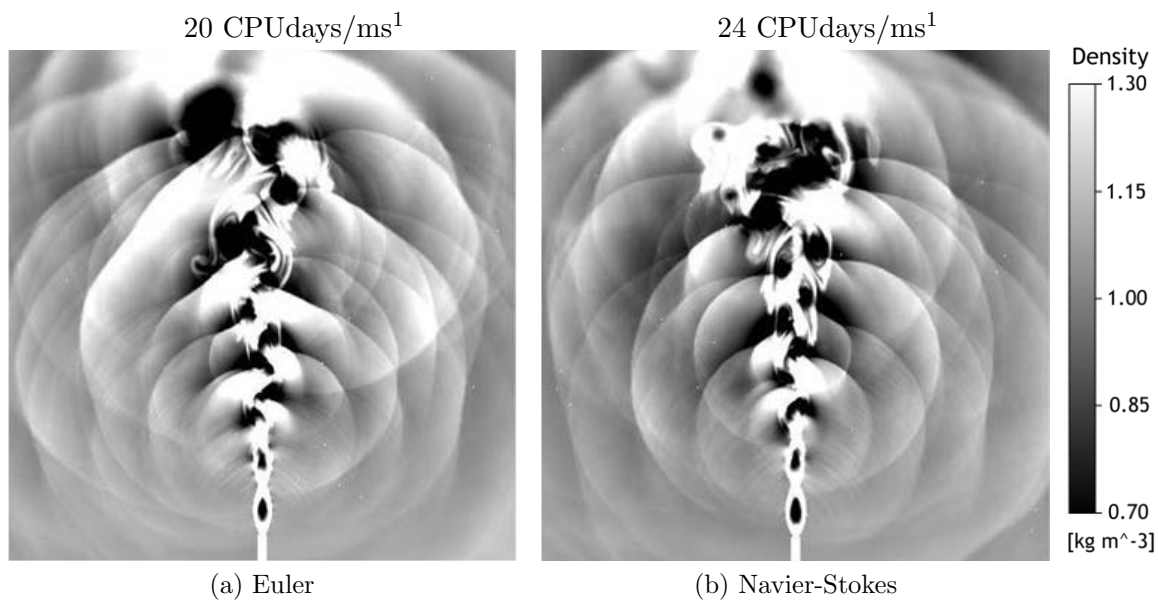
Figure 8.6: Comparison of Euler and Navier-Stokes in NSDG2D, 6th order

8.2.4 p-Adaptivity

Manually optimizing the mesh and setting a *global* solver order (Sec. 8.2.2) is actually not very efficient. It does not only mean a lot of preceding work and the need for previous knowledge about the flow but the result would still always be a guess rather than the optimum. In fact, the stakes are high: Using sixth order accuracy for an element where second order would have been sufficient, for example, is seven times more expensive (scales with the DoF essentially, Eq. 8.1). In 3D it would be even 14 times as expensive due to the relation

$$\text{DoF}|_{3D} = \text{DoF}|_{2D} * \frac{\text{Order} + 2}{3} \, . \tag{8.2}$$

Hence, it is more reasonable to locally and automatically adapt the element order to the actual needs instead.

The chosen test case is the initial opening blast and jet formation of the sixth order setup, during which the local solver requirements are changing a lot in time (Fig. 8.7). Based on the current flow an error indicator detects regions where the numerical resolution defined by mesh resolution and element order is insufficient (red) or exceeds the current requirements (green and blue) to resolve the flow. Based on this information the respective element orders are increased or decreased before the next time step (p-adaptivity). For the sake of simplicity, element orders are restricted to a range between 3 and 6 in this example. Practicable ranges are between 2 and 8, though.

---

[1]Intel Dual-Core Xeon 2.6GHz
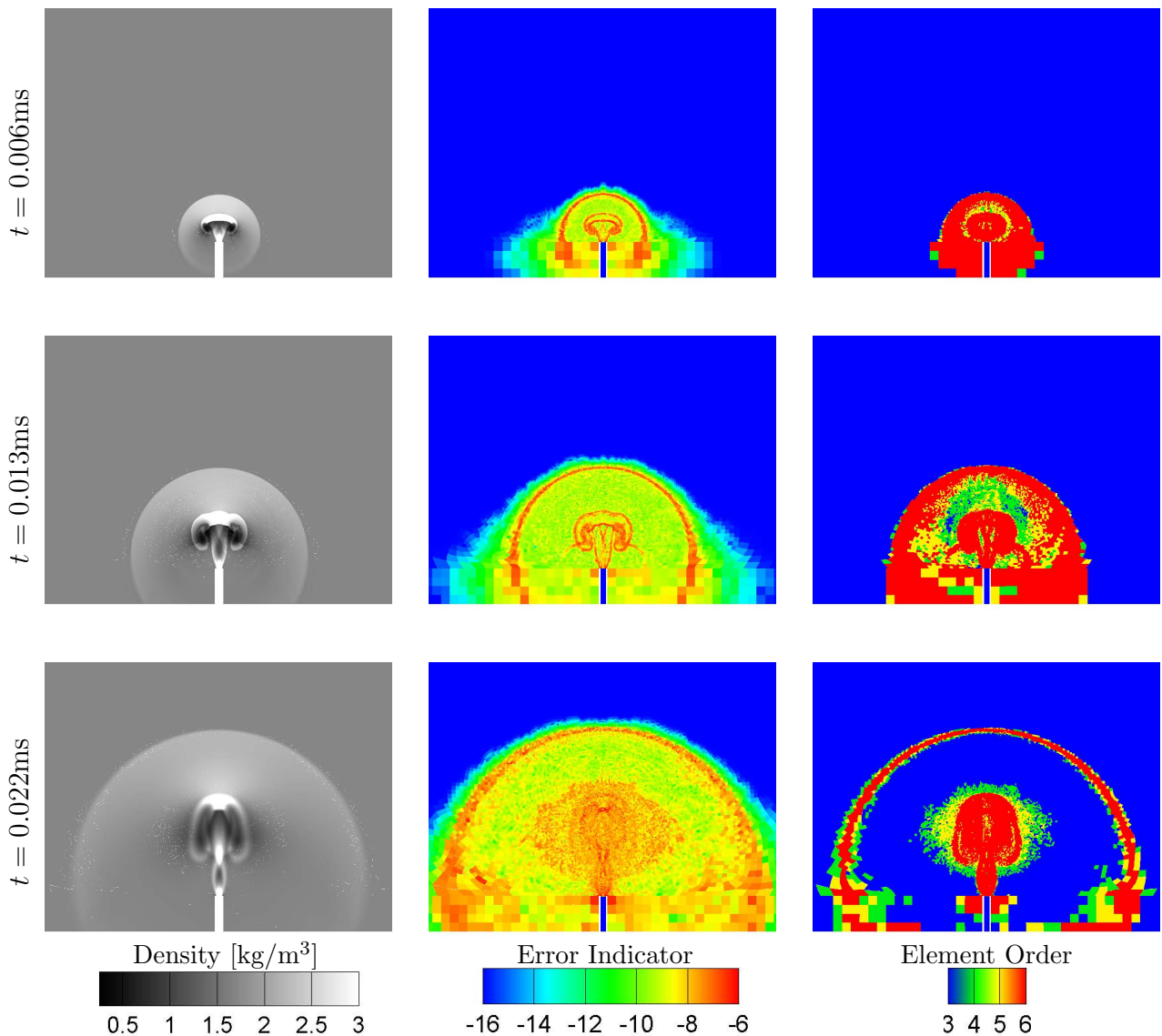
Figure 8.7: p-adaptivity during jet build-up

The steep gradients of the initial shock wave and at the vortex edges is reliably marked by the indicator as too weakly resolved. Hence, the element order is increased to the maximum there. In return, the region between shock wave and vortices is too well resolved for the comparably smooth flow. Consequently, the element order is reduced to the minimum there. Eventually, the solver adapts to the transient problem and concentrates higher-order elements in the shock wave and the jet while the remains are of cheaper third order accuracy only. A smooth medium-leveled error indicator (yellow) then shows that the resolution is as objected. Alternatively or additionally, the respective elements can be refined or joined (h-adaptivity) if the range of element orders is not sufficient over a longer period of time for example.

This automatic adaption is obviously a big advantage for all problems featuring a locally and transiently varying flow solution. A global computational cost advantage is hard to

determine, though, as it is very problem-dependent. Anyway, the additional costs for the adaptivity feature are very low such that some computational cost advantage is nearly always guaranteed.

8.3 Potential and Outlook

The documented potential and actual superiority of NSDG2D over ANSYS CFX is based on various features which might prove advantageous for numerous other unsteady flow problems featuring a wide spread of scales as well. For the 2D ejection problem the solution quality is shown to be noticeably improved while the simulation costs are reasonably reduced at the same time.

Local time-stepping and explicit time-marching is probably the most influential feature. Furthermore the combination of higher order accuracy and local hp-adaptivity might reduce simulation costs noticeably. Last not least the possibility to solve the Euler equations and the probable future incorporation into a heterogeneous domain decomposition framework[1], fully two-way coupling N.-S., Euler, linear Euler and wave equation domains respectively, increases the value of NSDG2D.

However it is not just the computational costs but also the preceding meshing effort that is greatly reduced. The ability to handle arbitrary, mixed-type and even irregular meshes with hanging nodes allows very quick mesh generation which otherwise could require days or even weeks for 3D geometries as well. In fact, in combination with hp-adaptivity NSDG2D enables something like a "one mesh fits all" strategy. Without the need for detailed knowledge about the emerging flow a first-guess mesh is sufficient. Local adaption will make sure the solution is correct and fast nonetheless. This is especially advantageous for highly unsteady problems like the pulsed injection and for sensitvity analyses where the flow alters reasonably for different boundary condition settings. Then the same mesh can be employed for all variants with good conscience.

The functionality of the new features has been shown for the 2D jet example. Applicability to industry-scale applications requires further enhancements and testing however. Provided a (LES) turbulence model is implemented and the 3D version of the code is completed and validated a noticeably cost reduction over ANSYS CFX with SAS turbulence modeling can be projected for the 3D injection as well though (Fig. 9.1). Additionally, the solution quality will be surely better since the SAS turbulence modeling with CFL>1 degrades the turbulent solution and needs a timestep study to detect the bounds of physical validity.

---

[1]e.g. KOP3D developed at the Institut für Aerodynamik and Gasdynamik at the Universität Stuttgart

Chapter 9

Summary and Outlook

The gas injection as a representative for numerous other e.g. pneumatic applications is characterized by small model dimensions and large pressure drops resulting in supersonic jet velocities. Very small flow structures have to be resolved and fix the grid resolution to a level close to DNS. Hence there is virtually no room for considerably coarser meshes in LES or URANS approaches. The high jet velocity on the other hand calls for very small timesteps to comply with the CFL condition such that an unnecessarily wide noise frequency range is produced as well. Remarkably, those demands vary locally by magnitudes indeed. In terms of acoustics, nonlinear propagation, noise blocking by supersonic flow regions, acoustic feedback from nearby walls and a heavily fluctuating base flow have to be considered. Hence fast direct noise simulation is essential rather than hybrid methods.

altered   **Reference: LES with ANSYS CFX**   altered

Modeling   4256 CPU-days/5ms   Numerics

URANS/SAS with ANSYS CFX	
Globally larger timesteps	*1/40
SAS-SST turbulence model	*1.42
Timestep convergence (coeff. loops)	*1.48
	*1/19
224 CPU-days/5ms	

LES locally adaptive with NSDG	
Local timestepping	*1/10
Locally adaptive solver order	*1/2
Euler instead of Navier-Stokes	*0.8
Efficiency (explicit solver, load balancing)	*1/2
	*1/50
approx. 85 CPU-days/5ms[1]	

+   Commercial software, applicable today
+   Widely robust, technical support available
−   Loss of information due to time-averaging
−   Problem-dependent optimum timestep
−   Inherently suboptimal for aeroacoustics (strong dissipation, low order of accuracy)
−   No access to the code, few chances for own enhancements (e.g. non-reflecting boundaries)

+   Very fast and accurate aeroacoustic simulations
+   Very simple mesh generation, automatic dynamic adaption to the problem
+   Code access, very flexible for own enhancements
−   No turbulence model yet, little experience in 3D
−   Research code, no GUI, no official support
−   Code development in progress, bugs & instabilities probable, further research required
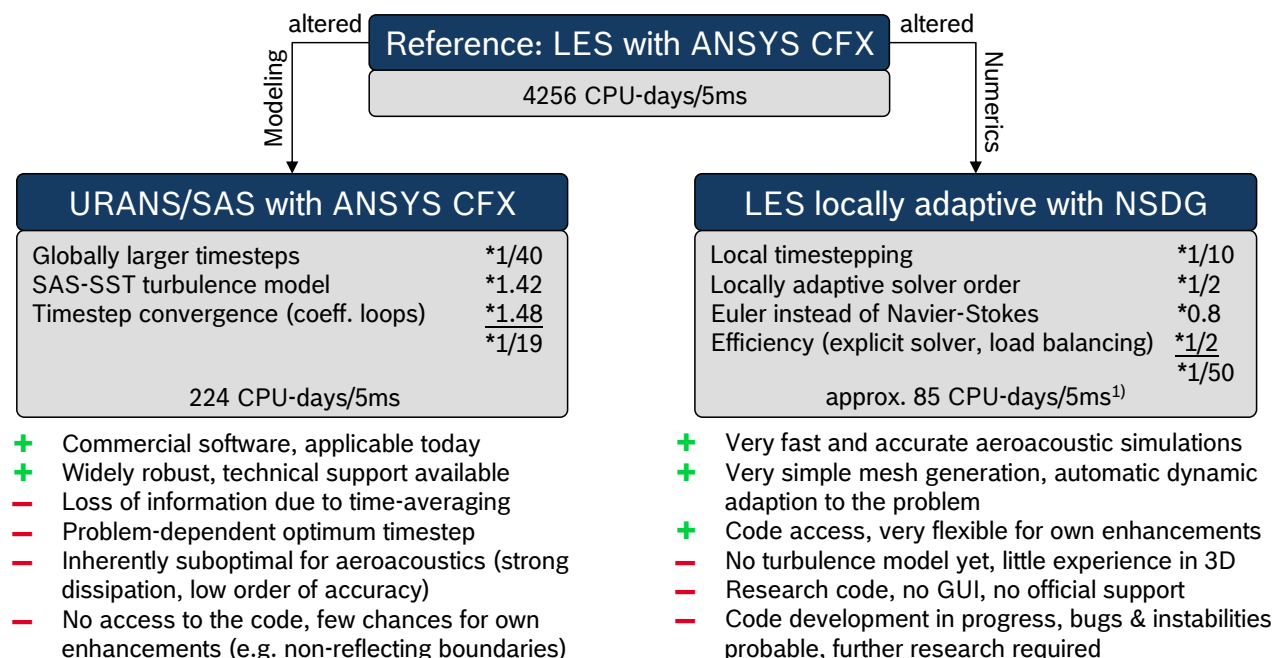
Figure 9.1: Comparison of simulation approaches for the gas injection problem

---

[1]Conservative estimation. For large Mach numbers and optimized code the costs might be lower indeed.

Various approaches were pursued in order to develop an efficient aeroacoustic simulation methodology (Fig. 9.1). Starting with an initial approach based on the well accepted LES and the commercial tool ANSYS CFX it became quickly clear that especially the very small global timestepping makes the simulation intolerably expensive for the problem in focus here. Since the mesh is fixed by the problem there are basically two paths the simulation effort can be reduced: either by a different physical modeling allowing larger timesteps or by more efficient solver numerics featuring local adaption.

The novel SAS-SST turbulence model implemented in ANSYS CFX represents such an alternative modeling approach. It is shown to allow a reasonable timestep increase while remaining numerically stable and producing the necessary broadband turbulence levels. In this work it is validated for the aeroacoustics of the gas injection problem with well agreement to measurements. Since a significantly degrading solution quality has to be considered for strongly increased timesteps, a timestep study was performed in order to identify a favorable setting for the injection application. Thus a computational cost reduction by the factor of 19 is achieved with passable loss of information and quite well reproduced sensitivities. Guidelines for the prediction of the optimum timestep, e.g. with respect to the global CFL number, can not be generalized, though. Hence, applied to other problems new timestep studies could become necessary instead. The presented methodology is applicable today and allows to draw conclusions about the generated noise and its influence parameters based on commercial software. However, this approach is still too costly for employment within an optimization framework.

ANSYS CFX is inherently very limited when it comes to adaption to locally varying problems or to alter the solver numerics. Thus the research code NSDG2D is applied instead as a representative for the approach focused at improved numerics. It is dedicated to highly efficient and accurate simulations of strongly unsteady and locally varying compressible problems. Indeed it is shown to reduce the simulation costs and improve simulation quality at the same time. Its dynamic adaptivity furthermore reduces the preprocessing and meshing effort reasonably. Unfortunately turbulence modeling and extension to 3D were still missing during this work. However, in view of the substantial research effort conduced at the Institute of Aerodynamics and Gasdynamics, NSDG2D will be quickly extended to a broader field of applications and allow simulations for the actual intake manifold configuration in near future indeed. Here the computational cost projections are very promising.

Transient effects during pulsed injection have been shown to play a dominant role for aeroacoustic noise levels. Injector opening and closing contribute shot-like shock waves which then are repeatedly reflected within the intake manifold, interact with the gas jet and cause increased noise levels. Thus the next step developing a comprehensive simulation methodology with even better significance for the real application should comprise the extension to a com-

plete injection cycle including a moving inlet valve and just forming cross-flow. Furthermore the internal injector flow has to be repeated. Here special care must be taken that inlet valve and injector needle are indeed closed at $t = 0\,\mathrm{s}$ in order to avoid contamination by poor domain initialization.

Besides, it is of practical interest to predict the noise contribution by gas injection as people are actually exposed to it. Depending on the impingement location, the intake manifold material and structural eigenmodes the internally generated noise translates to externally audible noise. Some frequencies might be attenuated or amplified differently than others. Hence the aeroacoustic simulation could be coupled to vibroacoustics or a transfer function approach [22] to make statements on the effect that parameter variations and noise reduction means have on the noise level observable by customers.

Considering further research and optimization of the injection parameters it is sufficient to pull just WC1 up for comparison. It represents the aeroacoustic worst case in many locations within the intake manifold with often little variation to the other WCs. Furthermore impingement is guaranteed and people are bothered most since the engine is idling at 2000rpm and noise coming from other components is reduced.

Appendix A

CCL Code in Ansys CFX

A.1 Transient Inlet Boundary Condition

The following variables are to be defined in the USER section of ANSYS CFX-Pre for proper function of the junction box routine. Consider profile files exported from a preceding simulation or interpolated in time by Matlab with the names `<path/fileprefix><file id>.csv` and the columns `<Velocity u>`, `<Velocity v>`, `<Velocity w>`, `<Pressure>`, `<Temperature>`. The files have no header.

```
USER:
  User Printing = <Yes|No>        % output debug information
  Input File Prefix = <path/fileprefix>
  File Digits = <number>          % number of file id digits used after the prefix
  File Offset = <number>          % file id to begin with
  Last Input File = <number>      % file id to stop with
  Cycle Files = <Yes|No>          % re-cycle the chosen list of files
  Table NCOL = <number>           % number of columns in file
  Update Interval = <number>      % set new profile every <number> of timesteps
END
```

Furthermore the USER routines for interpolation as well as loading a new profile in the beginning and each timestep must link to a functions defined within a given library. The library is compiled using `cfxmkext` and a Fortran compiler.

```
USER ROUTINE DEFINITIONS:
  USER ROUTINE: InletprofileU
    Calling Name = user_inletprofile_u
    Library Name = transientinlet
    Library Path = <path>
    Option = User CEL Function
  END
  USER ROUTINE: InletprofileV
    Calling Name = user_inletprofile_v
    Library Name = transientinlet
    Library Path = <path>
    Option = User CEL Function
  END
  ...
  USER ROUTINE: TransInletInit
```

```
        Calling Name = user_input
        Junction Box Location = User Input
        Library Name = transientinlet
        Library Path = <path>
        Option = Junction Box Routine
      END
    USER ROUTINE: TransInletTimestep
        Calling Name = user_input
        Junction Box Location = Start of Time Step
        Library Name = transientinlet
        Library Path = <path>
        Option = Junction Box Routine
      END
  END
```

The interpolating USER routines are mapped to library functions applicable within ANSYS CFX-Pre. Argument and result units are defined respectively. The unit of x,y,z is meters. Matching units of exported variables and the new setup has to be ensured by the user.

```
  LIBRARY:
    CEL:
      FUNCTION: InletVelocityU
        Argument Units = [m, m]
        Option = User Function
        Result Units = [m s^-1]
        User Routine Name = InletprofileU
      END
      ...
    END
  END
```

This eventually allows to define an inlet boundary condition in ANSYS CFX with reference to a Fortran library which is doing the actual interpolation each timestep.

```
  BOUNDARY: Inflow
    Boundary Type = INLET
    Location = INJECTOR INLET
    BOUNDARY CONDITIONS:
      FLOW REGIME:
        Option = Supersonic
      END
      HEAT TRANSFER:
        Option = Total Temperature
        Total Temperature = InletTemp(x,y)
      END
      MASS AND MOMENTUM:
        Option = Cartesian Velocity Components and Pressure
        Relative Static Pressure = InletPressure(x,y) - 1 [bar]
        U = InletVelocityU(x,y)
        V = InletVelocityV(x,y)
        W = InletVelocityW(x,y)
      END
    END
  END
```

In order to ensure that the interpolation tables are always up to date the solver must be setup to call the Junction Boxe routines reading the respective profile files.

```
SOLVER CONTROL:
  ..
  JUNCTION BOX ROUTINES:
    Junction Box Routine List = TransInletInit,TransInletTimestep
  END
  ..
END
```

A.2 Characteristic Non-Reflective Boundary Condition

To enable the characteristic non-reflective boundary condition the option `acoustic reflectivity` has to be enabled in ANSYS CFX-Pre. In release 10 this required to directly access the CCL code and was only available for outlets. Other boundary conditions such as openings had to be defined as outlets with disabled `artificial wall` flag in order to allow inflow.

```
BOUNDARY: Domain 1 Default
  Boundary Type = OUTLET
  Coord Frame = Coord 1
  Location = BOTTOM,OUTFLOWPLANE
  BOUNDARY CONDITIONS:
    FLOW REGIME:
      Option = Subsonic
    END
    MASS AND MOMENTUM:
      Option = Average Static Pressure
      Relative Pressure = 0 [Pa]
      ACOUSTIC REFLECTIVITY:
        Option = Nonreflective
      END
    END
    PRESSURE AVERAGING:
      Option = Average Over Whole Outlet
    END
  END
```

Since release 11 the acoustic reflectivity flag is accessible directly via the GUI as an official beta feature. It is supposed however that internally nothing was changed.

A.3 Artificial Viscosity Sponge Layer

The dynamic viscosity can be defined as a function in dependency of variables known at runtime. The variable `subdomain` is useful in particular since it is within a modeled subdomain, e.g. a sponge layer, and zero everywhere else.

```
MATERIAL: Air Ideal Gas
  ..
  PROPERTIES:
    ..
    DYNAMIC VISCOSITY:
      Dynamic Viscosity = 1.831e-05 [kg/m/s] + subdomain*0.1[kg/m/s]
      Option = Value
    END
  END
END
```

Alternatively expressions containing the actual location (x,y,z) or USER Fortran routines returning the result of a more complex definition are thinkable as well.

A.4 Continuity Source Implicit Sponge Layer

A general continuity source is defined in order to suppress acoustic waves. The USER Fortran routine `SpongeContSource(x,y,z)` returns a smoothly blended sponge strength also for complex geometries. It needs to be setup and recompiled for new simulation models.

```
SUBDOMAIN: Sponge
  Coord Frame = Coord 0
  Location = SPONGE
  SOURCES:
    EQUATION SOURCE: continuity
      Option = Fluid Mass Source
      Source = -SpongeContSource(x,y,z)*Pressure
      VARIABLE: T
        Option = Value
        Value = Temperature
      END
      VARIABLE: ed
        Option = Value
        Value = Turbulence Eddy Dissipation
      END
      VARIABLE: ke
        Option = Value
        Value = Turbulence Kinetic Energy
      END
      VARIABLE: vel
        Option = Cartesian Vector Components
        xValue = Velocity u
        yValue = Velocity v
        zValue = Velocity w
      END
    END
  END
```

The other specified variables mark the fluid state that is employed for added or subtracted mass. Using the current local fluid state ensures that other state variables than the pressure remain unchanged.

Bibliography

[1] M. B. Alkislar, A. Krothapalli, and L. M. Lourenco. Structure of a screeching rectangular jet: a stereoscopic particle image velocimetry study. *Journal of Fluid Mechanics*, 489:121–154, 2003.

[2] F. S. Alvi, C. Shih, R. Elavarasan, G. Garg, and A. Krothapalli. Control of supersonic impinging jet flows using supersonic microjets. *AIAA Journal*, 41(7):1347–1355, 2003.

[3] N. Andersson, L.-E. Eriksson, and L. Davidson. Effects of inflow conditions and sub-grid model on les for turbulent jets. In *11th AIAA/CEAS Aeroacoustics Conference*, Monterey, California, 2005.

[4] V. H. Arakeri et al. On the use of microjets to suppress turbulence in a Mach 0.9 axisymmetric jet. *Journal of Fluid Mechanics*, 490:75–98, 2003.

[5] A. Bayliss and E. Turkel. Far-field boundary conditions for compressible flows. *Journal of Computational Physics*, 48:182–199, 1982.

[6] J.-P. Berenger. Three-dimensional perfectly matched layer for the absorption of electro-magnetic waves. *Journal of Computational Physics*, 127:363–379, 1996.

[7] S. J. Beresh, J. F. Henfling, R. J. Erven, and R. W. Spillers. Penetration of a transverse supersonic jet into a subsonic compressible crossflow. *AIAA Journal*, 43(2):83–122, 2005.

[8] W. P. Bi, V. Pagneuxy, and D. Lafarge. Sound propagation in varying cross section ducts lined with non-uniform impedance by multimode propagation method. In *11th AIAA/CEAS Aeroacoustics Conference*, Monterey, California, 2005.

[9] M. Billson, L.-E. Eriksson, and L. Davidson. Jet noise prediction using stochastic turbulence modeling. In *9th AIAA/CEAS Aeroacoustics Conference and Exhibit*, Hilton Head, South Carolina, 2003.

[10] M. Billson, L.-E. Eriksson, and L. Davidson. Acoustic source terms for the linearized euler equations in conservative form. *AIAA Journal*, 43(4):752–759, 2005.

[11] D. J. Bodony. *Aeroacoustic prediction of turbulent free shear flows*. PhD thesis, Department Of Aeronautics And Astronautics, Stanford University, 2004.

[12] D. J. Bodony. Analysis of sponge zones for computational fluid mechanics. *Journal of Computational Physics*, 212:681–702, 2006.

[13] D. J. Bodony and S. K. Lele. Generation of low frequency sound in turbulent jets. In *11th AIAA/CEAS Aeroacoustics Conference*, Monterey, California, 2005.

[14] D. J. Bodony and S.K. Lele. A statistical subgrid scale noise model: Formulation. In *9th AIAA/CEAS Aeroacoustics Conference*, Hilton Head, SC, 2003.

[15] C. Bogey and C. Bailly. Three–dimensional non–reflective boundary conditions for acoustic simulations: far field formulation and validation test cases. *ACTA Acustica United With Acustica*, 88:463–471, 2002.

[16] C. Bogey, C. Bailly, and D. Juve. Computation of flow noise using source terms in linearized Euler's equations. *AIAA Journal*, 40(2):235–243, 2002.

[17] T.S. Cheng and K.S. Lee. Numerical simulations of underexpanded supersonic jet and free shear layer using weno schemes. *International Journal of Heat and Fluid Flow*, 26(5):755–770, 2005.

[18] B. Cockburn. Discontinuous Galerkin methods. *Journal of Applied Mathematics and Mechanics*, 83(11):731 – 754, 2003.

[19] T. Colonius, S. K. Lele, and P. Moin. Boundary conditions for direct computation of aerodynamic sound generation. *AIAA Journal*, 31(9):1574–1582, 1993.

[20] T. Colonius, K. Mohseni, J. B. Freund, S. K. Lele, and P. Moin. Evaluation of noise radiation mechanisms in a turbulent jet. In *Proceedings of the Summer Program 1998*, Center for Turbulence Research at Stanford University, 1998.

[21] L. Cortelezzi and A. R. Karagozian. On the formation of the counter-rotating vortex pair in transverse jets. *Journal of Fluid Mechanics*, 446:347–373, 2001.

[22] A. Cummings. Sound transmission through duct walls. *Journal of Sound and Vibration*, 239(4):731–765, 2001.

[23] L. Davidson. Evaluation of the SST-SST model: Channel flow, asymmetric diffuser and axi-symmetric hill. In *European Conference on Computational Fluid Dynamics (ECCOMAS CFD)*, Delft, 2006.

[24] J. R. DeBonis and J. N. Scott. Large-eddy simulation of a turbulent compressible round jet. *AIAA Journal*, 40(7):1346–1354, 2002.

[25] R. P. Dougherty. A wave-splitting technique for nacelle acoustic propagation. In *3rd AIAA/CEAS Aeroacoustics Conference*, Atlanta, GA, 1997.

[26] M. Dumbser, J.-M. Moschetta, and J. Gressier. A matrix stability analysis of the carbuncle phenomenon. *Journal of Computational Physics*, 197:647–670, 2004.

[27] M. Dumbser and C.-D. Munz. Arbitrary high order discontinuous Galerkin schemes. *Journal of Computational Physics*, 221(2):693–723, 2007.

[28] K. Ehrenfried. Skript zur Vorlesung Strömungsakustik I. Technische Universität Berlin, 2003.

[29] K. Ehrenfried. Vorläufiges Skript zur Vorlesung Strömungsakustik II. Technische Universität Berlin, 2003.

[30] J. A. Ekaterinaris. Performance of high-order-accurate, low-diffusion numerical schemes for compressible flow. *AIAA Journal*, 42(3):493–500, 2004.

[31] R. Ewert and W. Schröder. Acoustic pertubation equations based on flow decomposition via source filtering. *Journal of Computational Physics*, 188:365–398, 2003.

[32] J. B. Freund. Proposed inflow/outflow boundary condition for direct computation of aerodynamic sound. *AIAA Journal*, 35:740–742, 1997.

[33] J. B. Freund. Proposed inflow/outflow boundary conditions for direct computation of aerodynamic sound. *AIAA Journal*, 35:740–742, 1997.

[34] J. B. Freund, S. K. Lele, and P. Moin. Direct numerical simulation of a Mach 1.92 turbulent jet and its sound field. *AIAA Journal*, 38(11):2023–2031, 2000.

[35] R. Friedrich, J. Sesterhenn, D. Juve, and C. Bailly. Sub-project SP2: Shock induced noise in supersonic jets. Technical report, DFG-CNRS, 2005.

[36] R. J. Gaeta, K. K. Ahuja, D. B. Schein, and W. D. Solomon Jr. Large jet–noise reductions through distributed nozzles. In *8th AIAA/CEAS Aeroacoustics Conference*, 2002.

[37] T. Gandhi. Simulation of port flow and cylinder inflow with cng injection systems. Master's thesis, Ruhr University, Bochum, 2006.

[38] G. Gassner, F. Lörcher, and C.-D. Munz. A discontinuous Galerkin scheme based on a space-time expansion II. Viscous flow equations in multi dimensions. *Journal of Scientific Computing*, 34(3), 2008.

[39] E. Groeschel, M. Meinke, and W. Schroeder. Noise prediction for a turbulent jet using different hybrid methods. In *11th AIAA/CEAS Aeroacoustics Conference*, Monterey, California, 2005.

[40] X. He and J. Herring. Turbulence dissipation processes of 2-D and 3-D vortices in numerical simulations. In *27th AIAA Aerospace Sciences Meeting & Exhibit*, Reno, NV, 1989.

[41] B. Henderson. The connection between sound production and jet structure of the supersonic impinging jet. *Journal of the Acoustical Society of America*, 111(2):735–747, 2002.

[42] J. Hileman and M. Samimy. Turbulence structures and the acoustic far field of a Mach 1.3 jet. *AIAA Journal*, 39(9):1716–1727, 2001.

[43] F. Q. Hu. A perfectly matched layer absorbing boundary condition for linearized euler equations with a non-uniform mean flow. *Journal of Computational Physics*, 208:469–492, 2005.

[44] C. W. Kerechanin II, M. Samimy, and J.-H. Kim. Effects of nozzle trailing edge modifications on noise radiation in a supersonic rectangular jet. In *38th AIAA Aerospace Sciences Meeting and Exhibit*, Reno, Nevada, 2002.

[45] P. Jordan and Y. Gervais. Modelling self– and shear–noise mechanisms in inhomogeneous, anisotropic turbulence. *Journal of Sound and Vibration*, 279:529–555, 2005.

[46] P. C. E. Jorgenson and C. Y. Loh. Computing axisymmetric jet screech tones using unstructured grids. *AIAA–2002–3889*, National Aeronautics and Space Administration, Glenn Research Center at Lewis Field, Brookpark, Ohio, 2002.

[47] A. Khavarana and J. Bridges. Modelling of fine-scale turbulence mixing noise. *Journal of Sound and Vibration*, 279:1131–1154, 2005.

[48] S. I. Kim and S. O Park. Numerical analysis of the oscillatory behaviors of supersonic impinging jet flow. In *24th International Congress of the Aeronautival Sciences*, 2004.

[49] V. F. Kopiev, N. N. Ostrikov, S. A. Chernyshev, and J. W. Elliott. On the possibility of noise control in corrugated supersonic jets. In *10th AIAA/CEAS Aeroacoustics Conference*, 2004.

[50] A. Krothapalli, M. B. Alkislar, and L. M. Lourenco. The role of large scale coherent structures on screech amplitude. *AIAA paper 2001-2144*, 2001.

[51] A. Krothapalli, B. Greska, and V. Arakeri. High speed jet noise reduction using micro-jets. In *8th AIAA/CEAS Aeroacoustics Conference*, 2002.

[52] A. Krothapalli, E. Rajakuperan, F. Alvi, and L. Lourenco. Flow field and noise characteristics of a supersonic impinging jet. *Journal of Fluid Mechanics*, 392:155–181, 1999.

[53] Y.-H. Kweon, Y. Miyazato, T. Aoki, H.-D. Kim, and T. Setoguchi. The effect of a cross wire device on supersonic jet noise. In *11th AIAA/CEAS Aeroacoustics Conference*, 2005.

[54] E. W. Lemmon, M. O. McLinden, and D. G. Friend. *NIST Chemistry WebBook*, chapter Thermophysical Properties of Fluid Systems. National Institute of Standards and Technology, NIST Standard Reference Database Number 69, (http://webbook.nist.gov), 2005.

[55] R. C. K. Leung, X. M. Li, and R. M. C. So. Comparative study of nonreflecting boundary condition for one-step duct aeroacoustics simulation. *AIAA Journal*, 44:664–667, 2006.

[56] X. D. Li and J. H. Gao. Numerical simulation of axisymmetric supersonic screech tones. In *10th AIAA/CEAS Aeroacoustics Conference*, 2004.

[57] M. J. Lighthill. On sound generated aerodynamically - I. General theory. In *Proceedings of the Royal Society of London, Series A: Mathematical and Physical Sciences*, volume 211 of *1107*, pages 564–587, London, 1952.

[58] F. Lörcher, G. Gassner, and C.-D. Munz. A discontinuous Galerkin scheme based on a space–time expansion. I. Inviscid compressible flow in one space dimension. *Journal of Scientific Computing*, 32(2), 2007.

[59] H. Lou. *Control of Supersonic Impinging Jets Using Microjets*. PhD thesis, The Florida State University, College of Engineering, 2005.

[60] H. Lou, F. S. Alvi, C. Shih, J. Choi, and A. Annaswamy. Active control of supersonic impinging jets: Flowfield properties and closed-loop strategies. In *1st AIAA Flow Control Conference and Exhibit*, St. Louis, Missouri, 2002.

[61] H. Lou, C. Shih, and F.S. Alvi. A PIV study of supersonic impinging jet. In *9th AIAA/CEAS Aeroacoustics Conference and Exhibit*, Hilton Head, South Carolina, 2003.

[62] C. Lui and S. K. Lele. A numerical investigation of broad-band shock noise. *AIAA paper 2002-0074*, 2002.

[63] C. Lui and S. K. Lele. A numerical study of shock-associated noise. *AIAA paper 2002-2530*, 2002.

[64] C. Lui and S. K. Lele. Generation mechanism of shock-associated noise. In *9th AIAA/CEAS Aeroacoustics Conference and Exhibit*, Hilton Head, South Carolina, 2003.

[65] B. Maté et al. Experimental and numerical investigation of an axisymmetric supersonic jet. *Journal of Fluid Mechanics*, 426:177–197, 2001.

[66] F. Menter. Zonal two equation k-omega turbulence models for aerodynamic flows. In *24th AIAA Fluid Dynamics Meeting*, Orlando, 1993.

[67] F. Menter, R. Bender, and M Kuntz. A scale-adaptive simulation model using two-equation models. In *43st AIAA Aerospace Sciences Meeting & Exhibit*, Reno, NV, 2005.

[68] I. M. Milanovic. Fluid dynamics of highly pitched and yawed jets in crossflow. *AIAA Journal*, 42(5):874–882, 2004.

[69] C. Millet and G. Casalis. Selection of acoustic modes in the vicinity of supersonic jets. In *8th AIAA/CEAS Aeroacoustics Conference*, 2002.

[70] K. Mohseni, T. Colonius, and J. B. Freund. An evaluation of linear instability waves as sources of sound in a supersonic turbulent jet. *Physics of Fluids*, 14(10):3593–3600, 2002.

[71] P. J. Morris and F. Farassat. Acoustic analogy and alternative theories for jet noise prediction. *AIAA Journal*, 40(4):671–680, 2002.

[72] M. L. Munjal. On the cut-on frequencies of a large round duct with azimuthal as well as radial partitions. *Journal of Acoustical Society of America*, 84:1936–1939, 1988.

[73] A. H. Nayfeh and D. Telionis. Acoustic propagation in ducts with varying cross sections. *Journal of the Acoustical Society of America*, 54(6):1654—1661, 1973.

[74] A. Nielsen, D. Torres, and E. Coutsias. Decaying two-dimensional turbulence in bounded flows. In *International Congress on Plasma Physics and 25th EPS Conference on Controlled Fusion and Plasma Physics*, 1998.

[75] J. Panda and R. G. Seasholtz. Experimental investigation of density fluctuations in high–speed jets and correlation with generated noise. *Journal of Fluid Mechanics*, 450:97–130, 2002.

[76] J. Panda, R. G. Seasholtz, et al. Effect of heating on turbulent density fluctuations and noise generation from high speed jets. In *10th AIAA/CEAS Aeroacoustics Conference*, 2004.

[77] S. Paul Pao and Khaled S. Abdol-Hamid. Numerical simulation of jet aerodynamics using the three-dimensional Navier-Stokes code PAB3D. Technical Report NASA Technical Paper 3596, National Aeronautics and Space Administration, Langley Research Center, Hampton, Virginia, 23681-0001, 1996.

[78] J. Paret and P. Tabeling. Experimental observation of the two-dimensional inverse energy cascade. *Physical Review Letters*, 79:4162–4165, 1997.

[79] K. M. Peery and S. T. Imlay. Blunt body flow simulations. *AIAA Paper*, 88-2924, 1988.

[80] B. P. Petitjean, P. J. Morris, and D. K. McLaughlin. On the nonlinear propagation of shock-associated jet noise. In *11th AIAA/CEAS Aeroacoustics Conference*, 2005.

[81] T. J. Poinsot and S. K. Lele. Boundary conditions for direct simulations of compressible viscous flows. *Journal of Computational Physics*, 101:104—129, 1992.

[82] L. J. Poldervaart, A. P. J. Wijnands, and L. Bronkhorst. Aerosonic games with the aid of control elements and externally generated pulses. *AGARD Conf. Proc., Noise Mechanisms*, 131:20.1–20.4, 1973.

[83] S. B. Pope. *Turbulent Flows*. Cambridge University Press, 2000.

[84] A. Powell. On the mechanism of choked jet noise. *Proceedings of the Physical Society London*, 66:1039–1056, 1953.

[85] E. J. Rice and G. Raman. Enhanced mixing of a rectangular supersonic jet by natural and induced screech. *AIAA–93–3263*, National Aeronautics and Space Administration, Lewis Research Center, Cleveland, Ohio, 1993.

[86] S.K. Richards, X. Zhang, X.X. Chen, and P.A. Nelson. The evaluation of non-reflecting boundary conditions for duct acoustic computation. *Journal of Sound and Vibration*, 270:539–557, 2004.

[87] S. W. Rienstra. Sound propagation in slowly varying lined flow ducts of arbitrary cross-section. *Journal of Fluid Mechanics*, 495:157–173, 2003.

[88] W. De Roeck, G. Rubio, and W. Desmet. On the use of filtering techniques for hybrid methods in computational aero-acoustics. In *international conference on noise and vibration engineering (ISMA2006)*, Leuven, Belgium, 2006.

[89] K. Senesh and V. Babu. Numerical simulation of subsonic and supersonic jets. In *11th AIAA/CEAS Aeroacoustics Conference*, 2005.

[90] H. Shen and C. K. W. Tam. Three-dimensional numerical simulation of the jet screech phenomenon. *AIAA Journal*, 40(1):33–41, 2001.

[91] K. Sinha and G. V. Candler. Turbulent dissipation-rate equation for compressible flows. *AIAA Journal*, 41(6):1017–1021, 2003.

[92] S. H. Smith and M. G. Mungal. Mixing, structure and scaling of the jet in crossflow. *Journal of Fluid Mechanics*, 35:83–122, 1998.

[93] M. Soteriou, R. Reba, and T. Maeder. Numerical study of the impact of streamwise vorticity on jet noise. In *8th AIAA/CEAS Aeroacoustics Conference*, 2002.

[94] P. R. Spalart. Young-person's guide to detached eddy simulation grids. Technical Report NASA/CR-2001-211032, NASA, 2001.

[95] P. R. Spalart, W-H. Jou, M. Strelets, and S. R. Allmaras. Comments on the feasibility of les for wings, and on a hybrid RANS/LES approach. In *1st AFOSR Int. Conf. On DNS/LES*, Greyden Press, Columbus, OH, 1997.

[96] Chu B. T. and Kovasnay L. S. G. Interactions in a viscous heat-conducting compressible gas. *Journal of Fluid Mechanics*, 3(5), 1958.

[97] S. Ta'asan and D. M. Nark. An absorbing buffer zone technique for acoustic wave propagation. In *38th AIAA Aerospace Sciences Meeting and Exhibit*, pages 9–12, Reno, Nevada, 1995.

[98] C. K. W. Tam. The shock-cell structures and screech tone frequencies of rectangular and non-axisymmetric supersonic jets. *Journal of Sound and Vibration*, 121(1):135–147, 1988.

[99] C. K. W. Tam. Computational aeroacoustics: issues and methods. *AIAA Journal*, 33:1788–1796, 1995.

[100] C. K. W. Tam, L. Auriault, and F. Cambuli. Perfectly matched layer as an absorbing boundary condition for the linearized euler equations in open and ducted domains. *Journal of Computational Physics*, 144:213–234, 1998.

[101] C. K. W. Tam and N. N. Pastouchenko. Noise from fine-scale turbulence of nonaxisymmetric jets. *AIAA Journal*, 40(3):456–464, 2002.

[102] C. K. W. Tam, J. M. Seiner, and J. C. Yu. Proposed relationship between broadband shock associated noise and screech tones. *Journal of Sound and Vibration*, 110:309, 1986.

[103] C. K.W. Tam, N. N. Pastouchenkoa, and R. H. Schlinker. Noise source distribution in supersonic jets. *Journal of Sound and Vibration*, 291(1-2):192–201, 2006.

[104] A. T. Thies and C. K. W. Tam. Computation of turbulent axisymmetric and nonaxisymmetric jet flows using the k–ε model. *AIAA Journal*, 34(2):309–316, 1996.

[105] K. W. Thompson. Time dependent boundary conditions for hyperbolic systems. *Journal of Computational Physics*, 89:439–4612, 1990.

[106] B. Thurow, M. Samimy, and W. Lempert. Structure of a supersonic impinging rectangular jet via real-time optical diagnostics. In *32nd AIAA Fluid Dynamics Conference*, St. Louis, Missouri, 2002.

[107] A. Uzun, G. A. Blaisdell, and A. S. Lyrintzis. 3-d large eddy simulation for jet aeroacoustics. In *9th AIAA/CEAS Aeroacoustics Conference*, Hilton Head, SC, 2003.

[108] J. Varnier and W. Raguenet. Experimental characterization of the sound power radiated by impinging supersonic jets. *AIAA Journal*, 40(5):825–831, 2002.

[109] K. Viswanathan. Aeroacoustics of hot jets. In *8th AIAA/CEAS Aeroacoustics Conference*, 2002.

[110] R. von Kaenel, L. Kleiser, N. A. Adams, and J. B. Vos. Large-eddy simulation of shock-turbulence interaction. *AIAA Journal*, 42(12):2516–2528, 2004.

[111] T. Yaguchi and K. Sugihara. A new characteristic non-reflecting boundary condition for the multidimensional Navier-Stokes equations. In *11th AIAA/CEAS Aeroacoustics Conference*, 2005.

[112] W. Zhao, S. H. Frankel, and L. Mongeau. Effects of spatial filtering on sound radiation from a subsonic axisymmetric jet. *AIAA Journal*, 38(11):2032 – 2039, 2000.

[113] O. C. Zienkiewicz, R. L. Taylor, and J. Z. Zhu. *The Finite Element Method Set*, volume 1 and 3. Elsevier, 6th edition, 2005.